UNIVERSITÀ DEGLI STUDI DI MODENA E REGGIO EMILIA

Dottorato di ricerca in Matematica

In convenzione con l'Università degli Studi di Ferrara e l'Università degli Studi di Parma

Ciclo XXXIV

Energetic Boundary Element Method for 2D Elastodynamics Problems in Time Domain

Relatore:
Prof.ssa Alessandra Aimi

Correlatore:
Prof.ssa Chiara Guardasoni

Coordinatore del Corso di Dottorato:
Prof. Cristian Giardinà

Candidato: Giulia Di Credico

Ai miei nonni, Vanna e Cesare.

Abstract (english version)

The aim of this thesis is to investigate various aspects of the application of the *Energetic Boundary Element Method* (Energetic BEM) for the resolution of elastodynamic problems in bidimensional unbounded domains. The first part of the work is dedicated to the introduction of the differential problem, rewritten in terms of different *Boundary Integral Equations* (BIEs), depending on characteristic integral operators and suitable to solve problems equipped by Dirichlet or Neumann datum at the boundary. These BIEs are set in a space-time weak form, based on energy arguments, and numerically solved by means of the Energetic BEM. All the considered weak BIEs, once discretized, give rise to linear systems with lower triangular block Toeplitz matrix, whose entries are quadruple space-time integrals. Thus, a consistent part of the thesis discusses the quadrature formulas employed to compute numerically these elements with high accuracy, taking into account the characteristic space singularities and performing an accurate study of the integration domain, in local variables, that allows to overcome the issues of the integration of peculiar step functions that feature all the integral kernels. A theoretical analysis of the indirect weak form with single layer operator is also executed and numerous numerical results are presented to confirm the correctness and the effectiveness of the Energetic BEM.

A part of the thesis takes into account different types of space discretization, that turn out to be useful, for instance, to catch the asymptotic behaviour of the single layer and the hypersingular BIEs solutions at the endpoints of open obstacles or at the corners of polygonal closed arcs. Meshes geometrically or algebraically refined at these critical points improve the convergence of the proposed methods. An in depth analysis of the error decay, in energy norm, is shown with respect to different types of refinement (h-version, p-version and hp-version are in particular considered). Several numerical tests, arising from the implementation of the Energetic BEM, are shown, in order to validate the theoretical results by showing the slope of the estimated error related to the presented discretization methods.

The following issue is moreover considered in this thesis work: the BEM matrices are composed by time-dependent blocks that are generally fully populated, leading to considerable computational costs and memory requirements of the energetic BEM, that can prevent its application to large scale realistic problems. Thus, a fast technique, based on the *Adaptive Cross Approximation* (ACA), is provided in order to get a low rank approximation of the time blocks, hence reducing drastically the number of the original entries to be evaluated. This procedure leads to a drop in the computational time, spent to assemble and solve the linear system, as well as in the memory storage requirements, which are generally relevant. The effectiveness of this strategy is theoretically and numerically proved for the single layer weak formulation, both in the contexts of acoustic and elastic wave propagation problems.

Abstract (versione italiana)

L'obbiettivo di questa tesi è lo studio dell'applicazione del *Metodo agli Elementi di Contorno di tipo Energetico* (Energetic BEM) per la risoluzione di problemi di elastodinamica in domini bidimensionali illimitati. Nella prima parte del lavoro viene introdotto il problema differenziale, riscritto in termini di diversi tipi di *Equazioni Integrali di Contorno* (BIE), dipendenti da operatori integrali caratteristici e che risultano essere utili alla risoluzione di problemi con dato di Dirichlet o di Neumann sull'ostacolo. Queste BIE sono ridefinite in formulazioni deboli nel dominio del tempo, basate sull'energia del sistema, e risolte numericamente tramite Energetic BEM. Le formulazioni deboli considerate, una volta discretizzate, danno luogo a sistemi lineari con matrici triangolari inferiori con struttura di Toeplitz a blocchi, i cui elementi risultano essere integrali quadrupli in spazio e tempo. Pertanto, una parte consistente di tesi è incentrata sull'analisi delle formule di quadratura impiegate nell'approssimazione numerica, ad alta precisione, di questi integrali, tenendo conto delle singolarità spaziali caratteristiche e eseguendo un accurato studio del dominio di integrazione, in variabili locali, che permette di evitare l'integrazione diretta delle funzioni di Heaviside comuni a tutti i tipi di nuclei integrali. Viene inoltre illustrata l'analisi teorica della formulazione debole con operatore di strato singolo e numerosi test numerici vengono presentati a conferma della correttezza e dell'efficacia dell'Energetic BEM.

Parte della tesi prende in considerazione diversi tipi di discretizzazione spaziale, con l'obbiettivo di approssimare correttamente le soluzioni delle BIE, associate a operatori di strato singolo e ipersingolare, asintotiche vicino agli estremi di un ostacolo aperto o nei pressi degli angoli di un arco poligonale chiuso. Un raffinamento di tipo geometrico o algebrico della mesh vicino a questi punti critici migliora la convergenza del metodo numerico: viene mostrata pertanto un'analisi approfondita del decadimento dell'errore in norma energetica rispetto all'uso di vari metodi di raffinamento spaziale (quali la tecnica h, la tecnica p e la tecnica hp). Anche in questo caso, diversi test numerici, ottenuti tramite l'implementazione dell'Energetic BEM, vengono mostrati con l'obbiettivo di verificare le stime teoriche dell'errore relative ai vari metodi di discretizzazione discussi.

Un'ulteriore questione è argomento di questo lavoro di tesi: le matrici BEM sono composte da blocchi temporali che diventano generalmente densi con l'avanzare del tempo, comportando un considerevole dispendio di costi computazionali e di memoria per l'implementazione dell'Energetic BEM, rendendo la sua applicazione a problemi realistici su larga scala molto onerosa. Viene pertanto proposta una tecnica veloce, basata sull'*Adaptive Cross Approximation* (ACA), che permette un'approssimazione a basso rango dei blocchi temporali, riducendo drasticamente il numero degli elementi originari della matrice da valutare. Ciò porta anche ad una riduzione della memoria richiesta e dei tempi di assemblaggio e di risoluzione del sistema lineare. La fattibilità della strategia è dimostrata teoricamente e numericamente nello specifico per la formulazione debole di singolo strato, risolvendo problemi di propagazione sia di onde acustiche che elastiche.

Contents

Introduction

Historycal background

The XIX century was fundamental for the growing of studies in continuum mechanics. In this period in fact, the impulse to the development of first practical applications came especially from the expansion of railways and structural mechanical projects. In this thriving context for engineering and mechanical sciences, the theory of materials was perfected, laying the foundations for the theory of elasticity [20, 60].
The fundamentals of this theory can be found in the French school of the early 1800s, mainly in the works of Navier, Cauchy, Poisson, Lamé, Clapeyron and, successively, of Barré de Saint-Venant. Before their studies, there wasn't a valid mathematical formalization of the subject. The point of view developed by Cauchy in the 1820s was particularly decisive, but in two memories presented by Navier to the Académie des Sciences of Paris (1821-1822) for the first time we can find the equations of elasticity for an isotropic body, elaborated by the mathematician considering a phenomenological molecular model of a medium. We also owe to Navier his fundamental contribution to fluid dynamics and in particular to the elaboration of the Navier-Stokes equations. A general analysis for anisotropic bodies was developed later by Poisson (1839), who moreover established the propagation of body waves (pressure and shear) in elastic medium. Other contributes were given by Lord Rayleigh (1885), who discovered another type of elastic surface waves, denominated in his honour Rayleigh waves. These theoretical studies on elastic waves propagation were confirmed at the end of the XIX centuries when, thanks to an earthquake recording, Oldhan recognized the three types of characteristic waves theorized by Poisson and Rayleigh.
From the second half of 1800s the research direction followed the idea of formalizing solutions of Partial Differential Equations (PDEs) by boundary integral formulations (for various physical and mechanical problems, not only for elasticity). The contribution of the Italian mathematicians Betti and Somigliana was considerable, anyway, even with integral formulations, deriving the analytical solution only for limited class of problems depending on the simplest geometries.
The major impetus given to the research in elasticity, and more generally to the accurate approximation of the solutions to the PDEs of physical mathematics, came with the advent of computers, starting from the sixties of the XX century. Implementations of powerful methodologies for the numerical resolution of this kind of problems have been possible only since those years.

The Finite Element Method

The Finite Element Method (FEM) is a versatile instrument for PDEs that, after a suitable discretization of the domain of interest, allows to approximate the solution with an accuracy depending on the refinement of the mesh. The advatage is the straightforward construction of the linear system that implies the discretization of the weak formulation of the problem. A surveys of applications of FEMs to many physical problems (such as plane strain, heat transfer and fluid flow) can be found in the book of Zienkiewicz et al. [78]. For a deepening on the construction of the method and applications to linear elastodynamics see the Andersen's book [14]. In the works of Bielak and co-authors [23] and Toshinawa and Ohmachi [76] we can find an intersting case of study about a seismic event compared with the data furnished by the application of FEM to the resulution of specific wave propagation problems. For the time dependent case, FEM is generally used to discretize the equation of motion in the space variables, while the remaining system in the time variable is resolved by a time stepping scheme which does not require a further matrix factorization, as in [1] and [49] (this last one presents also analysis on error estimates). An interesting application for elastic problems with the emphasis on the calculation of the shear and the pressure components of the solution and energetic considerations are presented by Burel, Impériale and Joly in [25].
The drawback in the context of elastodynamics problems defined in unbounded domains is the need to terminate the mesh imposing arbitrary conditions on the artificial boundary, which may reflect spurious waves that can invalidate the results.

The Boundary Element Method

In this scenario, elastodynamic problems can be efficiently solved using a Boundary Element Method (BEM), which requires, for the implementation, to express the solution over the domain of interest by an integral representation formula where integrals are not defined on the entire domain, but only on the boundary, leading to the advantage of a reduction of the dimensional complexity w.r.t the applications of other standard methods such as FEM and finite differences. Moreover, this kind of integral formulations incorporates automatically the propagation at infinity and can be easily adapted (formulations are basically the same with just a change in sign) to diffusion problems in unbounded medium.
First examples of use of integral formulations in elasticity can be found in the work of Cruse and Rizzo [27] and results of reference in this field are reported by Manolis an Beskos in [57]. In these papers the integral formula has a switch from the time variables to the Laplace domain, where the problem is discretized. Then, to catch the transient behaviour of the solution an inverse transformation is necessary. Anyway working with a time domain approach (TD-BEM) is preferable since it allows to observe the phenomenon as it evolves and results do not depend on the parameters of the Laplace transform.
Time domain standard BEM approach has been developed by many authors, discretizing the boundaries (2D countour or 3D surfaces) and then collocating the Boundary Integral Equations (BIEs) at the nodal points. Examples of applications are furnished by Frangi in [35] and Birgisson in [24].
Alternative strategies to manage the temporal discretization, known as CQ-BEM, is to operate with the Lubich quadrature formulas (see [54] and [55]). This technique fits the

nature of integration formulas, which are nothing more than convolution products both in time and in space. Instances of implementation in elastodynamics are in the works of Schanz and Antes [72, 73] and in the papers of Falletta and co-authors for application to elastodynamics problems [33] and for the resolution of wave propagation problems [32].
A novelty in the discretization approach of the integral representazion formulas can be found in the recent paper of Pölz and Schanz [69] where, in particular the time variable is considered as an additional spatial coordinate, inducing the approximation of the BIE unknown by shape functions that do not separate the space-time variables.
Standard implementation of TD-BEM with Galerkin and collocation may present numerical instabilities in time, as dicussed in the paper by Frangi and Novati [36], while genuine convergence results for the acustic wave propagation can be found in the pionering works of Bamberger, Ha-Duong and Bècache (wave propagation problems in [15, 16] and hard-scattering in elastodynamics in [19]) that apply an energetic approach. The Energetic BEM in case of scalar waves propagation (see the works by Aimi and collaborators [9, 8, 12]) shows a long-time stability and guarantees excellent approximation accuracy. In this thesis, the extension to elastodynamic problems is considered, starting from a former analysis presented in [5].

Graded mesh and *hp* methods

In the application of the BEM to elastic or scalar wave diffusion we have no constraints in the type of mesh and in the choice of the degree of accuracy we can impose to discretize the boundary and to approximate the unknowns of the BIEs at hand. Nevertheless these solutions, or their spatial derivatives, are characterized by a singular behaviour near the limits or at the angular points of the obstacle. Studies and theoretical results for what concerns the integral solution of the scalar wave equation in conical and cilindrical shape domains are carried out by Plamenevskiĭ and collaborators in [50, 68]. Regarding the singularity of the boundary unknowns in elastodynamics, from the works of Nicaise and Grisvard [66, 44], thanks to the analysis of the singular expansion of the displacement solution at a corner point of the arc, we discover how the amplitude of the angle affects the singular behaviour. Thus, combining BEM with spatial refinement methods, such as graded mesh and p and hp refinement, allows to better approximate these solutions in order to limit the error in energy norm without augmenting the spatial DOF of the problem. Interesting results of applications of graded mesh and hp refinements BEM for scalar problems can be found in the works by Gimperlein and collaborators in [38, 41], with a priori error estimates in dependence with the parameters of the discretization. For the case of adaptive mesh methods see also [42].

Fast BEMs

The accurate results coming from application of BEM to the above cited problems are counterbalanced by the fact that the matrix arising from the discretization phase is full for static problems, and analogously the time blocks in transient case, thus computation of full BEM matrices becomes a challenge in case of large-scale problems. Methods that allow to overcome this issue are various. First of all the panel clustering, with which sparsification of BEM matrices is obtained by an algorithm that builds an indexing tree structure

dependent on the elements of spatial discretization. For the Laplace's equation we refer to the work [48] and for the scalar wave propagation we suggest [34].
Another technique apt to the sparsification of matrices is contemplated by the hierarchical methods [47]: these algorithms exploit the low-ranking structure of the sub-blocks of the BEM matrices, which can therefore be decomposed by Singular Value Decomposition (SVD) or Adaptive Cross Approximation (ACA) into the product of matrices with fewer elements. For application in 3D elastodynamics we suggest the work in [26], developed in frequency domain.
Moreover wavelet functions for the spatial approximations of the boundary unknowns can be employed to obtain sparse blocks, thanks to the localization and vanishing moments properties of this kind of basis functions. For the algorithm to construct these particular basis we refer to [13] and for combination with the CQ-BEM approach for scalar wave problem we suggest [28, 21].

Outlines of the thesis

This thesis investigates several aspects of the Energetic BEM applied to the resolution of elastodynamic propagation problems in a 2D domain.

In Chapter 1 we provide all the fundamental notations about the model problem we intend to solve by BEM in a bidimensional domain Ω with smooth and Lipschitz boundary $\partial\Omega = \Gamma$. The unknown displacement of the 2D vectorial equation governing the motion is rewritten in terms of an integral representation formula depending on the elastodynamics fundamental 2D solution $\mathbf{G^{uu}}$. Exploiting the type of condition set at the boundary (Dirichlet, Neumann or mixed) we derive different types of BIEs which can be assembled starting from the definition of the single layer operator V, of the double layer potentials K and K^* and of the hypersingular operator D. The BIEs are successively rewritten in terms of space-time weak formulations associated with the energy $\mathcal{E}$ of the elastodynamics system and the bilinear form depending on the single layer integral operator is theoretical analyzed in Section 1.4, in order to set up the Sobolev functional spaces where coerciveness and continuity of the related weak problem hold.
All the considered weak BIEs, once discretized in space and time, give rise to linear systems with lower triangular Toeplitz matrix, whose entries, after a double analytical integration in time variables, are double integrals defined on the mesh elements set on the boundary Γ. The peculiar kernels characterizing these integral elements, in relation to the corresponding discretized integral operator, are presented in Section 1.5 and numerous numerical implementations of the energetic BEM are exposed in Section 1.6, both for the resolution of Neumann and for Dirichlet elastodynamics problems, confirming the correctness and the effectiveness of the method.

In Chapter 2, we prove that the unknown displacement of the elastodynamics equation and the related boundary traction are featured by a singular behaviour near the corners of a polyhedral domain, in the 3D case, and of a polygon, in a 2D problem. We therefore propose different types of spatial discretization of the energetic weak formulations, for both Dirichlet and Neumann constraints at the boundary, in order to catch as best as possible the asymptotic behaviour of the related weak solutions. This asymptotic behaviour

in particular has order strictly connected to the amplitude of the considered corner, as shown in Section 2.1. Meshes geometrically or algebraically refined near these of critical points improve the convergence towards the solution and an accurate analysis of the error committed in relation to the parameters of space discretization is provided in Section 2.3. The numerical results exposed in Section 2.4 are related to 2D elastodynamics problems in polygonal domains or external to open flat obstacles, and they verify the theoretical slopes estimated for the error induced by the resolution of the related Galerkin energetic weak formulations with Dirichlet and Neumann conditions.

In Chapter 3, we provide a remedy for the high computational costs required for the assembly and the memory storage of the Toeplitz matrix representing, at a discrete level, the energetic weak elastodynamics problem we intend to solve. This matrix in fact is composed of temporal blocks that reveal to be fully populated as the corresponding time index increases: this issue could prevent the application of the energetic BEM for problems discretized by a high number of spatial and temporal degrees of freedom (DOFs).
Since we treat in this chapter both problems of acoustic and elastic waves propagation, we introduce them in Sections 3.1-3.2 with the related implementations of the Energetic BEM.
In Section 3.3 we prove, both for the acoustic and the elastic case, that is possible to rewrite the matrix elements of the Galerkin weak problem in a low rank expansion, which suggests us that each temporal block can be decomposed as the product of two low rank matrices. This decomposition can be performed by the *Adaptive Cross Approximation*, which is an algebraic tool easy to implement and that does not require a previous computation of the entire matrix.
In Section 3.4, numerous numerical experiments are presented, showing in particular the memory and the computational time saved in the resolution of problems with high number of DOFs, demonstrating moreover that the quality of the results is not affected by the application of the proposed compression algorithm.

Chapter 4 is dedicated to the presentation of the quadrature formulas employed to approximate, with high precision, the integrals in space variables involved in the computation of the entries of the discretized integral operators. In Section 4.1 we proceed with an accurate study of the integration domains in local variables, highlighting the fact that the shape of these integral domains depends on the mutual position of the boundary mesh elements. The aim is to determine the regions, in local coordinates, where the peculiar step functions characteristic of the fundamental solution $\mathbf{G^{uu}}$ have positive argument. If these domains present points where the boundaries are not differentiable, they are further split into subdomains. Following this splitting technique, in Section 4.2 we take also into consideration the characteristic space singularities: $\mathcal{O}(\log(r))$ for the single layer integral operator, $\mathcal{O}(1/r)$ for the double layer integral operator and $\mathcal{O}(1/r^2)$ for the hypersingular integral operator, in order to furnish the quadrature rules that allow to overcome at best these singularity issues.

In the Appendix we show the computational details of the exact time integration with which we obtain the integral form of the entries of all the discretized integral operators

V, K, K^* and D and in the final Chapter, Conclusions and Future perspectives, we provide some final remarks about the entire thesis work.

Notation Remarks. The elastic problems are of a vector nature and therefore, if not otherwise specified, summations are implied in case of repeated indices, in order to avoid burdening of notations along the thesis.
All the vectorial quantities are written in bold font, as the fields of displacements and tractions $\mathbf{u}$ and $\mathbf{p}$. Scalar quantities, like the components of a vectorial field, are indicated with an italic font, for example u_i and p_i.

Chapter 1

Elastodynamics by energetic BEM

1.1 The 2D model problem

In this chapter we focus on the propagation of elastic waves into a 2D bounded domain $\Omega \subset \mathbf{R}^2$ occupied by a linear, homogeneous, elastic and isotropic medium. The set Ω is characterized by a Lipschitz closed boundary $\Gamma = \partial\Omega$, the latter acting as an obstacle for the waves propagation. We define also the unbounded complementary set $\Omega_e = \mathbf{R}^2 \setminus \overline{\Omega}$. We introduce then all the fundamental notations and formulas we need to present the theory of elasticity, starting from the physical characteristics of the medium, which are incorporated in the mass density ϱ and in the so called *Lamè parameters* λ and μ

$$\lambda = \frac{\nu E}{(1+\nu)(1-2\nu)} > 0, \quad \mu = \frac{E}{2(1+\nu)} > 0, \tag{1.1}$$

depending on the positive *Young moduls* E and on the *Poisson ratio* ν. Since we deal with a linear model, these physical quantities are constants independent from the space variable $\mathbf{x} \in \mathbf{R}^2$, which is described by its cartesian components $\mathbf{x} = (x_1, x_2)^\top$. Therefore, the time-domain evolution of the motion is governed by a system of linear PDEs, derived by the application of the *Cauchy first law of motion* in the x_i-direction:

$$\frac{\partial \sigma_{ij}[\mathbf{u}]}{\partial x_j}(\mathbf{x},t) + \varrho b_i(\mathbf{x},t) = \varrho \frac{\partial^2 u_i}{\partial t^2}(\mathbf{x},t), \quad i = 1,2,\ (\mathbf{x},t) \in \Omega \times (0,T]. \tag{1.2}$$

The vector field $\mathbf{b} = (b_1, b_2)^\top$ in (1.2) represents a body force per mass unity and $\mathbf{u} = (u_1, u_2)^\top$ is the unknown displacement. It is trivial to observe that equation (1.2) remains true also in case of outer propagation, namely for $\mathbf{x} \in \Omega_e$.
In equation (1.2) we recognize the components of the 2D stress tensor $\boldsymbol{\sigma} = (\sigma_{ij})_{i,j=1,2}$

$$\sigma_{ij}[\mathbf{u}](\mathbf{x},t) = C_{ij}^{kl} \frac{\partial u_k}{\partial x_l}(\mathbf{x},t), \quad \mathbf{x} \in \Omega, t \in (0,T],\ i,j = 1,2, \tag{1.3}$$

where, as the medium is isotropic, the constants

$$C_{ih}^{kl} = \lambda \delta_{ih}\delta_{kl} + \mu(\delta_{ik}\delta_{hl} + \delta_{il}\delta_{hk}), \quad i,h,k,l = 1,2, \tag{1.4}$$

are the elements of the fourth order *Hooke tensor* $\mathbf{C} = \left(C_{ih}^{kl}\right)_{i,h,k,l=1,2}$, depending only on the Lamé parameters and on the *Kronecker delta* δ_{ij} and for which the following symmetry properties hold:

$$C_{ih}^{kl} = C_{hi}^{kl} = C_{ih}^{lk} = C_{kl}^{ih}. \tag{1.5}$$

We observe that the stress tensor (1.3), thanks to definition (1.4), can be rewritten in the form

$$\sigma_{ij}[\mathbf{u}](\mathbf{x},t) = \lambda\delta_{ij}\varepsilon_{kk}[\mathbf{u}](\mathbf{x},t) + 2\mu\varepsilon_{ij}[\mathbf{u}](\mathbf{x},t), \quad i,j = 1,2,$$

where the *deformation tensor* $\boldsymbol{\varepsilon}$ acts on $\mathbf{u}$ as follows

$$\varepsilon_{ij}[\mathbf{u}](\mathbf{x},t) = \frac{1}{2}\left(\frac{\partial u_i}{\partial x_j}(\mathbf{x},t) + \frac{\partial u_j}{\partial x_i}(\mathbf{x},t)\right), \quad i,j = 1,2. \tag{1.6}$$

By using the definition of the stress tensor $\boldsymbol{\sigma}$ in (1.3) we introduce another fundamental vectorial field, the traction $\mathbf{p} = (p_1, p_2)^\top$:

$$p_i(\mathbf{x},t) = \sigma_{ih}[\mathbf{u}](\mathbf{x},t)n_h(\mathbf{x}), \quad \mathbf{x} \in \Omega, t \in (0,T],\ i = 1,2, \tag{1.7}$$

where $\mathbf{n}(\mathbf{x}) = (n_1(\mathbf{x}), n_2(\mathbf{x}))^\top$ is the unit normal vector associated to the field point $\mathbf{x}$ (if Γ^- and Γ^+ denote respectively the lower and the upper face of the obstacle and $\mathbf{x} \in \Gamma$, then $\mathbf{n}(\mathbf{x})$ is oriented from Γ^- to Γ^+). Equation (1.2) can be rewritten by different compact notations: the first one is

$$\nabla \cdot \boldsymbol{\sigma}[\mathbf{u}] + \varrho\mathbf{b} = \varrho\ddot{\mathbf{u}}, \quad \mathbf{x} \in \Omega,\ t \in (0,T], \tag{1.8}$$

where the upper dots indicate the second time derivative, while the second one, obtained by (1.3), has the following vectorial form, usually identified in literature as *Navier equation*:

$$(\lambda+\mu)\nabla(\nabla\cdot\mathbf{u}) + \mu\Delta\mathbf{u} + \varrho\mathbf{b} = \varrho\ddot{\mathbf{u}}, \quad \mathbf{x} \in \Omega,\ t \in (0,T]. \tag{1.9}$$

with ∇ and Δ being in the formula the *Nabla* and the *Laplace* operators, that act on a scalar function $f : \Omega \times (0,T] \to \mathbf{R}$ performing the following derivatives in the space variables x_1, x_2:

$$\nabla f := \left(\frac{\partial f}{\partial x_1}, \frac{\partial f}{\partial x_2}\right)^\top, \quad \Delta f := \frac{\partial^2 f}{\partial x_1^2} + \frac{\partial^2 f}{\partial x_2^2},$$

and whose application can be naturally extended to a vectorial field $\mathbf{f} : \Omega \times (0,T] \to \mathbf{R}^2$ in this way:

$$\nabla \cdot \mathbf{f} := \frac{\partial f_1}{\partial x_1} + \frac{\partial f_2}{\partial x_2}, \quad \Delta\mathbf{f} = \mathbf{g}, \text{ with } g_i = \frac{\partial^2 f_i}{\partial x_1^2} + \frac{\partial^2 f_i}{\partial x_2^2},\ i = 1,2.$$

Equation (1.8) or (1.9) has to be equipped by initial conditions for $\mathbf{u}$ and the velocity $\dot{\mathbf{u}}$ and by suitable boundary constrains, as discussed in the next session.

We finally observe that the vector displacement satisfies the hypothesis of the *Helmholtz decomposition* for a 2D vector field, depending on the scalar functions $\psi_{\mathtt{S}}(\mathbf{x},t)$ and $\psi_{\mathtt{P}}(\mathbf{x},t)$ (for further details on the Helmholtz decomposition for a 2D vector field see [2, 33]):

$$\mathbf{u} = \mathbf{u}_{\mathtt{P}} + \mathbf{u}_{\mathtt{S}}, \tag{1.10}$$

where $\mathbf{u}_\mathtt{P} = \nabla\psi_\mathtt{P}$ and $\mathbf{u}_\mathtt{S} = R\nabla\psi_\mathtt{S}$. In particular, R is the anticlockwise rotation matrix of angle $\pi/2$:

$$R = \begin{pmatrix} 0 & 1 \\ -1 & 0 \end{pmatrix},$$

and the operator $R\nabla$ applied to a scalar field corresponds to the operator **curl** defined in [33]. Substituting decomposition (1.10) in the vectorial equation (1.9) and setting null external body forces ($\mathbf{b} = 0$), we obtain the following formula:

$$(\lambda+\mu)\nabla\left[\nabla\cdot(\nabla\psi_\mathtt{P} + R\nabla\psi_\mathtt{S})\right]+\mu\Delta\left(\nabla\psi_\mathtt{P} + R\nabla\psi_\mathtt{S}\right) = \varrho\frac{\partial^2}{\partial t^2}\left(\nabla\psi_\mathtt{P} + R\nabla\psi_\mathtt{S}\right), \mathbf{x}\in\Omega, t\in(0,T].$$

It is trivial to observe that, if the scalar field fits the hypothesis of the *Schwarz theorem* [37], then $\nabla\cdot R\nabla\psi_\mathtt{P} \equiv 0$, allowing to rewrite the previous equation in the form

$$(\lambda+2\mu)\nabla\left(\Delta\psi_\mathtt{P}\right) + \mu R\nabla\left(\Delta\psi_\mathtt{S}\right) = \varrho\left(\nabla\ddot{\psi}_\mathtt{P} + R\nabla\ddot{\psi}_\mathtt{S}\right), \quad \mathbf{x}\in\Omega,\ t\in(0,T] \tag{1.11}$$

since for the scalar field f it holds $\nabla\cdot\nabla f = \Delta f$ and $\nabla(\Delta f) = \Delta(\nabla f)$. Equation (1.11) is identically satisfied if $\psi_\mathtt{P}$ and $\psi_\mathtt{S}$ are solution of the following scalar wave equations

$$\begin{cases} c_\mathtt{P}^2\Delta\psi_\mathtt{P}(\mathbf{x},t) = \ddot{\psi}_\mathtt{P}(\mathbf{x},t) & (\mathbf{x},t)\in\Omega\times(0,T] \\ c_\mathtt{S}^2\Delta\psi_\mathtt{S}(\mathbf{x},t) = \ddot{\psi}_\mathtt{S}(\mathbf{x},t) & (\mathbf{x},t)\in\Omega\times(0,T] \end{cases}$$

where

$$c_\mathtt{P} = \sqrt{\frac{\lambda+2\mu}{\varrho}} > c_\mathtt{S} = \sqrt{\frac{\mu}{\varrho}} \tag{1.12}$$

are the propagation phase speeds of $\mathbf{u}_\mathtt{P}$ and $\mathbf{u}_\mathtt{S}$, which can be finally seen as the longitudinal and the transversal displacement, respectively. An example of resolution of 2D elastodynamics problems by BEM, with displacement $\mathbf{u}$ rewritten in terms of longitudinal and transversal directions can be found in [33].

1.2 Representation formula and Boundary Integral Equations

From now on, for the sake of simplicity, we consider only the resolution of equation (1.9) with null external body forces, $b_i = 0$ for $i = 1, 2$, and homogeneous initial conditions

$$\mathbf{u}(\mathbf{x},0) = 0,\ \dot{\mathbf{u}}(\mathbf{x},0) = 0, \quad \mathbf{x}\in\Omega. \tag{1.13}$$

Otherwise, the integral formulations we will expose in the following to identify the unknown displacement in $\Omega\times(0,T]$ require the computation of integrals depending on the non-trivial initial conditions and on the extrenal force, as shown in [14]. In the simple case we treat, the type of constrains set at the boundary Γ determines the three kinds of vectorial problems we can solve by BEM and the related behaviour of the vectorial unknown $\mathbf{u}$:

- Dirichlet problem ($P_\mathcal{D}$):

$$\begin{cases} (\lambda+\mu)\nabla(\nabla\cdot\mathbf{u}) + \mu\Delta\mathbf{u} = \varrho\ddot{\mathbf{u}}, & \forall(\mathbf{x},t)\in\Omega\times(0,T], \\ \mathbf{u}(\mathbf{x},t) = \mathbf{g}_\mathcal{D}(\mathbf{x},t), & \forall(\mathbf{x},t)\in\Sigma := \Gamma\times(0,T], \end{cases}$$

- Neumann problem ($P_{\mathcal{N}}$):

$$\begin{cases} (\lambda+\mu)\nabla(\nabla\cdot\mathbf{u})+\mu\Delta\mathbf{u}=\varrho\ddot{\mathbf{u}}, & \forall(\mathbf{x},t)\in\Omega\times(0,T], \\ \mathbf{p}(\mathbf{x},t)=\mathbf{g}_{\mathcal{N}}(\mathbf{x},t), & \forall(\mathbf{x},t)\in\Sigma:=\Gamma\times(0,T], \end{cases}$$

- Mixed boundary conditions problem ($P_{\mathcal{D},\mathcal{N}}$): If we define with $\Gamma_{\mathcal{D}}$ and $\Gamma_{\mathcal{N}}$ the two portions of boundary where the Dirichlet and the Neumann boundary data are respectively given and such that $\overline{\Gamma}=\overline{\Gamma}_{\mathcal{D}}\cup\overline{\Gamma}_{\mathcal{N}}$ and $\Gamma_{\mathcal{D}}\cap\Gamma_{\mathcal{N}}=\emptyset$, then

$$\begin{cases} (\lambda+\mu)\nabla(\nabla\cdot\mathbf{u})+\mu\Delta\mathbf{u}=\varrho\ddot{\mathbf{u}}, & \forall(\mathbf{x},t)\in\Omega\times(0,T], \\ \mathbf{u}(\mathbf{x},t)=\mathbf{g}_{\mathcal{D}}(\mathbf{x},t), & \forall(\mathbf{x},t)\in\Sigma_{\mathcal{D}}:=\Gamma_{\mathcal{D}}\times(0,T], \\ \mathbf{p}(\mathbf{x},t)=\mathbf{g}_{\mathcal{N}}(\mathbf{x},t), & \forall(\mathbf{x},t)\in\Sigma_{\mathcal{N}}:=\Gamma_{\mathcal{N}}\times(0,T]. \end{cases}$$

To approximate the displacement $\mathbf{u}$ by a BEM technique, we introduce the fundamental solution tensor $\mathbf{G}^{\mathbf{uu}}=(G^{\mathbf{uu}}_{ij})_{i,j=1,2}$ of (1.9), i.e. the solution of the following differential problem

$$C^{kl}_{ih}\frac{\partial^2 G^{\mathbf{uu}}_{kj}}{\partial x_h\partial x_l}(\mathbf{x},\boldsymbol{\xi};t,\tau)+\varrho b_{ij}(\mathbf{x},\boldsymbol{\xi};t,\tau)=\varrho\frac{\partial^2 G^{\mathbf{uu}}_{ij}}{\partial t^2}(\mathbf{x},\boldsymbol{\xi};t,\tau),\quad i,j=1,2,\ \mathbf{x},\boldsymbol{\xi}\in\mathbf{R}^2,\ \tau<t. \tag{1.14}$$

where a punctual body source force with components $b_{ij}(\mathbf{x},\boldsymbol{\xi};t,\tau)=\frac{\delta_{ij}}{\varrho}\delta(\mathbf{x}-\boldsymbol{\xi})\delta(t-\tau)$ is applied in the propagation domain ($\delta(\cdot)$ is the *Dirac distribution*).
The tensor $\mathbf{G}^{\mathbf{uu}}$, that can be deduced by classical arguments reported in the Andersen book [14], results to be symmetric and has the following expression:

$$\begin{aligned} G^{\mathbf{uu}}_{ij}(\mathbf{x},\boldsymbol{\xi};t,\tau):=&\frac{H[c_{\mathrm{P}}(t-\tau)-r]}{2\pi\varrho c_{\mathrm{P}}}\left\{\frac{r_ir_j}{r^4}\frac{2c_{\mathrm{P}}^2(t-\tau)^2-r^2}{\sqrt{c_{\mathrm{P}}^2(t-\tau)^2-r^2}}-\frac{\delta_{ij}}{r^2}\sqrt{c_{\mathrm{P}}^2(t-\tau)^2-r^2}\right\} \\ &-\frac{H[c_{\mathrm{S}}(t-\tau)-r]}{2\pi\varrho c_{\mathrm{S}}}\left\{\frac{r_ir_j}{r^4}\frac{2c_{\mathrm{S}}^2(t-\tau)^2-r^2}{\sqrt{c_{\mathrm{S}}^2(t-\tau)^2-r^2}}-\frac{\delta_{ij}}{r^2}\frac{c_{\mathrm{S}}^2(t-\tau)^2}{\sqrt{c_{\mathrm{S}}^2(t-\tau)^2-r^2}}\right\}, \end{aligned} \tag{1.15}$$

having set the vector $\mathbf{r}=(r_1,r_2)^\top=\mathbf{x}-\boldsymbol{\xi}=(x_1-\xi_1,x_2-\xi_2)^\top$, with norm $r=\|\mathbf{r}\|_2=\sqrt{r_1^2+r_2^2}$ and where $H[\cdot]$, the *Heaviside function*, models the primary and the secondary wave fronts propagation. We further observe that the tensor function (1.15) depends on the space and time arguments only through the differences $\mathbf{x}-\boldsymbol{\xi}$ and $t-\tau$. The knowledge of an explicit expression for the 2D fundamental solution allows to express the displacement by an integral representation formula, that can be deduced making a space-time integral of the matrix-vector product of the fundamental tensor $\mathbf{G}^{\mathbf{uu}}$ by the equation (1.2), considering this last one as a column vector:

$$0=\int_\Omega\int_0^t\left\{G^{\mathbf{uu}}_{ij}(\mathbf{x},\boldsymbol{\xi};t,\tau)C^{kl}_{jh}\frac{\partial^2 u_k}{\partial\xi_h\partial\xi_l}(\boldsymbol{\xi},\tau)-G^{\mathbf{uu}}_{ij}(\mathbf{x},\boldsymbol{\xi};t,\tau)\varrho\frac{\partial^2}{\partial\tau^2}u_j(\boldsymbol{\xi},\tau)\right\}d\tau d\boldsymbol{\xi},\ i=1,2. \tag{1.16}$$

For the time variable we proceed integrating twice by parts: since the components of the fundamental solution $G^{\mathbf{uu}}_{ij}$ and of its first temporal derivative $\partial G^{\mathbf{uu}}_{ij}/\partial\tau$ are null at $t=\tau$ and

considering the homogeneous initial conditions, we obtain from (1.16)

$$\begin{aligned}
0 &= \int_\Omega \int_0^t G_{ij}^{\mathbf{uu}}(\mathbf{x},\boldsymbol{\xi};t,\tau) C_{jh}^{kl} \frac{\partial^2 u_k}{\partial \xi_h \partial \xi_l}(\boldsymbol{\xi},\tau) d\tau d\boldsymbol{\xi} \\
&\quad - \int_\Omega G_{ij}^{\mathbf{uu}}(\mathbf{x},\boldsymbol{\xi};t,\tau) \varrho \frac{\partial}{\partial \tau} u_j(\boldsymbol{\xi},\tau)\Big|_0^t d\boldsymbol{\xi} + \int_\Omega \int_0^t \frac{\partial}{\partial \tau} G_{ij}^{\mathbf{uu}}(\mathbf{x},\boldsymbol{\xi};t,\tau) \varrho \frac{\partial}{\partial \tau} u_j(\boldsymbol{\xi},\tau) d\tau d\boldsymbol{\xi} \\
&= \int_\Omega \int_0^t G_{ij}^{\mathbf{uu}}(\mathbf{x},\boldsymbol{\xi};t,\tau) C_{jh}^{kl} \frac{\partial^2 u_k}{\partial \xi_h \partial \xi_l}(\boldsymbol{\xi},\tau) d\tau d\boldsymbol{\xi} \\
&\quad - \int_\Omega G_{ij}^{\mathbf{uu}}(\mathbf{x},\boldsymbol{\xi};t,\tau) \varrho \frac{\partial}{\partial \tau} u_j(\boldsymbol{\xi},\tau)\Big|_0^t d\boldsymbol{\xi} + \int_\Omega \varrho \frac{\partial}{\partial \tau} G_{ij}^{\mathbf{uu}}(\mathbf{x},\boldsymbol{\xi};t,\tau) u_j(\boldsymbol{\xi},\tau)\Big|_0^t d\boldsymbol{\xi} \\
&\quad - \int_\Omega \int_0^t \varrho \frac{\partial^2}{\partial \tau^2} G_{ij}^{\mathbf{uu}}(\mathbf{x},\boldsymbol{\xi};t,\tau) u_j(\boldsymbol{\xi},\tau) d\tau d\boldsymbol{\xi}, \ i = 1,2,
\end{aligned}$$

and then we get

$$\int_\Omega \int_0^t G_{ij}^{\mathbf{uu}}(\mathbf{x},\boldsymbol{\xi};t,\tau) C_{jh}^{kl} \frac{\partial^2 u_k}{\partial \xi_h \partial \xi_l}(\boldsymbol{\xi},\tau) dt d\boldsymbol{\xi} - \int_\Omega \int_0^t \varrho \frac{\partial^2}{\partial \tau^2} G_{ij}^{\mathbf{uu}}(\mathbf{x},\boldsymbol{\xi};t,\tau) u_j(\boldsymbol{\xi},\tau) dt d\boldsymbol{\xi} = 0, \quad i = 1,2. \tag{1.17}$$

Regarding the integration in space, we focus on the first term of (1.17). Applying the Gauss-Green formula we write

$$\begin{aligned}
&\int_\Omega G_{ij}^{\mathbf{uu}}(\mathbf{x},\boldsymbol{\xi};t,\tau) C_{jh}^{kl} \frac{\partial^2 u_k}{\partial \xi_h \partial \xi_l}(\boldsymbol{\xi},\tau) d\boldsymbol{\xi} \\
&= \int_\Gamma G_{ij}^{\mathbf{uu}}(\mathbf{x},\boldsymbol{\xi};t,\tau) C_{jh}^{kl} \frac{\partial u_k}{\partial \xi_l}(\boldsymbol{\xi},\tau) n_h(\boldsymbol{\xi}) d\Gamma_{\boldsymbol{\xi}} - \int_\Omega \frac{\partial}{\partial \xi_h} G_{ij}^{\mathbf{uu}}(\mathbf{x},\boldsymbol{\xi};t,\tau) C_{jh}^{kl} \frac{\partial u_k}{\partial \xi_l}(\boldsymbol{\xi},\tau) d\boldsymbol{\xi} \\
&= \int_\Gamma G_{ij}^{\mathbf{uu}}(\mathbf{x},\boldsymbol{\xi};t,\tau) C_{jh}^{kl} \frac{\partial u_k}{\partial \xi_l}(\boldsymbol{\xi},\tau) n_h(\boldsymbol{\xi}) d\Gamma_{\boldsymbol{\xi}} - \int_\Gamma \frac{\partial}{\partial \xi_h} G_{ij}^{\mathbf{uu}}(\mathbf{x},\boldsymbol{\xi};t,\tau) C_{jh}^{kl} u_k(\boldsymbol{\xi},\tau) n_l(\boldsymbol{\xi}) d\Gamma_{\boldsymbol{\xi}} \\
&\quad + \int_\Omega \frac{\partial^2}{\partial \xi_l \partial \xi_h} G_{ij}^{\mathbf{uu}}(\mathbf{x},\boldsymbol{\xi};t,\tau) C_{jh}^{kl} u_k(\boldsymbol{\xi},\tau) d\boldsymbol{\xi}, \ i = 1,2.
\end{aligned} \tag{1.18}$$

Considering the symmetry properties of the Hooke tensor reported in (1.5) and the traction definition in (1.7), we can rewrite the terms in (1.18) as follows:

$$\int_\Gamma G_{ij}^{\mathbf{uu}}(\mathbf{x},\boldsymbol{\xi};t,\tau) C_{jh}^{kl} \frac{\partial u_k}{\partial \xi_l}(\boldsymbol{\xi},\tau) n_h(\boldsymbol{\xi}) d\Gamma_{\boldsymbol{\xi}} = \int_\Gamma G_{ij}^{\mathbf{uu}}(\mathbf{x},\boldsymbol{\xi};t,\tau) p_j(\boldsymbol{\xi},\tau) d\Gamma_{\boldsymbol{\xi}}, \ i = 1,2, \tag{1.19}$$

$$\begin{aligned}
\int_\Gamma \frac{\partial}{\partial \xi_h} G_{ij}^{\mathbf{uu}}(\mathbf{x},\boldsymbol{\xi};t,\tau) C_{jh}^{kl} u_k(\boldsymbol{\xi},\tau) n_l(\boldsymbol{\xi}) d\Gamma_{\boldsymbol{\xi}} &= \int_\Gamma C_{jh}^{kl} \frac{\partial}{\partial \xi_l} G_{ik}^{\mathbf{uu}}(\mathbf{x},\boldsymbol{\xi};t,\tau) u_j(\boldsymbol{\xi},\tau) n_h(\boldsymbol{\xi}) d\Gamma_{\boldsymbol{\xi}} \\
&= \int_\Gamma G_{ij}^{\mathbf{up}}(\mathbf{x},\boldsymbol{\xi};t,\tau) u_j(\boldsymbol{\xi},\tau) d\Gamma_{\boldsymbol{\xi}}, \ i = 1,2,
\end{aligned} \tag{1.20}$$

$$\int_\Omega \frac{\partial^2}{\partial \xi_l \partial \xi_h} G_{ij}^{\mathbf{uu}}(\mathbf{x},\boldsymbol{\xi};t,\tau) C_{jh}^{kl} u_k(\boldsymbol{\xi},\tau) d\boldsymbol{\xi} = \int_\Omega C_{jh}^{kl} \frac{\partial^2}{\partial \xi_l \partial \xi_h} G_{ik}^{\mathbf{uu}}(\mathbf{x},\boldsymbol{\xi};t,\tau) u_j(\boldsymbol{\xi},\tau) d\boldsymbol{\xi}, \ i = 1,2. \tag{1.21}$$

We observe that, by the way, we have introduced in (1.20) the fundamental traction $\mathbf{G}^{\mathbf{up}} = (G_{ij}^{\mathbf{up}})_{i,j=1,2}$, defined by

$$G_{ij}^{\mathbf{up}}(\mathbf{x},\boldsymbol{\xi};t,\tau) = C_{jh}^{kl} \frac{\partial}{\partial \xi_l} G_{ik}^{\mathbf{uu}}(\mathbf{x},\boldsymbol{\xi};t,\tau) n_h(\boldsymbol{\xi}). \tag{1.22}$$

Substituting (1.19)-(1.20)-(1.21) in (1.18) and going back to (1.17), we obtain the following identity:

$$-\int_\Omega \int_0^t \left\{ C_{jh}^{kl} \frac{\partial^2}{\partial \xi_l \partial \xi_h} G_{ik}^{\mathbf{uu}}(\mathbf{x}, \boldsymbol{\xi}; t\tau) - \varrho \frac{\partial^2}{\partial \tau^2} G_{ij}^{\mathbf{uu}}(\mathbf{x}, \boldsymbol{\xi}; t\tau) \right\} u_j(\boldsymbol{\xi}, \tau) d\tau d\boldsymbol{\xi}$$
$$= \int_\Gamma \int_0^t G_{ij}^{\mathbf{uu}}(\mathbf{x}, \boldsymbol{\xi}; t, \tau) p_j(\mathbf{x}, \tau) d\tau d\Gamma_{\boldsymbol{\xi}} - \int_\Gamma \int_0^t G_{ij}^{\mathbf{up}}(\mathbf{x}, \boldsymbol{\xi}; t, \tau) u_j(\mathbf{x}, \tau) d\tau d\Gamma_{\boldsymbol{\xi}}, \ i = 1, 2. \tag{1.23}$$

Taking into account the symmetry of the fundamental solution $\mathbf{G}^{\mathbf{uu}}$ and the fact that its components verify equation (1.14), we get to the following equality usually denominated in literature *Somigliana Identity*:

$$u_i(\mathbf{x}, t) = \int_\Gamma \int_0^t G_{ij}^{\mathbf{uu}}(\mathbf{x}, \boldsymbol{\xi}; t, \tau) p_j(\boldsymbol{\xi}, \tau) d\tau d\Gamma_{\boldsymbol{\xi}} - \int_\Gamma \int_0^t G_{ij}^{\mathbf{up}}(\mathbf{x}, \boldsymbol{\xi}; t, \tau) u_j(\boldsymbol{\xi}, \tau) d\tau d\Gamma_{\boldsymbol{\xi}},$$
$$(\mathbf{x}, t) \in \Omega \times (0, T], \ i = 1, 2. \tag{1.24}$$

Equations (1.24) furnish us a way to represent in the interior domain the components of the unknown displacement employing two integral operators defined at the boundary Γ. Formula (1.24) can be rewritten in the following compact notation:

$$\mathbf{u}(\mathbf{x}, t) = V\mathbf{p}(\mathbf{x}, t) - K\mathbf{u}(\mathbf{x}, t), \quad (\mathbf{x}, t) \in \Omega \times (0, T], \tag{1.25}$$

where the integral tensor operators V and K, usually called in literature *Single Layer* and *Double Layer* integral operators, respectively, act on the components of $\mathbf{u}$ and $\mathbf{p}$ as follows:

$$(V\mathbf{p})_i(\mathbf{x}, t) = \int_\Gamma \int_0^t G_{ij}^{\mathbf{uu}}(\mathbf{x}, \boldsymbol{\xi}; t, \tau) p_j(\boldsymbol{\xi}, \tau) d\tau d\Gamma_{\boldsymbol{\xi}}, \ i = 1, 2, \tag{1.26}$$

$$(K\mathbf{u})_i(\mathbf{x}, t) = \int_\Gamma \int_0^t G_{ij}^{\mathbf{up}}(\mathbf{x}, \boldsymbol{\xi}; t, \tau) u_j(\boldsymbol{\xi}, \tau) d\tau d\Gamma_{\boldsymbol{\xi}}, \ i = 1, 2. \tag{1.27}$$

We recall that, although we have presented a representation formula for interior propagation, we can pose $(P_{\mathcal{D}})$, $(P_{\mathcal{N}})$ and $(P_{\mathcal{D},\mathcal{N}})$ in the exterior domain $\Omega_e = \mathbf{R}^2 \setminus \overline{\Omega}$. Therefore to obtain a representation formula for the exterior propagation, we just consider the inverse direction of the normal vector $\mathbf{n}$, which implies a change of sign for formulas (1.24) and (1.25):

$$\mathbf{u}(\mathbf{x}, t) = -V\mathbf{p}(\mathbf{x}, t) + K\mathbf{u}(\mathbf{x}, t), \quad (\mathbf{x}, t) \in \Omega_e \times (0, T] \tag{1.28}$$

At this stage, considering both equations (1.28) and (1.25), we can globally determine the propagation in $\Omega \cup \Omega_e$ by means of the following integral representation formulas:

$$\mathbf{u}(\mathbf{x}, t) = V[\mathbf{p}]_\Gamma(\mathbf{x}, t) - K[\mathbf{u}]_\Gamma(\mathbf{x}, t), \quad (\mathbf{x}, t) \in \Omega \cup \Omega_e \times (0, T] \tag{1.29}$$

where the square brackets $[\cdot]_\Gamma$ denote the jump of the traction and of the displacement across the boundary Γ.

The various integral representation formulas presented before can be suitably modified to solve problems with specific boundary conditions. For instance, if we want to solve

problem $(P_{\mathcal{D}})$ and we consider formula (1.25), taking the limit from the space variable $\mathbf{x}$ in the interior domain Ω towards a point $\mathbf{x}$ belonging to the boundary Γ and exploiting the Dirichlet datum $\mathbf{u}_{|\Gamma} \equiv \mathbf{g}_{\mathcal{D}}$, we get to the following *Boundary Integral Equation*, usually indicated by the acronym BIE:

$$c_\Gamma(\mathbf{x})\mathbf{g}_{\mathcal{D}}(\mathbf{x},t) = V\mathbf{p}(\mathbf{x},t) - K\mathbf{g}_{\mathcal{D}}(\mathbf{x},t), \quad (\mathbf{x},t) \in \Sigma = \Gamma \times (0,T]. \tag{1.30}$$

In formula (1.30), the integral on Γ related to the double layer operator K has to be intended as a *Cauchy Principal Value* integral, as indicated in Section 4.2.3.
For what concerns the function c_Γ which multiplies the Dirichlet datum in (1.30), it derives from the consequences of the limiting process related to the Double Layer operator K, in fact

$$\lim_{\mathbf{x}\in\Omega\to\mathbf{x}\in\Gamma} K\mathbf{u}(\mathbf{x},t) = K\mathbf{u}(\mathbf{x},t) - (1 - c_\Gamma(\mathbf{x}))\mathbf{u}(\mathbf{x},t),$$

were $c_\Gamma \equiv 1/2$ for differentiable boundaries. If instead we are dealing with non-smooth contours, the factor $c_\Gamma(\mathbf{x})$ depends on the local geometry determined by the corner points: in fact, $c_\Gamma(\mathbf{x}) = \omega/2\pi$ if $\mathbf{x}$ is an apex of the propagation domain Ω with inner angle of amplitude ω, as indicated in [14]. Considering the introduced representation formulas, we collect the different BIEs used for the experiments with soft scattering conditions reported in the next chapters:

	representation formula		**BIE**	
$(\mathcal{D}_1)$	$\mathbf{u} = V\mathbf{p} - K\mathbf{u},$	$\forall(\mathbf{x},t) \in \Omega \times (0,T]$	$V\mathbf{p} = (K + c_\Gamma)\mathbf{g}_{\mathcal{D}},$	$\forall(\mathbf{x},t) \in \Sigma$
$(\mathcal{D}_2)$	$\mathbf{u} = K\mathbf{u} - V\mathbf{p},$	$\forall(\mathbf{x},t) \in \Omega_e \times (0,T]$	$V\mathbf{p} = (K - c_\Gamma)\mathbf{g}_{\mathcal{D}},$	$\forall(\mathbf{x},t) \in \Sigma$
$(\mathcal{D}_3)$	$\mathbf{u} = V\boldsymbol{\Phi},$	$\forall(\mathbf{x},t) \in \Omega \cup \Omega_e \times (0,T]$	$V\boldsymbol{\Phi} = \mathbf{g}_{\mathcal{D}},$	$\forall(\mathbf{x},t) \in \Sigma$

The unknown $\boldsymbol{\Phi}$ of the representation formula and the BIE of type $(\mathcal{D}_3)$ corresponds to the jump of the traction across Γ

$$\boldsymbol{\Phi} = [\mathbf{p}]_\Gamma \tag{1.31}$$

and it is deduced from (1.29), in which we are assuming a continuous displacement on Γ, namely $[\mathbf{u}]_\Gamma \equiv 0$.

To obtain boundary integral equations suitable for the resolution of problems with hard-scattering conditions as in $(P_{\mathcal{N}})$, we need to manipulate formula (1.24): applying the Cauchy stress tensor (1.3) to the displacement components, in order to obtain the traction $\mathbf{p}$ as defined in (1.7), we get to the representation formula

$$p_i(\mathbf{x},t) = \int_\Gamma \int_0^t G_{ij}^{\mathbf{pu}}(\mathbf{x},\boldsymbol{\xi};t,\tau)p_j(\boldsymbol{\xi},\tau)dtd\Gamma_{\boldsymbol{\xi}} - \int_\Gamma \int_0^t G_{ij}^{\mathbf{pp}}(\mathbf{x},\boldsymbol{\xi};t,\tau)u_j(\boldsymbol{\xi},\tau)dtd\Gamma_{\boldsymbol{\xi}},$$
$$(\mathbf{x},t) \in \Omega \times (0,T],\ i = 1,2, \tag{1.32}$$

where the new introduced tensors $\mathbf{G}^{\mathbf{pu}} = (G_{ij}^{\mathbf{pu}})_{i,j=1,2}$ and $\mathbf{G}^{\mathbf{pp}} = (G_{ij}^{\mathbf{pp}})_{i,j=1,2}$ are defined by

$$G_{ij}^{\mathbf{pu}}(\mathbf{x},\boldsymbol{\xi};t,\tau) = C_{ih}^{kl}\frac{\partial}{\partial x_l}G_{kj}^{\mathbf{uu}}(\mathbf{x},\boldsymbol{\xi};t,\tau)n_h(\mathbf{x}), \tag{1.33}$$

$$G_{ij}^{\mathbf{pp}}(\mathbf{x},\boldsymbol{\xi};t,\tau) = C_{ih}^{kl}\frac{\partial}{\partial x_l}G_{kj}^{\mathbf{up}}(\mathbf{x},\boldsymbol{\xi};t,\tau)n_h(\mathbf{x}) = C_{ih}^{kl}C_{j\alpha}^{\beta\gamma}\frac{\partial^2 G_{k\beta}^{\mathbf{uu}}}{\partial x_l \partial \xi_\gamma}(\mathbf{x},\boldsymbol{\xi};t,\tau)n_h(\mathbf{x})n_\alpha(\boldsymbol{\xi}). \tag{1.34}$$

Representation formula (1.32) is rewritable in the following compact notation

$$\mathbf{p}(\mathbf{x},t) = K^*\mathbf{p}(\mathbf{x},t) - D\mathbf{u}(\mathbf{x},t), \quad (\mathbf{x},t) \in \Omega \times (0,T] \tag{1.35}$$

where K^* is the adjoint of the double layer operator K and D is usually known in literature as *Hypersingular* integral operator. They respectively act on $\mathbf{p}$ and $\mathbf{u}$ as follows:

$$(K^*\mathbf{p})_i(\mathbf{x},t) = \int_\Gamma \int_0^t G_{ij}^{\mathbf{pu}}(\mathbf{x},\boldsymbol{\xi};t,\tau)p_j(\boldsymbol{\xi},\tau)dtd\Gamma_{\boldsymbol{\xi}},\ i=1,2, \tag{1.36}$$

$$(D\mathbf{u})_i(\mathbf{x},t) = \int_\Gamma \int_0^t G_{ij}^{\mathbf{pp}}(\mathbf{x},\boldsymbol{\xi};t,\tau)u_j(\boldsymbol{\xi},\tau)dtd\Gamma_{\boldsymbol{\xi}},\ i=1,2. \tag{1.37}$$

With similar considerations done to deduce the equation (1.30) and exploiting the Neumann datum $\mathbf{p}_{|\Gamma} \equiv \mathbf{g}_\mathcal{N}$, we get to the following BIE:

$$c_\Gamma(\mathbf{x})\mathbf{g}_\mathcal{N}(\mathbf{x},t) = K^*\mathbf{g}_\mathcal{N}(\mathbf{x},t) - D\mathbf{u}(\mathbf{x},t), \quad (\mathbf{x},t) \in \Sigma, \tag{1.38}$$

remarking that in formula (1.38) the integrals on Γ related to the double layer operator K^* and the hypersingular operator D have to be treated, respectively, as *Cauchy Principal Value* and *Hadamard Finite Part* integrals, as indicated in Sections 4.2.3 and 4.2.4.
Also in this case, we can summarize the different BIE for Neumann problems, mostly used for the numerical experiments:

	representation formula		**BIE**	
$(\mathcal{N}_1)$	$\mathbf{p} = K^*\mathbf{p} - D\mathbf{u},$	$\forall(\mathbf{x},t) \in \Omega \times (0,T]$	$D\mathbf{u} = (K^* - c_\Gamma)\mathbf{g}_\mathcal{N},$	$\forall(\mathbf{x},t) \in \Sigma$
$(\mathcal{N}_2)$	$\mathbf{p} = D\mathbf{u} - K^*\mathbf{p},$	$\forall(\mathbf{x},t) \in \Omega_e \times (0,T]$	$D\mathbf{u} = (K^* + c_\Gamma)\mathbf{g}_\mathcal{N},$	$\forall(\mathbf{x},t) \in \Sigma$
$(\mathcal{N}_3)$	$\mathbf{p} = D\boldsymbol{\Psi},$	$\forall(\mathbf{x},t) \in \Omega \cup \Omega_e \times (0,T]$	$D\boldsymbol{\Psi} = \mathbf{g}_\mathcal{N},$	$\forall(\mathbf{x},t) \in \Sigma$

where in particular the unknown $\boldsymbol{\Psi}$ of the representation formula and the BIE of type $(\mathcal{N}_3)$ corresponds to the jump of the displacement across Γ:

$$\boldsymbol{\Psi} = [\mathbf{u}]_\Gamma\,. \tag{1.39}$$

We again observe that $(\mathcal{N}_3)$ is deduced from formula (1.29), in which the jump of the traction is supposed to be null and onto which the traction defined in (1.7) is applyed.
We recall moreover that representation formulas and BIEs defined in $(\mathcal{D}_3)$ and $(\mathcal{N}_3)$ can be used, without modifications, in problems of propagation external to open Lipschitz obstacles Γ. In this case, the representation formulas are defined in $\mathbf{R}^2 \setminus \Gamma$ and, for the continuity required by the displacement $\mathbf{u}$, to solve BIE $(\mathcal{N}_3)$ we have to impose $\boldsymbol{\Psi}_{|\partial\Gamma} \equiv 0$.

Mixed boundary condition problems as in $(P_{\mathcal{D},\mathcal{N}})$ can be treated by the simultaneous use of two BIEs: one defined on the portion $\Gamma_\mathcal{D}$, where the Dirichlet datum is known, and one defined on $\Gamma_\mathcal{N}$, where it is possible to make explicit the Neumann condition. Representation formulas and related BIEs to solve are collected in the following table:

	representation formula	system of **BIEs**
$(\mathcal{DN}_1)$	$\mathbf{u} = V\mathbf{p} - K\mathbf{u},$ $\forall(\mathbf{x},t) \in \Omega \times (0,T]$	$\begin{cases} V(\mathbf{p}\vert_{\Gamma_\mathcal{D}}) - K(\mathbf{u}\vert_{\Gamma_\mathcal{N}}) = \mathbf{f}_\mathcal{D} & \forall(\mathbf{x},t) \in \Sigma_\mathcal{D} \\ K^*(\mathbf{p}\vert_{\Gamma_\mathcal{D}}) - D(\mathbf{u}\vert_{\Gamma_\mathcal{N}}) = \mathbf{f}_\mathcal{N} & \forall(\mathbf{x},t) \in \Sigma_\mathcal{N} \end{cases}$
$(\mathcal{DN}_2)$	$\mathbf{u} = K\mathbf{u} - V\mathbf{p},$ $\forall(\mathbf{x},t) \in \Omega_e \times (0,T]$	$\begin{cases} -V(\mathbf{p}\vert_{\Gamma_\mathcal{D}}) + K(\mathbf{u}\vert_{\Gamma_\mathcal{N}}) = \mathbf{f}_\mathcal{D} & \forall(\mathbf{x},t) \in \Sigma_\mathcal{D} \\ -K^*(\mathbf{p}\vert_{\Gamma_\mathcal{D}}) + D(\mathbf{u}\vert_{\Gamma_\mathcal{N}}) = \mathbf{f}_\mathcal{N} & \forall(\mathbf{x},t) \in \Sigma_\mathcal{N} \end{cases}$

where the right-hand-side of the BIE, respectively defined on $\Sigma_{\mathcal{D}}$ and on $\Sigma_{\mathcal{N}}$, are

$$\mathbf{f}_{\mathcal{D}} = -V\mathbf{g}_{\mathcal{N}} + (K + c_\Gamma)\,\mathbf{g}_{\mathcal{D}}, \quad \mathbf{f}_{\mathcal{N}} = D\mathbf{g}_{\mathcal{D}} - (K^* - c_\Gamma)\,\mathbf{g}_{\mathcal{N}}$$

in case of internal propagation, type $(\mathcal{DN}_1)$, while for exterior propagation, type $(\mathcal{DN}_2)$, it holds

$$\mathbf{f}_{\mathcal{D}} = V\mathbf{g}_{\mathcal{N}} - (K - c_\Gamma)\,\mathbf{g}_{\mathcal{D}}, \quad \mathbf{f}_{\mathcal{N}} = -D\mathbf{g}_{\mathcal{D}} + (K^* + c_\Gamma)\,\mathbf{g}_{\mathcal{N}}.$$

The symmetry properties of the fundamental tensors $\mathbf{G^{uu}}, \mathbf{G^{up}}, \mathbf{G^{pu}}$ and $\mathbf{G^{pp}}$ can be summarized as follows:

$$G_{ij}^{\mathbf{hk}}(\mathbf{x}, \boldsymbol{\xi}; t, \tau) = G_{ji}^{\mathbf{kh}}(\boldsymbol{\xi}, \mathbf{x}; t, \tau) \quad \mathbf{h}, \mathbf{k} = \mathbf{u}, \mathbf{p},\ i, j = 1, 2, \tag{1.40}$$

and they turn out to be useful in solving the mixed boundary problems since the discretized integral operators that occur in the related formulation can be assembled taking advantage of the equality above cited.

Lastly, we want to focus on the importance of working with the various integral representation formulas exposed in this section: they allow to represent $\mathbf{u}$ in an unbounded (or bounded) bidimensional domain just by integrals defined at the boundary, leading to a reduction of the dimensional complexity of the problem and to the possibility of approximating the exterior propagation without imposing artificial conditions, as usual with FEM, that can create spurious reflections.
The next step is to concentrate on the BIEs listed above and on a proper weak formulation that allows us to approximate the related unknowns by stable methods, in order to replace the latter in the related representation formulas and get the approximation of the unknown displacement $\mathbf{u}$ of equation (1.9).

1.3 Energetic weak problem

In this section we deduce the expression of the energy of the elastodynamics system and we elaborate a weak formulation of the above cited BIEs linked to that positive quantity. At first we consider the resolution of the Dirichlet problem $(P_{\mathcal{D}})$ by the use of the representation formula and the related integral equation of type $(\mathcal{D}_3)$, meaning that the displacement is considered continuous across the boundary Γ and the traction is characterized by a jump discontinuity. With the additional hypothesis for which the unknown displacement is defined in the union $\Omega \cup \Omega_e$, we perform a scalar product of the Navier equation (1.9) by the time derivative $\dot{\mathbf{u}}$, exploiting the definition by components in (1.2):

$$\varrho \ddot{u}_i(\mathbf{x}, t)\dot{u}_i(\mathbf{x}, t) - C_{ih}^{kl}\frac{\partial^2 u_k}{\partial x_h \partial x_l}(\mathbf{x}, t)\dot{u}_i(\mathbf{x}, t) = 0, \quad \mathbf{x} \in \Omega \cup \Omega_e,\ t \in (0, T].$$

Integrating by parts over $\Omega \cup \Omega_e$, we obtain

$$\begin{aligned} &\frac{1}{2}\int_{\Omega\cup\Omega_e} \varrho\frac{\partial}{\partial t}\|\dot{\mathbf{u}}(\mathbf{x}, t)\|_2^2 d\mathbf{x} + \int_{\Omega\cup\Omega_e} C_{ih}^{kl}\frac{\partial u_k}{\partial x_l}(\mathbf{x}, t)\frac{\partial \dot{u}_i}{\partial x_h}(\mathbf{x}, t)d\mathbf{x} \\ &= \int_\Gamma \left[C_{ih}^{kl}\frac{\partial u_k}{\partial x_l}(\mathbf{x}, t)n_h(\mathbf{x})\right]_\Gamma \dot{u}_i(\mathbf{x}, t)d\Gamma_{\mathbf{x}}, \end{aligned} \tag{1.41}$$

Due to the symmetry properties of the Hooke tensor defined in (1.4), it holds

$$\frac{\partial}{\partial t}\left(C_{ih}^{kl}\frac{\partial u_k}{\partial x_l}(\mathbf{x},t)\frac{\partial u_i}{\partial x_h}(\mathbf{x},t)\right) = 2C_{ih}^{kl}\frac{\partial u_k}{\partial x_l}(\mathbf{x},t)\frac{\partial \dot{u}_i}{\partial x_h}(\mathbf{x},t), \tag{1.42}$$

and, recalling the definition of the deformation tensor $\boldsymbol{\varepsilon}$ in (1.6), we have

$$\begin{aligned} C_{ih}^{kl}\frac{\partial u_k}{\partial x_l}(\mathbf{x},t)\frac{\partial u_i}{\partial x_h}(\mathbf{x},t) &= C_{ih}^{kl}\frac{\partial u_k}{\partial x_l}(\mathbf{x},t)\frac{1}{2}\left(\frac{\partial u_i}{\partial x_h}(\mathbf{x},t)+\frac{\partial u_h}{\partial x_i}(\mathbf{x},t)\right) \\ &= \boldsymbol{\sigma}[\mathbf{u}](\mathbf{x},t):\boldsymbol{\varepsilon}[\mathbf{u}](\mathbf{x},t), \end{aligned} \tag{1.43}$$

where the operation:

$$\boldsymbol{\sigma}[\mathbf{u}](\mathbf{x},t):\boldsymbol{\varepsilon}[\mathbf{u}](\mathbf{x},t) = \sigma_{ih}[\mathbf{u}](\mathbf{x},t)\varepsilon_{ih}[\mathbf{u}](\mathbf{x},t)$$

denotes the contraction between the stress and the deformation tensors. At this point, by integrating equation (1.41) in the time interval $[0,T]$ and using the equalities (1.42) and (1.43), we obtain the following *Energy Indentity*:

$$\mathcal{E}(\mathbf{u},T) := \frac{1}{2}\int_{\Omega\cup\Omega_e}\left[\varrho\|\dot{\mathbf{u}}(\mathbf{x},T)\|_2^2 d\mathbf{x} + \boldsymbol{\sigma}[\mathbf{u}](\mathbf{x},T):\boldsymbol{\varepsilon}[\mathbf{u}](\mathbf{x},T)\right]d\mathbf{x} \tag{1.44}$$

$$= \int_0^T\int_\Gamma \dot{u}_i(\mathbf{x},t)\Phi_i(\mathbf{x},t)d\Gamma_{\mathbf{x}}dt, \tag{1.45}$$

where $\mathcal{E}(\mathbf{u},T)$ is the energy of the system at the final instant T and $\boldsymbol{\Phi}$ is the field defined in (1.31). As introduced at the beginning of this section, this quantity turns out to be positive since it holds:

$$\boldsymbol{\sigma}[\mathbf{u}]:\boldsymbol{\varepsilon}[\mathbf{u}] = \lambda(\nabla\cdot\mathbf{u})^2 + \mu\left[2\left(\frac{\partial u_1}{\partial x_1}\right)^2 + 2\left(\frac{\partial u_2}{\partial x_2}\right)^2 + \left(\frac{\partial u_1}{\partial x_2}+\frac{\partial u_2}{\partial x_1}\right)^2\right].$$

Then, the identity (1.45) suggests us to consider the following *energetic weak formulation* of the BIE of type $(\mathcal{D}_3)$:

find the solution $\boldsymbol{\Phi} = (\Phi_1,\Phi_2)^\top$ *of the weak problem*

$$\langle(V_{ij}\dot{\Phi}_j),\phi_i\rangle_{L^2(\Sigma)} = \langle\dot{g}_{\mathcal{D},i},\phi_i\rangle_{L^2(\Sigma)}, \tag{1.46}$$

where $\boldsymbol{\phi} = (\phi_1,\phi_2)^\top$ *is a suitable test function belonging to the functional space of the traction* $\mathbf{p}$.

If instead we solve the Neumann problem $(P_{\mathcal{N}})$ with the representation formula and the BIE of type $(\mathcal{N}_3)$, we suppose to search for a displacement with jump discontinuity and we impose a continuous traction $\mathbf{p}$ on Γ. Due to that, retracing passages similar to (1.41)-(1.45), we obtain a slightly different energy identity for the hard scattering problem:

$$\mathcal{E}(\mathbf{u},T) = \int_\Gamma\int_0^T \dot{\Psi}_i(\mathbf{x},t)p_i(\mathbf{x},t)dtd\Gamma_{\mathbf{x}}, \tag{1.47}$$

where $\mathbf{\Psi}$ is the field defined in (1.39). Thus, by identity (1.47), we deduce the *energetic weak formulation* of BIEs of type $(\mathcal{N}_3)$:

find the solution $\mathbf{\Psi} = (\Psi_1, \Psi_2)^\top$ *of the weak problem*

$$\langle (D_{ij}\Psi_j), \dot{\psi}_i \rangle_{L^2(\Sigma)} = \langle g_{\mathcal{N},i}, \dot{\psi}_i \rangle_{L^2(\Sigma)}, \tag{1.48}$$

where $\boldsymbol{\psi} = (\psi_1, \psi_2)^\top$ *is a suitable test function belonging to the functional space of the displacement* $\mathbf{u}$.

Similar weak formulations can be deduced for the other integral equations introduced previously. For those of type $(\mathcal{D}_1)$ and $(\mathcal{D}_2)$, the related BIEs have to be derived in the time variable and projected by a $L^2(\Sigma)$ product onto the functional space of the traction $\mathbf{p}$. Instead, for the Neumann BIEs $(\mathcal{N}_1)$ and $(\mathcal{N}_2)$, the projection has to be done employing the time derivative of test functions belonging to the functional space of the displacement $\mathbf{u}$.

For what concerns the mixed boundary condition problems, the energetic weak formulations combine the projections of all the integral operator V, K, K^* and D onto suitable spaces, depending on the portion of arc along which the BIEs of the system of type $(\mathcal{DN}_1)$ are defined. Therefore, the energetic weak formulation we intend to solve for the inner problem case is the following:

calculate, for $i = 1, 2$, *the components* p_i *and* u_i *solution of the following system*

$$\begin{cases} \langle (\dot{V_{ij}} p_j), \phi_i \rangle_{L^2(\Sigma_D)} - \langle (\dot{K_{ij}} u_j), \phi_i \rangle_{L^2(\Sigma_D)} = \langle \dot{f_{\mathcal{D},i}}, \phi_i \rangle_{L^2(\Sigma_D)} \\ \langle D_{ij} u_j, \dot{\psi}_i \rangle_{L^2(\Sigma_N)} - \langle K^*_{ij} p_j, \dot{\psi}_i \rangle_{L^2(\Sigma_N)} = \langle f_{\mathcal{N},i}, \dot{\psi}_i \rangle_{L^2(\Sigma_N)} \end{cases} \tag{1.49}$$

where $\boldsymbol{\phi} = (\phi_1, \phi_2)^\top$, *defined on* Σ_D, *and* $\boldsymbol{\psi} = (\psi_1, \psi_2)^\top$, *defined on* Σ_N, *are test functions belonging respectively to the functional spaces of* $\mathbf{p}$ *and* $\mathbf{u}$.

Equivalently the weak form of $(\mathcal{DN}_2)$ can be obtained with a change in sign. All the above stated energetic weak formulations are characterized by bilinear forms whose connection with the energy (1.44) is essential to show good properties of coerciveness and continuity. These allow to establish the spaces where the weak problem has a unique solution, depending in a continuous way on the boundary data. The related theoretical proof, that is also reported in Author's paper [7] (currently under review), is shown in the following section and the results are collected for the single layer and the hypersingular weak formulation in Lemma 1.4.2.

1.4 Coercivity and continuity of the bilinear form

We introduce here space–time anisotropic Sobolev spaces, defined on the boundary Γ, as a convenient functional analytic setting for the analysis of the time dependent boundary integral operators V and D, defined respectively in (1.26) and (1.37). A detailed exposition of the following arguments may be found in [46, 40]. In the case of an open arc, namely

$\partial\Gamma \neq \emptyset$, we first extend Γ to a closed, orientable Lipschitz manifold $\widetilde{\Gamma}$. We recall the usual Sobolev spaces of supported distributions, associated with Γ:

$$\widetilde{H}^s(\Gamma) = \left\{ u \in H^s\left(\widetilde{\Gamma}\right) : \ supp(u) \subset \overline{\Gamma} \right\}, \qquad s \in \mathbf{R}.$$

The Sobolev space $H^s(\Gamma)$ we consider is the quotient space $H^s\left(\widetilde{\Gamma}\right) / \widetilde{H}^s\left(\widetilde{\Gamma} \setminus \overline{\Gamma}\right)$. For the latter, we need to define a family of Sobolev norms. To do this, we set partition of unity $\{\alpha_i\}_{i\in I}$ subordinated to $\{B_i\}_{i\in I}$, which represents a covering of $\widetilde{\Gamma}$ by open sets, I being a finite set of indexes. Given, for each $i \in I$, a diffeomorphism φ_i from B_i to the unit square in $\mathbf{R}^2$, Sobolev norms are induced from $\mathbf{R}^2$, with parameter $\omega \in \mathbb{C} \setminus \{0\}$:

$$||u||_{s,\omega,\widetilde{\Gamma}} = \left(\sum_{i\in I} \int_{\mathbf{R}^2} (|\omega|^2 + |\boldsymbol{\xi}|^2)^s |\mathcal{F}_{\mathbf{x}\mapsto\boldsymbol{\xi}} \left\{ (\alpha_i u) \circ \varphi_i^{-1} \right\} (\boldsymbol{\xi})|^2 d\boldsymbol{\xi} \right)^{\frac{1}{2}}. \tag{1.50}$$

Here, $\mathcal{F}_{\mathbf{x}\mapsto\boldsymbol{\xi}}$ denotes the Fourier transform

$$\mathcal{F}_{\mathbf{x}\mapsto\boldsymbol{\xi}}\varphi(\boldsymbol{\xi}) = \widehat{\varphi}(\boldsymbol{\xi}) = \int_{\mathbf{R}^2} e^{-i\mathbf{x}\cdot\boldsymbol{\xi}} \varphi(\mathbf{x}) \, d\mathbf{x}.$$

Different values of ω in (1.50) induce equivalent norms on $H^s(\Gamma)$, $\|u\|_{s,\omega,\Gamma} = \inf_{v\in\widetilde{H}^s(\widetilde{\Gamma}\setminus\overline{\Gamma})} \|u+v\|_{s,\omega,\widetilde{\Gamma}}$ and on $\widetilde{H}^s(\Gamma)$, $\|u\|_{s,\omega,\Gamma,*} = \|e_+(u)\|_{s,\omega,\widetilde{\Gamma}}$, with e_+ extending the distribution u by 0 from Γ to $\widetilde{\Gamma}$. When a specific ω is fixed, we write $H^s_\omega(\Gamma)$ for $H^s(\Gamma)$, respectively $\widetilde{H}^s_\omega(\Gamma)$ for $\widetilde{H}^s(\Gamma)$. We moreover recall that the norm $\|u\|_{s,\omega,\Gamma,*}$ is stronger than $\|u\|_{s,\omega,\Gamma}$. We can now define a family of space-time anisotropic Sobolev spaces, in order to furnish a precise functional setting for for the next proof: given $\sigma > 0$, $r, s \in \mathbf{R}$

$$H^r_\sigma\left(\mathbf{R}^+; H^s(\Gamma)\right) = \left\{ u \in \mathcal{D}'_+(H^s(\Gamma)) : e^{-\sigma t}u \in \mathcal{S}'_+(H^s(\Gamma)) \text{ and } ||u||_{r,s,\Gamma} < \infty \right\}, \tag{1.51}$$

$$H^r_\sigma\left(\mathbf{R}^+; \widetilde{H}^s(\Gamma)\right) = \left\{ u \in \mathcal{D}'_+(\widetilde{H}^s(\Gamma)) : e^{-\sigma t}u \in \mathcal{S}'_+(\widetilde{H}^s(\Gamma)) \text{ and } ||u||_{r,s,\Gamma,*} < \infty \right\}. \tag{1.52}$$

Here, $\mathcal{D}'_+(E)$ denotes the space of all distributions on $\mathbf{R}$ with support in $[0,\infty)$, taking values in a Hilbert space $E = H^s(\Gamma)$ and $E = \widetilde{H}^s(\Gamma)$, respectively. $\mathcal{S}'_+(E) \subset \mathcal{D}'_+(E)$ denotes the subspace of tempered distributions. Spaces (1.51)-(1.52) are equipped with the norms

$$\|u\|_{r,s} := \|u\|_{r,s,\Gamma} = \left(\int_{-\infty+i\sigma}^{+\infty+i\sigma} |\omega|^{2r} \, \|\hat{u}(\omega)\|^2_{s,\omega,\Gamma} \, d\omega \right)^{\frac{1}{2}},$$

$$\|u\|_{r,s,*} := \|u\|_{r,s,\Gamma,*} = \left(\int_{-\infty+i\sigma}^{+\infty+i\sigma} |\omega|^{2r} \, \|\hat{u}(\omega)\|^2_{s,\omega,\Gamma,*} \, d\omega \right)^{\frac{1}{2}}$$

and they result properly Hilbert spaces. For $r = s = 0$ they correspond to the weighted L^2-space with scalar product

$$\int_0^\infty e^{-2\sigma t} \int_\Gamma u\overline{v} d\Gamma_{\mathbf{x}} \, dt.$$

Since Γ is a Lipschitz boundary, these spaces are independent of the choice of α_i and φ_i when $|s| \leq 1$, as for standard Sobolev spaces.
We will use the norms $\|u\|_{r,s,(t_1,t_2]\times\Gamma}$ and $\|u\|_{r,s,(t_1,t_2]\times\Gamma,*}$ in the proofs of Chapter 2 to identify restrictions on the time interval $(t_1, t_2]$.

Let now $\widetilde{\Gamma} = \partial\Omega$ be the boundary of a Lipschitz subset $\Omega \subset \mathbb{R}^2$ and $\Gamma \subset \widetilde{\Gamma}$ open, denoting moreover $\Omega_e = \mathbb{R}^2 \setminus \overline{\Omega}$. In this way next proof can cover both cases of elastodynamics problems with open or closed obstacle. For convenience of the reader, we recall basic properties of the following bilinear form

$$B_{\mathcal{D}}(\boldsymbol{\Phi}, \tilde{\boldsymbol{\Phi}}) := \int_{\mathbf{R}^+} \int_{\Gamma} e^{-2\sigma t} \frac{\partial}{\partial t} \left(V\boldsymbol{\Phi}(t, \mathbf{x})\right) \cdot \tilde{\boldsymbol{\Phi}}(t, \mathbf{x}) \, d\Gamma_{\mathbf{x}} \, dt \, , \tag{1.53}$$

that will be considered for a positive σ in the proof of the following preposition and that corresponds to the energetic single layer bilinear form of formula (1.46) for $\sigma = 0$. We will use in following proposition the symbol $f \lesssim g$, which means that exists a constant C such that $f \leqslant Cg$.

Proposition 1.4.1. *For every* $\boldsymbol{\Phi}, \tilde{\boldsymbol{\Phi}} \in H^1_\sigma \left(\mathbf{R}^+, H^{-\frac{1}{2}}(\Gamma)\right)^2$ *there holds:*

$$|B_{\mathcal{D}}(\boldsymbol{\Phi}, \tilde{\boldsymbol{\Phi}})| \lesssim \|\boldsymbol{\Phi}\|_{1,-\frac{1}{2},\Gamma,*} \|\tilde{\boldsymbol{\Phi}}\|_{1,-\frac{1}{2},\Gamma,*} \quad \textit{and} \quad \|\boldsymbol{\Phi}\|^2_{0,-\frac{1}{2},\Gamma,*} \lesssim B_{\mathcal{D}}(\boldsymbol{\Phi}, \boldsymbol{\Phi}).$$

Proof. For the proof we consider the elastic problem in the frequency domain:

$$\begin{cases} (\lambda + \mu)\nabla(\nabla \cdot \mathbf{u}) + \mu\Delta\mathbf{u} + \varrho\omega^2\mathbf{u} = \nabla \cdot \boldsymbol{\sigma}(\mathbf{u}) + \varrho\omega^2\mathbf{u} = 0, \quad \mathbf{x} \in \Omega \cup \Omega_e, \\ \mathbf{u}_+ = \mathbf{u}_- = \mathbf{g}, \quad \mathbf{x} \in \widetilde{\Gamma} \end{cases} , \tag{1.54}$$

obtained applying the Fourier transform in the time variable

$$\mathcal{F}_{t\mapsto\omega}\mathbf{v}(\omega) = \widehat{\mathbf{v}}(\omega) = \int_0^{+\infty} e^{i\omega t}\mathbf{v}(t)dt \tag{1.55}$$

to the equation (1.9) (or equivalently (1.8)) and assuming $\mathcal{I}m(\omega) \geq \sigma > 0$. In problem (1.54) $\mathbf{u}_+$ identifies the limit of the displacement towards $\widetilde{\Gamma}$ from the external domain Ω_e (respectively $\mathbf{u}_-$ represents the limit from the inner set Ω). We remark that the lower extreme of integration in (1.55) is 0 since the unknown $\mathbf{u}$ is causal in time (namely $\mathbf{u} \equiv 0$ for $t < 0$). To avoid burdening of notation, we will indicate only by square brackets $[\cdot]$, omitting then the subscript $\widetilde{\Gamma}$, the jump of a field across the boundary $\widetilde{\Gamma}$. Then, the energetic weak formulation for the single layer equation for the jump of the traction $[\mathbf{p}] = [\boldsymbol{\sigma}(\mathbf{u})\mathbf{n}]$ in frequency domain is given by:

Find $[\mathbf{p}] \in H_\omega^{-\frac{1}{2}} \left(\widetilde{\Gamma}\right)^2$ *such that*

$$B_{\mathcal{D},\omega}([\mathbf{p}], \overline{\boldsymbol{\Phi}}) = \langle -i\omega V_\omega[\mathbf{p}], \overline{\boldsymbol{\Phi}}\rangle_{\widetilde{\Gamma}} = \langle -i\omega\mathbf{g}, \overline{\boldsymbol{\Phi}}\rangle_{\widetilde{\Gamma}} \tag{1.56}$$

for all $\boldsymbol{\Phi} \in H_\omega^{-\frac{1}{2}} \left(\widetilde{\Gamma}\right)^2$.

It involves the single layer operator V_ω obtained from V defined in (1.26) by Fourier transformation. If we execute the scalar product between the conjugate of equation in (1.54) and $\mathbf{u}$ and we integrate by parts over $\Omega \cup \Omega_e$, using Green's formula as in [19], Theorem 3.1, we obtain the following equality:

$$\int_{\Omega\cup\Omega_e} \left(\overline{\boldsymbol{\sigma}(\mathbf{u})} : \boldsymbol{\varepsilon}(\mathbf{u}) - \varrho\omega^2|\mathbf{u}|^2\right) d\mathbf{x} = \int_{\widetilde{\Gamma}} \mathbf{u} \cdot \overline{[\boldsymbol{\sigma}(\mathbf{u})\mathbf{n}]}_{\widetilde{\Gamma}} d\widetilde{\Gamma} \equiv \langle V_\omega[\mathbf{p}], \overline{[\mathbf{p}]}\rangle_{\widetilde{\Gamma}}.$$

Observing that $|\langle -i\omega V_\omega[\mathbf{p}], \overline{[\mathbf{p}]}\rangle_{\widetilde{\Gamma}}| \geqslant \mathcal{R}e\left(i\overline{\omega}\langle V_\omega[\mathbf{p}], \overline{[\mathbf{p}]}\rangle_{\widetilde{\Gamma}}\right)$ we get to the estimate

$$\begin{aligned}\mathcal{R}e\left(i\overline{\omega}\langle \mathcal{V}_\omega[\mathbf{p}], \overline{[\mathbf{p}]}\rangle_{\widetilde{\Gamma}}\right) &= \mathcal{R}e\left(i\overline{\omega}\int_{\Omega_+\cup\Omega_-} \overline{\boldsymbol{\sigma}(\mathbf{u})} : \boldsymbol{\varepsilon}(\mathbf{u}) d\mathbf{x}\right) + \mathcal{R}e\left(-i\omega\int_{\Omega\cup\Omega_e} \varrho|\omega|^2|\mathbf{u}|^2 d\mathbf{x}\right) \\ &= 2\mathcal{I}m(\omega)\mathcal{E}_\omega \geqslant 0, \end{aligned} \tag{1.57}$$

with

$$\mathcal{E}_\omega = \frac{1}{2}\int_{\Omega\cup\Omega_e} \left(\overline{\boldsymbol{\sigma}(\mathbf{u})} : \boldsymbol{\varepsilon}(\mathbf{u}) + \varrho|\omega|^2|\mathbf{u}|^2\right) d\mathbf{x}\ .$$

Physically, $\mathcal{E}_\omega$ is the energy of the displacement $\mathbf{u}$, and (see Lemma 3.2 in [19]) it satisfies

$$\mathcal{E}_\omega \geqslant C_\sigma \|\mathbf{u}\|^2_{1,\omega,\Omega\cup\Omega_e} \tag{1.58}$$

for a positive constant C_σ. From (1.57) and (1.58) we deduce that

$$|\langle -i\omega\mathcal{V}_\omega[\mathbf{p}], \overline{[\mathbf{p}]}\rangle_{\widetilde{\Gamma}}| \geqslant \widetilde{C}_\sigma \|\mathbf{u}\|^2_{1,\omega,\Omega\cup\Omega_e}\ .$$

From the trace theorem (see [19]) there exists a positive constant C_{trace} such that

$$2C_{trace}\|\mathbf{u}\|^2_{1,\omega,\Omega\cup\Omega_e} \geqslant 2\|\mathbf{p}|_{\widetilde{\Gamma}_+}\|^2_{-1/2,\omega,\widetilde{\Gamma}} + 2\|\mathbf{p}|_{\widetilde{\Gamma}_-}\|^2_{-1/2,\omega,\widetilde{\Gamma}} \geqslant \|[\mathbf{p}]\|^2_{-1/2,\omega,\widetilde{\Gamma}}.$$

Coercivity in the frequency domain follows:

$$|\langle -i\omega V_\omega[\mathbf{p}], \overline{[\mathbf{p}]}\rangle_{\widetilde{\Gamma}}| \geqslant \frac{\widetilde{C}_\sigma}{2C_{trace}}\|[\mathbf{p}]\|^2_{-1/2,\omega,\widetilde{\Gamma}}. \tag{1.59}$$

Concerning the continuity of V_ω, we use (1.57), (1.58) and the trace theorem $\|\mathbf{u}\|^2_{1,\omega,\Omega\cup\Omega_e} \geqslant \hat{C}_\sigma\|\mathbf{u}|_{\widetilde{\Gamma}_+}\|^2_{1/2,\omega,\widetilde{\Gamma}}$ as in the appendix of [40]:

$$\mathcal{R}e\left(i\overline{\omega}\langle V_\omega[\mathbf{p}], \overline{[\mathbf{p}]}\rangle_{\widetilde{\Gamma}}\right) \geqslant C'_\sigma\|\mathbf{u}|_{\widetilde{\Gamma}_+}\|^2_{1/2,\omega,\widetilde{\Gamma}}. \tag{1.60}$$

Using the Cauchy-Schwartz inequality, we write

$$\mathcal{R}e\left(i\overline{\omega}\langle V_\omega[\mathbf{p}], \overline{[\mathbf{p}]}\rangle_{\widetilde{\Gamma}}\right) \leqslant |\omega|\|[\mathbf{p}]\|_{-1/2,\omega,\widetilde{\Gamma}}\|\mathbf{u}|_{\widetilde{\Gamma}_+}\|_{1/2,\omega,\widetilde{\Gamma}}. \tag{1.61}$$

Combining (1.60) and (1.61) we observe that

$$C'_\sigma\|\mathbf{u}|_{\widetilde{\Gamma}_+}\|_{1/2,\omega,\widetilde{\Gamma}} \leqslant |\omega|\|[\mathbf{p}]\|_{-1/2,\omega,\widetilde{\Gamma}}\ ,$$

and therefore

$$\|V_\omega[\mathbf{p}]\|_{1/2,\omega,\widetilde{\Gamma}} \leqslant \frac{|\omega|}{C'_\sigma}\|[\mathbf{p}]\|_{-1/2,\omega,\widetilde{\Gamma}}. \tag{1.62}$$

It remains to transfer the continuity (1.62) and coercivity (1.59) from the frequency domain into the time domain. Integrating (1.56) in ω and using the Parseval identity, recalling the property $\mathcal{F}^{-1}_{\omega\mapsto t}\left(\widehat{\varphi}(\omega+i\sigma)\right)=\varphi(t)e^{-\sigma t}$, we get the identity

$$\int_{\mathbf{R}+i\sigma}\int_{\widetilde{\Gamma}} -i\omega V_\omega\widehat{\mathbf{\Phi}}\cdot\overline{\widehat{\mathbf{\Phi}}}d\widetilde{\Gamma}d\omega = \int_0^{+\infty}\int_{\widetilde{\Gamma}} e^{-2\sigma t}\frac{\partial}{\partial t}\left(V\mathbf{\Phi}\right)\cdot\mathbf{\Phi}d\widetilde{\Gamma}dt = B_{\mathcal{D}}\left(\mathbf{\Phi},\mathbf{\Phi}\right).$$

To show continuity we use (1.62), the definition of the space-time Sobolev norms and the Cauchy-Schwartz inequality:

$$\begin{aligned} B_{\mathcal{D}}\left(\mathbf{\Phi},\tilde{\mathbf{\Phi}}\right) \leqslant \int_{\mathbf{R}+i\sigma}\left|\int_{\widetilde{\Gamma}} -i\omega V_\omega\widehat{\mathbf{\Phi}}\cdot\overline{\widehat{\tilde{\mathbf{\Phi}}}}d\widetilde{\Gamma}\right|d\omega &\leqslant \frac{1}{C'_\sigma}\int_{\mathbf{R}+i\sigma}|\omega|^2\|\widehat{\mathbf{\Phi}}\|_{-1/2,\omega,\widetilde{\Gamma}}\|\widehat{\tilde{\mathbf{\Phi}}}\|_{-1/2,\omega,\widetilde{\Gamma}}d\omega \\ &\leqslant \frac{1}{C'_\sigma}\|\mathbf{\Phi}\|_{1,-1/2,\widetilde{\Gamma}}\|\tilde{\mathbf{\Phi}}\|_{1,-1/2,\widetilde{\Gamma}}\,. \end{aligned} \tag{1.63}$$

For the coerciveness, we similarly use (1.59):

$$Re\, B_{\mathcal{D}}\left(\mathbf{\Phi},\mathbf{\Phi}\right) = \int_{\mathbf{R}+i\sigma}\mathcal{R}e\, i\overline{\omega}\langle V_\omega\widehat{\mathbf{\Phi}},\overline{\widehat{\mathbf{\Phi}}}\rangle_{\widetilde{\Gamma}} \geqslant \frac{\widetilde{C}_\sigma}{2C_{trace}}\int_{\mathbf{R}+i\sigma}\|\widehat{\mathbf{\Phi}}\|^2_{-1/2,\omega,\widetilde{\Gamma}}d\omega\,. \tag{1.64}$$

Therefore

$$\left|B_{\mathcal{D}}\left(\mathbf{\Phi},\mathbf{\Phi}\right)\right| \geqslant \frac{\widetilde{C}_\sigma}{2C_{trace}}\|\mathbf{\Phi}\|^2_{0,-1/2,\widetilde{\Gamma}}\,.$$

Proposition 1.4.1 follows by restricting to distributions supported in $\Gamma\subset\widetilde{\Gamma}$. □

Proposition 1.4.1 can be generalized in the Sobolev space $H^r_\sigma\left(\mathbf{R}^+LH^{-\frac{1}{2}}(\Gamma)\right)^2$ just recasting formulas (1.63) and (1.64) with $\omega^r\widehat{\mathbf{\Phi}}$ and $\omega^r\widehat{\tilde{\mathbf{\Phi}}}$, instead of $\widehat{\mathbf{\Phi}}$ and $\widehat{\tilde{\mathbf{\Phi}}}$, for an exponent $r\in\mathbf{R}$.

Proof of Proposition 1.4.1 furnishes us a theoretical setting for the energetic weak formulations depending on a single layer bilinear form as in (1.46), while for the hypersingular operator D, and the related energetic weak formulations, we refer for the knowledge of the reader to the proof in [19]. Therefore, Lax-Milgram hypothesis (for details see [71]) are verified in the introduced Sobolev spaces for both the energetic weak formulations (1.46) and (1.48), allowing us to state the following Lemma:

Lemma 1.4.2. *Let $\sigma>0$, $r\in\mathbf{R}$:*
a) assume that $\mathbf{g}_{\mathcal{D}}\in H^{r+1}_\sigma(\mathbf{R}^+;H^{\frac{1}{2}}(\Gamma))^2$. Then there exists a unique solution $\mathbf{\Phi}\in H^r_\sigma(\mathbf{R}^+;\widetilde{H}^{-\frac{1}{2}}(\Gamma))^2$ of (1.46) and

$$\|\mathbf{\Phi}\|_{r,-\frac{1}{2},\Gamma,*}\lesssim_\sigma \|\mathbf{g}_{\mathcal{D}}\|_{r+1,\frac{1}{2},\Gamma}, \tag{1.65}$$

b) assume that $\mathbf{g}_{\mathcal{N}} \in H^{r+1}_{\sigma}(\mathbf{R}^+; H^{-\frac{1}{2}}(\Gamma))^2$. *Then there exists a unique solution* $\mathbf{\Psi} \in H^{r}_{\sigma}(\mathbf{R}^+; \widetilde{H}^{\frac{1}{2}}(\Gamma))^2$ *of* (1.48) *and*

$$\|\mathbf{\Psi}\|_{r,\frac{1}{2},\Gamma,*} \lesssim_{\sigma} \|\mathbf{g}_{\mathcal{N}}\|_{r+1,-\frac{1}{2},\Gamma}, \tag{1.66}$$

where the symbol $f \lesssim_{\sigma} g$, *means that exists a constant* C_{σ}, *depending on* σ, *such that* $f \leqslant C_{\sigma} g$

Remark. Coercivity and continuity are well established in Sobolev spaces depending on a parameter $\sigma > 0$. Anyway, the latter can be considered as small as we prefer. To be specific, for the sake of simplicity of the algorithmic implementation, we will consider the limit $\sigma \to 0^+$, meaning that all the formulation (1.46), (1.48) and (1.49) are reworked, in the next section, in a discretized form independent of σ.

1.5 Space-time discretization

1.5.1 Single Layer and Hypersingular integral operators

To solve the energetic weak formulations (1.46) and (1.48) in a discretized form, we consider a uniform decomposition of the time interval $[0, T]$ setting the time knots $t_n = n\Delta t$, $n = 0, \ldots, N$, with time step $\Delta t = T/N$. We define the corresponding space $V_{\Delta t,s}$ of piece-wise polynomial functions of degree s in time (continuous and vanishing at $t = 0$ if $s \geq 1$).
For the space discretization, we introduce a boundary mesh constituted by a set of straight segments $\mathcal{T} = \{e_1, ..., e_M\}$ such that $h_i := length(e_i) \leqslant h$, $e_i \cap e_j = \emptyset$ if $i \neq j$ and $\cup_{i=1}^{M} \overline{e}_i = \overline{\Gamma}$ if Γ is polygonal: otherwise, $\cup_{i=1}^{M} \overline{e}_i$ can be considered a fine approximation of $\overline{\Gamma}$. We also introduce the set of the $M + 1$ mesh points $\mathcal{T}_{\mathbf{o}} = \{\mathbf{o}_1, \ldots, \mathbf{o}_{M+1}\}$ such that $e_i = \overline{\mathbf{o}_i \mathbf{o}_{i+1}}$ for all $i = 1, ..., M$, adding the condition $\mathbf{o}_{M+1} = \mathbf{o}_1$ for closed Γ. On $\mathcal{T}$, once defined $\mathcal{P}_p$ as the set of polynomials of degree p, we consider the spaces of piece-wise polynomial functions

$$X^{-1}_{h,p}(\Gamma) = \left\{ w \in L^2(\Gamma) \ : \ w_{|_{e_i}} \in \mathcal{P}_p \, \forall e_i \in \mathcal{T} \right\} \tag{1.67}$$

and

$$X^{0}_{h,q}(\Gamma) = \left\{ w \in C^0(\Gamma) \ : \ w_{|_{e_i}} \in \mathcal{P}_q \, \forall e_i \in \mathcal{T}, \ w_{|_{\partial\Gamma}} = 0 \text{ if } \partial\Gamma \neq \emptyset \right\}. \tag{1.68}$$

After having chosen an appropriate degree p for the approximation of Φ_i in space, the Galerkin approximation of (1.46) reads:

find $\Phi_{i,h,\Delta t} \in V_{\Delta t,0} \otimes X^{-1}_{h,p}(\Gamma)$, $i = 1, 2$ *such that*

$$\langle (V_{ij} \dot{\Phi}_{j,h,\Delta t}), \phi_{i,h,\Delta t} \rangle_{L^2(\Sigma)} = \langle \dot{g}_{\mathcal{D},i}, \phi_{i,h,\Delta t} \rangle_{L^2(\Sigma)}, \tag{1.69}$$

for all $\boldsymbol{\phi}_{h,\Delta t} = (\phi_{1,h,\Delta t}, \phi_{2,h,\Delta t})^{\top} \in \left(V_{\Delta t,0} \otimes X^{-1}_{h,p}(\Gamma) \right)^2$.

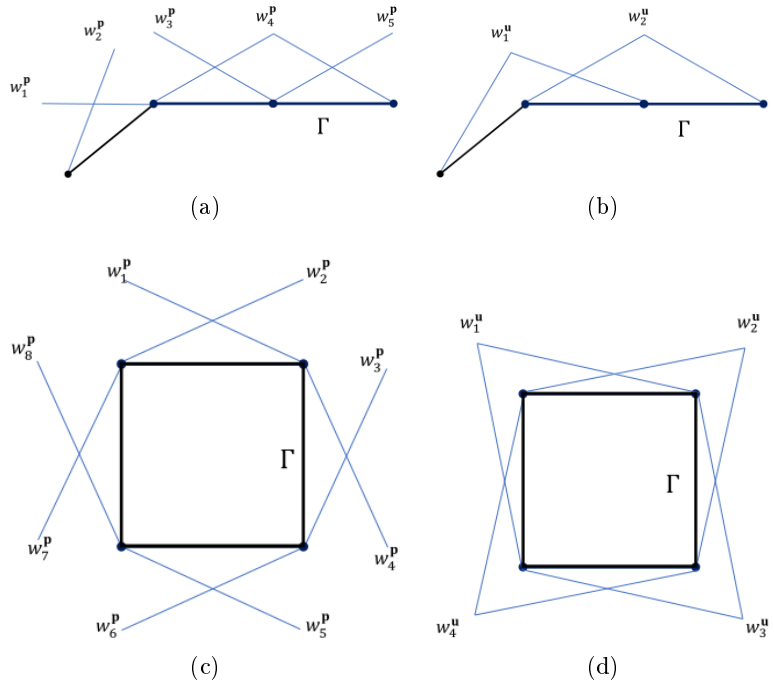

Figure 1.1: Here a graphical representation of linear basis functions constructed on the elements of a polygonal arc Γ is shown. Figures in the first column represent the linear basis of the functional space $X^{-1}_{h,1}$, for an open and a closed polygonal arc ((a) and (c)): this functional space is the space for the approximation of the traction components, so the basis has to be split at the corners because the normal vector cannot be uniquely determined. In the second column, the basis for the space $X^{0}_{h,1}$ is shown ((b) and (d)): in this case the basis has to represent the continuous of the displacement components, namely the basis functions result continuous at the corner points, and null at the edges of an open arc.

Setting q as the degree for the polynomials approximating Ψ_i in space, the Galerkin formulation related to (1.48) instead reads:

$$\textit{find } \Psi_{i,h,\Delta t} \in V_{\Delta t,1} \otimes X^0_{h,q}(\Gamma),\ i = 1,2 \textit{ such that}$$
$$\langle D_{ij}\Psi_{j,h,\Delta t}, \dot{\psi}_{i,h,\Delta t}\rangle_{L^2(\Sigma)} = \langle g_{\mathcal{N},i}, \dot{\psi}_{i,h,\Delta t}\rangle_{L^2(\Sigma)}, \tag{1.70}$$
$$\textit{for all } \boldsymbol{\psi}_{h,\Delta t} = (\psi_{1,h,\Delta t}, \psi_{2,h,\Delta t})^\top \in \left(V_{\Delta t,1} \otimes X^0_{h,q}(\Gamma)\right)^2.$$

Once established these discrete weak formulations, we proceed introducing the set $\left\{w^{\mathbf{p}}_m(\mathbf{x})\right\}_{m=1}^{M_{\mathbf{p}}}$ containing the basis functions of $X^{-1}_{h,p}(\Gamma)$, which are piece-wise polynomials depending on the Lagrangian functions defined on each element e_i. Similarly, the set $\{w^{\mathbf{u}}_m(\mathbf{x})\}_{m=1}^{M_{\mathbf{u}}}$ corresponds to a basis of the functional space $X^0_{h,q}(\Gamma)$. For a graphical representation of the two sets of basis in case of $p = q = 1$ we refer to Figure 1.1.
In time, we choose piece-wise constant functions for the approximation of $\mathbf{\Phi}$:

$$v_n(t) = H[t - t_n] - H[t - t_{n+1}], \quad n = 0, ..., N-1, \tag{1.71}$$

and ramp functions for the approximation of $\boldsymbol{\Psi}$:

$$r_n(t) = \frac{t-t_n}{\Delta t} H[t-t_n] - \frac{t-t_{n+1}}{\Delta t} H[t-t_{n+1}], \quad n = 0, ..., N-1. \tag{1.72}$$

Hence, the components of the discrete BIE solutions $\boldsymbol{\Phi}_{h,\Delta t}$ and $\boldsymbol{\Psi}_{h,\Delta t}$ can be expressed as follows

$$\Phi_{i,h,\Delta t}(\mathbf{x},t) = \sum_{n=0}^{N-1} \sum_{m=1}^{M_{\mathbf{p}}} \alpha_{nm}^{\mathbf{p},i} w_m^{\mathbf{p}}(\mathbf{x}) v_n(t), \quad i = 1,2, \tag{1.73}$$

and

$$\Psi_{i,h,\Delta t}(\mathbf{x},t) = \sum_{n=0}^{N-1} \sum_{m=1}^{M_{\mathbf{u}}} \alpha_{nm}^{\mathbf{u},i} w_m^{\mathbf{u}}(\mathbf{x}) r_n(t), \quad i = 1,2. \tag{1.74}$$

For what regards the test functions, $\phi_{i,h,\Delta t}(\mathbf{x},t)$ in (1.69) is replaced by the product $w_{\widetilde{m}}^{\mathbf{p}}(\mathbf{x}) v_{\widetilde{n}}(t)$ for every $\widetilde{m} = 0, ..., M_{\mathbf{p}}$ and $\widetilde{n} = 0, ..., N-1$, while $\psi_{i,h,\Delta t}(\mathbf{x},t)$ in (1.70) is substituted by the product $w_{\widetilde{m}}^{\mathbf{u}}(\mathbf{x}) r_{\widetilde{n}}(t)$ for every $\widetilde{m} = 0, ..., M_{\mathbf{u}}$ and $\widetilde{n} = 0, ..., N-1$. Replacing the linear combinations (1.73) in (1.69), solving the space-time Galerkin equation for the considered Dirichlet problem translates into the resolution of the linear system $\mathbb{E}_V \boldsymbol{\alpha}^{\mathbf{p}} = \boldsymbol{\beta}^{\mathcal{D}}$, which is featured by the following structure:

$$\begin{pmatrix} \mathbb{E}_V^{(0)} & 0 & 0 & \cdots & 0 \\ \mathbb{E}_V^{(1)} & \mathbb{E}_V^{(0)} & 0 & \cdots & 0 \\ \mathbb{E}_V^{(2)} & \mathbb{E}_V^{(1)} & \mathbb{E}_V^{(0)} & \cdots & 0 \\ \vdots & \vdots & \vdots & \ddots & \vdots \\ \mathbb{E}_V^{(N-1)} & \mathbb{E}_V^{(N-2)} & \mathbb{E}_V^{(N-3)} & \cdots & \mathbb{E}_V^{(0)} \end{pmatrix} \begin{pmatrix} \boldsymbol{\alpha}_{(0)}^{\mathbf{p}} \\ \boldsymbol{\alpha}_{(1)}^{\mathbf{p}} \\ \boldsymbol{\alpha}_{(2)}^{\mathbf{p}} \\ \vdots \\ \boldsymbol{\alpha}_{(N-1)}^{\mathbf{p}} \end{pmatrix} = \begin{pmatrix} \boldsymbol{\beta}_{(0)}^{\mathcal{D}} \\ \boldsymbol{\beta}_{(1)}^{\mathcal{D}} \\ \boldsymbol{\beta}_{(2)}^{\mathcal{D}} \\ \vdots \\ \boldsymbol{\beta}_{(N-1)}^{\mathcal{D}} \end{pmatrix}. \tag{1.75}$$

For all $l = 0, ..., N-1$ the entries of the linear system are organized as below (the notation employed is similar to the one used in [5]):

$$\mathbb{E}_V^{(l)} = \begin{pmatrix} \mathbb{E}_{V,11}^{(l)} & \mathbb{E}_{V,12}^{(l)} \\ \mathbb{E}_{V,21}^{(l)} & \mathbb{E}_{V,22}^{(l)} \end{pmatrix}, \quad \boldsymbol{\alpha}_{(l)}^{\mathbf{p}} = \begin{pmatrix} \alpha_{l1}^{\mathbf{p},1} \\ \vdots \\ \alpha_{lM_{\mathbf{p}}}^{\mathbf{p},1} \\ \alpha_{l1}^{\mathbf{p},2} \\ \vdots \\ \alpha_{lM_{\mathbf{p}}}^{\mathbf{p},2} \end{pmatrix}, \quad \boldsymbol{\beta}_{(l)}^{\mathcal{D}} = \begin{pmatrix} \beta_{l1}^{\mathcal{D},1} \\ \vdots \\ \beta_{lM_{\mathbf{p}}}^{\mathcal{D},1} \\ \beta_{l1}^{\mathcal{D},2} \\ \vdots \\ \beta_{lM_{\mathbf{p}}}^{\mathcal{D},2} \end{pmatrix}.$$

Solving (1.75) by backward substitution leads to a marching-on-time time stepping scheme (MOT), i.e. at every time instant t_l with $l = 0, \ldots, N-1$, one computes

$$\mathbf{z}_{(l)} = \boldsymbol{\beta}_{(l)}^{\mathcal{D}} - \sum_{j=1}^{l} \mathbb{E}_V^{(j)} \boldsymbol{\alpha}_{(l-j)}^{\mathbf{p}} \tag{1.76}$$

and then solves the reduced linear system

$$\mathbb{E}_V^{(0)} \boldsymbol{\alpha}_{(l)}^{\mathbf{p}} = \mathbf{z}_{(l)}. \tag{1.77}$$

We remarks that only the LU-factorization of the first block $\mathbb{E}_V^{(0)}$ is required to get the solution of the entire system. An important advantage in the implementation costs and in the memory storage is given by the Toeplitz structure of $\mathbb{E}_V$, for which the construction and storage of only the first column of temporal blocks is required.
To obtain the generic matrix entry of the sub-block $\mathbb{E}_V^{(l)}$, where $l = \widetilde{n} - n$ is a non negative difference between two time indexes, we can perform in the bilinear form of (1.69) an analytical integration in the time variables t and τ, as indicated in the Appendix chapter, Section A.1, leading to the formula

$$\left(\mathbb{E}_{V,ij}^{(l)}\right)_{\widetilde{m},m} = -\sum_{\xi,\varsigma=0}^{1} \frac{(-1)^{\xi+\varsigma}}{2\pi\varrho} \int_\Gamma \int_\Gamma w_{\widetilde{m}}^{\mathbf{p}}(\mathbf{x}) w_m^{\mathbf{p}}(\boldsymbol{\xi}) \nu_{ij}^V(\mathbf{r}; \Delta_{\widetilde{n}+\xi,n+\varsigma}) d\Gamma_{\boldsymbol{\xi}} d\Gamma_{\mathbf{x}}, \tag{1.78}$$

for all $i,j = 1,2$, $m,\widetilde{m} = 1,...,M_{\mathbf{p}}$ and $n,\widetilde{n} = 0,...,N-1$, with the time difference $t_{\widetilde{n}+\xi} - t_{n+\varsigma} = \Delta_{\widetilde{n}+\xi,n+\varsigma} \geqslant 0$ and the integration kernel

$$\begin{aligned}\nu_{ij}^V(\mathbf{r};\Delta) = \left(\frac{r_i r_j}{r^4} - \frac{\delta_{ij}}{2r^2}\right)\left[\frac{H[c_{\mathtt{P}}\Delta - r]}{c_{\mathtt{P}}}\Delta\varphi_{\mathtt{P}}(r;\Delta) - \frac{H[c_{\mathtt{S}}\Delta - r]}{c_{\mathtt{S}}}\Delta\varphi_{\mathtt{S}}(r;\Delta)\right] \\ + \frac{\delta_{ij}}{2}\left[\frac{H[c_{\mathtt{P}}\Delta - r]}{c_{\mathtt{P}}^2}\widehat{\varphi}_{\mathtt{P}}(r;\Delta) + \frac{H[c_{\mathtt{S}}\Delta - r]}{c_{\mathtt{S}}^2}\widehat{\varphi}_{\mathtt{S}}(r;\Delta)\right].\end{aligned} \tag{1.79}$$

For each $\gamma = \mathtt{P},\mathtt{S}$, the specific kernel functions are given by

$$\varphi_\gamma(r;\Delta) := \sqrt{c_\gamma^2\Delta^2 - r^2}, \tag{1.80}$$

$$\widehat{\varphi}_\gamma(r;\Delta) := \log\left(\sqrt{c_\gamma^2\Delta^2 - r^2} + c_\gamma\Delta\right) - \log(r). \tag{1.81}$$

If $0 < r \leqslant c_{\mathtt{S}}\Delta_{\widetilde{n}+\xi,n+\varsigma} < c_{\mathtt{P}}\Delta_{\widetilde{n}+\xi,n+\varsigma}$ the kernel ν_{ij}^V has a reduced form:

$$\nu_{ij}^V(\mathbf{r};\Delta_{\widetilde{n}+\xi,n+\varsigma}) = h_{1,ij}^V(\mathbf{r};\Delta_{\widetilde{n}+\xi,n+\varsigma}) + h_{2,ij}^V(\mathbf{r};\Delta_{\widetilde{n}+\xi,n+\varsigma}), \tag{1.82}$$

where

$$\begin{aligned}h_{1,ij}^V(\mathbf{r};\Delta) = \frac{c_{\mathtt{P}}^2 - c_{\mathtt{S}}^2}{c_{\mathtt{P}}c_{\mathtt{S}}}\left(\frac{r_i r_j}{r^2} - \frac{\delta_{ij}}{2}\right)\frac{\Delta}{c_{\mathtt{P}}\sqrt{c_{\mathtt{S}}^2\Delta^2 - r^2} + c_{\mathtt{S}}\sqrt{c_{\mathtt{P}}^2\Delta^2 - r^2}} \\ + \frac{\delta_{ij}}{2}\left[\frac{1}{c_{\mathtt{P}}^2}\log\left(c_{\mathtt{P}}\Delta + \sqrt{c_{\mathtt{P}}^2\Delta^2 - r^2}\right) + \frac{1}{c_{\mathtt{S}}^2}\log\left(c_{\mathtt{S}}\Delta + \sqrt{c_{\mathtt{S}}^2\Delta^2 - r^2}\right)\right],\end{aligned} \tag{1.83}$$

$$h_{2,ij}^V(\mathbf{r};\Delta) = -\frac{c_{\mathtt{P}}^2 + c_{\mathtt{S}}^2}{c_{\mathtt{P}}^2 c_{\mathtt{S}}^2}\frac{\delta_{ij}}{2}\log(r). \tag{1.84}$$

In particular, the reduced form of the kernel highlights the space singularity of kind $\mathcal{O}(\log(r))$ for $r \to 0$, well-studied for boundary integral operators related to 2D elliptic problems.
Instead, if $c_{\mathtt{S}}\Delta_{\widetilde{n}+\xi,n+\varsigma} < r \leqslant c_{\mathtt{P}}\Delta_{\widetilde{n}+\xi,n+\varsigma}$, the kernel ν_{ij}^V assumes the expression:

$$\nu_{ij}^V(\mathbf{r};\Delta_{\widetilde{n}+\xi,n+\varsigma}) = h_{3,ij}^V(\mathbf{r};\Delta_{\widetilde{n}+\xi,n+\varsigma}) + h_{4,ij}^V(\mathbf{r};\Delta_{\widetilde{n}+\xi,n+\varsigma}), \tag{1.85}$$

where the functions $h^V_{3,ij}$ and $h^V_{4,ij}$ have the form

$$h^V_{3,ij}(\mathbf{r};\Delta) = \left(\frac{r_i r_j}{r^4} - \frac{\delta_{ij}}{2r^2}\right)\frac{\Delta}{c_{\mathtt{P}}}\sqrt{c^2_{\mathtt{P}}\Delta^2 - r^2} + \frac{\delta_{ij}}{2c^2_{\mathtt{P}}}\log\left(c_{\mathtt{P}}\Delta + \sqrt{c^2_{\mathtt{P}}\Delta^2 - r^2}\right), \tag{1.86}$$

$$h^V_{4,ij}(\mathbf{r};\Delta) = -\frac{\delta_{ij}}{2c^2_{\mathtt{P}}}\log(r). \tag{1.87}$$

Since the reduce form (1.85) is obtained specifically for $c_{\mathtt{S}}\Delta_{\widetilde{n}+\xi,n+\varsigma} \leqslant r$, the kernel ν^V_{ij} in this case is not affected by any type of singularity.
The generic component of $\boldsymbol{\beta}^{\mathcal{D}}$, right-hand-side of the linear system (1.75), can be obtained recalling the right-hand-side of the Galerkin weak formula (1.69) and performing a trivial integration in the time variable t:

$$\beta^{\mathcal{D},i}_{l\widetilde{m}} = \int_0^T \int_\Gamma \dot{g}_{\mathcal{D},i}(\mathbf{x},t) w^{\mathbf{p}}_{\widetilde{m}}(\mathbf{x}) v_l(t) d\Gamma_{\mathbf{x}} dt = -\sum_{\xi=1}^{2}(-1)^{\xi}\int_\Gamma g_{\mathcal{D},i}(\mathbf{x},t_{l+\xi}) w^{\mathbf{p}}_{\widetilde{m}}(\mathbf{x}) d\Gamma_{\mathbf{x}},$$

for all $i = 1,2$, $\widetilde{m} = 1,...,M_{\mathbf{p}}$ and $l = 0,...,N-1$.

The use of the discrete function $\boldsymbol{\Psi}_{i,h,\Delta t}$ in the weak formulation (1.70) gives rise to the linear system $\mathbb{E}_D\boldsymbol{\alpha}^{\mathbf{u}} = \boldsymbol{\beta}^{\mathcal{N}}$, having a structure comparable to the one obtained by the discretization of the single layer operator V. In particular, the same Toeplitz structure is obtained in time, and the matrix entries are computed after an analytic integration in the time variables (computations are reported in the Appendix, Section A.3), leading to

$$\left(\mathbb{E}^{(l)}_{D,ij}\right)_{\widetilde{m},m} = -\sum_{\xi,\varsigma=0}^{1}\frac{(-1)^{\xi+\varsigma}}{2\pi\varrho\Delta t^2}\int_\Gamma\int_\Gamma w^{\mathbf{u}}_{\widetilde{m}}(\mathbf{x}) w^{\mathbf{u}}_m(\boldsymbol{\xi})\nu^D_{ij}(\mathbf{r};\Delta_{\widetilde{n}+\xi,n+\varsigma}) d\Gamma_{\boldsymbol{\xi}} d\Gamma_{\mathbf{x}}, \tag{1.88}$$

for all $i,j = 1,2$; $m,\widetilde{m} = 1,...,M_{\mathbf{u}}$ and $n,\widetilde{n} = 0,...,N-1$, with the integration kernel

$$\begin{aligned}\nu^D_{ij}(\mathbf{r};\Delta) =& \frac{H[c_{\mathtt{P}}\Delta - r]}{c^3_{\mathtt{P}}}\left[\left(D^{ij}_{\varphi,c_{\mathtt{P}}}\Delta + D^{ij}_{c_{\mathtt{P}}}\frac{\Delta^3 c^2_{\mathtt{P}}}{r^2}\right)\frac{\varphi_{\mathtt{P}}(r;\Delta)}{r^2} + D^{ij}_{\widehat{\varphi},c_{\mathtt{P}}}\frac{\widehat{\varphi}_{\mathtt{P}}(r;\Delta)}{c_{\mathtt{P}}}\right] \\ &- \frac{H[c_{\mathtt{S}}\Delta - r]}{c^3_{\mathtt{S}}}\left[\left(D^{ij}_{\varphi,c_{\mathtt{S}}}\Delta + D^{ij}_{c_{\mathtt{S}}}\frac{\Delta^3 c^2_{\mathtt{S}}}{r^2}\right)\frac{\varphi_{\mathtt{S}}(r;\Delta)}{r^2} + D^{ij}_{\widehat{\varphi},c_{\mathtt{S}}}\frac{\widehat{\varphi}_{\mathtt{S}}(r;\Delta)}{c_{\mathtt{S}}}\right],\end{aligned} \tag{1.89}$$

where the coefficients $D^{ij}_{\varphi,c_\gamma}$, $D^{ij}_{c_\gamma}$ and $D^{ij}_{\widehat{\varphi},c_\gamma}$ are defined in Appendix. If $0 < r \leqslant c_{\mathtt{S}}\Delta_{\widetilde{n}+\xi,n+\varsigma} < c_{\mathtt{P}}\Delta_{\widetilde{n}+\xi,n+\varsigma}$ the expression of the kernel ν^D_{ij} reduces to the following:

$$\nu^D_{ij}(\mathbf{r};\Delta_{\widetilde{n}+\xi,n+\varsigma}) = h^D_{1,ij}(\mathbf{r};\Delta_{\widetilde{n}+\xi,n+\varsigma}) + h^D_{2,ij}(\mathbf{r};\Delta_{\widetilde{n}+\xi,n+\varsigma}) + h^D_{3,ij}(\mathbf{r};\Delta_{\widetilde{n}+\xi,n+\varsigma}) \tag{1.90}$$

where the functions $h^D_{1,ij}$, $h^D_{2,ij}$ and $h^D_{3,ij}$ are expressed as

$$h^D_{1,ij}(\mathbf{r};\Delta) = \frac{1}{r^2}\left(D^{ij}_{c_\mathrm{P}} \frac{c_\mathrm{P}^2 - c_\mathrm{S}^2}{c_\mathrm{P} c_\mathrm{S}} \frac{\Delta^3}{c_\mathrm{P}\sqrt{c_\mathrm{S}^2\Delta^2 - r^2} + c_\mathrm{S}\sqrt{c_\mathrm{P}^2\Delta^2 - r^2}} \right.$$
$$\left. + \frac{D^{ij}_{\varphi,c_\mathrm{P}}\Delta}{c_\mathrm{P}^3}\sqrt{c_\mathrm{P}^2\Delta^2 - r^2} - \frac{D^{ij}_{\varphi,c_\mathrm{S}}\Delta}{c_\mathrm{S}^3}\sqrt{c_\mathrm{S}^2\Delta^2 - r^2} \right),$$
$$h^D_{2,ij}(\mathbf{r};\Delta) = \frac{D^{ij}_{\widehat{\varphi},c_\mathrm{P}}}{c_\mathrm{P}^4}\log\left(c_\mathrm{P}\Delta + \sqrt{c_\mathrm{P}^2\Delta^2 - r^2}\right) - \frac{D^{ij}_{\widehat{\varphi},c_\mathrm{S}}}{c_\mathrm{S}^4}\log\left(c_\mathrm{S}\Delta + \sqrt{c_\mathrm{S}^2\Delta^2 - r^2}\right),$$
$$h^D_{3,ij}(\mathbf{r};\Delta) = \left(\frac{D^{ij}_{\widehat{\varphi},c_\mathrm{S}}}{c_\mathrm{S}^4} - \frac{D^{ij}_{\widehat{\varphi},c_\mathrm{P}}}{c_\mathrm{P}^4}\right)\log(r).$$

For $r \to 0$, the function $h^D_{1,ij}$ presents a singularity of order $\mathcal{O}\left(r^{-2}\right)$, while $h^D_{3,ij}$ is characterized by a log weak singularity similar to the one encountered in the discretization of single layer operator.
We also have to take into account that both kernels ν^V_{ij} and ν^D_{ij} depend on the difference $c_\gamma\Delta_{\widetilde{n}+\xi,n+\varsigma} - r$ through the Heaviside function $H[c_\gamma\Delta_{\widetilde{n}+\xi,n+\varsigma} - r]$, which leads to a jump at the points where the argument vanishes. To overcome this issue, we adopt suitable quadrature strategies explained in details in Chapter 4.

1.5.2 Mixed boundary problems

For what concerns the mixed boundary value problems and the associated energetic weak formulation (1.49), we proceed establishing a Galerkin weak problem similar to (1.46) and (1.48). We choose to approximate the unknowns $\mathbf{p}$ and $\mathbf{u}$ respectively in the discrete space $V_{\Delta t,0} \otimes X^{-1}_{h,p}(\Gamma_\mathcal{D})$ and $V_{\Delta t,1} \otimes X^0_{h,q}(\Gamma_\mathcal{N})$, replacing their components with the following linear combinations

$$p_{i,h,\Delta t}(\mathbf{x},t) = \sum_{n=0}^{N-1}\sum_{m=1}^{M_\mathbf{p}} \alpha^{\mathbf{p},i}_{nm} w^\mathbf{p}_m(\mathbf{x}) v_n(t), \quad i = 1,2, \tag{1.91}$$
$$u_{i,h,\Delta t}(\mathbf{x},t) = \sum_{n=0}^{N-1}\sum_{m=1}^{M_\mathbf{u}} \alpha^{\mathbf{u},i}_{nm} w^\mathbf{u}_m(\mathbf{x}) r_n(t), \quad i = 1,2. \tag{1.92}$$

where the basis functions in space and time are the same defined in Section 1.5.1. Indeed, the consequent discretized problem is algebraically represented by the following linear system:

$$\begin{pmatrix} \mathbb{E}^{(0)} & 0 & 0 & \cdots & 0 \\ \mathbb{E}^{(1)} & \mathbb{E}^{(0)} & 0 & \cdots & 0 \\ \mathbb{E}^{(2)} & \mathbb{E}^{(1)} & \mathbb{E}^{(0)} & \cdots & 0 \\ \vdots & \vdots & \vdots & \ddots & \vdots \\ \mathbb{E}^{(N-1)} & \mathbb{E}^{(N-2)} & \mathbb{E}^{(N-3)} & \cdots & \mathbb{E}^{(0)} \end{pmatrix} \begin{pmatrix} \boldsymbol{\alpha}_{(0)} \\ \boldsymbol{\alpha}_{(1)} \\ \boldsymbol{\alpha}_{(2)} \\ \vdots \\ \boldsymbol{\alpha}_{(N-1)} \end{pmatrix} = \begin{pmatrix} \boldsymbol{\beta}_{(0)} \\ \boldsymbol{\beta}_{(1)} \\ \boldsymbol{\beta}_{(2)} \\ \vdots \\ \boldsymbol{\beta}_{(N-1)} \end{pmatrix}, \tag{1.93}$$

where the RHS and the unknown vector of the linear system have a structure comparable with the vectors in (1.75). In particular both the unknown coefficients of formulas (1.91)

and (1.92) are stored in $\boldsymbol{\alpha}$, representing the approximation of the traction and the displacement at the nodal points of the time interval and of the boundary mesh. Regarding the structure of matrix $\mathbb{E}$, the generic l-th block is organized as below indicated:

$$\mathbb{E}^{(l)} = \begin{pmatrix} \mathbb{E}_{11}^{(l)} & \mathbb{E}_{12}^{(l)} \\ \mathbb{E}_{21}^{(l)} & \mathbb{E}_{22}^{(l)} \end{pmatrix}, \quad \mathbb{E}_{ij}^{(l)} = \begin{pmatrix} \mathbb{E}_{V,ij}^{(l)} & \mathbb{E}_{K,ij}^{(l)} \\ \mathbb{E}_{K^*,ij}^{(l)} & \mathbb{E}_{D,ij}^{(l)} \end{pmatrix}.$$

The elements of the sublocks $\mathbb{E}_{V,ij}^{(l)}$ and $\mathbb{E}_{D,ij}^{(l)}$ have been already defined in (1.78) and (1.88), while blocks $\mathbb{E}_{K,ij}^{(l)}$ and $\mathbb{E}_{K^*,ij}^{(l)}$ are derived by the discretization of the double layer operators K and K^*. Due to the symmetry properties (1.40), we need just to calculate the elements of $\mathbb{E}_{K,ij}^{(l)}$, that after an exact time integration (see Section A.2 in the Appendix), is composed by entries of the form

$$\left(\mathbb{E}_{K,ij}^{(l)}\right)_{\widetilde{m},m} = \sum_{\xi,\varsigma=0}^{1} \frac{(-1)^{\xi+\varsigma}}{\pi\varrho\Delta t} \int_{\Gamma_{\mathcal{D}}} \int_{\Gamma_{\mathcal{N}}} w_{\widetilde{m}}^{\mathbf{p}}(\mathbf{x}) w_{m}^{\mathbf{u}}(\boldsymbol{\xi}) \nu_{ij}^{K}(\mathbf{r}; \Delta_{\widetilde{n}+\xi,n+\varsigma}) d\Gamma_{\boldsymbol{\xi}} d\Gamma_{\mathbf{x}}, \tag{1.94}$$

for all $i,j = 1,2$, $m = 1,...,M_{\mathbf{u}}$, $\widetilde{m} = 1,...,M_{\mathbf{p}}$ and $n,\widetilde{n} = 0,...,N-1$. Here, the integration kernel ν_{ij}^{K} is

$$\nu_{ij}^{K}(\mathbf{r};\Delta) = H[c_{\mathtt{P}}\Delta - r]\frac{\varphi_{\mathtt{P}}(r;\Delta)}{c_{\mathtt{P}} r}\left(\frac{K_{\mathtt{P}}^{ij}}{c_{\mathtt{P}}^2} + \frac{\Delta^2 \widetilde{K}_{\mathtt{P}}^{ij}}{r^2}\right) - H[c_{\mathtt{S}}\Delta - r]\frac{\varphi_{\mathtt{S}}(r;\Delta)}{c_{\mathtt{S}} r}\left(\frac{K_{\mathtt{S}}^{ij}}{c_{\mathtt{S}}^2} + \frac{\Delta^2 \widetilde{K}_{\mathtt{S}}^{ij}}{r^2}\right) \tag{1.95}$$

with coefficients $K_{\mathtt{P}}^{ij}$, $K_{\mathtt{S}}^{ij}$ $\widetilde{K}_{\mathtt{P}}^{ij}$ and $\widetilde{K}_{\mathtt{S}}^{ij}$ defined in the Appendix. The kernel (1.95) shows a strong singularity $\mathcal{O}(1/r)$ for $r \to 0$, typical of double layer integral operators. In fact, for $0 < r \leqslant c_{\mathtt{S}}\Delta_{\widetilde{n}+\xi,n+\varsigma}$, it holds

$$\nu_{ij}^{K}(\mathbf{r};\Delta) = \frac{1}{r}\left(\frac{K_{\mathtt{P}}^{ij}}{c_{\mathtt{P}}^3}\sqrt{c_{\mathtt{P}}^2\Delta^2 - r^2} - \frac{K_{\mathtt{S}}^{ij}}{c_{\mathtt{S}}^3}\sqrt{c_{\mathtt{S}}^2\Delta^2 - r^2} + \frac{c_{\mathtt{P}}^2 - c_{\mathtt{S}}^2}{c_{\mathtt{P}}c_{\mathtt{S}}}\frac{\Delta^2 \widetilde{K}_{\mathtt{P}}^{ij}}{c_{\mathtt{P}}\sqrt{c_{\mathtt{S}}^2\Delta^2 - r^2} + c_{\mathtt{S}}\sqrt{c_{\mathtt{P}}^2\Delta^2 - r^2}}\right). \tag{1.96}$$

1.6 Numerical results

To validate the correctness and the effectiveness of the energetic BEM approach, in this section we present and discuss some results stemming from the application of the method to some exterior problems defined on open and closed boundaries Γ. We divide the section in two parts, the first devoted to the resolution of equation (1.9) with soft-scattering condition on Γ, making a comparison between the formulations $(\mathcal{D}_2)$ and $(\mathcal{D}_3)$ in the study of external propagation problems, and the second one related to the resolution of equation (1.9) with hard-scattering datum on Γ. We recall that simulations associated with mixed boundary value problems are not treated in this thesis, since the related code is not available yet.

1.6.1 Dirichlet Problems

Formulation $V\boldsymbol{\Phi} = \mathbf{g}_{\mathcal{D}}$

Next experiments are solved by the representation formula and the BIE of type $(\mathcal{D}_3)$, as exposed Section 1.2. In particular, the Galerkin problem we consider is (1.69), for which we set piece-wise constant basis functions, $p = 0$, for the space approximation, if not otherwise specified, and a uniform decomposition of the boundary Γ in segments with length h. The mass density everywhere is $\varrho = 1$.

Experiment 1. Let us consider a flat open obstacle, i.e. $\Gamma = \left\{(x_1, 0)^\top \in \mathbf{R}^2 \,:\, x_1 \in [-0.5, 0.5]\right\}$. In this case, one can observe that

$$\mathbf{r} = \mathbf{x} - \boldsymbol{\xi} = (r_1, r_2)^\top = (x_1 - \xi_1, 0)^\top,$$

inducing in (1.15) a reduction of the Green's tensor components $\mathbf{G}^{\mathbf{uu}}_{12} = \mathbf{G}^{\mathbf{uu}}_{21} = 0$, leading to two uncoupled scalar integral equations

$$\left(\begin{bmatrix} V_{11} & 0 \\ 0 & V_{22} \end{bmatrix} \begin{bmatrix} \Phi_1 \\ \Phi_2 \end{bmatrix} \right)(\mathbf{x}, t) = \begin{bmatrix} g_{\mathcal{D},1} \\ g_{\mathcal{D},2} \end{bmatrix}(\mathbf{x}, t).$$

Setting the function

$$f(t) = \begin{cases} \sin^2(4\pi t), & t \in [0, 1/8] \\ 1, & t > 1/8 \end{cases}, \tag{1.97}$$

the Dirichlet condition $g_{\mathcal{D},i}(\mathbf{x}, t) = H[t]f(t)x_1$, $i = 1, 2$, is applied for all $\mathbf{x} \in \Gamma$. The datum at the boundary becomes independent of time for $t > 1/8$, therefore, as time increases, both components $\Phi_i(\mathbf{x}, t)$ of the BIE solution tend to the stationary function

$$\Phi_\infty(\mathbf{x}) = \frac{2c_{\mathtt{P}}^2 c_{\mathtt{S}}^2}{c_{\mathtt{P}}^2 + c_{\mathtt{S}}^2} \frac{2x}{\sqrt{1/4 - x_1^2}},$$

representing both components of the solution of the BIE related to the reference elastostatic problem

$$\begin{cases} (\lambda + \mu)\nabla(\Delta \cdot \mathbf{u})(\mathbf{x}) + \mu\Delta\mathbf{u}(\mathbf{x}) = 0, & \mathbf{x} \in \mathbf{R}^2 \setminus \Gamma \\ \mathbf{u}(\mathbf{x}) = \mathbf{g}_{\mathcal{D},\infty}(\mathbf{x}), & \mathbf{x} \in \Gamma \end{cases}$$

with $\mathbf{g}_{\mathcal{D},\infty}(\mathbf{x}) = \lim_{t\to\infty} \mathbf{g}_{\mathcal{D}}(\mathbf{x}, t)$. In Figure 1.2, the story of the vertical and the horizontal components Φ_i, $i = 1, 2$, calculated at the obstacle point $(1/4, 0)^\top$ and for the time interval $[0, 2]$ is represented. The Lamè parameters are chosen as $\lambda = 2$ and $\mu = 1$, in order to have the peculiar velocities $c_{\mathtt{S}} = 1$ and $c_{\mathtt{P}} = 2$. The four figures are obtained with a different refinement of the temporal and the spatial meshes, maintaining anyhow the ratio between spatial and temporal steps $h/\Delta t = c_{\mathtt{S}}$. We can observe that a halved space-time step (Figures 1.2(b, d)) leads to a wave front reaching at the peak a higher value than the one obtained with a coarser step (Figures 1.2(a, c)). All the results show up stability in time, but the approximation of the wave profile, especially at the beginning of the motion, is not optimal because the value of the discrete speed $h/\Delta t$ prevents us from correctly capturing the primary perturbations related to the velocity $c_{\mathtt{P}}$.
Thus, a ratio $h/\Delta t = c_{\mathtt{P}}$ has been set for the simulations in the Figures 1.3(a,b), where

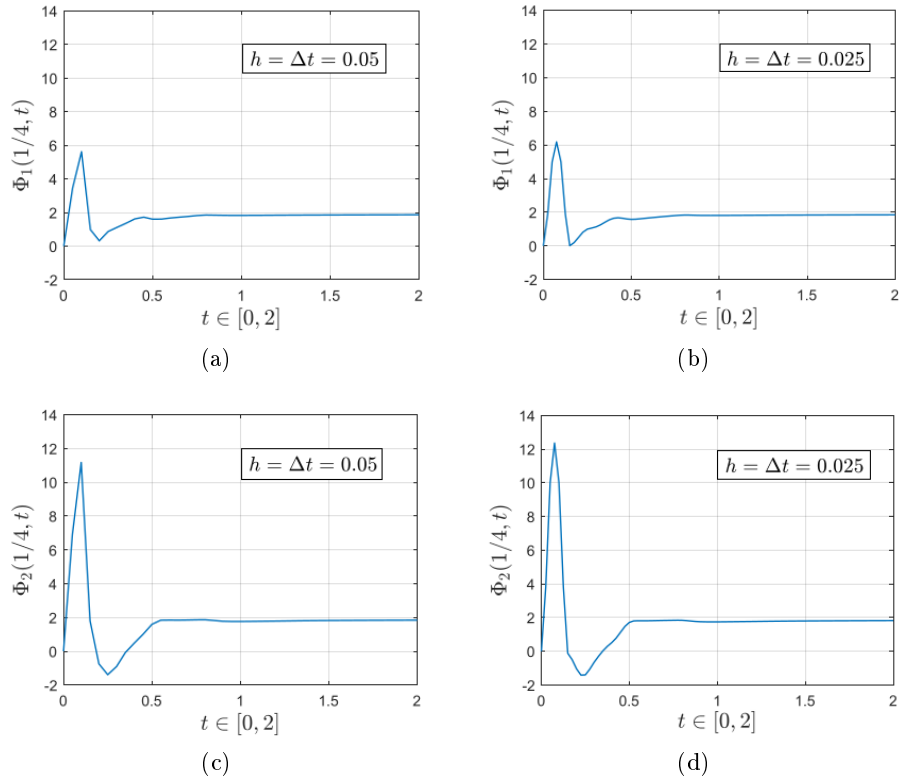

Figure 1.2: Story of the components Φ_i, $i = 1, 2$ at point $(1/4, 0)^\top \in \Gamma$ and for the velocities $c_S = 1$, $c_P = 2$. Figures (a, c) are obtained with the space-time mesh $h = \Delta t = 0.05$. To obtain Figures (b, d) a halved spatial-temporal mesh has been applied: $h = \Delta t = 0.025$.

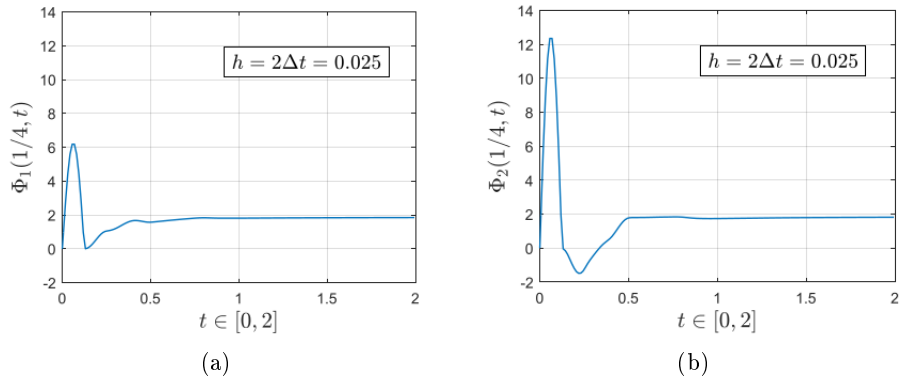

Figure 1.3: Story of the components Φ_1 and Φ_2 at point $(1/4, 0)^\top \in \Gamma$ and for the velocities $c_S = 1$, $c_P = 2$. Both simulations are obtained with the space-time mesh $h = 2\Delta t = 0.025$.

the story of Φ_i, $i = 1, 2$, is calculated for the new discrete speed. This value of the ratio in fact leads to a better description of the initial evolution of the approximate solution.
In Figure 1.4 we have calculated again the vertical component Φ_2 at the same point of Γ

and during the same time interval set for the previous figures. The difference in this test is the velocity $c_{\mathrm{P}} = 4$ ($\lambda = 14$, $\mu = 1$): experimenting different values of the ratio $h/\Delta t$, we observe that the choice $h/\Delta t = c_{\mathrm{P}}$ guarantees again the best approximation of the wave profile.

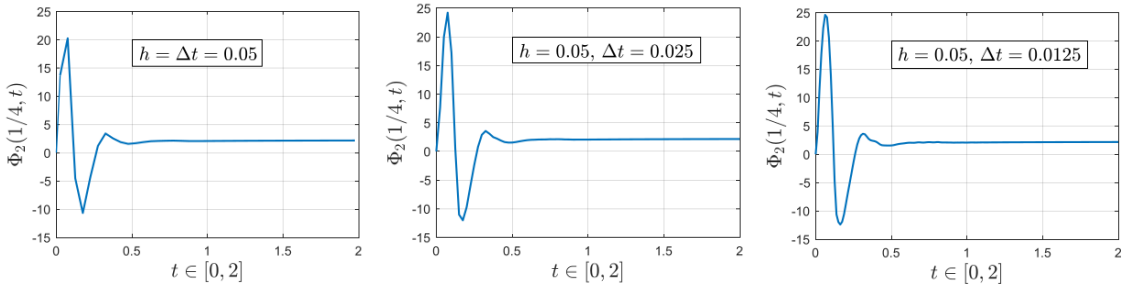

(a) (b) (c)

Figure 1.4: Vertical component Φ_2 at point $(1/4, 0)^\top \in \Gamma$ and for the velocities $c_{\mathrm{S}} = 1$, $c_{\mathrm{P}} = 4$. The value of the ratio $h/\Delta t$ is $c_{\mathrm{P}}/4$ for figure (a), $c_{\mathrm{P}}/2$ for figure (b) and c_{P} for figure (c).

We have also analyzed the convergence to the static solution Φ_∞ w.r.t the degree p of the polynomial spatial basis functions used to approximate the components Φ_1 and Φ_2. In this test we have set the velocities $c_{\mathrm{S}} = 1$ and $c_{\mathrm{P}} = 2$ and we have imposed a mesh on Γ composed by 10 segments with length $h = 0.1$ and a fixed time step $\Delta t = 0.05$, in order to maintain the optimal ratio $h/\Delta t = c_{\mathrm{P}}$. In Figure 1.5 we observe, for the final instant $T = 10$, the comparison between the static solution Φ_∞ and the approximated horizontal component Φ_1 along the boundary Γ: the overlapping of the two functions improves for an increasing value of p, even at the endpoints of Γ where the stationary solution is characterized by a high gradient.

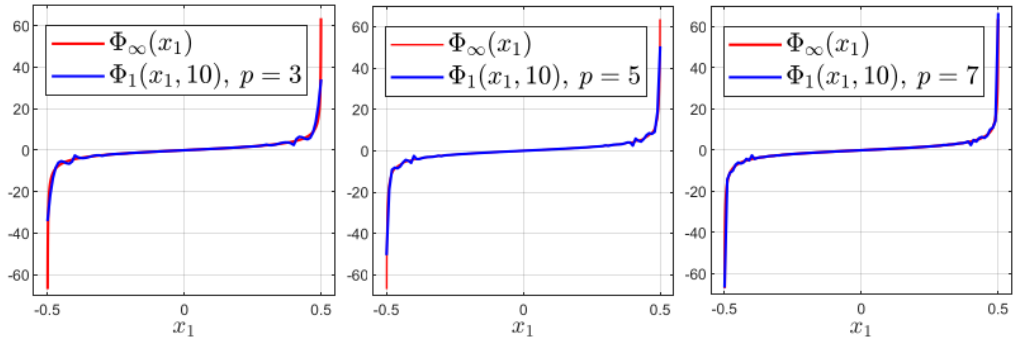

Figure 1.5: Plot of horizontal component Φ_1 calculated along the obstacle Γ, for $t = 10$, using spatial basis functions with polynomial degree $p = 3, 5, 7$. The related analytical stationary solution Φ_∞ is also shown.

We consider moreover the decay of the error achieved approximating Φ_1 and Φ_2 with spatial basis functions with an ever-increasing polynomial degree. The analysis proceeds, as suggested in [70], calculating the energy norm between the static solution and the transient solution, the latter obtained with spatial basis functions with polynomial degree

p and at the time instant $t = 10$:

$$E_{p,i} = \|\Phi_\infty(\cdot) - \Phi_i(\cdot, 10)\|_{H^{-1/2}(\Gamma)} = \sqrt{< g_{\mathcal{D},\infty}(\cdot), \Phi_\infty(\cdot) - \Phi_i(\cdot, 10) >_{L^2(\Gamma)}}, \quad i = 1, 2.$$

Table 1.1: Convergence of $\Phi_1(\cdot, 10)$ and $\Phi_2(\cdot, 10)$ to the analytical stationary solution Φ_∞

p	$E_{p,1}$	$\text{rate}_{p,1}$	$E_{p,2}$	$\text{rate}_{p,2}$
1	$1.58 \cdot 10^{-01}$	0.55	$1.60 \cdot 10^{-01}$	0.53
2	$1.08 \cdot 10^{-01}$	0.64	$1.11 \cdot 10^{-01}$	0.60
3	$8.35 \cdot 10^{-02}$	0.68	$8.71 \cdot 10^{-02}$	0.62
4	$6.86 \cdot 10^{-02}$	0.70	$7.29 \cdot 10^{-02}$	0.61
5	$5.87 \cdot 10^{-02}$	0.70	$6.37 \cdot 10^{-02}$	0.58
6	$5.16 \cdot 10^{-02}$	0.69	$5.73 \cdot 10^{-02}$	0.55
7	$4.64 \cdot 10^{-02}$	–	$5.26 \cdot 10^{-02}$	–

In Table 1.1, for both components, a good decay of the error is shown and the rate

$$\text{rate}_{p,i} = \log\left(E_{p,i}/E_{p+1,i}\right) / \log\left((p+1)/p\right), \quad i = 1, 2,\ p = 1, ..., 6$$

allows to establish experimentally that the error in static energy norm, and consequently the speed of convergence w.r.t the degree p, is $\mathcal{O}\left(p^{-\eta}\right)$ with η equal to $0.5 \sim 0.7$. The time dependence of the problem leads to an error decay slightly different w.r.t the results shown in [70], where, for Laplacian problems on straight obstacle, a similar boundary datum is considered. Results more in accordance with the paper can by achieved setting a smaller time step Δt.

Experiment 2. We recall that from now on to the end of Subsection 1.6.1, piece-wise constant basis functions are set for the space approximation. In particular, for the second simulation we consider the following semicircular obstacle

$$\Gamma = \left\{ \mathbf{x} \in \mathbf{R}^2 \ : \ \mathbf{x} = (\cos\alpha, \sin\alpha)^\top \ , \ \alpha \in [0, \pi] \right\}$$

where we impose a uniform mesh with spatial step $h \simeq 0.08$ (40 segments) and the time step $\Delta t = 0.04$. We discuss about two problems, for both of them the velocities are $c_{\mathtt{S}} = 1$, $c_{\mathtt{P}} = 2$ and the datum on the arc depends on the clockwise angle α. In the first case the horizontal component of the Dirichlet datum $\mathbf{g}_\mathcal{D} = (g_{\mathcal{D},1}, g_{\mathcal{D},2})^\top$ is null and the vertical component is antisymmetric w.r.t. the angle $\alpha = \frac{\pi}{2}$:

$$\begin{cases} g_{\mathcal{D},1}(\alpha, t) = 0 \\ g_{\mathcal{D},2}(\alpha, t) = H[t] f(t) \cos\alpha \end{cases}, \quad \alpha \in [0, \pi],$$

with $f(t)$ defined in (1.97). In Figure 1.6, on the left, we see a schematic representation of the arc Γ together with the antisymmetric trend in the vertical component of the vectorial datum $\mathbf{g}_\mathcal{D}$. On the right one can observe that the story of Φ_2 preserves the same antisymmetric behaviour, while Φ_1 is totally symmetric w.r.t the angle $\alpha = \frac{\pi}{2}$: in fact the

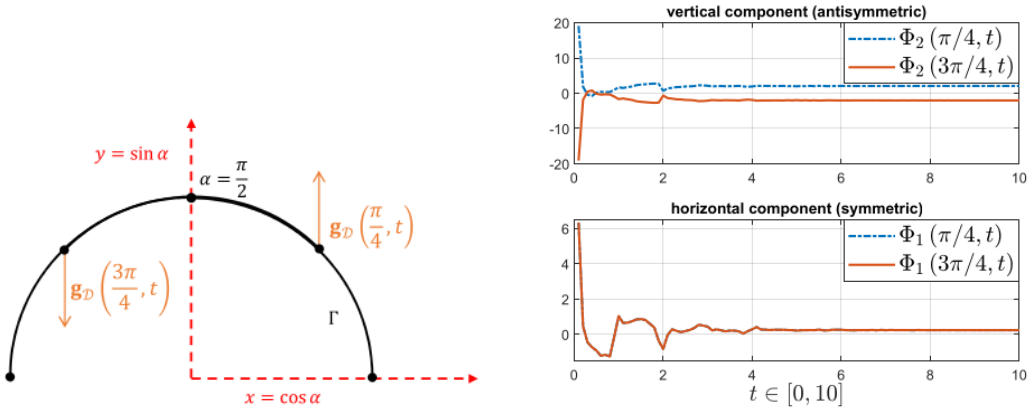

(a) (b)

Figure 1.6: In Figure (a) we have a schematic representation of the vectorial Dirichlet datum at the Γ points with $\alpha = \frac{\pi}{4}$ and $\alpha = \frac{3\pi}{4}$. Figure (b) shows the story of Φ_1 and Φ_2 at the same points of the arc.

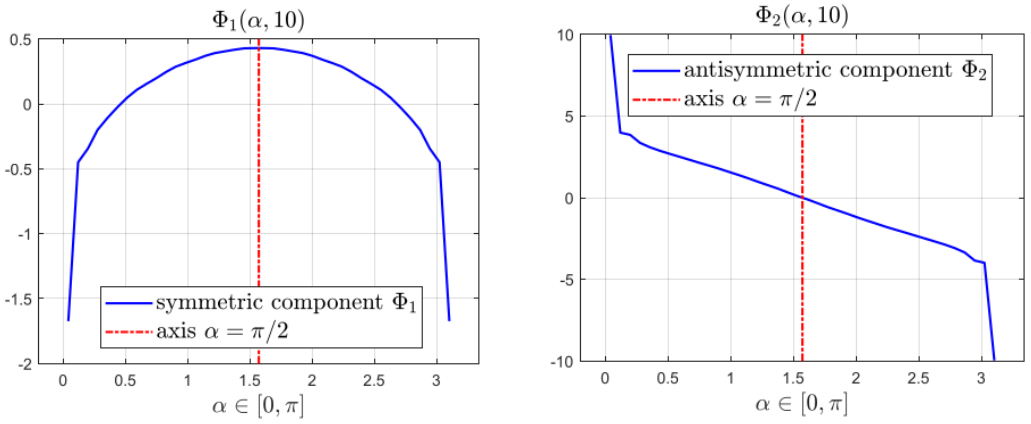

(a) (b)

Figure 1.7: Horizontal component Φ_1 and vertical component Φ_2 calculated at $t = 10$ and for all $\alpha \in [0, \pi]$. Each component, for a large t, preserves respectively a symmetric and an antisymmetric trend.

story graph of Φ_1 in $\frac{\pi}{4}$ overlaps the one obtained for $\alpha = \frac{3\pi}{4}$. Both components evolve in time without instabilities and, due to the particular datum employed on Γ, they tend for $t \to +\infty$ to stationary solutions, represented in Figure 1.7. We observe that Φ_1 and Φ_2 both preserve the behaviour depending on the clockwise angle α.

For the second simulation on the semicircular obstacle, we employ a vectorial datum $\mathbf{g}_{\mathcal{D}}$ at the boundary with oblique direction w.r.t the axis of symmetry of the semicircular arc:

$$\begin{cases} g_{\mathcal{D},1}(\alpha, t) = H[t] f(t) \cos\alpha \\ g_{\mathcal{D},2}(\alpha, t) = H[t] f(t) |\cos\alpha| \end{cases}, \quad \alpha \in [0, \pi].$$

The schematic representation of the arc Γ and the new vectorial datum $\mathbf{g}_{\mathcal{D}}$ are illustrated

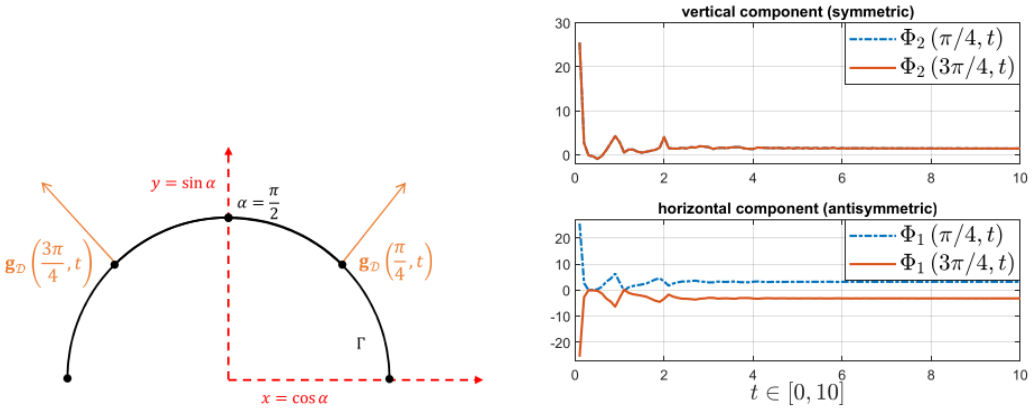

(a) (b)

Figure 1.8: In Figure (a) we have a schematic representation of the vectorial Dirichlet datum at the Γ points with $\alpha = \frac{\pi}{4}$ and $\alpha = \frac{3\pi}{4}$. Figure (b) shows the story of Φ_1 and Φ_2 at the same points of the arc.

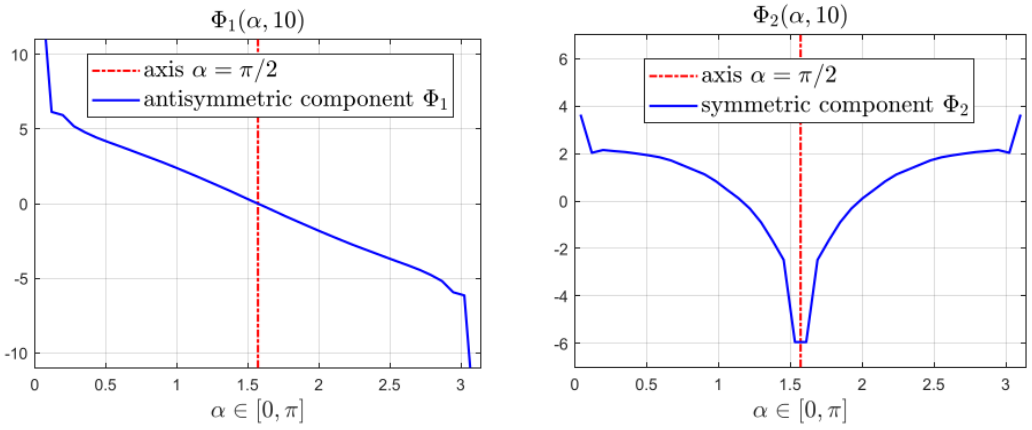

(a) (b)

Figure 1.9: Horizontal component Φ_1 and vertical component Φ_2 calculated at $t = 10$ and for all $\alpha \in [0, 2\pi]$. Each component, for a large t, preserves respectively an antisymmetric and a symmetric trend.

in Figure 1.8, on the left, allowing us to detect the direction w.r.t. to the axis of symmetry of the obstacle. We observe once again that the stories of the horizontal component Φ_1 and of the vertical one Φ_2 preserve the same symmetry behaviour of the Dirichlet datum. Also in this simulation, Φ_1 and Φ_2 tend for $t \to +\infty$ to the stationary solutions, represented in Figure 1.9, without showing instability effects.

Experiment 3. Until now, in all simulations we have looked just at the approximation,

by energetic BEM, of the unknown $\mathbf{\Phi}$ of BIE $(\mathcal{D}_3)$: thus, in the following, we will focus on the computation of the external displacement $\mathbf{u}$ by the use of the representation formula $(\mathcal{D}_3)$. We want also to remark that in the next experiments we will refer to the theory of plane waves propagation (for references see [14, 31]). A generic plane wave spreading with direction $\mathbf{k} \in \mathbf{R}^2$ is defined as

$$\mathbf{u}(\mathbf{x}, t) = \mathbf{v}\gamma(ct - \mathbf{k} \cdot \mathbf{x}), \quad \mathbf{x} \in \mathbf{R}^2,\ t \in \mathbf{R}$$

where c is the velocity phase and $\gamma(\cdot)$ is an arbitrary scalar function. The vector $\mathbf{v}$ determines how $\mathbf{u}$ perturbs the propagation domain: for $\mathbf{v} = \mathbf{k}$ the resulting displacement $\mathbf{u}$ is a pressure wave, namely the external medium is perturbed in the direction of the propagation, while, for $\mathbf{v} = \mathbf{k}^{\perp}$, $\mathbf{u}$ is a shear waves and the displacement takes place transversely w.r.t the direction of propagation.

$$g(t) = \begin{cases} t - \frac{1}{2}, & t \in [0.5, 0.6] \\ \frac{-30t+19}{10}, & t \in [0.6, 0.7] \\ \frac{40t-30}{10}, & t \in [0.7, 0.8] \\ \frac{-30t+26}{10}, & t \in [0.8, 0.9] \\ t - 1, & t \in [0.9, 1] \\ 0, & \text{otherwise} \end{cases} .$$

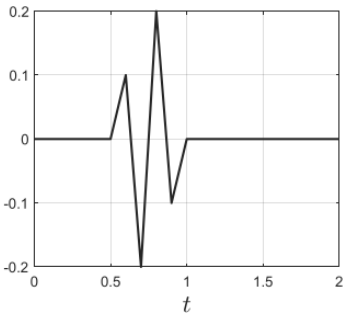

Figure 1.10: Function $g(t)$.

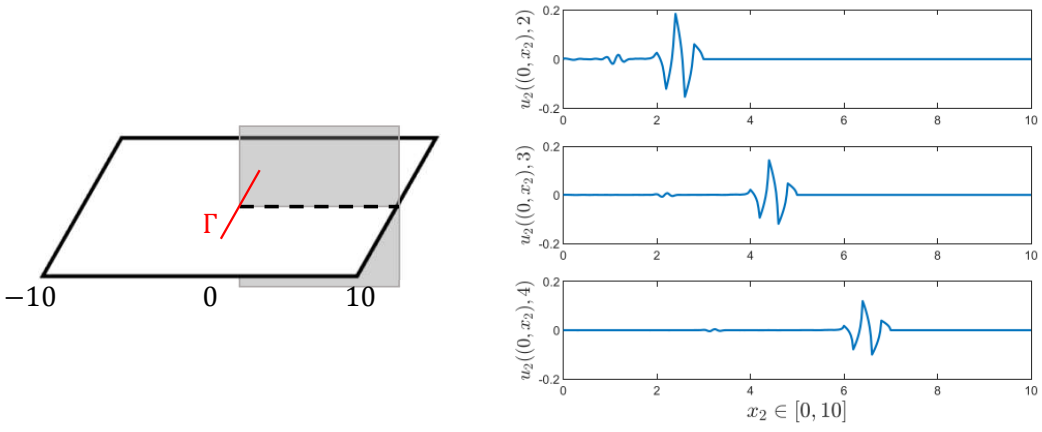

(a) (b)

Figure 1.11: Figure (a) represents the square domain $[-10, 10]^2$ containing the obstacle Γ: along the dash black line, orthogonal to the segment at its middle point, we reproduce the vertical component u_2 at the time instant $t = 2, 3, 4$ (Figure (b)).

We work again on the arc $\Gamma = \left\{(x_1, 0)^{\top} \in \mathbf{R}^2 \ : \ x_1 \in [-0.5, 0.5]\right\}$, refined with a uniform mesh of 10 segments $(h = 0.1)$, and we set the time step $\Delta t = 0.05$. We assign a Dirichlet

datum $\mathbf{g}_{\mathcal{D}} = (g_{\mathcal{D},1}, g_{\mathcal{D},2})^\top$ such that $g_{\mathcal{D},1}(\mathbf{x},t) = 0$ and $g_{\mathcal{D},2}(\mathbf{x},t) = g(t)$ is independent of the space variable, in accordance to the definition in Figure 1.10.
This Dirichlet datum corresponds to an incident plane wave of pressure type propagating in the vertical direction $\mathbf{k} = (0,1)^\top$, orthogonal to the obstacle. The vertical component of the displacement has been plotted, for three time instants (Figure 1.11(b)), along a segment of length 10 and orthogonal to the obstacle Γ in its middle point (Figure 1.11(a)). We recognize in each simulation the profile of the secondary wave that follows the primary one, which is faster. We remark that a pressure or a shear wave that impacts orthogonally on an infinite flat obstacle generally produces the reflection of a pure pressure or shear wave respectively having the same direction: for a crack, instead, circular perturbations with phase velocities c_{S} and c_{P} are generated at the endpoints and affect the propagation of the pressure wave. The secondary wave we observe in Figure 1.11(b) is precisely due to these phenomena.

In Figure 1.12 we set a new obstacle $\Gamma = \left\{(x,0)^\top \in \mathbf{R}^2 \,:\, x \in [-6,6]\right\}$ and a new boundary datum $g_{\mathcal{D},1}(\mathbf{x},t) = g_{\mathcal{D},2}(\mathbf{x},t) = g(t)$, which datum can be considered as the sum of a pres-

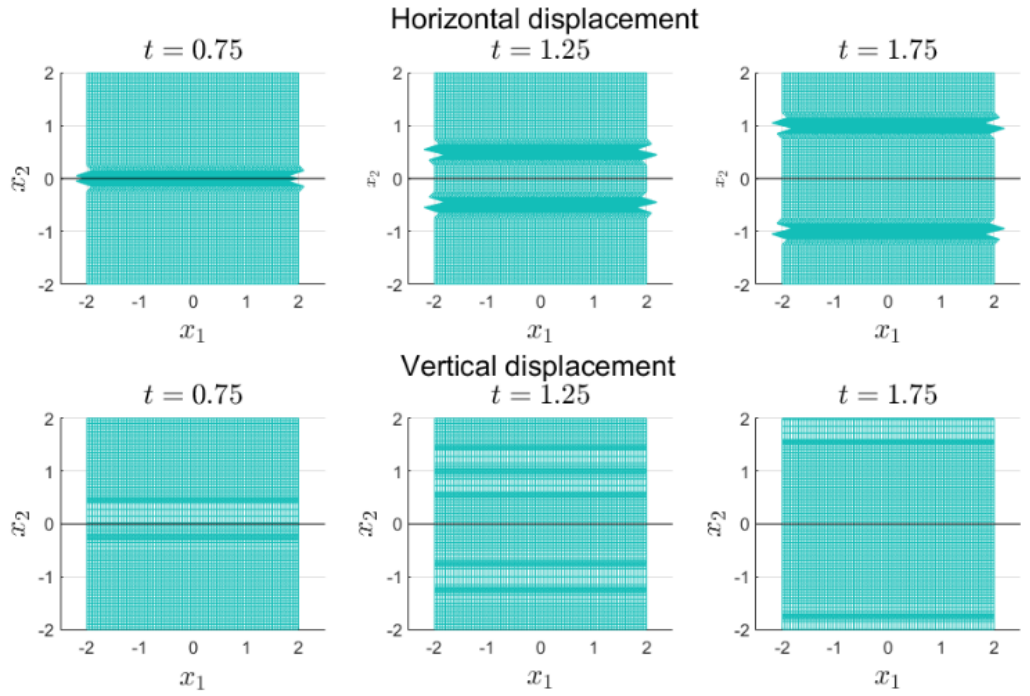

Figure 1.12: In this simulation we have set $\Gamma = \left\{(x_1,0)^\top \in \mathbf{R}^2 \mid x_1 \in [-6,6]\right\}$ and a Dirichlet datum $g_1(\mathbf{x},t) = g_2(\mathbf{x},t) = \gamma(t)$. For the time instants $t = 0.75, 1.25, 1.75$, the horizontal displacement $\mathbf{x} + (u_1(\mathbf{x},t),0)^\top$ and the vertical displacement $\mathbf{x} + (0,u_2(\mathbf{x},t))^\top$ are represented at some the grid points $\mathbf{x} \in [-2,2]^2$.

sure wave and a shear wave propagating again in a direction orthogonal to the obstacle, since $\mathbf{g}_{\mathcal{D}} = (g_{\mathcal{D},1},0)^\top + (0,g_{\mathcal{D},2})^\top$. In particular we observe the perturbation caused by the horizontal and the vertical displacement, separately, over all the square $[-2,2]^2$ (which contains a portion of segment Γ). We remark that the horizontal displacement behaves like

a shear wave, spreading with velocity $c_{\mathrm{S}} = 1$. Instead, the vertical displacement is a pressure wave of velocity $c_{\mathrm{P}} = 2$ and creates, during the time interval, a series of compressions and distensions of the propagation domain. In the considered time interval, the circular waves generated at the crack tips do not perturb the points of the square $[-2, 2]^2$.

Experiment 4. In the next pages we will consider problems of elastic wave propagations in a open domain Ω_e exterior to a regular closed boundary Γ, set as a unit radius circumference centred at the origin of the reference system and the domain Ω_e in which we explore the

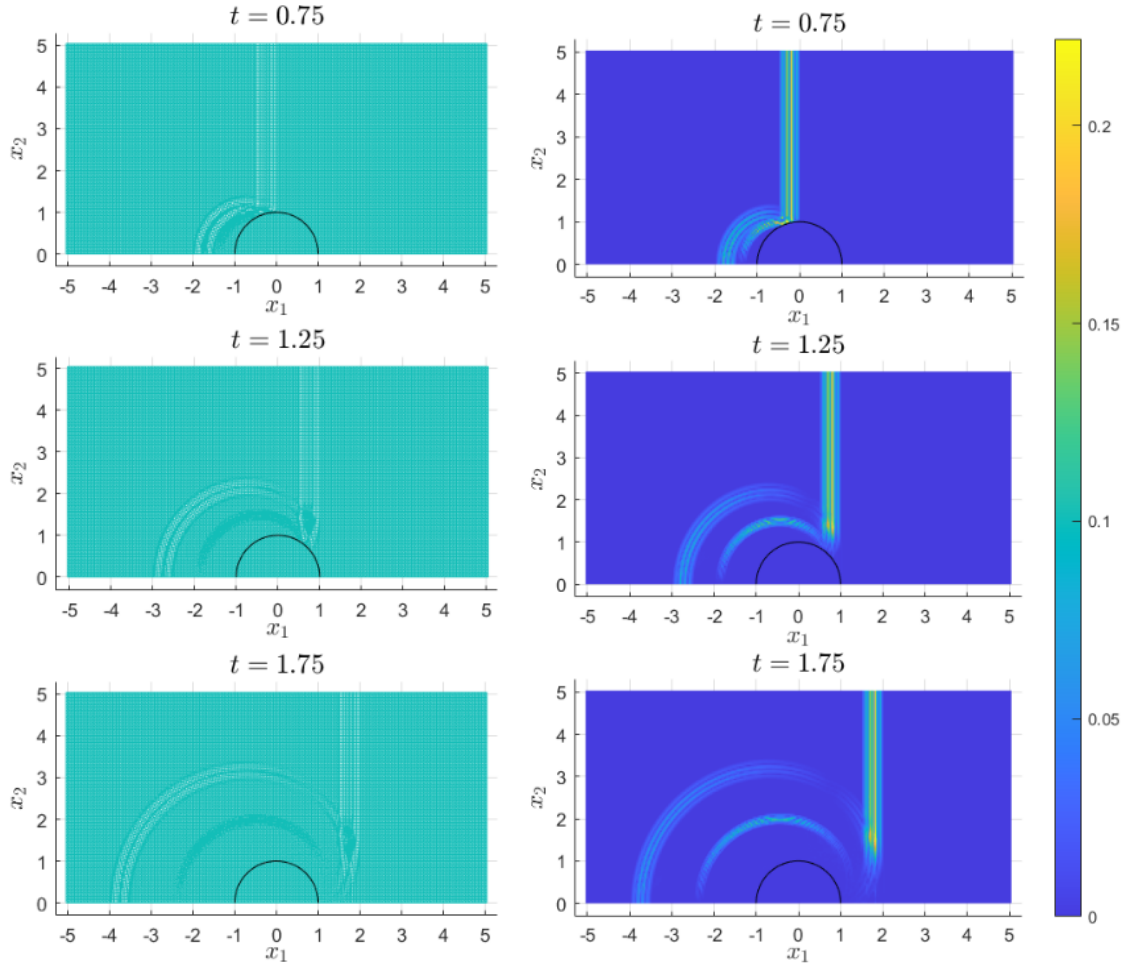

(a) (b)

Figure 1.13: Incident pressure wave: in Figure (a) some snapshots at the time instants $t = 0.75, 1.25, 1.75$ of a portion of the external domain Ω_e are shown: the grid points $\mathbf{x}$ are perturbed by the total displacement $\mathbf{x} + \mathbf{u}^c(\mathbf{x}, t)$. In Figure (b), at the same time instants the intensity of the module $\|\mathbf{u}^c(\mathbf{x}, t)\|_2$ is represented.

dynamics is

$$\Omega_e = \left\{ (x_1, x_2)^\top \in \mathbf{R}^2 \ : \ x_1^2 + x_2^2 > 1 \right\}.$$

We firstly consider an incident plane pressure wave $\mathbf{u}^{inc}$, that propagates along the horizontal direction $\mathbf{k} = (1, 0)^\top$ with phase velocity c_P and impacts on the left side of Γ at the time instant $t = 0.25$:

$$\mathbf{u}^{inc}(\mathbf{x}, t) = -\mathbf{k} g(c_\mathrm{P} t - \mathbf{k} \cdot \mathbf{x}),$$

with $g(\cdot)$ defined in Figure 1.10 and the peculiar velocities set with the value $c_\mathrm{P} = 2$ and $c_\mathrm{S} = 1$. To study the response of the closed boundary to this perturbation we have to

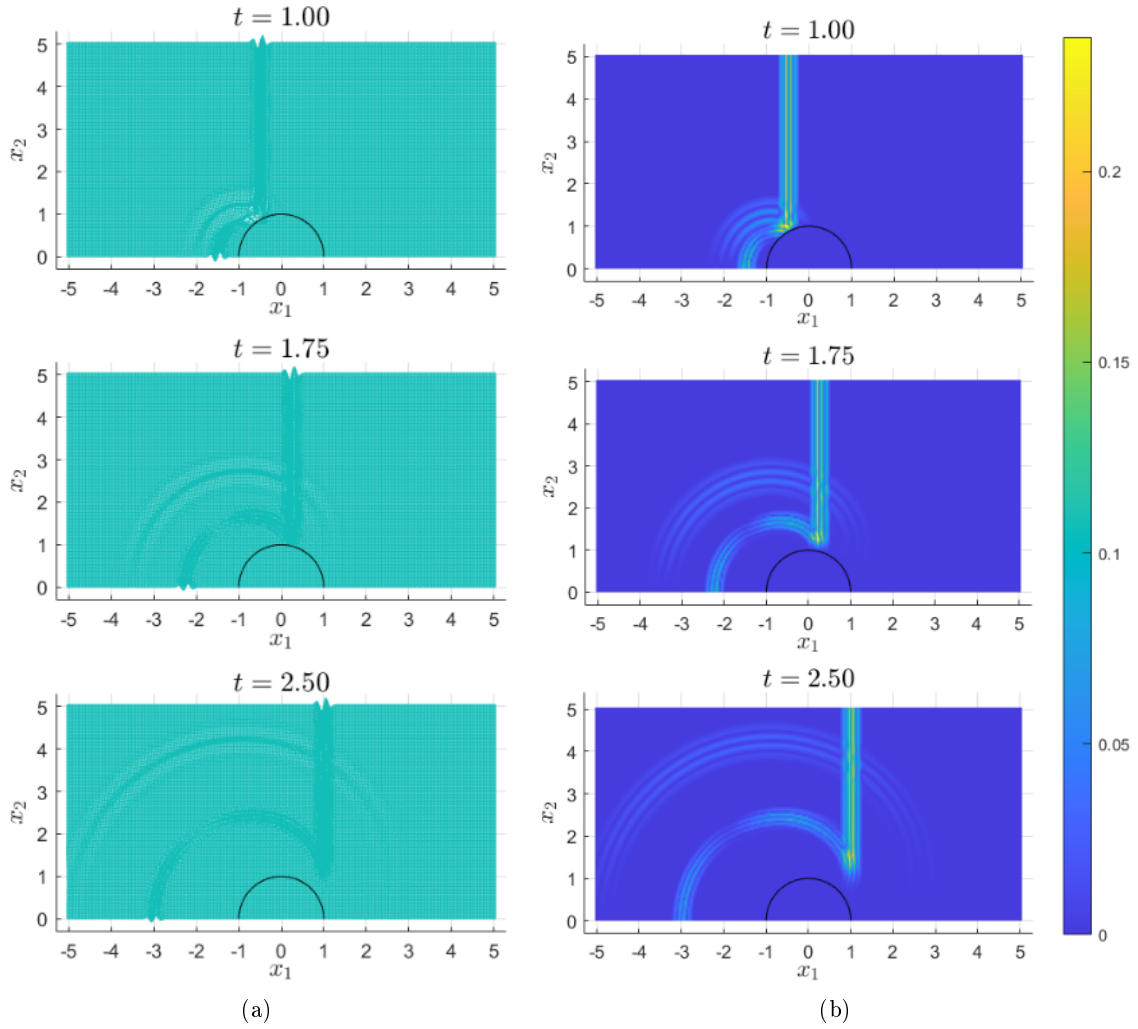

(a) (b)

Figure 1.14: Incident shear wave: in Figure (a) some snapshots at the time instants $t = 1.00, 1.75, 2.50$ of a portion of the external domain Ω_e are shown: the grid points $\mathbf{x}$ are perturbed by the total displacement $\mathbf{x} + \mathbf{u}^c(\mathbf{x}, t)$. In Figure (b), at the same time instants the intensity of the module $\|\mathbf{u}^c(\mathbf{x}, t)\|_2$ is represented.

impose the Dirichlet datum $\mathbf{g}_\mathcal{D}(\mathbf{x}, t) = -\mathbf{u}^{inc}(\mathbf{x}, t)$, $\mathbf{x} \in \Gamma$, $t > 0$. Therefore, to get the complete displacement $\mathbf{u}^c$ in the post-processing phase we sum up the incident wave $\mathbf{u}^{inc}$ with the field $\mathbf{u}$ obtained from the representation formula $(\mathcal{D}_3)$, since the latter only reproduces the displacement caused by the diffracted waves. In the simulations we have calculated

the complete displacement on the set $\Omega_e^+ = \left\{(x_1, x_2)^\top \in \Omega_e \,:\, x_2 > 0\right\}$ since the problem is symmetric w.r.t the axis $x_2 = 0$. We have discretized the circular boundary with 320 segments with length $h \simeq 0.02$ and we have imposed the time step $\Delta t = 0.01$. In Figure 1.13(a), the points of a portion of Ω_e^+, perturbed by the total displacement $\mathbf{u}^c = \mathbf{u} + \mathbf{u}^{inc}$, are represented considering a square grid of spatial step equal to 0.04: at each time instants, it is easy to observe that the impact of the incident wave produces the reflection of a pressure and a shear wave, spreading outside the circumference respectively with the peculiar velocities $c_{\mathtt{P}}$ and $c_{\mathtt{S}}$. We remark that the points $(x_1, 0)^\top$ with abscissas $x_1 < -1$ are perturbed only by the reflected pressure wave: the direction of the incident wave is orthogonal w.r.t the tangent to the arc Γ at the boundary point $(-1, 0)^\top$ and this particular configuration leads to the reflection of a pure pressure wave along the horizontal axis $x_2 = 0$. It is possible to catch this behaviour also in Figure 1.13(b) where, at the same time instants considered previously, the magnitude of the module $\|\mathbf{u}^c(\mathbf{x}, t)\|_2 = \sqrt{u_1^c(\mathbf{x}, t)^2 + u_2^c(\mathbf{x}, t)^2}$ is represented by a coloured scale chart.

We have also considered the case of an incident wave of shear kind: therefore, to study the response of the obstacle, we set

$$\mathbf{u}^{inc}(\mathbf{x}, t) = -\mathbf{v} g(c_{\mathtt{S}} t - \mathbf{k} \cdot \mathbf{x}),$$

with $\mathbf{v} = \mathbf{k}^\perp = (0, 1)^\top$, $c_{\mathtt{S}} = 1$ and $c_{\mathtt{P}} = 2$. The incident wave once again spreads in the external domain along the horizontal direction and impacts on the left side of Γ at the time instant $t = 0.25$. The results of this experiment are collected in Figure 1.14(a): here we observe how the external grid points are perturbed at various time instants. The impact of the incident wave produces the reflection of both a shear and a pressure wave, having respectively the peculiar velocities $c_{\mathtt{S}}$ and $c_{\mathtt{P}}$. The reflected pressure wave is faster than the incident one and that is why we observe an overlapping of the two waves as the time goes on. Also in this case the points $(x_1, 0)^\top$ with $x_1 < -1$ are perturbed only by the reflected shear wave and that is because the direction of propagation is orthogonal w.r.t the tangent of Γ at $(-1, 0)^\top$. The reflection along the axis of a pure shear wave is visible also in Figure 1.14(b) in which the intensity of the module $\|\mathbf{u}^c(\mathbf{x}, t)\|_2$ of the total displacement is represented with a coloured scale.

Experiment 5. Lastly, we consider again the diffusion domain Ω_e external to the same circular boundary Γ, but we impose a Dirichlet datum $\mathbf{g}_{\mathcal{D}}$ that models a sort of explosive impulse generated at a unique source point, located at the centre of circumference:

$$\mathbf{g}_{\mathcal{D}}(\mathbf{x}, t) = \frac{c_{\mathtt{P}}}{2\pi} \frac{H[c_{\mathtt{P}}(t + 1/c_{\mathtt{P}}) - 1]}{\sqrt{c_{\mathtt{P}}^2 (t + 1/c_{\mathtt{P}})^2 - 1}} \mathbf{x} + \frac{c_{\mathtt{S}}}{2\pi} \frac{H[c_{\mathtt{S}}(t + 1/c_{\mathtt{S}}) - 1]}{\sqrt{c_{\mathtt{S}}^2 (t + 1/c_{\mathtt{S}})^2 - 1}} \begin{pmatrix} 0 & 1 \\ -1 & 0 \end{pmatrix} \mathbf{x}, \quad \mathbf{x} \in \Gamma,\, t > 0.$$

This condition generates two impulses propagating both in radial direction w.r.t the centre of Γ. One impulse is the primary wave, with phase speed $c_{\mathtt{P}} = 2$ and behaving like a pressure wave which creates a displacement of the point parallel to the propagation direction, while the other is the secondary wave with phase speed $c_{\mathtt{S}} = 1$ and behaving like a shear wave which moves the points orthogonally w.r.t the propagation direction. We remark that a radial boundary condition creates an external perturbation which is equal at the points

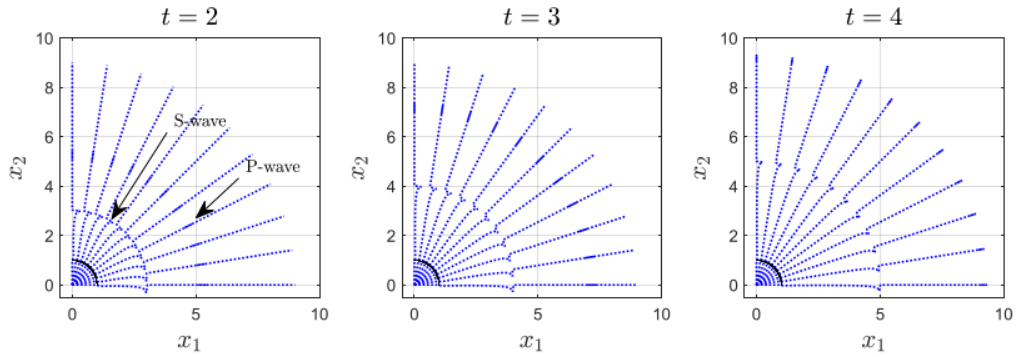

Figure 1.15: Snapshots of the radial perturbation at the time instants $t = 2, 3, 4$ in $\{(x_1, x_2)^\top \in \Omega \mid x_1 \geqslant 0, x_2 \geqslant 0\}$: the grid points $\mathbf{x}$, set along radial direction, are perturbed by the displacement $\mathbf{x} + \mathbf{u}(\mathbf{x}, t)$.

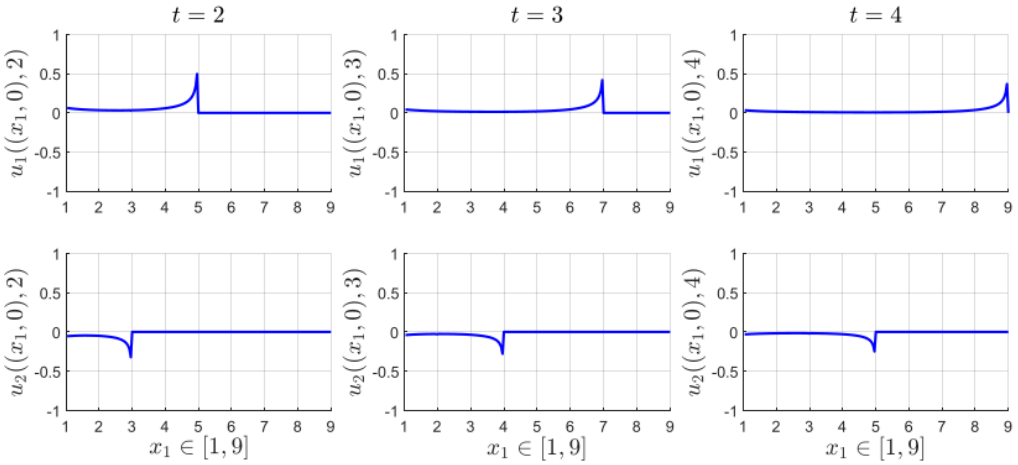

Figure 1.16: Snapshots of the radial and tangential perturbations at the time instants $t = 2, 3, 4$ in $\{(x_1, x_2)^\top \in \mathbf{R}^2 \mid x_1 \geq 1, x_2 = 0\}$: in this set the horizontal displacement corresponds to the primary wave, with velocity phase c_{P}, while the vertical displacement corresponds to the secondary wave, with velocity phase c_{S}.

having the same distance from the origin: that is why in Figure 1.15 we have considered only the solution of the problem in the set $\{(x_1, x_2)^\top \in \Omega : x_1 \geqslant 0, x_2 \geqslant 0\}$, calculating the displacement along radial axis and not in a square grid. For this simulation, we have imposed the spatial and temporal steps $h \simeq 0.04$ and $\Delta t = 0.02$ and, as one can observe, for each considered time instant, the primary wave moves the points along the radial direction, while the secondary wave generates a distortion orthogonal w.r.t the direction of propagation. In Figure 1.16 we focus on the axis $\{(x_1, x_2)^\top \in \Omega : x_1 > 1, x_2 = 0\}$ and we observe that the horizontal displacement corresponds to the primary wave while the vertical one corresponds to the secondary wave and for both the peak decreases as the time goes on.

Remark. All the numerical results presented above are collected in Author's paper [6], written in collaboration with Professors Alessandra Aimi, Chiara Guardasoni and Mauro

Diligenti (University of Parma). The paper, submitted to *Journal of Computational and Applied Mathematics*, was recently accepted.

Comparison between BIEs $V\mathbf{\Phi} = \mathbf{g}_{\mathcal{D}}$ and $V\mathbf{p} = (K - 1/2)\mathbf{g}_{\mathcal{D}}$

In the following we present two numerical examples, presented in the recent paper by the author [29], regarding the resolution of problem $(P_{\mathcal{D}})$ by the use of both the representation formulas indicated in $(\mathcal{D}_2)$ and $(\mathcal{D}_3)$. Although they depend on different unknowns to be calculated on the boundary, they will show a numerically comparable approximation of the external displacement $\mathbf{u}$.
We remark that the Galerkin weak formulation of BIE in $(\mathcal{D}_2)$, which will be indicated in this section as *direct* BIE, is the following: :

$$\begin{aligned}
&\textit{find } p_{i,h,\Delta t} \in V_{\Delta t,0} \otimes X^{-1}_{h,p}(\Gamma),\ i = 1,2 \textit{ such that}\\
&\quad \langle (V_{ij}\dot{p_{j,h,\Delta t}}), \phi_{i,h,\Delta t}\rangle_{L^2(\Sigma)} = \langle (K_{ij} - 1/2\delta_{ij}))\dot{g_{\mathcal{D},j}}, \phi_{i,h,\Delta t}\rangle_{L^2(\Sigma)}, \quad i = 1,2, \qquad (1.98)\\
&\textit{for all } \boldsymbol{\phi}_{h,\Delta t} = (\phi_{1,h,\Delta t}, \phi_{2,h,\Delta t})^{\top} \in \left(V_{\Delta t,0} \otimes X^{-1}_{h,p}(\Gamma)\right)^2.
\end{aligned}$$

with $p_{i,h,\Delta t}$, for $i = 1,2$, discretized components of the unknown traction vector $\mathbf{p}$. Following the fundamentals of discretization reported at the beginning of Section 1.5, we choose to approximate both in space and time the unknowns $\mathbf{\Phi}$ and $\mathbf{p}$ with piece-wise constant functions, subordinated to a uniform decomposition of Γ with segments of length h. We specify that, in the right-hand-side of (1.98), the product $\langle K_{ij}\dot{g}_{\mathcal{D},j}, \phi_{i,h,\Delta t}\rangle_{L^2(\Sigma)}$ is evaluated by an approximation of the two components of the boundary datum with a linear combination of space–time basis functions:

$$g_{\mathcal{D},i}(\mathbf{x},t) \simeq \widehat{g}_{\mathcal{D},i}(\mathbf{x},t) = \sum_{n=0}^{N-1}\sum_{m=1}^{M_{\mathbf{P}}} \beta^i_{nm} w^{\mathbf{P}}_m(\mathbf{x}) r_n(t), \quad i = 1,2, \quad (\mathbf{x},t) \in \Sigma.$$

where $r_n(t)$ are the temporal ramp basis defined in (1.72) and $w^{\mathbf{P}}_m$ are the piece-wise constant basis modeling both the unknown traction $\mathbf{p}$ and the datum in space. To have a correct interpolation of the boundary datum, the condition $g_{\mathcal{D},i}(\mathbf{x}_m, t_k) \simeq \widehat{g}_{\mathcal{D},i}(\mathbf{x}_m, t_k)$, for all $m = 1, ..., M$ and $k = 0, ...N-1$, is imposed: t_k are the temporal knots while the spatial nodes $\mathbf{x}_m$ are the middle points of the mesh elements e_m. With this substitution, the evaluation of $\langle K_{ij}\dot{g}_{\mathcal{D},j}, \phi_{i,h,\Delta t}\rangle_{L^2(\Sigma)}$ becomes the computation of a matrix-vector product involving the double layer matrix $\mathbb{E}_K$, whose elements are the double space integrals defined in (1.94).
If we indicate instead that we are solving the Dirichlet problem by *indirect* formulation, we refer at the resolution of the energetic weak problem (1.46) and its Galerkin form (1.69).

In the next experiments, the following elastic parameters are set: $\lambda = 2$, $\mu = 1$ and $\varrho = 1$, namely $c_{\mathtt{P}} = 2$ and $c_{\mathtt{S}} = 1$.

Experiment 1. We firstly consider the flat crack $\Gamma = \left\{(x_1, 0)^{\top} : x_1 \in [-0.5, 0.5]\right\}$ on which we impose the Dirichlet condition $\mathbf{g}_{\mathcal{D}}$ such that $g_{\mathcal{D},1}(x_1, t) = 0$ and $g_{\mathcal{D},2}(x_1, t) =$

$g(t+0.45)$, where the temporal profile $g(t)$ is the same introduced in (1.97). We set the final instant $T = 4$ and we impose on Γ a uniform decomposition with step $h = 0.025$ (40 segments) and a time step of size $\Delta t = 0.0125$. As shown in a very similar experiment of

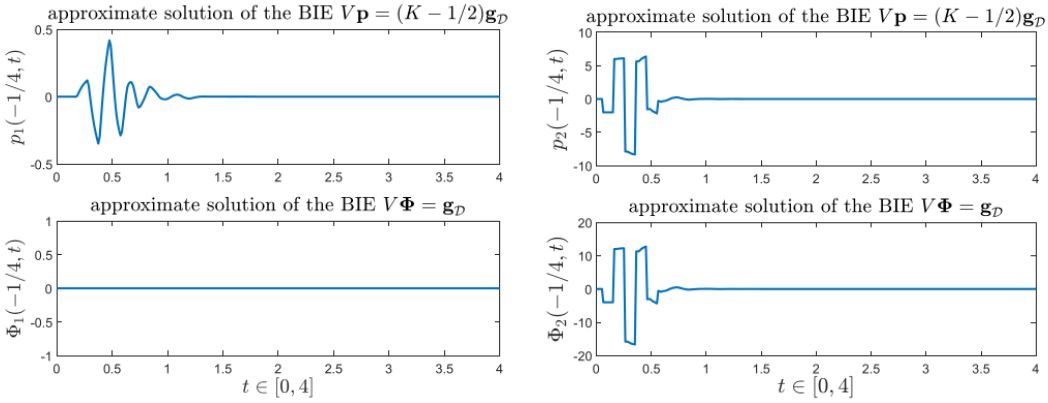

(a) (b)

Figure 1.17: Horizontal and vertical components of the vector solutions $\mathbf{p}$ and $\mathbf{\Phi}$ of the weak problems (1.98) and (1.69) calculated at point $(-1/4, 0)^\top \in \Gamma$ and during the time interval $[0, 4]$.

the previous subsection (see Figure 1.11), this kind of boundary datum models a uniform scattering by the obstacle with vertical direction. In particular, in Figures 1.17(a) and 1.17(b) the solution vectors $\mathbf{p}$ and $\mathbf{\Phi}$ of the energetic weak formulations are shown: in particular there is the time history of the horizontal and the vertical components of $\mathbf{p}$ and $\mathbf{\Phi}$ at the point $(-1/4, 0) \in \Gamma$. It is possible to observe that Φ_1 is trivial. This is due to the fact that the condition $\mathbf{g}_\mathcal{D}$ is completely vertical and, on a flat horizontal obstacle, the Green tensor defined in formula (1.15) has null components for $i \neq j$. This leads to a reduction of the indirect BIE in $(\mathcal{D}_3)$, which is decoupled in two scalar equations: $V_{11}\Phi_1 = 0$ and $V_{22}\Phi_2 = g_{\mathcal{D},2}$. The right-hand-side of the direct weak form instead depends also on the double layer operator, meaning that the components of $(K - 1/2)\mathbf{g}_D$ in formula (1.98) are both active. Anyway, both approaches let us to calculate approximate results showing long time stability.

Solutions of the energetic weak formulations have then been employed in the respective integral representation formulas $\mathbf{u} = V\mathbf{\Phi}$ and $\mathbf{u} = K\mathbf{u} - V\mathbf{p}$, in order to compute the displacement $\mathbf{u}$ in the points of the axis $(0, x_2)$ with $x_2 \in [0, 6.5]$. Snapshots of the vertical displacement at the time instants 1, 2 and 3 are shown in Figure (1.18): in Figure (1.18)(a) the component u_2 is calculated replacing the approximate traction $\mathbf{p}$ in the representation formula $(\mathcal{D}_2)$, while Figure (1.18)(b) have been obtained by the indirect in $(\mathcal{D}_3)$, leading to a comparable results for the external propagation.

Lastly, a numerical comparison is reported in Table 1.2, where the numbers represent the difference in L^2 norm between the external displacements obtained by the two different formulations evaluated at different time instants. We take into account only the vertical displacement u_2, since the horizontal one is null in the considered axes. The estimated errors are $\mathcal{O}(10^{-3})$, as expected considering the magnitude of the imposed spatial and temporal discretization steps h and Δt.

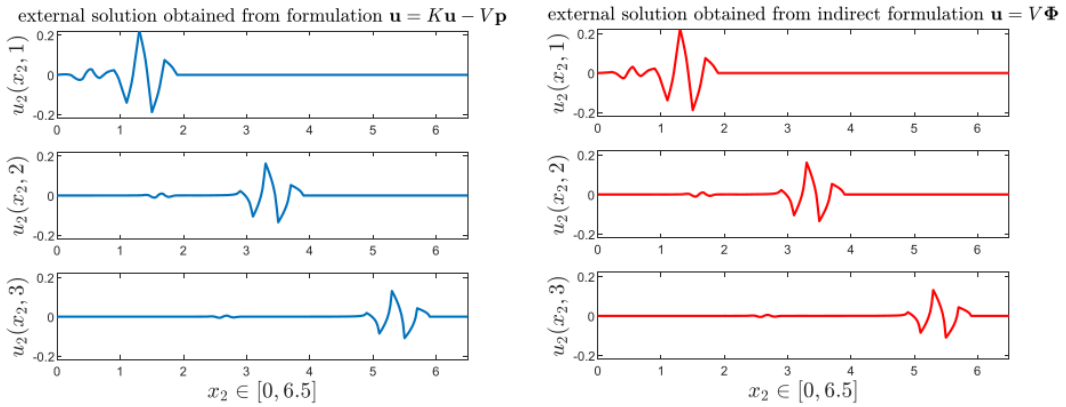

(a) (b)

Figure 1.18: External displacement calculated, for different time instants, along the vertical axes $(0, x_2)$ with $x_2 \in [0, 6.5]$. Solutions have been obtained by the discretization of the weak form (1.98) (a) and the indirect weak form (1.69) (b).

Table 1.2: L^2-error for $x_2 \in [0, 6.5]$ of the vertical components u_2 for some time instants.

$\|u_{2,\mathbf{p}}(\cdot,t) - u_{2,\boldsymbol{\Phi}}(\cdot,t)\|_{L^2([0,6.5])}$	$t = 1$	$t = 2$	$t = 3$
	$6.96\ 10^{-3}$	$8.15\ 10^{-4}$	$6.64\ 10^{-4}$

Experiment 2. We now consider the circular arc $\Gamma = \left\{(x_1, x_2)^\top : x_1^2 + x_2^2 = 1\right\}$ and the Dirichlet condition $\mathbf{g}_D(\mathbf{x}, t)$ on Γ such that $g_{i,\mathcal{D}}(\mathbf{x}, t) = \gamma(t)x_i$ for $i = 1, 2$, where the function $\gamma(t) = 0.2\sin^2(40t)H[\pi/40 - t]$ is the temporal profile. We set the final instant

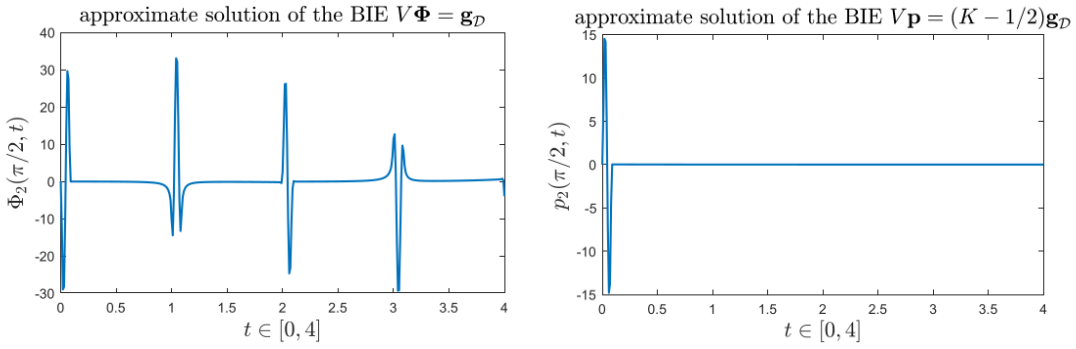

(a) (b)

Figure 1.19: Vertical components of the vector solutions $\mathbf{p}$ and $\boldsymbol{\Phi}$ of the weak problems (1.69) and (1.98) calculated at point $(0, 1)^\top \in \Gamma$ (corresponding to the clockwise angle $\pi/2$) and during the time interval $[0, 4]$.

$T = 4$ and we impose on Γ a uniform decomposition with step $h \simeq 0.02$ (320 segments) and we choose a time step of size $\Delta t = 0.01$. We recall that with this problem geometry, the

boundary datum models a uniform scattering by the obstacle with radial direction with respect to the centre of Γ. In Figure 1.19 we represent the time history of the vertical components of $\mathbf{p}$ and $\mathbf{\Phi}$, obtained respectively by the discretized weak form (1.98) and (1.69), at the point $(0,1) \in \Gamma$. Since we are solving an external problem, the traction $\mathbf{p}$ on Γ presents just an initial perturbation of length $\pi/40$, effect of the pulse generated by the Dirichlet boundary condition (see Figure 1.19(a)). Differently, the density $\mathbf{\Phi}$ in Figure 1.19(b) presents a series of pulsations since it depends also on the interior wave reflections against Γ. In Figure 1.20, three snapshots of the vertical external displacement $\mathbf{u}$ are represented, obtained respectively solving the discretized weak form of equations $V\mathbf{p} = (K - 1/2)\mathbf{g}_{\mathcal{D}}$ and $V\mathbf{\Phi} = \mathbf{g}_{\mathcal{D}}$ (Figure 1.20(a) and Figure 1.20(b)), along the vertical axis $(0, x_2)$ with $x_2 \in [1, 8]$. Externally we have the diffusion of a pure radial perturbation with the peculiar velocity c_{P}. There are no crack tips perturbations since the arc is closed. Also for the circular obstacle, we have a numerical comparison in Table 1.3, where the

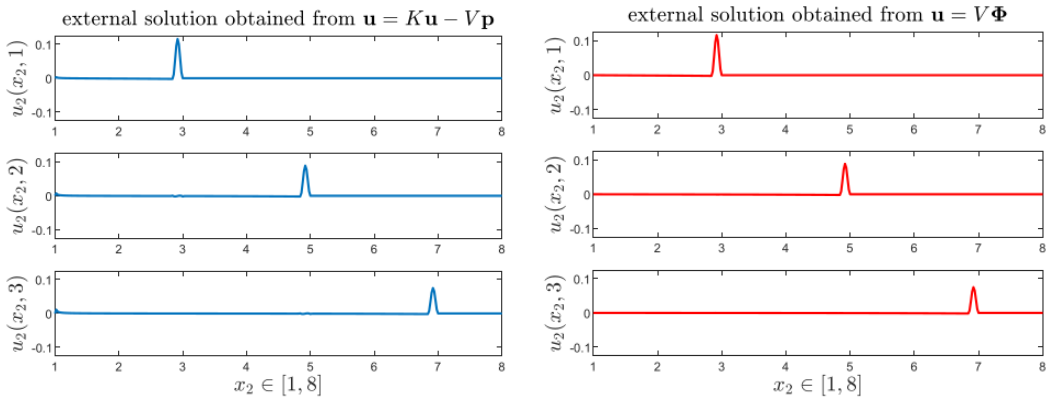

(a) (b)

Figure 1.20: External displacement calculated, for different time instants, at the points $(0, x_2)$ with $x_2 \in [1, 8]$. Solutions have been obtained by the discretization of the weak form (1.98) (a) and the indirect weak form (1.69) (b).

difference in L^2-norm between the external displacements obtained by the two different formulations is reported. Also in this case the horizontal component u_1 is trivial along the considered axes and the errors are consistent with the fixed discretization space-time steps.

Table 1.3: L^2-error for $x_2 \in [1, 8]$ of the vertical components u_2 for some time instants.

$\|u_{2,\mathbf{p}}(\cdot, t) - u_{2,\mathbf{\Phi}}(\cdot, t)\|_{L^2([1,8])}$	$t = 1$	$t = 2$	$t = 3$
	$5.32\ 10^{-4}$	$1.36\ 10^{-3}$	$2.07\ 10^{-3}$

As a final remark, we want to highlight that both formulations $V\mathbf{\Phi} = \mathbf{g}_{\mathcal{D}}$ and $V\mathbf{p} = (K - 1/2)\mathbf{g}_{\mathcal{D}}$, rewritten in a weak energetic mode, lead to comparable and stable results for the external propagation, and they generate approximation errors in accord with the spatial and temporal level of discretization. This is owed to the accurate quadrature strategies applied to compute the spatial singular integrals deriving by the operators V

and K and discussed in Chapter 4. However, the direct formulation $V\mathbf{p} = (K - 1/2)\mathbf{g}_{\mathcal{D}}$ inevitably requires higher computational costs: nevertheless, its implementation and the comparison with the indirect formulation represent a necessary starting point for the future application of the energetic method to the resolution of more realistic problems. Indeed, the implementation of the double layer operator K is essential to the extension of the Energetic BEM to elastodynamic problems with mixed boundary conditions, as shown in Subsection 1.5.2.

1.6.2 Neumann Problems

Formulation $D\boldsymbol{\Psi} = \mathbf{g}_{\mathcal{N}}$

In this subsection we deal with the resolution of problems equipped with Neumann conditions prescribed at the boundary Γ, as stated in $(P_{\mathcal{N}})$. To treat them we employ the indirect representation formula in $(\mathcal{N}_3)$ and we reformulate the related BIE in the energetic Galerkin weak form (1.70). For all the following experiments we choose piece-wise linear basis for the space approximation (namely $q = 1$ in (1.70)) and we concentrate in particular on problems with condition $\mathbf{g}_{\mathcal{N}}(\mathbf{x}, t)$ that becomes static as the time t grows: in this case, the related BIE unknown $\boldsymbol{\Psi}(\mathbf{x}, t)$ tends in time to a static density $\boldsymbol{\Psi}_\infty(\mathbf{x})$, the latter related to the elastostatic problem

$$\begin{cases} (\lambda + \mu)\nabla(\Delta \cdot \mathbf{u})(\mathbf{x}) + \mu\Delta\mathbf{u}(\mathbf{x}) = 0, & \mathbf{x} \in \mathbf{R}^2 \setminus \Gamma \\ \mathbf{p}(\mathbf{x}) = \mathbf{g}_{\mathcal{N},\infty}(\mathbf{x}), & \mathbf{x} \in \Gamma \end{cases}$$

where $\mathbf{g}_{\mathcal{N},\infty}(\mathbf{x}) = \lim_{t\to\infty} \mathbf{g}_{\mathcal{N}}(\mathbf{x}, t)$. In case of reference static condition uniform in space, namely $\mathbf{g}_{\mathcal{N},\infty}(\mathbf{x}) = \boldsymbol{\eta}$ with $\boldsymbol{\eta}$ non null 2D vector, then the components of reference static solution $\boldsymbol{\Psi}_\infty(\mathbf{x})$ can be calculated exactly on the crack $\Gamma = \left\{(x_1, 0)^\top \,:\, x_1 \in [-0.5, 0.5]\right\}$:

$$\Psi_{i,\infty}(\mathbf{x}) = \widetilde{\eta}_i\sqrt{1/4 - x_1^2}, \quad \widetilde{\eta}_i = -\frac{c_{\mathtt{P}}^2}{\varrho c_{\mathtt{S}}^2\left(c_{\mathtt{P}}^2 - c_{\mathtt{S}}^2\right)}\eta_i, \quad i = 1, 2. \tag{1.99}$$

Experiment 1. In the following problem we consider the above cited obstacle Γ and the elastic parameters $\lambda = 2$, $\mu = 1$ and $\rho = 1$, namely $c_{\mathtt{P}} = 2$ and $c_{\mathtt{S}} = 1$. We set the space and time discretization step $h = 0.025$ and $\Delta t = 0.0125$ and we impose the Neumann datum with components

$$g_{\mathcal{N},i}(\mathbf{x}, t) = \sigma_{ih}[\mathbf{u}](\mathbf{x}, t)n_h(\mathbf{x}), \quad \mathbf{x} \in \Omega, t \in (0, T],\ i = 1, 2, \tag{1.100}$$

where the stress tensor $\boldsymbol{\sigma}$ defined in (1.3) is applied to the pressure plane wave

$$\mathbf{u}(\mathbf{x}, t) = \gamma\left(t - t_0 - \frac{\mathbf{x}\cdot\mathbf{k}}{c_{\mathtt{P}}}\right)\mathbf{k}, \quad \gamma(t) = tH[t],\ t_0 = 0.15,\ \mathbf{k} = \left(\frac{1}{\sqrt{2}}, \frac{1}{\sqrt{2}}\right)^\top. \tag{1.101}$$

This transient datum corresponds to a plane wave impacting on the crack Γ with an angle of 45° and it tends to the static solution (1.99) with coefficients $\widetilde{\eta}_1 = 2/3$ and $\widetilde{\eta}_2 = 2$. In Figure 1.21, the horizontal and the vertical components of the unknown density $\boldsymbol{\Psi}$ are reported, approximated by the Galerkin formulation (1.70), at the final time instant $T = 7.5$ and for all the points of the crack. Together with the transient components, the static

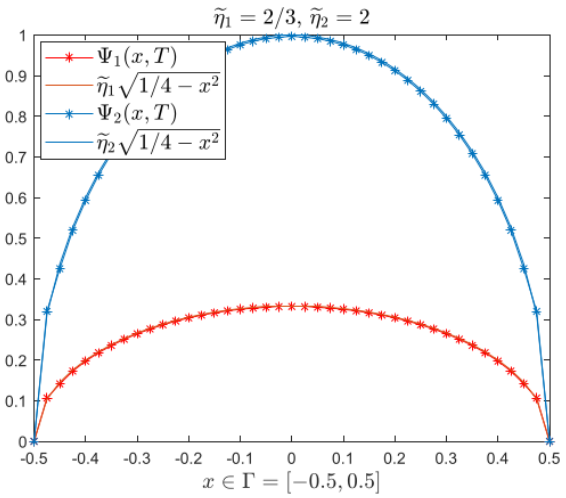

Figure 1.21: Vertical and horizontal components of the unknown density $\boldsymbol{\Psi}$ calculated at the final instant $T = 7.5$, together with the reference static solutions (1.99).

reference solutions $\Psi_{1,\infty}$ and $\Psi_{2,\infty}$ are shown, proving a good overlapping with the graphs of the corresponding time-dependent components of the density $\boldsymbol{\Psi}$. Since the datum corresponds to a plane wave propagating not orthogonally towards the obstacle Γ, the points of the arc are perturbed with a certain delay respect to the left extreme $(-0.5, 0)^\top$, which is the first point met by the pressure wave.

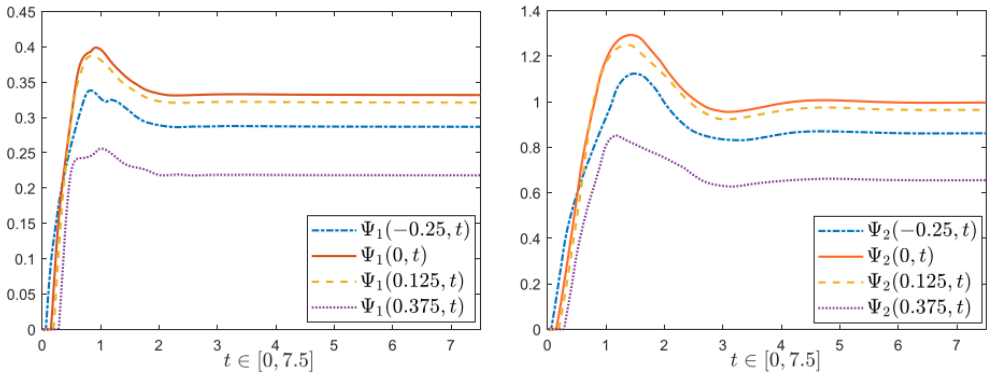

Figure 1.22: Time history of Ψ_1 and Ψ_2 in the points of the crack Γ corresponding to the abscissas $x = -0.25,\ 0,\ 0.125,\ 0.375$.

This delay is well visible in Figure 1.22, reporting the time history of Ψ_1 and Ψ_2, calculated both at different points of Γ. Despite the delay in the starting of the initial perturbation, both components show to become static in time in a stable way.

Experiment 2. In the second Neumann experiment we consider the resolution of a problem on the arc $\Gamma = \left\{\mathbf{x} \in \mathbf{R}^2 \ : \ \mathbf{x} = (\cos\alpha, \sin\alpha)^\top,\ \alpha \in [0, \pi]\right\}$. The arc is in particular discretized with 20 segments, namely $h \simeq 0.15$, while the time step is equal to $\Delta t \simeq 0.078$,

namely 128 time knots in the interval $[0, 10]$. The datum is again the stress tensor applied

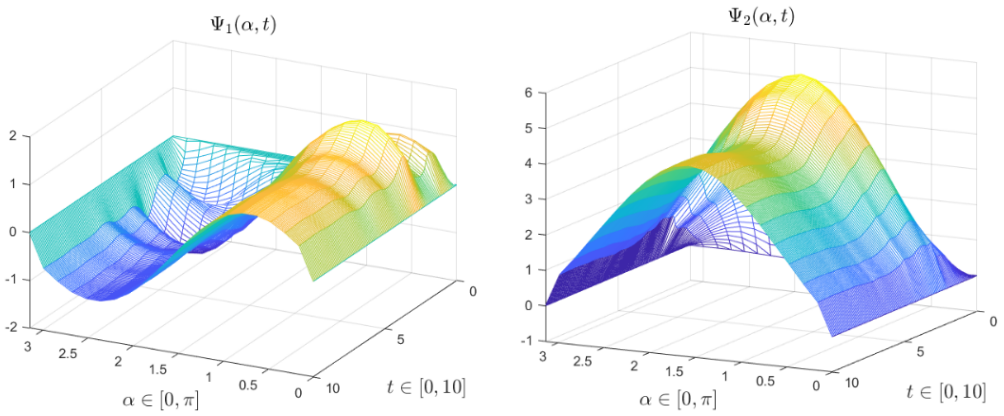

Figure 1.23: Horizontal and vertical and component $\Psi_1(\alpha, t)$ and $\Psi_2(\alpha, t)$ represented for $\alpha \in [0, \pi]$ and $t \in [0, 10]$.

to the pressure wave as in (1.101), with direction $\mathbf{k} = (0, 1)^\top$ and $t_0 = 0$. This datum becomes constant on the arc just after the plane wave has invested all the points of Γ, inducing two components solution of (1.70) reaching a stable behaviour in time. In Figure 1.23, the vertical density Ψ_2 has a "bell shape" similar to the reference solution that can be calculated for the flat obstacle, while Ψ_1 results to be antisymmetric with respect to the middle point of the arc. In Figure 1.24 instead we focus on the computation of the vertical components Ψ_2 at some points of Γ: it is evident that the dynamics starts in different instants for all of them since the plane wave, which has vertical direction, covers the arc from the extremes to the apex of Γ in $(0, 1)^\top$.

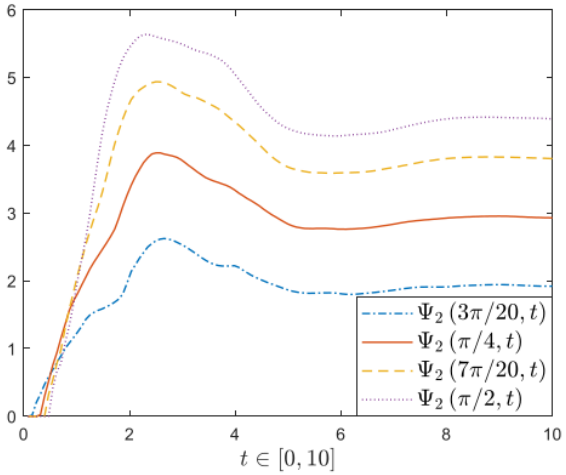

Figure 1.24: Time history of Ψ_2 at the points of the arc Γ corresponding to the clockwise angles $\alpha = 3\pi/20,\ \pi/4,\ ,7\pi/20,\ \pi/2$.

Chapter 2

Graded meshes and *hp* method for energetic BEM in elastodynamics

The solution $\mathbf{u}$ of the 2D elastodynamic equation (1.9) is featured by components with a high gradient in the neighborhood of a corner of a polygonal domain Ω and at the extremes of open obstacles Γ. This naturally translates into a singular behaviour of the traction field $\mathbf{p}$ at the same critical points. The 3D solution exhibits similar characteristics at the exterior corner of a polyhedral domain or at the edges of a screen. Thus, the focus of the chapter is to provide a detailed expansion of the singularities that allows to get quasi-optimal estimates for piece-wise polynomial approximations of the traces of $\mathbf{u}$ and $\mathbf{p}$ at the boundary Γ.
To get a accurate numerical approximation by Finite or Boundary Element Methods, it is convenient to take into account the non-smooth behaviour and to use local mesh refinements or high polynomial degrees to recover optimal convergence rates. Plamenevskiĭ and collaborators [50, 52, 58, 68] provided from the late 1990's a detailed investigation about the singular behaviour of solutions of hyperbolic problems on conical or wedge domains. Many authors then, thank to similar explicit asymptotic expansions, estimated the convergence rate of the approximated solution obtained by FEM (like Müller and Schwab for scalar and elastic wave problems [64, 65]) or by BEM (see the works of Gimperlein and collaborators [38, 41, 42]). In particular, the convergence rate is studied in relation to the application of particular meshes for the spatial discretization: these strategies are known in literature as h, p and hp methods, which have been studied for several decades. A compendium of application in conjunction with FEM and BEM can be moreover found respectively in [74] and [45].

Here in particular we will explore the application of the time-domain Boundary Elements Method for Dirichlet and Neumann elastodynamics problems, employing the theoretical results and the algorithmic details presented in Chapter 1, considering a spatial discretization as introduced in Section 1.5 and reformulated with the h, p and hp methods. To do that we will consider both 2D an 3D geometries and we will rewrite, in a neighbourhood of a corner of a polygon or near the angle of a wedge, the unknown displacement through a singular expansion, for which the order of singularity depends on the amplitude of the considered corner and that can be deduced by the study of the time independent elastic

equation. By the reformulation of $\mathbf{u}$, and consequently by its trace at these critical points, we will prove estimates of the error in energetic norm committed approximating the unknown by a BEM combined with the proposed discretization methods.
In the end we will present several results of BEM for the resolution of elastodynamics problems in combination with the *h*, *p* and *hp* discretization methods, in order to asses the theoretical error estimates.

Remark. The following results are based on the Autor's work [7], made in collaboration with Professors Alessandra Aimi, Heiko Gimperlein and Ernst P. Stephan (respectively from University of Parma, Heriot-Watt University of Edinburgh and Leibniz Universität of Hannover) and recently submitted to the journal *Numerische Matematik*. In particular in this paper, in which is reported also the theoretical analysis of Section 1.4, 3D geometries are investigated, like the apex of a cone or the wedge part of polyhedron, and for them the singular expansion of the time-domain solution of the elastodynamics equation is derived, yielding to accurate error estimates depending on the type of employed spatial mesh refinement. The 3D geometry of a wedge can be considered the natural extension of an angle point of a two-dimensional arc, then in the following we will report only the theoretical results that can be verbatim applied to the case of elastodynamics 2D problems in polygonal domains. Numerical results at the end of the chapter will deal only with experiments of energetic BEM applied to 2D elastodynamics Dirichlet and Neumann problems.

2.1 Regularity of solutions to the Dirichlet and Neumann problem

We briefly reintroduce the elastodynamics problem we intend to investigate, considering both the 2D and the 3D dynamics. Let us consider $\Omega \subset \mathbf{R}^n$, $n = 2, 3$, a bounded polyedral domain with boundary $\partial\Omega = \Gamma$ and let be Ω_e its complementary exterior region, thus $\Omega_e = \mathbf{R}^n \setminus \overline{\Omega}$ (the limit case of propagation in $\Omega_e = \mathbf{R}^n \setminus \overline{\Gamma}$ with Γ polygonal open obstacle for $n = 2$ and 3D screed for $n = 3$ can be also taken into account). We recall that much of the notation of Chapter 1 is suited for the 3D case as well. We rewrite then the Navier equation that describes, during the time interval $(0, T]$, the dynamics of elastic waves propagating in bounded domain Ω of $\mathbf{R}^n$, the latter identified by the generic cartesian coordinates $\mathbf{x} = (x_1, ..., x_n)^\top$:

$$(\lambda + \mu)\nabla(\nabla \cdot \mathbf{u}) + \mu\Delta\mathbf{u} + \rho\mathbf{b} = \varrho\ddot{\mathbf{u}}, \quad \mathbf{x} \in \Omega,\ t \in (0, T]. \tag{2.1}$$

The vector $\mathbf{b} = (b_1, ..., b_n)^\top$ is an external forcing per unity of mass and, as stated in Chapter 1, the unknown $\mathbf{u} = (u_1, ..., u_n)^\top$ represents the displacement and λ, μ and ρ are the physical parameters on which the velocities $c_\mathtt{P} > c_\mathtt{S}$ depend, according to formula (1.12). Equation (2.1) is equipped with null initial conditions as in (1.13) and we moreover consider two types of boundary constraint. The first is of Dirichlet type and it holds directly for $\mathbf{u}$ on $\Sigma = \Gamma \times (0, T]$:

$$\mathbf{u}(\mathbf{x}, t) = \mathbf{g}_\mathcal{D}(\mathbf{x}, t), \quad (\mathbf{x}, t) \in \Sigma, \tag{2.2}$$

while, for the second, we set a condition for the traction $\mathbf{p}$, defined by components in (1.7):

$$\mathbf{p}(\mathbf{x}, t) = \mathbf{g}_\mathcal{N}(\mathbf{x}, t), \quad (\mathbf{x}, t) \in \Sigma. \tag{2.3}$$

To implement the Boundary Element Method we employ the integral formulations $(\mathcal{D}_1)$ and $(\mathcal{N}_1)$, respectively suitable for Dirichlet and Neumann boundary problems with homogeneous force $\mathbf{b} \equiv 0$. For $n = 3$, the mentioned representation formulas and BIEs can be derived with the identical passages reported in Section 1.2, with the only exception that for 3D case the integral operators V, K, K^* and D are based on a different definition of the fundamental Green's function:

$$\begin{aligned} G_{ij}^{\mathbf{uu}}(\mathbf{x},\boldsymbol{\xi};t,\tau) :=& \frac{t}{4\pi\varrho r^2}\left(\frac{3r_ir_j}{r^3}-\frac{\delta_{ij}}{r}\right)(t-\tau)(H[c_{\mathtt{P}}(t-\tau)-r]-H[c_{\mathtt{S}}(t-\tau)-r]) \\ &+ \frac{r_ir_j}{4\pi\varrho r^3}\left(c_{\mathtt{P}}^{-2}\delta(c_{\mathtt{P}}(t-\tau)-r)-c_{\mathtt{S}}^{-2}\delta(c_{\mathtt{S}}(t-\tau)-r)\right) \\ &+ \frac{\delta_{ij}}{4\pi\varrho r c_{\mathtt{S}}^2}\delta(c_{\mathtt{S}}(t-\tau)-r), \qquad i,j=1,2,3. \end{aligned}$$

In the following, we indicate the unknown traces $\mathbf{p}_{|\Gamma}$ and $\mathbf{u}_{|\Gamma}$ respectively with the symbols $\boldsymbol{\Phi}$ and $\boldsymbol{\Psi}$, and we identify the entire right-hand-sides of the BIEs in $(\mathcal{D}_1)$ and $(\mathcal{N}_1)$ with the symbols $\widetilde{g}_{\mathcal{D},i}$ and $\widetilde{g}_{\mathcal{N},i}$. Thus, we rewrite the related energetic weak formulations of the BIEs as follows:

find $\boldsymbol{\Phi} = (\Phi_1, ..., \Phi_n)^\top \in H^1_\sigma(\mathbf{R}^+; \widetilde{H}^{-\frac{1}{2}}(\Gamma))^n$ *that solves*

$$\langle (V_{ij}\dot{\Phi}_j), \phi_i\rangle_{L^2(\Sigma)} = \langle \dot{\widetilde{g}}_{\mathcal{D},i}, \phi_i\rangle_{L^2(\Sigma)}, \tag{2.4}$$

where $\boldsymbol{\phi} = (\phi_1, ..., \phi_n)^\top$ *is a suitable test function belonging to the functional space of the trace* $\boldsymbol{\Phi}$,

for the Dirichlet problem, while for the Neumann one we solve the following:

find $\boldsymbol{\Psi} = (\Psi_1, ..., \Psi_n)^\top \in H^1_\sigma(\mathbf{R}^+; \widetilde{H}^{\frac{1}{2}}(\Gamma))^n$ *that solves*

$$\langle (D_{ij}\Psi_j), \dot{\psi}_i\rangle_{L^2(\Sigma)} = \langle \widetilde{g}_{\mathcal{N},i}, \dot{\psi}_i\rangle_{L^2(\Sigma)}, \tag{2.5}$$

where $\boldsymbol{\psi} = (\psi_1, ..., \psi_n)^\top$ *is a suitable test function belonging to the functional space of the trace* $\boldsymbol{\Psi}$.

Lemma 1.4.2 can be verbatim extended also for $n = 3$ with a similar proof and guarantees that weak problems (2.4) and (2.5) are well-posed in the indicated functional spaces.

In the next section precise results for the singular behaviour of the solution of the original initial-boundary value problem, with Dirichlet or Neumann conditions, considering region near corner points will be enunciated. This behaviour in particular can be analysed considering the singular expansion of solutions of equation (2.1), reformulated through polar coordinates, leading to decompositions also for the solutions of the integral weak problems in singular terms and more regular remainders.

2.1.1 Behavior of solutions in a 2D sector and in a wedge

We consider equation (2.1) for $n = 2$ and we introduce a new system of spatial coordinates r and ϕ, in order to describe the region near a corner point of Ω with amplitude ω.

Reformulating the related stress tensor (1.3) in cilindrical variables, as indicated in [75], it is possible to rewrite vectorial equation (2.1) as follows:

$$(2\mu+\lambda)\left(\partial_r^2 u_r+\frac{1}{r}\partial_r u_r-\frac{u_r}{r^2}\right)+\frac{\mu}{r^2}\partial_\phi^2 u_r+\frac{\lambda+\mu}{r}\partial_{r\phi}u_\phi-\frac{\lambda+3\mu}{r^2}\partial_\phi u_\phi+\varrho b_r=\varrho\partial_t^2 u_r,$$
$$\frac{\lambda+\mu}{r}\partial_{r\phi}u_r+\frac{\lambda+3\mu}{r^2}\partial_\phi u_r+\mu\partial_r^2 u_\phi+\mu\frac{1}{r}\partial_r u_\phi-\mu\frac{u_\phi}{r^2}+\frac{2\mu+\lambda}{r^2}\partial_\phi^2 u_\phi+\varrho b_\phi=\varrho\partial_t^2 u_\phi,$$

with ∂_r, ∂_ϕ, ∂_r^2, ∂_ϕ^2 and $\partial_{\phi r}^2$ being the derivatives in the new system of variables. Therefore, searching for a solution $\mathbf{u}$ whose radial and tangential components near the considered vertex behave as $u_r=r^{\nu^*}\varphi_r(\phi,t)$ and $u_\phi=r^{\nu^*}\varphi_\phi(\phi,t)$, the dynamics can be described by the following system:

$$r^{\nu^*-2}\left[\mu\partial_\phi^2\varphi_r+(\lambda+2\mu)((\nu^*)^2-1)\varphi_r+((\lambda+\mu)\nu^*-(\lambda+3\mu))\partial_\phi\varphi_\phi\right]+\varrho b_r=\varrho r^{\nu^*}\partial_t^2\varphi_r, \tag{2.6}$$

$$r^{\nu^*-2}\left[(\lambda+2\mu)\partial_\phi^2\varphi_\phi+\mu((\nu^*)^2-1)\varphi_\phi+((\lambda+\mu)\nu^*+(\lambda+3\mu))\partial_\phi\varphi_r\right]+\varrho b_\phi=\varrho r^{\nu^*}\partial_t^2\varphi_\phi. \tag{2.7}$$

The time independent solutions of (2.6)-(2.7), for $(b_r,b_\phi)=(0,0)$, are given by

$$(\cos(1+\nu^*)\phi,-\sin(1+\nu^*)\phi)^\top,\ (\sin(1+\nu^*)\phi,\cos(1+\nu^*)\phi)^\top,$$
$$(\cos(1-\nu^*)\phi,-\nu_2\sin(1-\nu^*)\phi)^\top,\ (\sin(1-\nu^*)\phi,\nu_2\cos(1-\nu^*)\phi)^\top,$$

with

$$\nu_2=\frac{3+\nu^*-4\nu}{3-\nu^*-4\nu},\quad \nu=\frac{\lambda}{2(\lambda+\mu)}.$$

We briefly examine the time independent problem with Dirichlet conditions $u_r(\pm\omega/2)=u_\varphi(\pm\omega/2)=0$. Setting arbitrary constants A,B,C,D we obtain the generic solutions

$$\varphi_r(\phi)=A\cos(1+\nu^*)\omega/2\pm B\sin(1+\nu^*)\omega/2+C\cos(1-\nu^*)\omega/2\pm D\sin(1-\nu^*)\omega/2=0,$$

$$\varphi_\phi(\phi)=\mp A\sin(1+\nu^*)\omega/2+B\cos(1+\nu^*)\omega/2\mp\nu_2 C\sin(1-\nu^*)\omega/2+\nu_2 D\cos(1-\nu^*)\omega/2=0,$$

from which we deduce the condition

$$\sin\nu^*\omega=\pm\frac{\nu_2-1}{\nu_2+1}\sin\omega\quad\text{with}\quad\frac{\nu_2-1}{\nu_2+1}=\frac{\nu^*}{3-4\nu}. \tag{2.8}$$

Since we can proceed analogously for Neumann boundary conditions, the following proposition for the time-independent problem holds [66].

Proposition 2.1.1. *Let* $\mathbf{b}\in H^{s-1}(\Omega)^2$ *and* $s>0$, $s\notin\mathcal{R}e(\nu_{jk}^*)$ *with* ν_{jk}^* *as in* (2.11), (2.12). *Then the weak solution* $\mathbf{u}\in H^1(\Omega)^2$ *of the time-independent equations* (2.6), (2.7) *admits with* C^∞ *cut-off functions* χ_j *near the vertex* t_j *with interior opening angle* ω_j *the decomposition*

$$\mathbf{u}=\mathbf{u}_0+\sum_{\mathcal{R}e(\nu_{jk}^*)<s}a_{jk}^*\mathbf{S}_{jk}^*(r,\phi)\chi_j(r) \tag{2.9}$$

with a regular part $\mathbf{u}_0 \in H^{1+s}(\Omega)^2$, $a_{jk} \in \mathbb{C}$ *and the singularity functions*

$$\mathbf{S}^*_{jk}(r,\phi) = \begin{cases} r^{\nu^*_{jk}} \boldsymbol{\varphi}^*_{jk}(\phi) \text{ for } \nu^*_{jk} \notin \mathbb{N}, \\ r^{\nu^*_{jk}} \ln r \ \boldsymbol{\varphi}^*_{jk}(\phi) + r^{\nu^*_{jk}} \tilde{\boldsymbol{\varphi}}^*_{jk}(\phi) \text{ for } \nu^*_{jk} \in \mathbb{N}. \end{cases} \tag{2.10}$$

Here the singular exponents $\nu^*_{jk} \in \mathbb{C}$ *with* $\mathcal{R}e(\nu^*_{jk}) > 0$ *are solutions of the following equations depending on the kind of boundary conditions at the two sides meeting at the corner* t_j

$$Dirichlet : \sin \nu^*_{jk}\omega_j = \pm \nu^*_{jk} k^{*-1} \sin \omega_j \tag{2.11}$$

$$Neumann : \sin \nu^*_{jk}\omega_j = \pm \nu^*_{jk} \sin \omega_j \tag{2.12}$$

The functions $\boldsymbol{\varphi}^*_{jk}$ *with the components* $(\varphi^*_{jk})_r$ *in r-direction and* $(\varphi^*_{jk})_\phi$ *in* ϕ*-direction are*

$$\varphi^*_{jk,r}(\phi) = A\cos(1+\nu^*_{jk})\phi + B\sin(1+\nu^*_{jk})\phi + C\cos(1-\nu^*_{jk})\phi + D\sin(1-\nu^*_{jk})\phi,$$

$$\varphi^*_{jk,\phi}(\phi) = -A\sin(1+\nu^*_{jk})\phi + B\cos(1+\nu^*_{jk})\phi - \gamma_{jk}C\sin(1-\nu^*_{jk})\phi + \gamma_{jk}D\cos(1-\nu^*_{jk})\phi,$$

with constants A,B, C, D $\in \mathbb{C}$ *depending on the type of boundary conditions at the corner. For what regards the constants* γ_{jk}, k^**, they are defined as follows*

$$\gamma_{jk} = \frac{3+\nu^*_{jk}-4\nu}{3-\nu^*_{jk}-4\nu}, \ k^* = 3-4\nu. \tag{2.13}$$

As remarked in [43], p. 73, for Dirichlet boundary conditions there exist two leading real roots ν^*_{jk} of the equation (2.11) in $(0,1)$.

Remark. For a crack, i.e. $\omega_j = 2\pi$, and for Dirichlet and Neumann boundary conditions, $\nu^*_{j1} = 1/2$ is solution of (2.11) and (2.12). More generally, we can use (2.11) to study the singular exponents for the solution of the Dirichlet problem near an angle ω when $\omega \to 0$, respectively $\omega \to 2\pi$. We obtain

$$\sin \nu^*\omega = \nu^* k^{*-1} \sin \omega = \frac{\nu^*\omega}{k^*} + o(\omega) \tag{2.14}$$

for $\omega \to 0$, or

$$\frac{\sin \nu^*\omega}{\nu^*\omega} \to \frac{1}{k^*}.$$

We conclude $\nu^* = \frac{c}{\omega} + O(1)$, where c satisfies $\frac{\sin c}{c} = \frac{1}{k^*}$.
For the corresponding exterior angle, $\omega = 2\pi - \varepsilon$ with $\varepsilon \to 0$, we set $\nu^* = \frac{1}{2} + \tilde{\nu}(\varepsilon)$. Then $\sin \nu^*\omega = \sin\left((\frac{1}{2} + \tilde{\nu}(\varepsilon))(2\pi - \varepsilon)\right)$, and Taylor expanding for $\varepsilon, \tilde{\nu}(\varepsilon) \to 0$ leads to

$$\sin \nu^*\omega = -2\pi\tilde{\nu}(\varepsilon) + \frac{\varepsilon}{2} + o(\varepsilon) \ .$$

On the other hand, from equation (2.11) $\sin \nu^*\omega = \frac{\nu^*}{k^*} \sin \omega = -\frac{\nu^*}{k^*}\varepsilon + o(\varepsilon)$, so that $-2\pi\tilde{\nu}(\varepsilon) + \frac{\varepsilon}{2} = -\frac{1}{2k^*}\varepsilon + o(\varepsilon)$, or $\tilde{\nu}(\varepsilon) = \frac{\varepsilon}{4\pi}\left(1 + \frac{1}{k^*}\right) + o(\varepsilon)$ and

$$\nu^* = \frac{1}{2} + \frac{\varepsilon}{4\pi}\left(1 + \frac{1}{k^*}\right) + o(\varepsilon) \ .$$

Figure 2.8 numerically illustrates ν^* as a function of ω, when $\lambda = 2$, $\mu = 1$ and $\rho = 1$. It confirms the above analysis.

A time-dependent expansion for the displacement solution $\mathbf{u}$ can be also provided for the 3D geometry in Figure 2.1, where it is well represented the exterior of a circular wedge with opening angle ω and edge $\{(x_1, x_2, 0) \in \mathbb{R}^3 : x_1^2 + x_2^2 = 1\}$. The 3D coordinates x_1, x_2, x_3, which the vectorial solution $\mathbf{u}$ depends on, in a neighborhood of the edge are reformulated by means of local cylindrical coordinates (r, ϕ, z): the distance to the edge is given by $r = |1 - \sqrt{x_1^2 + x_2^2}|$, ϕ is the polar angle in spherical coordinates, while the edge variable z is the azimuthal angle in the $x_1 - x_2$-plane, $\tan(z) = \frac{x_2}{x_1}$.
In particular, combining the results on the wedge obtained in [7] (Section 3.1) and in Proposition 2.1.1 for the expansion in a 2D sector, we cite the following Theorem, in which we furnish the expression of the singular expansion of $\mathbf{u}$ solution of the time dependent problem (2.1)-(2.2).

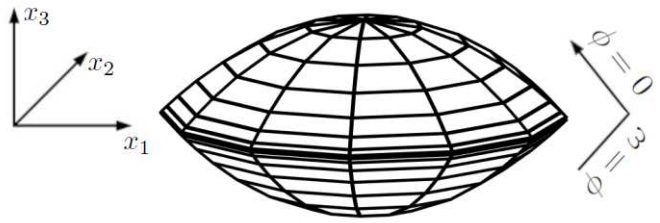

Figure 2.1: An example of 3D wedge.

Theorem 2.1.2. *Let $\gamma > 0$, $q \in \mathbb{N}_0$, $\beta \in (\beta_{r+1}, \beta_r)$ with $0 < \beta_r - \beta < 1$, $(\mathbf{b}, \mathbf{g}_{\mathcal{D}}) \in \mathcal{R}V_{\beta,q}(\Omega \times \mathbf{R}^+, \gamma)$ and assume the orthogonality condition in Theorem 9.9 of [7] holds for all ν_k, ν_k^* with $\mathcal{R}e(\nu_k), \mathcal{R}e(\nu_k^*) \in [1 - \beta_r, 1 - \beta_1]$. Then in the neighborhood of a vertex with interior opening angle ω the solution to* (2.1) - (2.2) *admits the expansion*

$$\mathbf{u}(x, y, z, t) = \mathbf{u}_0(x, y, z, t) + \sum_{\mathcal{R}e(\nu_k) < s} \sum_{0 \leqslant p < s - \mathcal{R}e(\nu_k)} (Xc_{k,p})(\mathbf{y}, z, t)\mathbf{S}_{k,p}(r, \phi)$$
$$+ \sum_{\mathcal{R}e(\nu_k^*) < s} \sum_{0 \leqslant p < s - \mathcal{R}e(\nu_k^*)} (Xc_{k,p}^*)(\mathbf{y}, z, t)\mathbf{S}_{k,p}^*(r, \phi). \tag{2.15}$$

where $s < \min\{\mathcal{R}e\ \nu_k, \mathcal{R}e\ \nu_k^*\} + p + 1 + \beta$ for all k and $\mathbf{u}_0 \in DV_{\beta,q}(\mathcal{Q}, \gamma)$.

The expansion of $\mathbf{u}$ in the 2D case naturally follows from (2.15) considering functions independent of the variable z. Note that the sum in k in (2.15) implicitly includes multiplicities of the eigenvalues. A correct definition of the functional spaces $\mathcal{R}V_{\beta,q}(\Omega \times \mathbf{R}^+, \gamma)$ and $DV_{\beta,q}(\Omega \times \mathbf{R}^+, \gamma)$ can be found in the Appendix of [7] and also in [64, 65, 51, 58] and we finally recall embedding results $DV_{\beta,q}(\Omega \times \mathbf{R}^+, \gamma) \subset H^r_\sigma(\mathbf{R}^+; H^s(\Omega))^n$ [64].

Remark. Theorem 2.1.2 states that, for given parameters β, γ, the solution can be written as the sum of a remainder term $\mathbf{u}_0 \in DV_{\beta,q}(\Omega \times \mathbf{R}^+, \gamma) \subset H^r_\sigma(\mathbf{R}^+; H^s(\Omega))^n$ and, depending on the order s, a finite number of singular functions $\mathbf{S}_{k,p}^*$, $\mathbf{S}_{k,p}$ (these functions

are identically defined as in (2.10) but the latter depends on singular exponents of type $\nu_k = k\omega/\pi$). This confirms that, with exception for the terms $(Xc^*_{k,p})(t)$, smooth in time, the singular expansion of the unknown displacement $\mathbf{u}$ in (2.15) for the time-dependent case depends, by the factors $\mathbf{S}^*_{k,p}$, on the singular functions reported in (2.10) and on the singular exponents that can be calculated as solutions of (2.11).

2.2 Space discretization with geometrically and algebraically graded meshes

To solve the energetic weak formulations (2.4) and (2.5) in a discretized form, we refer to the spatial and temporal decomposition exposed in Section 1.5 for the 2D case. Here we set a generic degree s for the approximation of $\mathbf{\Phi}$ and $\mathbf{\Psi}$ by piece-wise polynomials in time. We recall the definition of the discreet functional spaces $X^{-1}_{h,p}(\Gamma)$ and $X^0_{h,q}(\Gamma)$ in (1.67) and (1.68), that for $n = 2$ are subordinated to a decomposition of Γ with a set of non-intersecting straight segments $\mathcal{T} = \{e_1, ..., e_M\}$ such that $h_i := length(e_i) \leqslant h$. For $n = 3$, we assume that Γ is triangulated by a set of patches $\mathcal{T} = \{e_1, \cdots, e_M\}$, with $diam(e_i) \leqslant h$, $e_i \cap e_j = \emptyset$ if $i \neq j$ and if $\overline{e_i} \cap \overline{e_j} \neq \emptyset$, the intersection is either an edge or a vertex of both triangles.
The Galerkin weak formulation of the Dirichlet problem (2.1)-(2.2) and of the Neumann problem (2.1)-(2.3) respectively reads

find $\Phi_{i,h,\Delta t} \in V_{\Delta t,s} \otimes X^{-1}_{h,p}(\Gamma)$, $i = 1, ..., n$ *such that*

$$\langle (V_{ij}\dot{\Phi}_{j,h,\Delta t}), \phi_{i,h,\Delta t}\rangle_{L^2(\Sigma)} = \langle \dot{\widetilde{g}}_{\mathcal{D},i}, \phi_{i,h,\Delta t}\rangle_{L^2(\Sigma)}, \tag{2.16}$$

for all $\boldsymbol{\phi}_{h,\Delta t} = (\phi_{1,h,\Delta t}, ..., \phi_{n,h,\Delta t})^\top \in \left(V_{\Delta t,s} \otimes X^{-1}_{h,p}(\Gamma)\right)^n$.

for the Dirichlet problem, while for the Neumann condition we solve:

find $\Psi_{i,h,\Delta t} \in V_{\Delta t,s} \otimes X^0_{h,q}(\Gamma)$, $i = 1, ..., n$ *such that*

$$\langle D_{ij}\Psi_{j,h,\Delta t}, \dot{\psi}_{i,h,\Delta t}\rangle_{L^2(\Sigma)} = \langle \widetilde{g}_{\mathcal{N},i}, \dot{\psi}_{i,h,\Delta t}\rangle_{L^2(\Sigma)}, \tag{2.17}$$

for all $\boldsymbol{\psi}_{h,\Delta t} = (\psi_{1,h,\Delta t}, ..., \psi_{n,h,\Delta t})^\top \in \left(V_{\Delta t,s} \otimes X^0_{h,q}(\Gamma)\right)^n$.

We recall that the Galerkin weak problems above stated are equivalent to the linear systems $\mathbb{E}_V \boldsymbol{\alpha}^{\mathbf{p}} = \widetilde{\boldsymbol{\beta}}^{\mathcal{D}}$ and $\mathbb{E}_D \boldsymbol{\alpha}^{\mathbf{u}} = \widetilde{\boldsymbol{\beta}}^{\mathcal{N}}$, where the matrix elements of $\mathbb{E}_V$ and $\mathbb{E}_D$ are reported respectively for the case $s = 0$ and $s = 1$, for the 2D problem, in (1.78) and (1.88) respectively.

Unlike what we did with the numerical experiments in Chapter 1, where we only considered uniform decompositions of the boundary, in the numerical Section 2.4 we work with the approximation on quasiuniform and $\tilde{\beta}$-graded meshes, for a constant $\tilde{\beta} > 0$.
To introduce them for the discretization of boundaries of 2D polygonal domains, it is

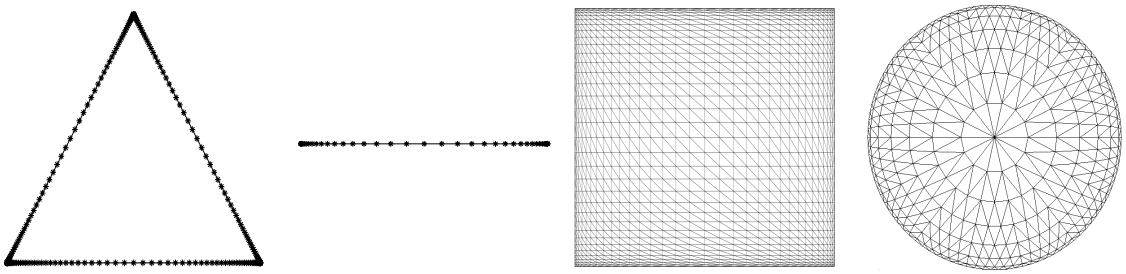

(a) (b)

Figure 2.2: $\tilde{\beta}$-graded meshes on 1D boundaries with $\tilde{\beta} = 3$ (a) and $\tilde{\beta}$-graded meshes for square and circular screens with $\tilde{\beta} = 2$ (b).

sufficient to define $\tilde{\beta}$-graded meshes on the interval $[-1, 1]$. The position of the nodes in the left interval $[-1, 0]$ are defined with the following sequence

$$x_k = -1 + \left(\frac{k}{N_l}\right)^{\tilde{\beta}}, \quad k = 1, ..., N_l. \tag{2.18}$$

With formula (2.18) we impose a set of knots tending to be gradually accumulated near the left extreme -1. The graded mesh on the right interval $[0, 1]$ can be simply calculated by symmetry. We remark that for $\tilde{\beta} = 1$, we simply obtain a uniform decomposition of the interval. A graphical representation of 3-graded meshes on an equilateral triangle and on a crack are shown in Figure 2.2(a).
On the circular screen of radius 1, for $\beta = 1$ we take a uniform mesh with nodes on concentric circles of radius $r_k = 1 - \frac{k}{N_l}$ for $k = 0, \ldots, N_l - 1$. For the $\tilde{\beta}$-graded mesh, the radii are moved to $r_k = 1 - (\frac{k}{N_l})^{\tilde{\beta}}$ for $k = 0, \ldots, N_l - 1$. While the triangles become increasingly flat near the boundary, their total number remains proportional to N_l^2. It is possible to proceed analogously on the square. Examples of 2-graded meshes on the square and the circular screens are depicted in Figure 2.2(b).
The global mesh size h in case of graded mesh, both for the 2D and the 3D case, represents the diameter of the largest element. Therefore, the diameter of the smallest one is of order $h^{\tilde{\beta}}$.

We also consider geometrically graded meshes for 2D problems with a crack obstacle Γ. We just define them on the reference interval $[-1, 1]$: for a refinement parameter $\sigma \in (0, 1/2]$, in $[-1, 0]$ we let $x_0 = -1$, and

$$x_k = \sigma^{N_l+1-k} - 1, \quad k = 1, \ldots, N_l. \tag{2.19}$$

In case of geometric mesh, the diameter of the smallest elements is equal to σ^{N_l} and the nodes in $[0, 1]$ are again determined by symmetry.

In Sections 2.3-2.4 we will consider as spatial discretization techniques the so called h, p and hp versions (or methods) that allow us to study how the discretization errors affect $\Phi_{h,\Delta}$ and $\Psi_{h,\Delta}$, solutions of the Galerkin problems (2.16) and (2.17), in relation of the

refinements of the spatial mesh or the increasing of the polynomial degree with which we compute these discrete solutions in space:

- with h version, or method, we intend the study of the solution of the weak Galerkin problem for a fixed polynomial degree p (or q) in space and refining the mesh increasing the value of the number N_l of the spatial nodes in formula (2.18);
- The p version, or method, corresponds to the study of Galerkin weak solution for fixed spatial mesh (in the Section (2.4) there are only uniform discretizations) and increasing uniformly the polynomial degree p (or q) of the spatial shape functions;
- for the *hp* version, or method, the polynomial degree p increases linearly, at every iteration of the spatial discretization with geometrically graded meshes, from $\partial\Gamma$: $p = \mu k$ in $[x_k, x_{k+1}]$ for a given $\mu > 0$.

Remark. Due to the continuity and coercivity of the bilinear forms (2.4) and (2.5), the discretized equations (2.16) and (2.17), admit a unique solution. Stability and a priori error estimates for the numerical error can be deduced as in [15].

2.3 Theorems on a priori error estimates

To proceed on the error estimates, depending on the h, p and *hp* discretization proposed above, we report from [7] the following propositions:

Proposition 2.3.1. *Let be $\gamma > 0$, $q \in \mathbf{N}_0$.*

a) Let be ν^* the leading singular exponent, the minimum of $\frac{\pi}{\omega}$ and the minimal root of (2.12). *Assume that $i\lambda = \nu^*$ is the only eigenvalue in the strip $\beta - 1 \leqslant \mathrm{Im}\ \lambda \leqslant 0$. Let $(\mathbf{b}, \mathbf{g}_{\mathcal{N}}) \in \mathcal{R}V_{\beta,q-1}(\Omega \times \mathbf{R}^+, \gamma)$ and assume that the orthogonality condition in Theorem 9.9 of [7] holds. Then the Dirichlet trace of the solution $\mathbf{u}$ of the Neumann problem* (2.1)-(2.3) *with right-hand-side $\mathbf{b}$, Neumann data $\mathbf{g}_{\mathcal{N}}$ and initial null conditions satisfies*

$$u_i(r, \phi, z, t)_{|\Gamma} = a_i(\phi, z, t) r^{\nu^*} + u_{i,0}(r, \phi, z, t) \ . \tag{2.20}$$

Here, a_i is smooth for smooth data and $u_{i,0}$ a less singular remainder.

b) Let be ν^* the leading singular exponent, the minimum of $\frac{\pi}{\omega}$ and the minimal root of (2.11). *Let $(\mathbf{b}, \mathbf{g}_{\mathcal{D}}) \in \mathcal{R}V_{\beta,q}(\Omega \times \mathbf{R}^+, \gamma)$ and assume that the orthogonality condition in Theorem 9.9 of [7] holds. Then the Neumann trace of the solution $\mathbf{u}$ of the Dirichlet problem* (2.1)-(2.2) *with right-hand-side $\mathbf{b}$, Dirichlet data $\mathbf{g}_{\mathcal{D}}$ and null initial conditions satisfies*

$$p_i(r, \phi, z, t)_{|\Gamma} = b_i(\phi, z, t) r^{\nu^* - 1} + \phi_{i,0}(r, \phi, z, t) \ . \tag{2.21}$$

Here, b_i is smooth for smooth data and $\phi_{i,0}$ a less singular remainder.

Also from Proposition 2.3.1, the expansion of $\mathbf{u}_{|\Gamma}$ and $\mathbf{p}_{|\Gamma}$ in the 2D case yields just not considering the z variable. The proposition confirms that the singular expansion (2.15) naturally translates in a singular expansion for the traces of the displacement $\mathbf{u}$ and the traction $\mathbf{p}$ on Γ. This also means that the boundary singularities are characteristic also of the solutions of the weak problems (2.4) and (2.5).

2.3.1 Approximation on graded meshes

At this point we proceed with the announcement and the demonstration of the following theorems on a priori error estimate in case of $\tilde{\beta}$-graded meshes:

Theorem 2.3.2. *Let $r \geqslant 0$ and $\varepsilon > 0$.*

a) Let $\mathbf{u}$ be a strong solution to the elastodynamic equation (2.1) with $\boldsymbol{b} \equiv 0$ and inhomogeneous Neumann boundary conditions $\mathbf{p}_{|\Gamma} = \mathbf{g}_{\mathcal{N}}$, with $\mathbf{g}_{\mathcal{N}}$ smooth. Further, let $\boldsymbol{\Psi}^{\tilde{\beta}}_{h,\Delta t} \in \left(V_{\Delta t,q} \otimes X^0_{h,1}\right)^n$ be the best approximation to $\mathbf{u}_{|\Gamma}$ in the norm of $H^r_\sigma(\mathbb{R}^+, \widetilde{H}^{\frac{1}{2}-s}(\Gamma))^n$ on a $\tilde{\beta}$-graded spatial mesh with $\Delta t \lesssim h_1$. Then

$$\|\mathbf{u}_{|\Gamma} - \boldsymbol{\Psi}^{\tilde{\beta}}_{h,\Delta t}\|_{r,\frac{1}{2}-s,\Gamma,*} \leqslant C_{\tilde{\beta},\varepsilon} h^{\min\{\tilde{\beta}(\mathcal{R}e(\nu^*)+s),\frac{3}{2}+s\}-\varepsilon},$$

where $s \in [0, \frac{1}{2}]$.

b) Let $\mathbf{u}$ be a strong solution to the elastodynamic equation (2.1) with $\boldsymbol{b} \equiv 0$ and with inhomogeneous Dirichlet boundary conditions $\mathbf{u}_{|\Gamma} = \mathbf{g}_{\mathcal{D}}$, with $\mathbf{g}_{\mathcal{D}}$ smooth. Further, let $\boldsymbol{\Phi}^{\tilde{\beta}}_{h,\Delta t} \in \left(V_{\Delta t,q} \otimes X^{-1}_{h,0}\right)^n$ be the best approximation to $\mathbf{p}$ in the norm of $H^r_\sigma(\mathbb{R}^+; \widetilde{H}^{-\frac{1}{2}}(\Gamma))^n$ on a $\tilde{\beta}$-graded spatial mesh with $\Delta t \lesssim h_1$. Then

$$\|\mathbf{p}_{|\Gamma} - \boldsymbol{\Phi}^{\tilde{\beta}}_{h,\Delta t}\|_{r,-\frac{1}{2},\Gamma,*} \leqslant C_{\tilde{\beta},\varepsilon} h^{\min\{\tilde{\beta}\mathcal{R}e(\nu^*),\frac{3}{2}\}-\varepsilon}.$$

We recall that $\|\cdot\|_{r,\pm\frac{1}{2},\Gamma,*}$ denotes the norm on $H^r_\sigma(\mathbb{R}^+, \widetilde{H}^{\pm\frac{1}{2}}(\Gamma))^n$, as stated in Section 1.4, and that h is the diameter of the largest element in the graded mesh. Theorem 2.3.2 implies a corresponding result for the solutions of the single layer and hypersingular integral equations:

Corollary 2.3.3. *Let $r \geqslant 0$ and $\varepsilon > 0$.*

a) Let $\boldsymbol{\Psi}$ be the solution to the hypersingular integral equation (2.5) and $\boldsymbol{\Psi}^{\tilde{\beta}}_{h,\Delta t} \in \left(V_{\Delta t,q} \otimes X^0_{h,1}\right)^n$ the best approximation to $\boldsymbol{\Psi}$ in the norm of $H^r_\sigma(\mathbb{R}^+, \widetilde{H}^{\frac{1}{2}-s}(\Gamma))^n$ on a $\tilde{\beta}$-graded spatial mesh with $\Delta t \lesssim h_1$. Then

$$\|\boldsymbol{\Psi} - \boldsymbol{\Psi}^{\tilde{\beta}}_{h,\Delta t}\|_{r,\frac{1}{2}-s,\Gamma,*} \leqslant C_{\tilde{\beta},\varepsilon} h^{\min\{\tilde{\beta}(\mathcal{R}e(\nu^*)+s),\frac{3}{2}+s\}-\varepsilon},$$

where $s \in [0, \frac{1}{2}]$.

b) Let $\boldsymbol{\Phi}$ be the solution to the single layer integral equation (2.4) and $\boldsymbol{\Phi}^{\tilde{\beta}}_{h,\Delta t} \in \left(V_{\Delta t,q} \otimes X^{-1}_{h,0}\right)^n$ the best approximation to $\boldsymbol{\Phi}$ in the norm of $H^r_\sigma(\mathbb{R}^+; \widetilde{H}^{-\frac{1}{2}}(\Gamma))^n$ on a $\tilde{\beta}$-graded spatial mesh with $\Delta t \lesssim h_1$. Then

$$\|\boldsymbol{\Phi} - \boldsymbol{\Phi}^{\tilde{\beta}}_{h,\Delta t}\|_{r,-\frac{1}{2},\Gamma,*} \leqslant C_{\tilde{\beta},\varepsilon} h^{\min\{\tilde{\beta}\mathcal{R}e(\nu^*),\frac{3}{2}\}-\varepsilon}.$$

Indeed, the solutions to the integral equations are given by $\mathbf{\Psi} = \mathbf{u}_{|\Gamma}$ in terms of the solution $\mathbf{u}$ whose related traction satisfies the condition $\mathbf{p}_{|\Gamma} = \mathbf{g}_{\mathcal{N}}$, respectively $\mathbf{\Phi} = \mathbf{p}_{|\Gamma}$ in terms of the solution $\mathbf{u}$ which satisfies Dirichlet condition $\mathbf{u}_{|\Gamma} = \mathbf{g}_{\mathcal{D}}$.

The proof is an extension of the arguments that can be found for the wave equation in [38], where $\nu^* = \frac{1}{2}$. It relies on the following approximation properties in 1D [67].

Lemma 2.3.4. *For $a > 0$ and $s \in [-1, -a + \frac{1}{2})$ there holds with the piece-wise constant interpolant $\Pi_r^0 r^{-a}$ of r^{-a} on a $\tilde{\beta}$-graded mesh*

$$\|r^{-a} - \Pi_r^0 r^{-a}\|_{\widetilde{H}^s([0,1])} \lesssim h^{\min\{\tilde{\beta}(-a-s+\frac{1}{2}),1-s\}-\varepsilon}.$$

Proof of Theorem 2.3.2. (b), wedge singularity: Approximating $\mathbf{p}$ on a rectangular mesh $\overline{\Gamma} = \bigcup_j \overline{\Gamma}_j$ with $diam(\Gamma_j) < h$ for each j, we obtain with the triangle inequality and the approximation properties in the time variable:

$$\begin{aligned}
&\|\mathbf{p} - \Pi_x\Pi_t\mathbf{p}\|_{r,-\frac{1}{2},\Gamma,*} \\
&\leqslant \sum_k \|\mathbf{p} - \Pi_t\mathbf{p}\|_{r,-\frac{1}{2},(t_k,t_{k+1}]\times\Gamma,*} + \sum_{k,j} \|\Pi_t\mathbf{p} - \Pi_x\Pi_t\mathbf{p}\|_{r,-\frac{1}{2},(t_k,t_{k+1}]\times\Gamma_j,*} \\
&\leqslant \sum_k (\Delta t)^a \|\mathbf{p}\|_{r+a,-\frac{1}{2},(t_k,t_{k+1}]\times\Gamma} + \sum_{k,j} \|\Pi_t\mathbf{p} - \Pi_x\Pi_t\mathbf{p}\|_{r,-\frac{1}{2},(t_k,t_{k+1}]\times\Gamma_j,*},
\end{aligned}$$

where Π_t, Π_x are generic interpolants respectively in the temporal and in the spatial variables. Now, we use the decomposition (2.21) for $\mathbf{p}$ and consider the singular and regular parts separately. For the second sum, we use the singular expansion of each component,

$$\begin{aligned}
\|\Pi_t p_i - \Pi_x\Pi_t p_i\|_{r,-\frac{1}{2},(t_k,t_{k+1}]\times\Gamma_j,*} \leqslant\ & \|\Pi_t b_i(\phi,z,t) r^{\nu^*-1} - \Pi_t\Pi_x b_i(\phi,z,t) r^{\nu^*-1}\|_{r,-\frac{1}{2},(t_k,t_{k+1}]\times\Gamma_j,*} \\
&+ \|\Pi_t\phi_{i,0} - \Pi_x\Pi_t\phi_{i,0}\|_{r,-\frac{1}{2},(t_k,t_{k+1}]\times\Gamma_j,*} \ .
\end{aligned}$$

For the first term deduce from Lemma 8 in [38]

$$\begin{aligned}
&\|\Pi_t b_i(\phi,z,t) r^{\nu^*-1} - \Pi_t\Pi_x b_i(\phi,z,t) r^{\nu^*-1}\|_{r,-\frac{1}{2},(t_k,t_{k+1}]\times\Gamma_j,*} \\
&\leqslant \|\Pi_t b_i(\phi,z,t) - \Pi_t\Pi_z b_i(\phi,z,t)\|_{r,\varepsilon-\frac{1}{2}} \|r^{\nu^*-1}\|_{-\varepsilon} + \|\Pi_t\Pi_z b_i(\phi,z,t)\|_{r,0} \|r^{\nu^*-1} - \Pi_r r^{\nu^*-1}\|_{-\frac{1}{2}} \ .
\end{aligned}$$

From Lemma 2.3.4 we have $\|r^{\nu^*-1} - \Pi_r r^{\nu^*-1}\|_{-\frac{1}{2}} \lesssim h^{\min\{\tilde{\beta}\mathcal{R}e(\nu^*),\frac{3}{2}\}-\varepsilon}$ and $\|\Pi_t b_i(\phi,z,t) - \Pi_t\Pi_z b_i(\phi,z,t)\|_{r,\varepsilon-\frac{1}{2}} \lesssim h^{3/2-\varepsilon}\|\Pi_t b_i\|_{r,H^1}$, by the approximation properties in z.
Finally, with Lemma 3 and Lemma 10 of [38], in the anisotropic rectangle R with side-lengths h_1, h_2 in the directions x_1 and x_2, respectively:

$$\begin{aligned}
&\|\Pi_t\phi_{0,i} - \Pi_x\Pi_t\phi_{0,i}\|_{r,-\frac{1}{2},(t_k,t_{k+1}]\times R,*} \\
&\lesssim (\Delta t)^{\rho-r} \|\partial_t^\rho \phi_{0,i}\|_{L^2([t_k,t_{k+1}]\times R)} \\
&+ \max\{h_1,h_2,\Delta t\}^{\frac{1}{2}} \left(h_1 \|\phi_{0,i,x_1}\|_{L^2([t_k,t_{k+1}]\times R)} + h_2 \|\phi_{0,i,x_2}\|_{L^2([t_k,t_{k+1}]\times R)} \right) \ .
\end{aligned}$$

Note that the approximation error for the smooth term is of higher order. By summing over all rectangles Γ_j of the mesh of the screen and all components, we conclude that $\|\mathbf{p} - \Pi_x\Pi_t\mathbf{p}\|_{r,-\frac{1}{2},\Gamma,*} \lesssim h^{\min\{\tilde{\beta}\mathcal{R}e(\nu^*),\frac{3}{2}\}-\varepsilon}$ if $\Delta t \leqslant \min\{h_1,h_2\}$. □

For sake of symplicity Proof of part a) of Theorem 2.3.2 is not reported in this thesis but can be found in our article [7]. We moreover observe that the demonstration extends from rectangular to triangular boundary mesh elements following similar arguments as in [67]. In Figure 2.4 we observe the predicted rates for $\tilde{\beta} = 1, 2, 3$, when $\nu^* = \frac{1}{2}$, and in Figure 2.10 for $\nu^* = 0.5451$. .

2.3.2 Approximation by *hp* method

For the error estimates related to the *hp* discretization, we prove the following proposition, based again on the singular expansion of the traces, reported in Proposition 2.3.1, and taking into account the degree p set for their spatial approximation:

Theorem 2.3.5. *Let $r \geqslant 0$ and $\varepsilon > 0$.*

a) Let $\mathbf{u}$ be a strong solution to the elastodynamic equation (2.1) with $\boldsymbol{b} \equiv 0$ and with inhomogeneous Neumann boundary conditions $\mathbf{p}_{|\Gamma} = \mathbf{g}_{\mathcal{N}}$, with $\mathbf{g}_{\mathcal{N}}$ smooth. Further, let $\boldsymbol{\Psi}_{h,\Delta t} \in \left(V_{\Delta t,p} \otimes X^0_{h,p}\right)^n$ be the best approximation in the norm of $H^r_\sigma(\mathbb{R}^+; \widetilde{H}^{\frac{1}{2}-s}(\Gamma))^n$ to the Dirichlet trace $\mathbf{u}_{|\Gamma}$ on a quasiuniform spatial mesh with $\Delta t \lesssim h$. Then for $p = 1, 2, 3, \ldots$

$$\|\mathbf{u}_{|\Gamma} - \boldsymbol{\Psi}_{h,\Delta t}\|_{r,\frac{1}{2}-s,\Gamma,*} \lesssim \left(\frac{h}{p^2}\right)^{\mathcal{R}e(\nu^*)+s-\varepsilon} + \left(\frac{\Delta t}{p}\right)^{p-r} + \left(\frac{h}{p}\right)^{-\frac{1}{2}+s+\eta},$$

where $r \in [0, p)$ and $\mathbf{u}_0 \in H^p_\sigma(\mathbb{R}^+; \widetilde{H}^\eta(\Gamma))^n$ is the regular part of the singular expansion of $\mathbf{u}$.

b) Let $\mathbf{u}$ be a strong solution to the elastodynamic equation (2.1) with $\boldsymbol{b} \equiv 0$ and with inhomogeneous Dirichlet boundary conditions $\mathbf{u}_{|\Gamma} = \mathbf{g}_{\mathcal{D}}$, with $\mathbf{g}_{\mathcal{D}}$ smooth. Further, let $\boldsymbol{\Phi}_{h,\Delta t} \in \left(V_{\Delta t,p} \otimes X^{-1}_{h,p}\right)^n$ be the best approximation in the norm of $H^r_\sigma(\mathbb{R}^+; \widetilde{H}^{-\frac{1}{2}}(\Gamma))^n$ to the traction $\mathbf{p}_{|\Gamma}$ on a quasiuniform spatial mesh with $\Delta t \lesssim h$. Then for $p = 0, 1, 2, \ldots$

$$\|\mathbf{p}_{|\Gamma} - \boldsymbol{\Phi}_{h,\Delta t}\|_{r,-\frac{1}{2},\Gamma,*} \lesssim \left(\frac{h}{(p+1)^2}\right)^{\mathcal{R}e(\nu^*)-\varepsilon} + \left(\frac{\Delta t}{p+1}\right)^{p+1-r} + \left(\frac{h}{p+1}\right)^{\frac{1}{2}+\eta},$$

where $r \in [0, p+1)$ and $\boldsymbol{\phi}_0 \in H^{p+1}_\sigma(\mathbb{R}^+; \widetilde{H}^\eta(\Gamma))^n$ is the regular part of the singular expansion of the traction $\mathbf{p}$.

Theorem 2.3.5 implies a corresponding result for the solutions of the single layer and hypersingular integral equations (2.16) and (2.17):

Corollary 2.3.6. *Let $r \geqslant 0$ and $\varepsilon > 0$. a) Let $\boldsymbol{\Psi}$ be the solution to the hypersingular integral equation (2.5) and $\boldsymbol{\Psi}_{h,\Delta t} \in \left(V_{\Delta t,p} \otimes X^0_{h,p}\right)^n$ the best approximation in the norm of $H^r_\sigma(\mathbb{R}^+; \widetilde{H}^{\frac{1}{2}-s}(\Gamma))^n$ to $\boldsymbol{\Psi}$ on a quasiuniform spatial mesh with $\Delta t \lesssim h$. Then for $p = 1, 2, 3, \ldots$*

$$\|\boldsymbol{\Psi} - \boldsymbol{\Psi}_{h,\Delta t}\|_{r,\frac{1}{2}-s,\Gamma,*} \lesssim \left(\frac{h}{p^2}\right)^{\mathcal{R}e(\nu^*)+s-\varepsilon} + \left(\frac{\Delta t}{p}\right)^{p+1-r} + \left(\frac{h}{p}\right)^{-\frac{1}{2}+s+\eta},$$

where $r \in [0,p)$, $s \in [0,\frac{1}{2}]$ *and* $\mathbf{u}_0 \in H^{p+1}_\sigma(\mathbb{R}^+;\widetilde{H}^\eta(\Gamma))^n$ *is the regular part of the singular expansion of* $\boldsymbol{\Psi} = \mathbf{u}_{|\boldsymbol{\Gamma}}$.

b) Let $\boldsymbol{\Phi}$ *be the solution to the single layer integral equation* (2.4) *and* $\boldsymbol{\Phi}_{h,\Delta t} \in \left(V_{\Delta t,p} \otimes X^{-1}_{h,p}\right)^n$ *the best approximation in the norm of* $H^r_\sigma(\mathbb{R}^+;\widetilde{H}^{-\frac{1}{2}}(\Gamma))^n$ *to* $\boldsymbol{\Phi}$ *on a quasiuniform spatial mesh with* $\Delta t \lesssim h$. *Then for* $p = 0,1,2,\ldots$

$$\|\boldsymbol{\Phi} - \boldsymbol{\Phi}_{h,\Delta t}\|_{r,-\frac{1}{2},\Gamma,*} \lesssim \left(\frac{h}{(p+1)^2}\right)^{\mathcal{R}e(\nu^*)-\varepsilon} + \left(\frac{\Delta t}{p+1}\right)^{p+1-r} + \left(\frac{h}{p+1}\right)^{\frac{1}{2}+\eta},$$

where $r \in [0,p+1)$ *and* $\boldsymbol{\phi}_0 \in H^{p+1}_\sigma(\mathbb{R}^+;\widetilde{H}^\eta(\Gamma))^n$ *is the regular part of the singular expansion of* $\boldsymbol{\Phi} = \mathbf{p}_{|\boldsymbol{\Gamma}}$.

For the proof, we recall the following lemma (see [22], Theorem 3.1):

Lemma 2.3.7. *For* $\varepsilon > 0$, $a < 1$ *and* $s \in [-1, \min\{-a+\frac{1}{2}, 0\})$ *there holds with the piece-wise polynomial interpolant of degree* p, $\Pi^p_r r^{-a}$, *of* r^{-a}

$$\|r^{-a} - \Pi^p_r r^{-a}\|_{s,[0,1],*} \lesssim \left(\frac{h}{(p+1)^2}\right)^{-a-s+\frac{1}{2}-\varepsilon}.$$

Proof of Theorem 2.3.5. (b), wedge singularity: We choose $\boldsymbol{\Phi}_{h,\Delta t} = \Pi^p_x \Pi^p_t \mathbf{p}$. Using the decomposition (2.21) for $\mathbf{p}$, we can separate the singular and regular parts on the rectangular mesh:

$$\begin{aligned}
&\|p_i - \Pi^p_x\Pi^p_t p_i\|_{r,-\frac{1}{2},\Gamma,*} \leqslant \|b_i(\phi,z,t)r^{\nu^*-1} - \Pi^p_t\Pi^p_x b_i(\phi,z,t)r^{\nu^*-1}\|_{r,-\frac{1}{2},\Gamma,*} + \|\phi_{i,0} - \Pi^p_t\Pi^p_x\phi_{i,0}\|_{r,-\frac{1}{2},\Gamma,*}\\
&\leqslant \|b_i(\phi,z,t)r^{\nu^*-1} - \Pi^p_t b_i(\phi,z,t)r^{\nu^*-1}\|_{r,-\frac{1}{2},\Gamma,*} + \|\Pi^p_t b_i(\phi,z,t)r^{\nu^*-1} - \Pi^p_t\Pi^p_x b_i(\phi,z,t)r^{\nu^*-1}\|_{r,-\frac{1}{2},\Gamma,*}\\
&\qquad + \|\phi_{i,0} - \Pi^p_t\Pi^p_x\phi_{i,0}\|_{r,-\frac{1}{2},\Gamma,*}\\
&\leqslant \|b_i(\phi,z,t) - \Pi^p_t b_i(\phi,z,t)\|_{r,\epsilon-\frac{1}{2}}\|r^{\nu^*-1}\|_{-\varepsilon,I,*} + \|\Pi^p_t b_i(\phi,z,t)r^{\nu^*-1} - \Pi^p_t\Pi^p_z b_i(\phi,z,t)r^{\nu^*-1}\|_{r,-\frac{1}{2},\Gamma,*}\\
&\qquad + \|\Pi^p_t\Pi^p_z b_i(\phi,z,t)r^{\nu^*-1} - \Pi^p_t\Pi^p_z b_i(\phi,z,t)\Pi^p_y r^{\nu^*-1}\|_{r,-\frac{1}{2},\Gamma,*} + \|\phi_{i,0} - \Pi^p_t\Pi^p_x\phi_{i,0}\|_{r,-\frac{1}{2},\Gamma,*}.
\end{aligned}$$

In the second term we used $\Pi^p_x = \Pi^p_z\Pi^p_r$. The first term was estimated using Lemma 8 of [38], and the result is now bounded by

$$\|b_i(\phi,z,t) - \Pi^p_t b_i(\phi,z,t)\|_{r,\epsilon-\frac{1}{2}} \lesssim \left(\frac{\Delta t}{p+1}\right)^{p+1-r}\|b_i(\phi,z,t)\|_{p+1,\epsilon-\frac{1}{2}}.$$

Using Lemma 8 of [38], we obtain for the second and third terms:

$$\begin{aligned}
&\|\Pi^p_t b_i(\phi,z,t)r^{\nu^*-1} - \Pi^p_t\Pi^p_z b_i(\phi,z,t)r^{\nu^*-1}\|_{r,-\frac{1}{2},\Gamma,*}\\
&+ \|\Pi^p_t\Pi^p_z b_i(\phi,z,t)r^{\nu^*-1} - \Pi^p_t\Pi^p_z b_i(\phi,z,t)\Pi^p_y r^{\nu^*-1}\|_{r,-\frac{1}{2},\Gamma,*}\\
&\lesssim \|\Pi^p_t b_i(\phi,z,t) - \Pi^p_t\Pi^p_z b_i(\phi,z,t)\|_{r,\varepsilon-\frac{1}{2}}\|r^{\nu^*-1}\|_{-\varepsilon,I,*}\\
&+ \|\Pi^p_t\Pi^p_z b_i(\phi,z,t)\|_{r,0}\|r^{\nu^*-1} - \Pi^p_r r^{\nu^*-1}\|_{-\frac{1}{2},I,*}.
\end{aligned}$$

We finally note that

$$\|r^{\nu^*-1} - \Pi_r^p r^{\nu^*-1}\|_{\frac{1}{2},I,*} \lesssim \left(\frac{h}{(p+1)^2}\right)^{\mathcal{R}e(\nu^*)-\varepsilon}$$

from Lemma 2.3.7, as well as

$$\|\Pi_t^p b_i(\phi,z,t) - \Pi_t^p \Pi_z^p b_i(\phi,z,t)\|_{r,\varepsilon-\frac{1}{2}} \lesssim \left(\frac{h}{p+1}\right)^{\frac{1}{2}+k-\epsilon} \|b_i(\phi,z,t)\|_{r,k} \ .$$

When the regular part $\boldsymbol{\phi}_0$ in (2.21) is H^η in space, we obtain from the approximation properties [41]:

$$\|\phi_{i,0} - \Pi_t^p \Pi_x^p \phi_{i,0}\|_{r,-\frac{1}{2},\Gamma,*} \lesssim_\sigma \left(\left(\frac{\Delta t}{p+1}\right)^{p+1-r} + \left(\frac{h}{p+1}\right)^{1/2+\eta} \right) \|\phi_{i,0}\|_{p+1,\eta,\Gamma} \ .$$

Combining these estimates, the asserted estimate follows for $\Delta t \lesssim h$

$$\|\mathbf{p} - \Pi_x^p \Pi_t^p \mathbf{p}\|_{r,-\frac{1}{2},\Gamma,*} \lesssim \left(\frac{h}{(p+1)^2}\right)^{\mathcal{R}e(\nu^*)-\varepsilon} + \left(\left(\frac{\Delta t}{p+1}\right)^{p+1-r} + \left(\frac{h}{p+1}\right)^{1/2+\eta} \right) \|\phi_{i,0}\|_{p+1,\eta,\Gamma} \ .$$

The approximation of the Dirichlet trace $\mathbf{u}_{|\Gamma}$ to prove part a) follows the above arguments. □

A similar estimate is obtained for $V_{\Delta t,1}$, with $(\Delta t)^p$ replaced by Δt.

Remark. In the following tests we will estimate empirically, for the 2D case, the errors reported in Corollaries 2.3.3 and 2.3.3, in norms $\|\cdot\|_{r,-\frac{1}{2},\Gamma,*}$ and $\|\cdot\|_{r,\frac{1}{2},\Gamma,*}$, by the use of the following weaker measures for the unknowns $\boldsymbol{\Phi}_{h,\Delta t}$ and $\boldsymbol{\Psi}_{h,\Delta t}$ of the weak BIEs (2.16) and (2.17):

$$\|\boldsymbol{\Phi}_{h,\Delta t}\|^2_{-1/2,\mathcal{E}} = (\boldsymbol{\alpha}^{\mathbf{p}})^\top \mathbb{E}_V \boldsymbol{\alpha}^{\mathbf{p}}, \quad \|\boldsymbol{\Psi}_{h,\Delta t}\|^2_{1/2,\mathcal{E}} = (\boldsymbol{\alpha}^{\mathbf{u}})^\top \mathbb{E}_D \boldsymbol{\alpha}^{\mathbf{u}}. \tag{2.22}$$

The introduced energetic norms depend on the discretization of the single layer and the hypersingular operators V and D and they are weaker or comparable, respectively, to the square of the norms in the spaces $H^0_\sigma\left(\mathbf{R}^+, H^{-1/2}(\Gamma)\right)^2$ and $H^0_\sigma\left(\mathbf{R}^+, H^{1/2}(\Gamma)\right)^2$. In particular, the squared errors committed approximating the exact solutions $\boldsymbol{\Phi}$, $\boldsymbol{\Psi}$ of the weak problems (2.4),(2.5) with the discrete solutions $\boldsymbol{\Phi}_{h,\Delta t}$,$\boldsymbol{\Psi}_{h,\Delta t}$ can be calculated as follows

$$\begin{aligned} Err^2_{-1/2,\mathcal{E}} &= \|\boldsymbol{\Phi}_{h,\Delta t}\|^2_{-1/2,\mathcal{E}} - \|\boldsymbol{\Phi}\|^2_{-1/2,\mathcal{E}}, \\ Err^2_{1/2,\mathcal{E}} &= \|\boldsymbol{\Psi}_{h,\Delta t}\|^2_{1/2,\mathcal{E}} - \|\boldsymbol{\Psi}\|^2_{1/2,\mathcal{E}}. \end{aligned} \tag{2.23}$$

In the numerical section we will confirm what theoretically stated in the previous theorems considering the energy errors (2.23), where the norms of the exact solutions $\|\boldsymbol{\Phi}\|^2_{-1/2,\mathcal{E}}$ and $\|\boldsymbol{\Psi}\|^2_{1/2,\mathcal{E}}$ are empirically extrapolated as indicated in [30].

2.4 Numerical results

The numerical experiments in this section consider h, p and hp methods for the resolution by energetic BEM of the homogeneous soft scattering problem (2.1)-(2.2) (Sections 2.4.1-2.4.2) and the homogeneous hard scattering problem (2.1)-(2.3) (Section 2.4.3) in the 2D case. They illustrate the singular behavior of the solution near the crack tips and the corners of the obstacle, confirming the convergence rates theoretically expected in Section 2.3.

Unless otherwise stated, for the h version on uniform or $\tilde{\beta}$-graded meshes, piece-wise constant basis functions in space and time are chosen to approximate the solution of the Dirichlet energetic weak problem (2.16). Piece-wise linear functions are instead used in case of Neumann weak problem (2.17) for the spatial and the temporal discretization in case of uniform or $\tilde{\beta}$-graded meshes set on Γ. The p and hp versions are implemented with higher polynomial degrees in space, up to $p = 7$. The Lamé parameters and the mass density, where it is not otherwise specified, are set to be $\lambda = 2$, $\mu = 1$ and $\varrho = 1$ for all the results presented in this section.

Remark. For sake of simplicity, all the numerical results related to Dirichlet problems are computed without assigning the datum $\mathbf{g}_{\mathcal{D}}$ on $\Gamma \times (0, T]$ to compute the term $\widetilde{\mathbf{g}}_{\mathcal{D}} = (K + c_\Gamma)\mathbf{g}_{\mathcal{D}}$ in (2.16), but prescribing directly a function defined on $\Gamma \times (0, T]$ to compute the term $\widetilde{\mathbf{g}}_{\mathcal{D}}$. Similar consideration is done for the implementation of the Galerkin weak form (2.17) in the resolution of Neumann problems.

2.4.1 Soft scattering problems on flat obstacle

Experiment 1. Here we consider the discrete weakly singular integral equation (2.16) on a flat obstacle $\Gamma = \{(x, 0) \in \mathbf{R} : x \in [-0.5, 0.5]\}$ up to time $T = 1$. The boundary datum imposed is $\widetilde{g}_{\mathcal{D},i}(x, t) = H[t]f(t)x^4$, $i = 1, 2$, where the function f is the one already introduced in (1.97). In Figure 2.3, the horizontal component of the discrete approximation

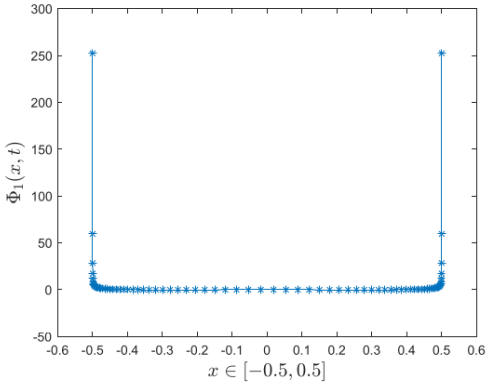

Figure 2.3: Approximation of the horizontal component of $\mathbf{\Phi}$, calculated on the obstacle Γ at the time instant $T = 1$. This plot is obtained imposing on Γ a 3-graded mesh with 81 nodes and $\Delta t = 0.00625$.

of solution $\mathbf{\Phi}$ of (2.4), by energetic BEM, is represented on the obstacle Γ at the final

instant: as we can observe from the plot, the behavior of the solution is singular near the crack tips. Tables 2.1, 2.2 and 2.3 contain the values of $\|\mathbf{\Phi}_{h,\Delta t}\|^2_{-1/2,\mathcal{E}}$, namely the squared energy norm of the Galerkin solution as defined in (2.22), in relation with the increasing number of spatial and temporal degrees of freedom (DOFs). For simplicity, in the following tables the number of DOFs is indicated only for one component of the vector-valued solution. The values reported in 2.1 are obtained by the application of a p version in space: the boundary is uniformly discretized with segments of length $h = 0.1$, while the degree p of the space basis function is increased. For $p = 1$ we set the time step $\Delta t = 0.025$ and we halve it whenever p increases. The energy values reported in Table

Table 2.1: Squared energy norm of the approximated solution for $T = 1$ (p version)

degree p	DOF	Δt	$\|\mathbf{\Phi}_{h,\Delta t}\|^2_{-1/2,\mathcal{E}}$
1	11	$2.50000 \cdot 10^{-2}$	$3.4108 \cdot 10^{-2}$
2	21	$1.25000 \cdot 10^{-2}$	$3.6257 \cdot 10^{-2}$
3	31	$6.25000 \cdot 10^{-3}$	$3.7012 \cdot 10^{-2}$
4	41	$3.12500 \cdot 10^{-3}$	$3.7338 \cdot 10^{-2}$
5	51	$1.56250 \cdot 10^{-3}$	$3.7511 \cdot 10^{-2}$
6	61	$7.81250 \cdot 10^{-4}$	$3.7615 \cdot 10^{-2}$
7	71	$3.90625 \cdot 10^{-4}$	$3.7684 \cdot 10^{-2}$

2.2 refer to the solution of the problem with the h version: we fix an algebraically graded mesh on the arc as in (2.18), for given grading parameter $\tilde{\beta} = 1,\ 2,\ 3$ and number of mesh points $2N + 1$.

Table 2.2: Squared energy norm of the approximated solution for $T = 1$ (h version with algebraically graded mesh)

Δt	DOF	$\|\mathbf{\Phi}_{h,\Delta t}\|^2_{-1/2,\mathcal{E}}$, $\tilde{\beta} = 1$	$\|\mathbf{\Phi}_{h,\Delta t}\|^2_{-1/2,\mathcal{E}}$, $\tilde{\beta} = 2$	$\|\mathbf{\Phi}_{h,\Delta t}\|^2_{-1/2,\mathcal{E}}$, $\tilde{\beta} = 3$
$1.2500 \cdot 10^{-2}$	10	$3.0143 \cdot 10^{-2}$	$3.6212 \cdot 10^{-2}$	$3.7315 \cdot 10^{-2}$
$6.2500 \cdot 10^{-3}$	20	$3.3906 \cdot 10^{-2}$	$3.7501 \cdot 10^{-2}$	$3.7835 \cdot 10^{-2}$
$3.1250 \cdot 10^{-3}$	40	$3.5933 \cdot 10^{-2}$	$3.7813 \cdot 10^{-2}$	$3.7903 \cdot 10^{-2}$
$1.5625 \cdot 10^{-3}$	80	$3.6943 \cdot 10^{-2}$	$3.7890 \cdot 10^{-2}$	$3.7914 \cdot 10^{-2}$

In Table 2.3 the discretization method used is the *hp* version. On Γ, the geometrically graded points, with parameter $\sigma \in (0, 1/2]$, are defined distinguishing the $N+1$ nodes $x_{L,j}$ in the left interval $[-1/2, 0]$ and the N nodes $x_{R,j}$ in the right interval $(0, 1/2]$:

$$\begin{cases} x_{0,L} = -\frac{1}{2},\ x_{L,j} = \frac{1}{2}\left(\sigma^{N+1-j} - 1\right) & j = 1, \dots, N+1 \\ x_{R,N+1} = \frac{1}{2},\ x_{R,j} = \frac{1}{2}\left(1 - \sigma^{j}\right), & j = 1, \dots, N \end{cases} . \tag{2.24}$$

In particular, the two geometrically graded meshes of type (2.24) are characterized by the values $\sigma = 0.2,\ 0.5$ and, for ease of programming, at each refinement of the mesh the degree p increases uniformly on all the space elements. The parameter L_σ in the table represents the length of the smallest segment of the mesh.

Table 2.3: Squared energy norm of the approximated solution for $T = 1$ (*hp* version geometrically graded)

p	$L_{0.5}$	$L_{0.2}$	DOF	Δt	$\|\mathbf{\Phi}_{h,\Delta t}\|^2_{-1/2,\mathcal{E}}$ $\sigma = 0.5$	$\|\mathbf{\Phi}_{h,\Delta t}\|^2_{-1/2,\mathcal{E}}$ $\sigma = 0.2$
0	$5.00000 \cdot 10^{-1}$	$5.0 \cdot 10^{-1}$	2	$2.500000 \cdot 10^{-1}$	$4.0730 \cdot 10^{-3}$	$4.0730 \cdot 10^{-3}$
1	$2.50000 \cdot 10^{-1}$	$1.0 \cdot 10^{-1}$	5	$1.250000 \cdot 10^{-1}$	$2.7847 \cdot 10^{-2}$	$3.4521 \cdot 10^{-2}$
2	$1.25000 \cdot 10^{-1}$	$2.0 \cdot 10^{-2}$	13	$6.250000 \cdot 10^{-2}$	$3.2960 \cdot 10^{-2}$	$3.4581 \cdot 10^{-2}$
3	$6.25000 \cdot 10^{-2}$	$4.0 \cdot 10^{-3}$	25	$3.125000 \cdot 10^{-2}$	$3.6745 \cdot 10^{-2}$	$3.7256 \cdot 10^{-2}$
4	$3.12500 \cdot 10^{-2}$	$8.0 \cdot 10^{-4}$	41	$1.562500 \cdot 10^{-2}$	$3.7618 \cdot 10^{-2}$	$3.7783 \cdot 10^{-2}$
5	$1.56250 \cdot 10^{-2}$	$1.6 \cdot 10^{-4}$	61	$7.812500 \cdot 10^{-3}$	$3.7828 \cdot 10^{-2}$	$3.7890 \cdot 10^{-2}$
6	$7.81250 \cdot 10^{-3}$	$3.2 \cdot 10^{-5}$	85	$3.906250 \cdot 10^{-3}$	$3.7888 \cdot 10^{-2}$	$3.7911 \cdot 10^{-2}$
7	$3.90625 \cdot 10^{-3}$	$6.4 \cdot 10^{-6}$	113	$1.953125 \cdot 10^{-3}$	$3.7906 \cdot 10^{-2}$	$3.7915 \cdot 10^{-2}$

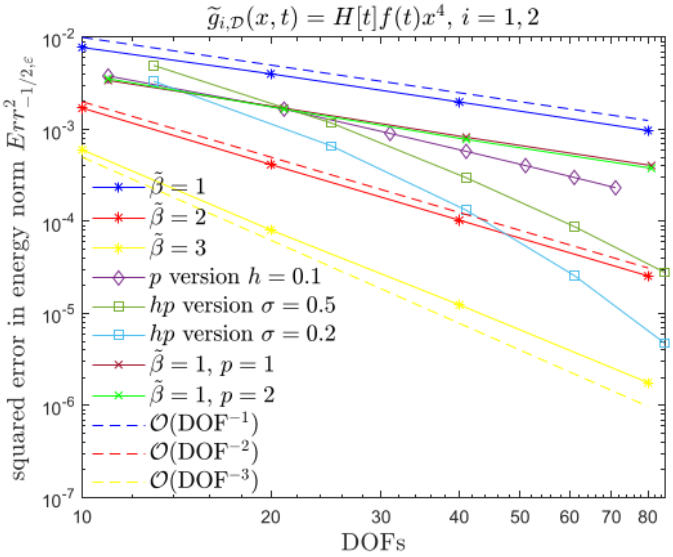

Figure 2.4: Squared error of the energy norm for various discretization methods.

The squared energy value $\|\mathbf{\Phi}_{h,\Delta t}\|^2_{-1/2,\mathcal{E}}$ presented in the tables increases towards the squared norm $\|\mathbf{\Phi}\|^2_{-1/2,\mathcal{E}}$, which is empirically extrapolated, with the augmentation of the DOFs for the tested discretization methods: as shown in Figure 2.4, where the slope of the squared error in energy norm $Err^2_{-1/2,\mathcal{E}}$, defined in (2.23), is illustrated for the various methods. We observe that the decay of the error follows a straight line in the logarithmic plots for both the p version on uniform mesh and the h version with $\tilde{\beta} = 1$, corresponding to algebraic convergence with rate 2 (p version), respectively 1 (h version) in terms of DOFs. This means that the error tends to 0 like p^{-1}, respectively $h^{1/2}$. This convergence rate is expected from Corollary 2.3.6. Indeed, by Proposition 1.4.1 the energy $\|\mathbf{\Phi}_{h,\Delta t}\|^2_{-1/2,\mathcal{E}}$ is bounded by the Sobolev norm considered in Corollary 2.3.6. Analogous results are obtained for the h version with polynomial degrees $p = 1, 2$ in space. On algebraically graded meshes with $\tilde{\beta} = 2$ and 3 the squared error $Err^2_{-1/2,\mathcal{E}}$ similarly decays along a straight line, but with slope $-\tilde{\beta}$ with the increasing of DOFs. In particular, the BEM on the graded

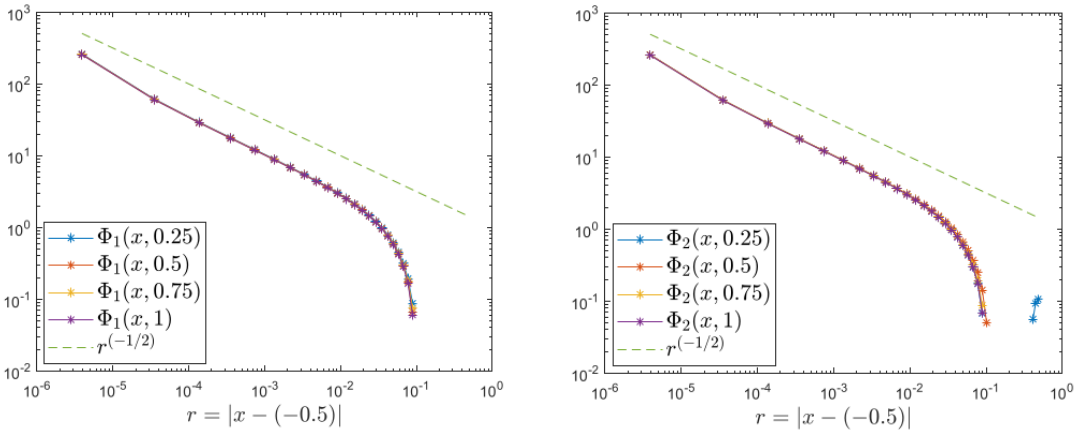

Figure 2.5: Asymptotic behaviour towards the left end of Γ

mesh (2.18) with $\tilde{\beta} = 3$, recovers the optimal convergence order $h^{3/2}$ expected in the energy norm for smooth solutions, as in Corollary 2.3.3. The fastest convergence in Figure 2.4 is obtained by the *hp* version, for which the squared error $Err^2_{-1/2,\mathcal{E}}$ decays faster than a straight line for both $\sigma = 0.2$ and 0.5. The graph of the squared error indicates exponential decay. Convergence is faster for $\sigma = 0.2$, which is close to the theoretically optimal $\sigma \simeq 0.17$, since the nodes in this case are more densely clustered near the endpoints of Γ than for $\sigma = 0.5$.

The discretization methods illustrated above are useful to better catch the singular behavior of the solution at the tips. In particular this trend is illustrated in Figure 2.5, where the horizontal and the vertical components of the approximated $\mathbf{\Phi}$ are represented with respect to the distance r towards the left end of the segment $(-0.5, 0)$ for various time instants: one observes that the singular behavior is independent of time, and the components increase as $\mathcal{O}(r^{-1/2})$ for $r \to 0$. This confirms the discussion in Section 2.1.1. To be specific, the solution in this figure is obtained from the h version on a 3-graded mesh with 81 nodes on Γ. We moreover remark that, in the left plot of Figure 2.5, the points corresponding to the horizontal component Φ_2, calculated at time $t = 0.25$, still describe the transient phase of the dynamics. This means that the behaviour of Φ_2, far from the end-points of Γ, can be subject to perturbations that lead to the positive values of the vertical component near the centre of the crack, indicated in particular by the dots in blue corresponding to the abscissas r in the range $[10^{-1}, 10^0]$.

Experiment 2. Similar results as in Example 1 are obtained also for other boundary data on the same flat obstacle $\Gamma = \{(x, 0) \in \mathbf{R} \,:\, x \in [-0.5, 0.5]\}$. We here set $\widetilde{g}_{\mathcal{D},i}(x, t) = H[t]f(t)x$, $i = 1, 2$, where the function f has the temporal profile defined in (1.97). The solution of the weak problem (2.4) is again singular at the end points of the segment and, as observed in the previous experiment, the components of $\mathbf{\Phi}$ increase as $\mathcal{O}(r^{-1/2})$ when the distance r tends to zero (see Figure 2.6).
We again study the decay of the squared error in energy norm for this new Dirichlet

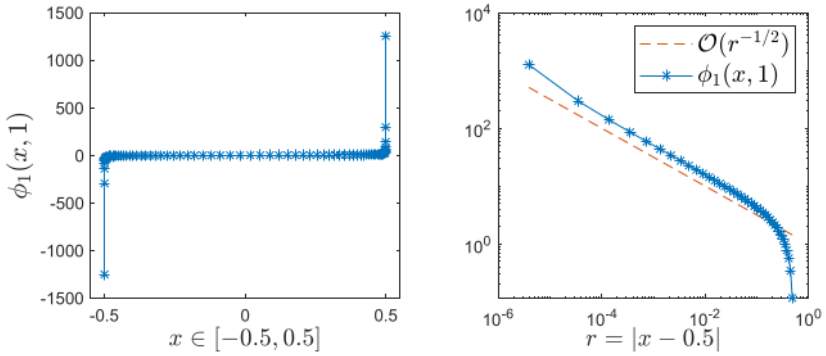

Figure 2.6: Behaviour of the horizontal component Φ_1 on Γ and w.r.t the distance towards the right endpoint at $T = 1$. Both plots are obtained imposing on Γ an algebraically 3-graded mesh of 81 mesh points.

condition, leading to similar considerations for the rate of convergence of the different discretization methods. The spatial and temporal discretization parameters for the h, p and hp version are chosen as in the previous experiment, and all the results are collected in Figure 2.7. The squared error $Err^2_{-1/2,\mathcal{E}}$ for the h version is $\mathcal{O}\left(h^{\tilde{\beta}}\right)$ on the algebraically $\tilde{\beta}$-graded mesh, as in Corollary 2.3.3. The corresponding result for the p version is $\mathcal{O}\left(p^{-2}\right)$, in agreement with Corollary 2.3.6. The convergence achieved by the hp version on a geometrically graded mesh is faster than the one obtained with the algebraic mesh.

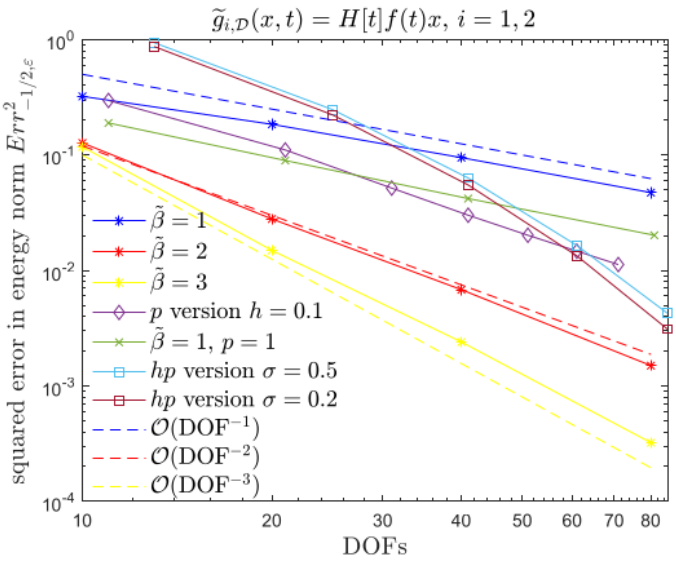

Figure 2.7: Squared error of the energy norm for various discretization methods

2.4.2 Soft scattering problems on polygonal obstacles

In the following we consider the weakly singular integral equation (2.4) on the different obstacle geometries Γ represented in Figure 2.8(b). From Section 2.1.1 we know that the

solution $\mathbf{u}$ calculated closely to a corner point of Γ locally behaves like a power of the distance r to the corner:

$$u_i \approx C_{i,\omega_j}(t) r^{\nu^*(\omega_j)}, \quad r \to 0, \quad i = 1, 2,\ j = ext, int,$$

where ω_{ext} or ω_{int} is the exterior and, respectively, the interior corner angle in which we decide to evaluate the displacement, while the exponent $\nu^*(\omega_j)$ is the smallest solution of the equation

$$\sin^2(\omega_j \nu^*) = \left(k^{-1}\nu^* \sin \omega_j\right)^2, \tag{2.25}$$

with positive real part, where $k = 3 - 2\lambda/(\lambda + \mu)$. The prefactor $C_{i,\omega_j}(t)$ is a smooth function in t, independent of r, so the leading singular behavior does not change with time. Since the solution $\mathbf{\Phi}$ of the boundary integral equation (2.4) depends on the trace of the traction $\mathbf{p}$ on the obstacle, its asymptotic behavior depends on the solution on both the amplitudes of the interior and exterior angle. It can be written as

$$\Phi_i \approx \widetilde{C}_{i,\omega_{ext}}(t) r^{\nu^*(\omega_{ext})-1} - \widetilde{C}_{i,\omega_{int}}(t) r^{\nu^*(\omega_{int})-1} \approx \overline{C}_i(t) r^{\nu^*-1},\ r \to 0,$$

with $\nu^* = \min\{\nu^*(\omega_{ext}), \nu^*(\omega_{int})\}$.
For Lamé parameters $\lambda = 2$, $\mu = 1$ and mass density $\varrho = 1$, Figure 2.8(a) shows the interior and exterior exponents, $\nu^*(\omega_{int})$ and $\nu^*(\omega_{ext}) = \nu^*(2\pi - \omega_{int})$, as a function of ω_{int}. Their minimum gives the exponent ν^* of the solution $\mathbf{\Phi}$. Red crosses indicate the exponents ν^* corresponding to the red corners of the polygons depicted on the right of Figure 2.8(b), for interior angles $\frac{7\pi}{24}$ ($\nu^* = 0.5372$), $\frac{\pi}{3}$ ($\nu^* = 0.5451$), $\frac{3\pi}{8}$ ($\nu^* = 0.5542$) and $\frac{3\pi}{5}$ ($\nu^* = 0.6306$).

Experiment 3. We consider the Galerkin solution of the weakly singular integral equation (2.16) on the polygons represented in Figure 2.8(b) up to time $T = 1$. In all cases the right-hand-side imposed is $\widetilde{g}_{\mathcal{D},1}(\mathbf{x}, t) = 0$, $\widetilde{g}_{\mathcal{D},2}(\mathbf{x}, t) = H[t] f(t) 100 |x|^{9.5}$.
The mesh on each side of polygons Γ_i, $i = 1, \ldots, 4$, is algebraically graded towards the corners following (2.18), for grading parameter $\tilde{\beta} = 3$. The polygons Γ_1 and Γ_4, which are both equilateral, are discretized with 80 segments per side, while for Γ_2 and Γ_3 we use 80 segments on the two sides which are of equal length and 75 and 87 segments on the basis, respectively, in order to have mesh elements with equal size that delimit the basis corners of these isosceles triangles. The time step is chosen as $\Delta t = 0.00625$ for all the next experiments of this subsection.
In Figure 2.9, for each geometry the Euclidean norm of $\mathbf{\Phi}$, approximated by energetic BEM, is plotted with respect to the distance r towards the corner indicated in Figure 2.8. We observe that the solution follows the expected behavior $\mathcal{O}(r^{-(1-\nu^*)})$. In particular, the asymptotic behavior for acute corners leads to stronger singularities ($1 - \nu^* \approx 0.5$) than for the obtuse angle of the pentagon ($1 - \nu^* \approx 0.37$), confirming what theoretically stated in Section 2.1.1.

We finally consider the convergence in energy norm on the polygonal obstacles. In particular, we examine the equilateral triangle Γ_1, discretized by meaning of different h versions with grading parameters $\tilde{b} = 1, 2, 3$. In Table 2.4 the value of the squared energy norm $\|\mathbf{\Phi}_{h,\Delta t}\|^2_{-1/2,\mathcal{E}}$ is reported for each level of the space discretization. The squared energy norm tends to a benchmark value with increasing number of DOFs (also in this case the

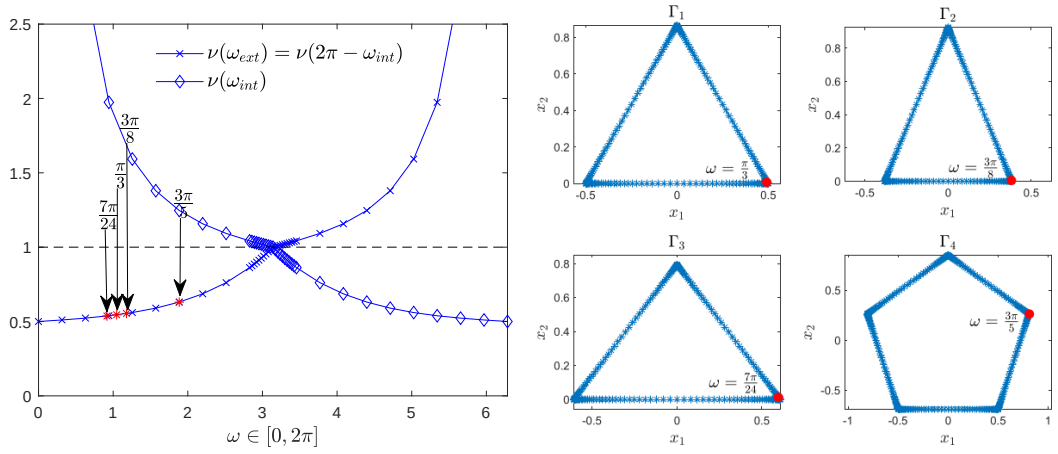

(a) (b)

Figure 2.8: Expected exponent with dependence on ω_{int} and on its complementary ($k = 5/3$) , figure (a). Pictures of the four considered polygonal boundaries, all discretized by 3-graded meshes set on each side, figure (b)

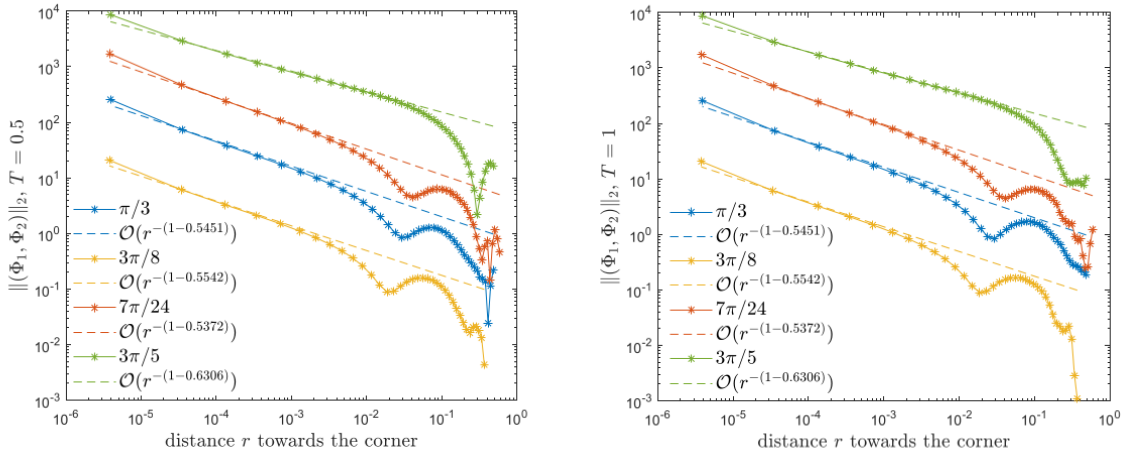

Figure 2.9: Asymptotic behavior towards the vertices

Table 2.4: Squared energy norm of the approximated solution for $T = 1$

Δt	DOF	$\|\mathbf{\Phi}_{h,\Delta t}\|^2_{-1/2,\mathcal{E}}$, $\tilde{\beta} = 1$	$\|\mathbf{\Phi}_{h,\Delta t}\|^2_{-1/2,\mathcal{E}}$, $\tilde{\beta} = 2$	$\|\mathbf{\Phi}_{h,\Delta t}\|^2_{-1/2,\mathcal{E}}$, $\tilde{\beta} = 3$
$5.00 \cdot 10^{-2}$	30	$5.7394 \cdot 10^{-2}$	$7.4875 \cdot 10^{-2}$	$7.6829 \cdot 10^{-2}$
$2.50 \cdot 10^{-2}$	60	$6.8490 \cdot 10^{-2}$	$7.6828 \cdot 10^{-2}$	$7.7460 \cdot 10^{-2}$
$1.25 \cdot 10^{-2}$	120	$7.3821 \cdot 10^{-2}$	$7.7448 \cdot 10^{-2}$	$7.7566 \cdot 10^{-2}$
$6.25 \cdot 10^{-3}$	240	$7.5989 \cdot 10^{-2}$	$7.7558 \cdot 10^{-2}$	$7.7582 \cdot 10^{-2}$

number refers to one component of the vector solution), and the related squared error $Err^2_{-1/2,\mathcal{E}}$ is shown in Figure 2.10. The decay of the squared error in a log scale plot is

linear, corresponding to $\mathcal{O}(\mathrm{DOF}^{-2\nu^*\tilde{\beta}})$, proving how the amplitude of the corner influences the decay of the error.

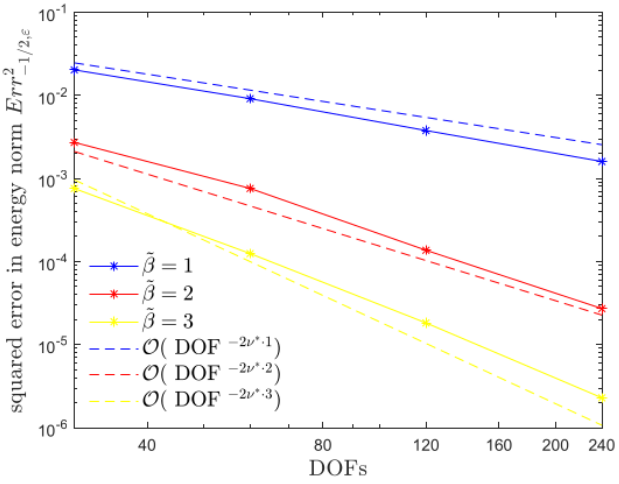

Figure 2.10: Squared error of the energy norm with h version on Γ_1, $\tilde{\beta}$-graded mesh

Experiment 4. In this example we show numerically that the singular behavior at the corners and the decay of the energy error do not depend on the boundary data imposed at the obstacle. We specifically consider the triangular obstacle Γ_2 in Figure 2.8(b). The approximated solution $\boldsymbol{\Phi}$ is calculated for a right-hand-side with null horizontal component $\widetilde{g}_{\mathcal{D},1}(\mathbf{x},t) = 0$ and different vertical components $\widetilde{g}_{\mathcal{D},2}(\mathbf{x},t) = H[t]f(t)$, $\widetilde{g}_{\mathcal{D},2}(\mathbf{x},t) = H[t]f(t)x^4$ and $\widetilde{g}_{\mathcal{D},2}(\mathbf{x},t) = 100H[t]f(t)|x|^{9.5}$. In Figure 2.11(a), we consider

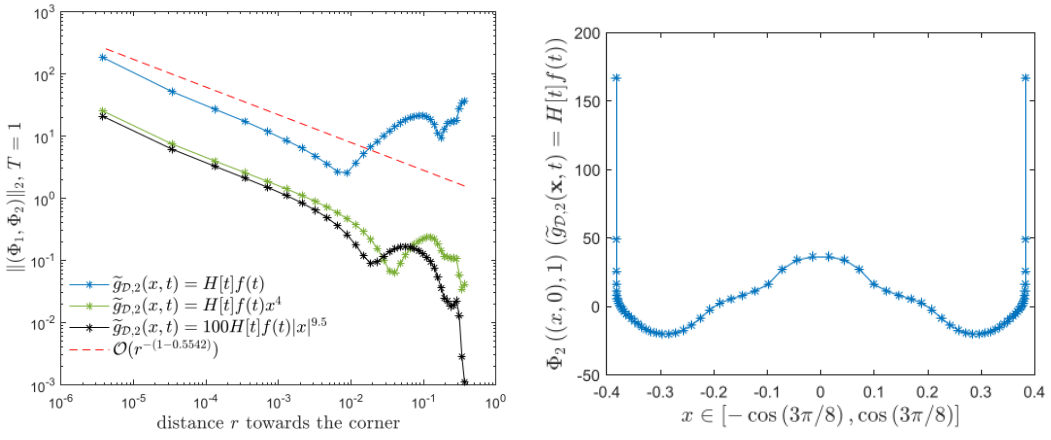

(a) (b)

Figure 2.11: Asymptotic behavior towards the vertices in Γ_2 for different boundary conditions (a) and plot of the vertical component of $\boldsymbol{\Phi}$ on the base of Γ_2 for the indicated boundary condition (b).

the behavior of the Euclidean norm of $\mathbf{\Phi}$ for these different boundary data, plotted as a function of the distance r to the vertex which is highlighted in red (Figure 2.8(b), geometry Γ_2). The singular exponent is expected to be $\nu^* \simeq 0.542$ for an angle at the base of amplitude $3\pi/8$. Indeed, we can detect that, in log scale, the slope of the norm for $r \to 0$ is parallel to the dashed line corresponding to $\mathcal{O}\left(r^{-(1-0.542)}\right)$ for each of the tested boundary data. In Figure 2.11(b) the vertical component of $\mathbf{\Phi}$ is shown on the base of Γ_2 at time $T = 1$, highlighting the singular behavior at the corners.

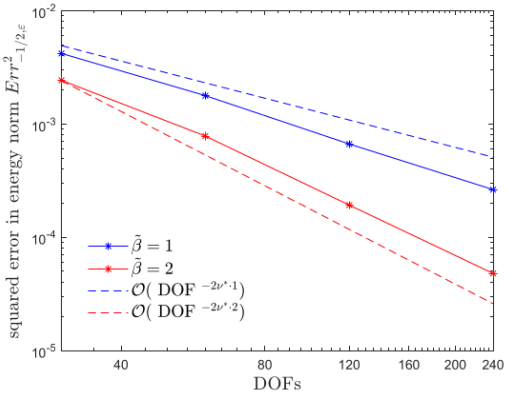

Figure 2.12: Squared error of the energy norm with h version on Γ_1, $\tilde{\beta}$-graded mesh, $\widetilde{g}_{\mathcal{D},2}(\mathbf{x},t) = H[t]f(t)x^4$

In Figure 2.12 we consider the equilateral triangle Γ_1 of 2.8(b) and study the decay of the error for increasing degrees of freedom for the h version. The number of mesh elements and the time step are the same considered in Table 2.4. The right-hand-side is here given by $\widetilde{g}_{\mathcal{D},1}(\mathbf{x},t) = 0$, $\widetilde{g}_{\mathcal{D},2}(\mathbf{x},t) = H[t]f(t)x^4$. An algebraically $\tilde{\beta}$-graded mesh is used on each side, where $\tilde{\beta} = 1, 2$. The energy tends to a benchmark value as the number of degrees of freedom increases, and the squared error $Err^2_{-1/2,\mathcal{E}}$ in energy norm in a log scale plot decays linearly as $\mathcal{O}(\text{DOF}^{-2\nu^*\tilde{\beta}})$, in agreement with Corollary 2.3.3.

2.4.3 Hard scattering problems on flat obstacle

In the following we consider a Neumann elastodynamics problem on the obstacle $\Gamma = \{(x,0) \in \mathbf{R} \,:\, x \in [-0.5, 0.5]\}$. We focus, in particular, on the solution of the discrete weak formulation (2.17) using h, p and hp versions.

Experiment 5. We set the Neumann data $\widetilde{g}_{\mathcal{N},i}(\mathbf{x},t) = 1$ for $i = 1, 2$. The datum at the boundary is independent of time. Therefore, as time increases, the components $\Psi_i(\mathbf{x},t)$ of the solution of the weak problem (2.5) tend to have stationary behaviour. Two different couples of velocities are considered, $c_{\mathtt{S}} = 1$, $c_{\mathtt{P}} = 2$ and $c_{\mathtt{S}} = 1$, $c_{\mathtt{P}} = 3$.
Figure 2.13 shows the time history of Ψ_1 and Ψ_2, calculated at the midpoint $(0,0)$ of Γ, for both the couples of velocities on the time interval $[0, 7.5]$. We observe that, after an initial transient phase, the solution approaches a stationary behaviour. For these plots, equation (2.17) is solved on a uniform space-time mesh with mesh size $h = 0.025$ and $\Delta t = 0.0125$, respectively.

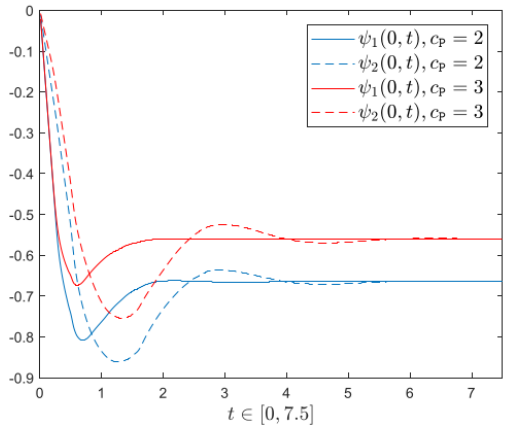

Figure 2.13: Time history of Ψ_1 and Ψ_2 calculated at the middle point of Γ for the couples of velocities $c_S = 1$, $c_P = 2$ and $c_S = 1$, $c_P = 3$.

To illustrate the behaviour of the solution near $\partial\Gamma$, Figure 2.14 shows the components of $-\boldsymbol{\Psi}$, for $c_S = 1$, $c_P = 2$, with respect to the distance r towards the right end point of the segment $(0.5, 0)^\top$ for various time instants: one observes that the singular behavior is independent of time, and the numerical solutions decrease like $r^{1/2}$ for r tending to zero. Figure 2.14 has been obtained using in particular the h version on a $\tilde{\beta}$-graded mesh with 81 nodes, with time step $\Delta t = 0.00625$ and $\tilde{\beta} = 2$.

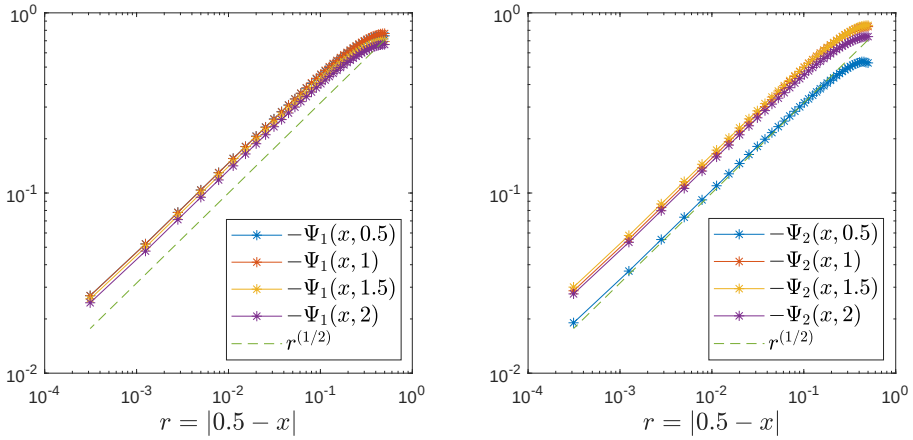

Figure 2.14: Asymptotic behaviour of $-\Psi_1$ and $-\Psi_2$ towards the right end of Γ for various time instants ($c_S = 1$, $c_P = 2$). The arc is discretized by a $\tilde{\beta}$-graded mesh with $\tilde{\beta} = 2$ and 81 mesh points.

For the case $c_S = 1, c_P = 2$, we study the decay of the squared error in energy norm $Err^2_{1/2,\mathcal{E}}$, as defined in (2.23), for the approximate solution of (2.17) up to time $T = 2$ analysing the squared energetic norm $\|\boldsymbol{\Psi}_{h,\Delta t}\|^2_{1/2,\mathcal{E}}$ of the approximate solution, which increases towards a common benchmark value for all tested discretization methods. The number of spatial DOFs in the following refers, as previously, to one component of the vector solution. For

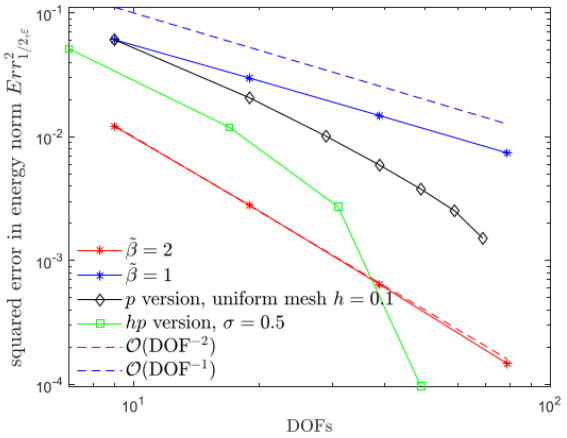

Figure 2.15: Squared error of the energy norm calculated up to time instant $T = 2$

the h version we choose a $\tilde{\beta}$-graded mesh on Γ with $\tilde{\beta} = 1, 2$ and $10, 20, 40$, respectively 80 segments. The time step $\Delta t = 0.05$ is set for 10 segments and it is halved at each refinement of the spatial mesh. The log scale plot in Figure 2.15(a) shows a linear decay of the error for the h version, parallel to the lines $\mathcal{O}(\mathrm{DOF}^{-\tilde{\beta}})$. The results confirm the prediction in Corollary 2.3.3. For the p version we consider a uniform discretization of the obstacle with $h = 0.1$ and a uniform time step $\Delta t = 1/(2{\cdot}\mathrm{DOF})$. The log scale plot shows a linear decay of the error parallel to the expected line $\mathcal{O}(\mathrm{DOF}^{-2})$. The hp version with a geometrically graded mesh with $\sigma = 1/2$ is considered for meshes on Γ with $4, 6, 8, 10$ and 12 segments. At each refinement of the mesh the degree p, starting from 2, increases uniformly on all the space elements. The time step is chosen as $\Delta t = 0.125$ for 4 segments and halved at each iteration. Similarly to the soft scattering problems presented above the hp method shows the fastest decay of the error with respect to increasing spatial DOFs.

Chapter 3

ACA Compression

Theory and experiments discussed in the previous chapters concretely prove the efficacy and the validity of the energetic BEM for different types of elastodynamics problems in $\mathbf{R}^2$. Unfortunately, the method presents a consistent drawback. This is not related to the quality and the stability of the approximated solution of the various discretized BIEs or to the calculation of $\mathbf{u}$ through the associated representation formula, rather in the overall cost required to compute the mentioned solutions. It is well known that indeed, if the space approximation is performed by means of shape functions $w^{\mathbf{p}}$ or $w^{\mathbf{u}}$ deriving from the Lagrangian polynomials defined over each segment of Γ discretization (see Figure 1.1 for instance in the linear case), the matrices $\mathbb{E}_V$, $\mathbb{E}_K$ and $\mathbb{E}_D$ (having Toeplitz structures comparable to the matrix in (1.75) have temporal blocks $\mathbb{E}_V^{(l)}$, $\mathbb{E}_K^{(l)}$ and $\mathbb{E}_D^{(l)}$ that become fully populated for growing values of the index l. This can prevent the application of the energetic BEM to large scale problems, since the memory required to store, for instance, matrix (1.75) is $\mathcal{O}(M_{\mathbf{p}}^2 N)$, $M_{\mathbf{p}}$ and N identifying the spatial and the temporal degrees of freedom. In this chapter we propose a compression technique, based on algebraic manipulations of the temporal blocks, that allows to rewrite them in a compressed format, in order to reduce the number of the original entries to be computed. The theory and the application of this strategy reveal to be very efficient in the resolution of problems depending on a high number of degrees of freedom and in the following this strategy is proposed to solve both acoustic and elastic wave propagation soft scattering problems by energetic BEM.

Remark. The following theoretical and numerical results are presented and discussed in Author's paper [3], written in collaboration with Professors Alessandra Aimi and Luca Desiderio (University of Parma) and recently submitted to *Computers & Mathematics with Applications*.

3.1 The acoustic and the elastic models

As announced in the introduction of the chapter, in the following we are interested in the resolution of two vectorial problems, both modelled by a partial differential equation with a specific diffusive term $\boldsymbol{\nabla} \cdot \boldsymbol{\sigma}$, different for each problem. We introduce then a common notation for both acoustic and elastic propagation, since the application of the energetic

BEM to solve them retraces comparable steps.
Here again we suppose that propagation occurs outside a bounded domain $\Omega \subset \mathbf{R}^2$ with a sufficiently smooth closed boundary $\Gamma := \partial\Omega$, and we denote by $\Omega_e := \mathbf{R}^2 \setminus \overline{\Omega}$ the exterior unbounded domain. The soft scattering differential problem is identified as follows:

$$\begin{cases} \boldsymbol{\nabla} \cdot \boldsymbol{\sigma}[\mathbf{u}](\mathbf{x},t) - \varrho \ddot{\mathbf{u}}(\mathbf{x},t) = \mathbf{0} & (\mathbf{x},t) \in \Omega_e \times [0,T] \\ \mathbf{u}(\mathbf{x},t) = \mathbf{g}_{\mathcal{D}}(\mathbf{x},t) & (\mathbf{x},t) \in \Sigma_T := \Gamma \times [0,T] \\ \mathbf{u}(\mathbf{x},0) = \dot{\mathbf{u}}(\mathbf{x},0) = \mathbf{0} & \mathbf{x} \in \Omega_e, \end{cases} \tag{3.1}$$

with $\mathbf{u} = (u_1, u_2)^\top$ denoting the unknown displacements with Dirichlet condition $\mathbf{g}_{\mathcal{D}} = (g_{\mathcal{D},1}, g_{\mathcal{D},2})^\top$ assigned at the boundary. In the general problem (3.1), homogeneous initial conditions are assumed at the first time of interest $t = 0$. As widely discussed in the previous chapters, implementation of the Boundary Element method requires to rewrite the unknown $\mathbf{u}$ by boundary integral reformulation of the problem (3.1). This can be done by using the arguments listed in Section 1.2 for the elastodynamics problems and that can be verbatim repeated for the acoustic model with the knowledge of the corresponding fundamental Green's tensor $\mathbf{G^{uu}} = (G_{ij}^{\mathbf{uu}})_{i,j=1,2}$. For the resolution of (3.1) we adopt an indirect single layer potential representation, written by components as:

$$u_i(\mathbf{x},t) = \int_0^t \int_\Gamma G_{ij}^{\mathbf{uu}}(\mathbf{x},\boldsymbol{\xi};t,\tau)\Phi_j(\boldsymbol{\xi},\tau)d\Gamma_{\boldsymbol{\xi}}d\tau, \quad \mathbf{x} \in \Omega_e,\ t \in [0,T], \quad i = 1,2. \tag{3.2}$$

where $\boldsymbol{\Phi} = (\Phi_1, \Phi_2)^\top$ is a suitable density field to be determined according to the differential problem we aim at solving. From the above formula, with a limiting process that makes a point $\mathbf{x} \in \Omega_e$ tending to a point $\mathbf{x} \in \Gamma$ and exploiting the Dirichlet boundary condition, we can obtain a system of two TD-BIEs:

$$g_{\mathcal{D},i}(\mathbf{x},t) = \int_0^t \int_\Gamma G_{ij}^{\mathbf{uu}}(\mathbf{x},\boldsymbol{\xi};t,\tau)\Phi_j(\boldsymbol{\xi},\tau)d\Gamma_{\boldsymbol{\xi}}d\tau =: \left(V_{ij}\Phi_j\right)(\mathbf{x},t), \quad (\mathbf{x},t) \in \Sigma_T,\ i = 1,2 \tag{3.3}$$

rewritable in the following vectorial form:

$$\left(\begin{bmatrix} V_{11} & V_{12} \\ V_{21} & V_{22} \end{bmatrix} \begin{bmatrix} \Phi_1 \\ \Phi_2 \end{bmatrix} \right)(\mathbf{x},t) = \begin{bmatrix} g_{\mathcal{D},1} \\ g_{\mathcal{D},2} \end{bmatrix}(\mathbf{x},t). \tag{3.4}$$

The energetic weak formulation of the BIEs (3.4), which can be calculated applying a time derivative to the entire BIE and projecting this last one onto the space of the unknown density $\boldsymbol{\Phi} = (\Phi_1, \Phi_2)^\top$, reads as follows:

find $\boldsymbol{\Phi} = (\Phi_1, \Phi_2)^\top$ *solution of the weak problem*

$$< (V_{ij}\dot{\Phi}_j), \phi_i >_{L^2(\Sigma_T)} = < \dot{g}_{\mathcal{D},i}, \phi_i >_{L^2(\Sigma_T)} . \tag{3.5}$$

for each test function $\boldsymbol{\phi} = (\phi_1, \phi_2)^\top$ *belonging to the same functional space of the unknown density* $\boldsymbol{\Phi}$.

Acoustics

Let us firstly consider the acoustic wave propagation problem identifying the corresponding *Cauchy stress tensor*:

$$\boldsymbol{\sigma}(\mathbf{x},t) := \varrho c^2 \boldsymbol{\nabla}\mathbf{u}(\mathbf{x},t), \tag{3.6}$$

where $c > 0$ denotes the speed of the wave propagation. In this case, simplifying the density ϱ, equation in (3.1) can be written as the vector acoustic wave equation:

$$c^2 \boldsymbol{\Delta}\mathbf{u}(\mathbf{x},t) - \ddot{\mathbf{u}}(\mathbf{x},t) = \mathbf{0} \qquad (\mathbf{x},t) \in \Omega_e \times [0,T]. \tag{3.7}$$

The components of the tensor $\mathbf{G}^{\mathbf{uu}}_{ij}(\mathbf{x},\boldsymbol{\xi};t,\tau)$ are given by:

$$G^{\mathbf{uu}}_{ij}(\mathbf{x},\boldsymbol{\xi};t,\tau) := \frac{c}{2\pi}\,\frac{H(c(t-\tau)-r)}{\sqrt{c^2(t-\tau)^2-r^2}}\delta_{ij}, \quad \text{with } r := \|\mathbf{r}\|_2 := \|\mathbf{x}-\boldsymbol{\xi}\|_2, \quad i,j = 1,2. \tag{3.8}$$

Consequently, the components of the unknown density $\boldsymbol{\Phi}$ decouple because of the *Kronecker delta* symbol δ_{ij}, leading to a recasting of the BIE (3.4) in the following form:

$$\left(\begin{bmatrix} V & 0 \\ 0 & V \end{bmatrix}\begin{bmatrix} \Phi_1 \\ \Phi_2 \end{bmatrix}\right)(\mathbf{x},t) = \begin{bmatrix} g_{\mathcal{D},1} \\ g_{\mathcal{D},2} \end{bmatrix}(\mathbf{x},t) \qquad \text{with} \qquad V := V_{11} = V_{22}. \tag{3.9}$$

Thus, we can retrieve the vector field $\boldsymbol{\Phi}$ by solving one scalar BIE with two different right-hand-sides. by introducing the energy of the wave equation (3.7) as follows (see [9])

$$\mathcal{E}(\mathbf{u},t) := \frac{1}{2}\left(\int_{\Omega\cap\Omega_e} \|\dot{\mathbf{u}}(\mathbf{x},t)\|_2^2\,(\mathbf{x},t)d\mathbf{x} + c^2\int_{\Omega\cap\Omega_e}\left[\|\nabla u_1(\mathbf{x},t)\|_2^2 + \|\nabla u_2(\mathbf{x},t)\|_2^2\right]d\mathbf{x}\right), \tag{3.10}$$

it turns out that the quadratic form related to the left-hand side of the energetic weak problem (3.5) satisfies the following *energy identity*

$$\mathcal{E}(\mathbf{u},T) = \int_\Gamma\int_0^T (V\dot{\Phi}_i)(\mathbf{x},t)\Phi_i(\mathbf{x},t)dtd\Gamma_{\mathbf{x}}, \qquad i = 1,2. \tag{3.11}$$

Elastodynamics

For what concerns the propagation of an elastic wave, all the fundamental notations have been already introduced in Chapter 1 and, therefore, we briefly list them in the following. In particular, the *Cauchy stress tensor* for elastodynamics is defined by components in (1.3), leading to a recast of the equation (3.1) in the form (1.9). The fundamental elastodynamic solution $\mathbf{G}^{\mathbf{uu}}$ is written, again by components, in (1.15), where it is immediate to observe the dependence the tensor on two different wave fronts, characterized by the peculiar velocities $c_{\mathtt{S}}$ and $c_{\mathtt{P}}$. Additionally, when Poisson's relation is satisfied, i.e. $\lambda = \mu$, we have $c_{\mathtt{P}} = \sqrt{3}c_{\mathtt{S}}$. In the elastodynamic case, the definition of the components $G^{\mathbf{uu}}_{ij}$ for $i \neq j$ is not trivial in general: as a consequence, the components of the unknown density $\boldsymbol{\Phi}$ do not decouple and equation (3.4) still represents a system of two BIEs, with the only simplification of the integral operator given by the identity $V_{ij} = V_{ji}$. The energy of the elastodynamic system, and the consequent energy identity for the elastodynamic case with Dirichlet condition, are provided in (1.44) and (1.45).

3.2 Galerkin discretization

For the discretization phase we can retrace the same steps taken for discretization of the indirect weak form of the Dirichlet elastodynamics problem in (1.46): then we choose to approximate the components of density $\mathbf{\Phi}$ in the functional spaces $V_{\Delta t,0}$ and $X_{h,0}^{-1}(\Gamma)$ (for details see Subsection 1.5.1), for the time and the space approximation respectively. In particular, since we chose piece-wise constant functions $w^{\mathbf{p}}$ for the space approximation (degree $p = 0$), it is easy to observe that the number $M_{\mathbf{p}}$ of polynomial basis corresponds to M, namely the number of mesh elements imposed on Γ. For the time approximation, the definition of the basis function can be found in (1.71). Thus, the unknown approximate solution of problem (3.5) is expressed as:

$$\Phi_i(\mathbf{x},t) \simeq \sum_{n=0}^{N-1}\sum_{m=1}^{M} \alpha_{nm}^{\mathbf{p},i} v_n(t) w_m^{\mathbf{p}}(\mathbf{x}) \qquad i=1,2, \tag{3.12}$$

and the test function are replaced by $\phi_i(\mathbf{x},t) = v_{\widetilde{n}}(t) w_{\widetilde{m}}^{\mathbf{p}}(\mathbf{x})$ for each $\widetilde{m} = 1,...,M$, $\widetilde{n} = 0,...,N-1$. As consequence of the approximation in (3.12), the energetic BEM discretization produces the linear system

$$\mathbb{E}_V \alpha^{\mathbf{p}} = \beta^D, \tag{3.13}$$

with structure identical to the one presented in (1.75). Here in particular we report the structure of the temporal blocks $\mathbb{E}_V^{(l)}$, with $l = \widetilde{n} - n$ corresponding to the non-negative difference between two time indexes:

$$\mathbb{E}_V^{(l)} = \begin{pmatrix} \mathbb{E}_{V,11}^{(l)} & \mathbb{E}_{V,12}^{(l)} \\ \mathbb{E}_{V,21}^{(l)} & \mathbb{E}_{V,22}^{(l)} \end{pmatrix} \qquad \text{with} \quad \mathbb{E}_{V,12}^{(l)} = \mathbb{E}_{V,21}^{(l)}. \tag{3.14}$$

We recall that, with the choice of piece-wise constant basis for the space discretization, the generic sub-block $\mathbb{E}_{V,ij}^{(l)}$ is an M-by-M matrix. The solution of (3.13) is obtained by a block forward substitution, as indicated in (1.76) and (1.77). Block $\mathbb{E}_V^{(0)}$ is the only one to be inverted, while all the other blocks $\mathbb{E}_V^{(l)}$ for $l > 0$ are used to update at each time step the right-hand side. In the following we focus on this latter type of blocks and on how the definition of their entries, in terms of double space integrals, allows for compression algorithm and, hence, for a memory requirement reduction for the storage of these matrices.

Acoustics

For what concerns the discretization of the energetic weak problem related to the acoustic model, we remark that the block $\mathbb{E}_V^{(l)}$ inherits the structure of the space-time integral operator $\mathbf{V}$ so that, due to (3.9), we have:

$$\mathbb{E}_V^{(l)} = \begin{pmatrix} \mathbb{E}^{(l)} & 0 \\ 0 & \mathbb{E}^{(l)} \end{pmatrix} \qquad \text{with} \quad \mathbb{E}_{V,11}^{(l)} := \mathbb{E}_{V,22}^{(l)} = \mathbb{E}^{(l)}. \tag{3.15}$$

After performing a double analytic integration in the time variables, the entries of the M-by-M matrix $\mathbb{E}^{(l)}$ are of the form:

$$\mathbb{E}^{(l)}_{\widetilde{m},m} = -\frac{1}{2\pi}\sum_{\xi,\zeta=0}^{1}(-1)^{\xi+\zeta}\int_{\Gamma} w^{\mathbf{p}}_{\widetilde{m}}(\mathbf{x})\int_{\Gamma} w^{\mathbf{p}}_{m}(\boldsymbol{\xi})\nu^{V}(r;\Delta_{\widetilde{n}+\xi,n+\zeta})d\Gamma_{\boldsymbol{\xi}}d\Gamma_{\mathbf{x}}, \tag{3.16}$$

where $l=\widetilde{n}-n$, $\Delta_{\widetilde{n}+\xi,n+\zeta}=t_{\widetilde{n}+\xi}-t_{n+\zeta}\geqslant 0$ and

$$\nu^{V}(r;t)=H(ct-r)\left[\log\left(ct+\sqrt{c^2t^2-r^2}\right)-\log(r)\right],\quad r=\|\mathbf{x}-\boldsymbol{\xi}\|_2. \tag{3.17}$$

In (3.17), the Heaviside function models the wave front propagation with velocity c. The space singularity of type $\mathcal{O}(\log(r))$, as $r\to 0$, is typical of the weakly singular kernels related to 2D elliptic problems and it is immediately visible in the definition of the acoustic kernel (3.17).

Elastodynamics

When we deal with elastic problems, all the four sub-blocks in (3.14) are non-zero and, after a double analytical integration in time variables, their generic entry for $i,j=1,2$ and $l=\widetilde{n}-n$ has the form

$$\left(\mathbb{E}^{(l)}_{V,ij}\right)_{\widetilde{m},m} = -\frac{1}{2\pi\varrho}\sum_{\xi,\zeta=0}^{1}(-1)^{\xi+\zeta}\int_{\Gamma} w^{\mathbf{p}}_{\widetilde{m}}(\mathbf{x})\int_{\Gamma} w^{\mathbf{p}}_{m}(\boldsymbol{\xi})\nu^{V}_{ij}(\mathbf{r};\Delta_{\widetilde{n}+\xi,n+\zeta})d\Gamma_{\boldsymbol{\xi}}d\Gamma_{\mathbf{x}}, \tag{3.18}$$

where the elastodynamic kernel ν^{V}_{ij} is defined in (1.79). We remark that if $0\leqslant r=\|\mathbf{x}-\boldsymbol{\xi}\|_2\leqslant c_{\mathrm{S}}\Delta_{\widetilde{n}+\xi,n+\zeta}<c_{\mathrm{P}}\Delta_{\widetilde{n}+\xi,n+\zeta}$ the kernel assumes the reduced form reported in formula (1.82), in which the space singularity of kind $\mathcal{O}(\log(r))$ is revealed.

3.3 Basic theory and ACA algorithm

Unfortunately, for growing l the blocks $\mathbb{E}^{(l)}_{V}$ in (3.14) are more and more populated until they become full matrices. This phenomenon, once fixed a time step Δt, depends on the speed of wave propagation. An example of the matrix filling process with respect to different value of the velocity c, associated to the acoustic model, can be found in Figure 3.1. Consequently, the memory storage requirement for the matrix $\mathbb{E}_V$ in (3.13) is of order $\mathcal{O}(M^2N)$, making the application of the energetic BEM inefficient in case of a large number of spatial and temporal DOFs. In the following, we propose a procedure to reduce the computational time and cost for the generation of the blocks $\mathbb{E}^{(l)}_{V}$, based on a subtler analysis of their entries. For simplicity of representation, we focus our attention on the acoustic problem, but the analysis we are going to propose can be easily extended to the elastic case.

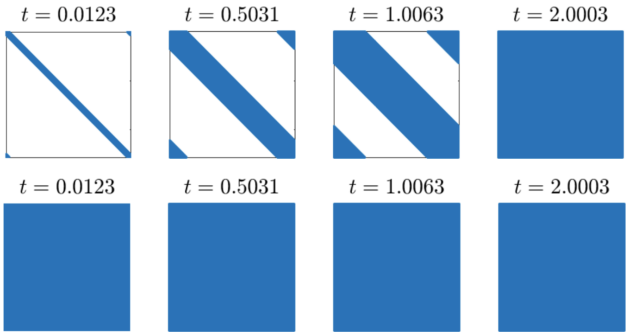

Figure 3.1: Structure of the acoustic sub-block $\mathbb{E}^{(l)}$ in (3.15) for $l = 1$, 41, 82, 163 and for the corresponding growing time instants $t = l\Delta t$. For the calculation of the matrix entries (3.16) we consider a circumference Γ with unitary radius, approximated uniformly by $M = 512$ segments, so that $\mathbb{E}^{(l)}$ is a 512-by-512 matrix. The problems evolves in the time interval $[0, 8\pi]$, decomposed uniformly by $N = 2048$ instants and characterized by the velocities $c = 1$ (first row plots) and $c = 343$ (second row plots).

Acoustics

For growing times, the inequality $c\,t_{l-1} > r$ becomes true, then, thanks to the summation in matrix entry (3.16), the latter reduces to

$$\mathbb{E}^{(l)}_{\widetilde{m},m} = -\frac{1}{2\pi}\int_{\Gamma} w^{\mathrm{P}}_{\widetilde{m}}(\mathbf{x}) \int_{\Gamma} w^{\mathrm{P}}_{m}(\boldsymbol{\xi})\widetilde{\nu}(r;t_l)\Gamma_{\boldsymbol{\xi}} d\Gamma_{\mathbf{x}} \tag{3.19}$$

where

$$\widetilde{\nu}(r;t) = \log\left(\frac{\left(ct+\sqrt{c^2t^2-r^2}\right)^2}{\left(c(t-\Delta t)+\sqrt{c^2(t-\Delta t)^2-r^2}\right)\left(c(t+\Delta t)+\sqrt{c^2(t+\Delta t)^2-r^2}\right)}\right). \tag{3.20}$$

We remark that the quantity $\mathrm{diam}(\Gamma)$ is the maximum value that the distance r can assume on Γ. Thus, when $ct_{l-1} > \mathrm{diam}(\Gamma)$, we do not observe any space singularity in all the matrix elements and the kernel function $\widetilde{\nu}(r(\mathbf{x},\boldsymbol{\xi});t_l)$ reveals to be smooth for $r \to 0$; further, we note that it is symmetric in space variables and in the limit for $t \to \infty$ it tends to become identically zero.
The reduction of the memory storage for the fully populated blocks $\mathbb{E}^{(l)}$, generated by the energetic BEM, is based on the property that the kernel $\widetilde{\nu}(r(\mathbf{x},\boldsymbol{\xi});t)$ admits a low-rank or degenerate expansion, i.e. it can be decomposed as follows:

$$\widetilde{\nu}(r(\mathbf{x},\boldsymbol{\xi});t) = \sum_{k=0}^{k_l^*} \chi_k(\mathbf{x},t)\omega_k(\boldsymbol{\xi};t) + R_{k_l^*}(\mathbf{x},\boldsymbol{\xi};t) := S_{k_l^*}(\mathbf{x},\boldsymbol{\xi};t) + R_{k_l^*}(\mathbf{x},\boldsymbol{\xi};t), \tag{3.21}$$

where k_l^* represents the rank of the decomposition and the residuum $R_{k_l^*}(\mathbf{x},\boldsymbol{\xi};t)$ tends to zero for $k_l^* \to \infty$. Going back to the definition (3.20) and to the properties of smoothness and symmetry of $\widetilde{\nu}(r(\mathbf{x},\boldsymbol{\xi});t)$, for a fixed t and Δt, it is well known (see [77]) that such

kind of kernels can be represented by a bilinear expansion in terms of eigenvalues and eigenfunctions in space variables. However, it is not easy to determine this representation in closed form, so, since we are interested in the estimation of k_l^* w.r.t the value of the residuum $R_{k_l^*}(\mathbf{x}, \boldsymbol{\xi}; t)$, it is better to work in the r variable. Here, we moreover stress that the following theoretical study is not necessary for the implementation of the method, since we will employ a rank revealing algorithm for the computation of the low-rank approximation of the matrices $\mathbb{E}^{(l)}$.
Taking into account the definition of the reduced integral kernel (3.20) and the fact that the shape functions in (3.19) are piece-wise constant, a generic matrix element can be approximated as follows:

$$\mathbb{E}^{(l)}_{\widetilde{m},m} \simeq -\frac{\Delta x^2}{2\pi}\widetilde{\nu}(r; t_l) \tag{3.22}$$

since the function $\widetilde{\nu}(r; t_l)$ is almost flat in r for a large time instant t_l. We proceed then in the estimate by applying to this smooth kernel a Taylor expansion in the r variable, centred in $r = 0$:

$$\mathbb{E}^{(l)}_{\widetilde{m},m} \simeq \sum_{k=0}^{+\infty} C_k(t_l) r^{2k} = S_{k_l^*}(r; t_l) + R_{k_l^*}(r; t_l), \tag{3.23}$$

where $S_{k_l^*}(r; t_l)$ and $R_{k_l^*}(r; t_l)$ represent the summation over the first $k_l^* + 1$ terms of the series and the related reminder, respectively. In particular, the coefficients $C_k(t)$ can be approximated, up to negligible terms for large t, as follows:

$$C_k(t) \simeq \widetilde{C}_k(t) := -\frac{(c\Delta x\, \Delta t)^2}{2\pi}\frac{(2k+1)!}{(k!)^2 4^k}\frac{1}{(ct)^{2k+2}}. \tag{3.24}$$

Now, we introduce the function

$$\widetilde{S}_{k_l^*}(r; t) := \sum_{k=0}^{k_l^*} \widetilde{C}_k(t) r^{2k} \tag{3.25}$$

and we observe that, since for each $k \geqslant 0$ it holds

$$\frac{(2k+1)(2k+1)}{2k+1}\frac{r^{2k}}{(ct)^{2k+2}} = -\frac{1}{c(2k+1)}\frac{\partial^2}{\partial t \partial r}\left(\frac{r^{2k+1}}{(ct)^{2k+1}}\right),$$

we obtain:

$$\begin{aligned}\widetilde{S}_{k_l^*}(r; t) &= \frac{c(\Delta x\, \Delta t)^2}{2\pi}\sum_{k=0}^{k_l^*}\frac{(2k)!}{(2k+1)(k!)^2 4^k}\frac{\partial^2}{\partial t \partial r}\left(\frac{r^{2k+1}}{(ct)^{2k+1}}\right) \\ &= \frac{c(\Delta x\, \Delta t)^2}{2\pi}\frac{\partial^2}{\partial t \partial r}\left[\sum_{k=0}^{k_l^*}\frac{(2k)!}{(2k+1)(k!)^2 4^k}\left(\frac{r}{ct}\right)^{2k+1}\right].\end{aligned} \tag{3.26}$$

The argument of the double derivative in formula (3.26) is the general term, calculated in $x = r/(ct)$, of the expansion centred in $x = 0$ of the function $\arcsin(x)$. Therefore, we

approximate the generic block element in (3.23) by a series of terms (3.26), having as limit for $k_l^* \to +\infty$ the following function:

$$\widetilde{S}_\infty(r;t) = \frac{c(\Delta x\,\Delta t)^2}{2\pi}\left[\frac{\partial^2}{\partial t\partial r}\arcsin\left(\frac{r}{ct}\right)\right] = -\frac{c(\Delta x\,\Delta t)^2}{2\pi}\left(\frac{1}{t\sqrt{c^2t^2-r^2}} + \frac{r^2}{t\,\sqrt[3/2]{c^2t^2-r^2}}\right).$$

Consequently, we can estimate the reminder $R_{k_l^*}(r;t)$ at a fixed k_l^* with the difference

$$R_{k_l^*}(r;t) \simeq \widetilde{S}_\infty(r;t) - \widetilde{S}_{k_l^*}(r;t). \tag{3.27}$$

Thus, we can conclude that, for a chosen accuracy $\varepsilon > 0$, it is possible to obtain a low-rank approximation of the matrix $\mathbb{E}^{(l)}$, k_l^* being the rank required to satisfy

$$\left|R_{k_l^*}(r;t_l)\right| \simeq \left|\widetilde{S}_\infty(r;t_l) - \widetilde{S}_{k_l^*}(r;t_l)\right| \leqslant \varepsilon\left|\widetilde{S}_\infty(r;t_l)\right|. \tag{3.28}$$

The decomposition (3.23) can be written as a matrix decomposition

$$\mathbb{E}^{(l)} = \mathbb{S}_{k_l^*} + \mathbb{R}_{k_l^*} \qquad \text{with} \quad \mathbb{S}_{k_l^*} := \mathbb{Q}\cdot\mathbb{W}^\top, \tag{3.29}$$

where $\mathbb{Q}$ and $\mathbb{W}$ are both M-by-k_l^* matrices and the residuum $\mathbb{R}_{k_l^*}$ is such that

$$\left\|\mathbb{R}_{k_l^*}\right\|_{\mathrm{F}} = \left\|\mathbb{E}^{(l)} - \mathbb{S}_{k_l^*}\right\|_{\mathrm{F}} = \left\|\mathbb{E}^{(l)} - \mathbb{Q}\cdot\mathbb{W}^\top\right\|_{\mathrm{F}} \leqslant \varepsilon\left\|\mathbb{E}^{(l)}\right\|_{\mathrm{F}},$$

where $\|\cdot\|_{\mathrm{F}}$ denotes the Frobenius norm of a real matrix and $\varepsilon > 0$ is a parameter representing the accuracy required to the approximation.

Such low-rank approximation can be computed by different algorithms: the best representation, up to a given accuracy, can be generated by Singular Value Decomposition (SVD) but it is an unattractive technique for the computational complexity, since it leads to slow procedures for large-scale computations. On the other hand, a purely algebraic algorithm as the partially pivoted Adaptive Cross Approximation (ACA) (see [17, 18]) appears to be very efficient for the application to the energetic BEM matrices, because it allows to attain the low-rank representation of the blocks $\mathbb{E}^{(l)}$ by computing adaptively just some selected rows and columns of the original matrix, until a stopping criterion related to the set accuracy $\varepsilon_{\mathrm{ACA}} > 0$ is satisfied.

The starting point of ACA is the property that each matrix of rank k can be obtained as the sum of k matrices of rank 1. Thus, the idea at the basis of ACA algorithm is to improve the accuracy of the approximation by adding iteratively rank-1 matrices. At iteration k, the matrix $\mathbb{S}_k$ is constituted by k rows $\mathbf{q}_i$ and k columns $\mathbf{w}_i$, i.e.

$$\mathbb{S}_k := \sum_{i=1}^{k}\mathbf{q}_i\mathbf{w}_i^\top = \mathbb{Q}\cdot\mathbb{W}^\top. \tag{3.30}$$

The information is shifted iteratively from the residual to the approximant. More precisely, at iteration k, given $\mathbb{S}_k$ and assuming the row index $\widetilde{m}^*$ is known, the algorithm is given by the following six steps:

1. generate the rows $\mathbf{a} := \mathbb{E}^{(l)\top}\mathbf{e}_{\widetilde{m}^*}$ and $\mathbb{R}_k^\top \mathbf{e}_{\widetilde{m}^*} := \mathbf{a} - \sum_{i=1}^{k} (\mathbf{q}_i)_{\widetilde{m}^*} \mathbf{w}_i$;
2. find the column index $m^* := \text{argmax}_m \left|(\mathbb{R}_k)_{\widetilde{m}^*,m}\right|$ and compute $\gamma_{k+1} := (\mathbb{R}_k)^{-1}_{\widetilde{m}^*,m^*}$;
3. generate of the columns $\mathbf{b} := \mathbb{E}^{(l)}\mathbf{e}_{m^*}$ and $\mathbb{R}_k\mathbf{e}_{m^*} := \mathbf{b} - \sum_{i=1}^{k} \mathbf{q}_i \, (\mathbf{w}_i)_{m^*}$;
4. find the next row index $\widetilde{m}^* := \text{argmax}_{\widetilde{m}} \left|(\mathbb{R}_k)_{\widetilde{m},m^*}\right|$;
5. compute vectors $\mathbf{q}_{k+1} := \gamma_{k+1}\mathbb{E}^{(l)}\mathbf{e}_{m^*}$ and $\mathbf{w}_{k+1} := \mathbb{E}^{(l)\top}\mathbf{e}_{\widetilde{m}^*}$;
6. update the approximation $\mathbb{S}_{k+1} = \mathbb{S}_k + \mathbf{q}_{k+1}\mathbf{w}_{k+1}^\top$.

The algorithm then stops when the new rank-1 approximation does not improve the accuracy of the approximation. Since at each iteration k it holds $\mathbb{S}_k - \mathbb{S}_{k-1} = \mathbf{q}_k\mathbf{w}_k^\top$, the stopping criteria reads

$$\|\mathbf{q}_k\|_2\|\mathbf{w}_k\|_2 \leqslant \varepsilon_{\text{ACA}}\|\mathbb{S}_k\|_{\text{F}}. \tag{3.31}$$

As we can see, ACA provides a purely algebraic and easy to implement tool for the approximation of the energetic BEM blocks, without requiring any a priori kernel expansion.

Remark. Citing the work of Bebendorf (see [17, 18]), the ACA algorithm was originally developed for asymptotic smooth kernels and for this class of operators its convergence and performances were theoretically investigated and assessed. Smooth kernels, like $\widetilde{\nu}(r(\mathbf{x},\boldsymbol{\xi});t)$, do not formally fit into the definition of asymptotic smoothness of a function. However, in this case the ACA algorithm can be interpreted as a rank-revealing decomposition applicable to kernels that admit degenerate approximations, as (3.21). As far as we know, one of the first application to smooth kernels can be found in [56].

Remark. Since the success of the proposed ACA based acceleration of the energetic BEM relies on the possibility of obtaining low-rank approximations of the blocks $\mathbb{E}^{(l)}$ we investigate such a property for a benchmark example. We take into account a problem on a circumference Γ with unitary radius, approximated by $M = 512$ segments with length $h = \pi/256$, so that $\mathbb{E}^{(l)}$ is a 512-by-512 matrix. The problems evolves in the time interval $[0, 8\pi]$, the latter decomposed uniformly by $N = 2048$ instants and characterized by the velocity $c = 1$. In the first row of Table 3.1, we report the evaluation of the ranks k_l of some time blocks obtained by the execution of the ACA compression with threshold $\varepsilon_{\text{ACA}} = 1.0e-04$ in the stopping criteria (3.31). Then a comparison is made considering the rank k_l^* obtained by the estimate of the reminder, calculated for $r = 2$, i.e. the diameter of Γ, and by setting the threshold $\varepsilon = 1.0e-04$ in (3.28). The results confirm how the estimate of the rank by the study of the reminder of the decomposition (3.23) is qualitatively significant and they give us an idea of how low the rank of the blocks behaves as the time increases. We note that k_l is bigger than k_l^* but this phenomenon is not surprising since the ACA does not provide the best numerical rank, rather a good approximation of it. However, we note that the two numerical ranks are of the same order.

l	256	512	768	1024	1280	1536	1792	2048
k_l	13	7	7	7	5	4	4	4
k_l^*	11	4	3	2	2	2	2	1

Table 3.1: Comparison between the estimates of the ranks of $\mathbb{E}^{(l)}$ given by the execution of the ACA algorithm with threshold $\varepsilon_{\text{ACA}} = 1.0e-04$ in (3.31), and by the evaluation of the reminder $R_{k_l^*}(r;t_l)$ with threshold $\varepsilon = 1.0e-04$ in (3.28).

Elastodynamics

Similar remarks as those made for the acoustic integration kernel are proposed below for the elastic problem. We start by observing that, for growing time, also the matrix element defined in (3.18) can be rewritten in a reduced form

$$\left(\mathbb{E}^{(l)}_{V,ij}\right)_{\widetilde{m},m} = -\frac{1}{2\pi\varrho}\int_\Gamma w_{\widetilde{m}}(\mathbf{x})\int_\Gamma w_m(\boldsymbol{\xi})\widetilde{\nu}_{ij}(\mathbf{r};t_l)d\Gamma_{\boldsymbol{\xi}}d\Gamma_{\mathbf{x}} \tag{3.32}$$

where the kernel

$$\widetilde{\nu}_{ij}(\mathbf{r};t) = \frac{\delta_{ij}}{2}\left[\frac{1}{c_{\text{P}}^2}\log\left(\frac{\left(c_{\text{P}}t+\sqrt{c_{\text{P}}^2t^2-r^2}\right)^2}{\left(c_{\text{P}}(t-\Delta t)+\sqrt{c_{\text{P}}^2(t-\Delta t)^2-r^2}\right)\left(c_{\text{P}}(t+\Delta t)+\sqrt{c_{\text{P}}^2(t+\Delta t)^2-r^2}\right)}\right)\right.$$
$$\left.+\frac{1}{c_{\text{S}}^2}\log\left(\frac{\left(c_{\text{S}}t+\sqrt{c_{\text{S}}^2t^2-r^2}\right)^2}{\left(c_{\text{S}}(t-\Delta t)+\sqrt{c_{\text{S}}^2(t-\Delta t)^2-r^2}\right)\left(c_{\text{S}}(t+\Delta t)+\sqrt{c_{\text{S}}^2(t+\Delta t)^2-r^2}\right)}\right)\right]$$
$$+\frac{c_{\text{P}}^2-c_{\text{S}}^2}{c_{\text{P}}c_{\text{S}}}\left(\frac{r_ir_j}{r^2}-\frac{\delta_{ij}}{2}\right)\left[\frac{2t}{c_{\text{P}}\sqrt{c_{\text{S}}^2t^2-r^2}+c_{\text{S}}\sqrt{c_{\text{P}}^2t^2-r^2}}\right.$$
$$\left.-\frac{t+\Delta t}{c_{\text{P}}\sqrt{c_{\text{S}}^2(t+\Delta t)^2-r^2}+c_{\text{S}}\sqrt{c_{\text{P}}^2(t+\Delta t)^2-r^2}}-\frac{t-\Delta t}{c_{\text{P}}\sqrt{c_{\text{S}}^2(t-\Delta t)^2-r^2}+c_{\text{S}}\sqrt{c_{\text{P}}^2(t-\Delta t)^2-r^2}}\right]$$

is obtained considering that, for $c_{\text{S}}t_{l-1} > \text{diam}(\Gamma)$, the single layer elastodynamics kernel defined in (1.79) is always expressed by its reduced form (1.82). The elastic kernel $\widetilde{\nu}_{ij}$ has the same properties of the reduced acoustic kernel $\widetilde{\nu}(\mathbf{r};t)$, i.e. it is smooth for $r \to 0$ and symmetric w.r.t to the space variables. Moreover, for a fixed r, in the limit for $t \to \infty$ it tends to become identically zero. Therefore the generic matrix entry defined in (3.32) can be approximated as follows

$$\left(\mathbb{E}^{(l)}_{V,ij}\right)_{\widetilde{m},m} \simeq -\frac{\Delta x^2}{2\pi\varrho}\widetilde{\nu}_{ij}(\mathbf{r};t_l), \tag{3.33}$$

which allows us to proceed with a generalised Taylor expansion in the vectorial variable $\mathbf{r} = (r_1, r_2)^\top$ of the right-hand-side of the previous relation. Then we can rewrite the element as a series of even terms:

$$\left(\mathbb{E}^{(l)}_{V,ij}\right)_{\widetilde{m},m} \simeq \sum_{\substack{k=0\\|\boldsymbol{\alpha}|=2k}}^{\infty} C_{\boldsymbol{\alpha},ij}(t_l)\mathbf{r}^\alpha, \tag{3.34}$$

where the argument of the summation depends on a multi-index $\boldsymbol{\alpha} := (\alpha_1, \alpha_2)$ with $|\boldsymbol{\alpha}| = \alpha_1 + \alpha_2$, and $\mathbf{C}_{\boldsymbol{\alpha}}(t) = (C_{\boldsymbol{\alpha},ij}(t))_{i,j=1,2}$ is a fourth-order tensor whose entries have a behaviour in time as $\mathcal{O}(1/(c_S t)^{|\boldsymbol{\alpha}|+2})$. Consequently, we can conclude that the reduced elastodynamic kernels $\widetilde{\nu}_{ij}(\mathbf{r}; t)$ admit a low-rank expansion and that the ACA algorithm is applicable for the computation of each sub-block $\mathbb{E}^{(l)}_{V,ij}$, $i, j = 1, 2$, in (3.14).

Remark. We recall that a "straightforward generalization of the scalar-value ACA to the matrix-valued version is not possible", since the research of a suitable pivot could fail for the reasons listed by Messner and Schanz in [59]. Therefore, in the elastic case we apply the ACA following their approach, namely considering the partition of the matrix $\mathbb{E}^{(l)}_V$ into a 2×2 block matrix, as indicated in (3.14), and applying the proposed compression strategy to each of the four sub-blocks. This leads to the implementation of four distinct iterative pivoting-algorithms that can be efficiently executed with parallel processes.

3.4 Numerical results

This section contains two main parts: the first deals with the numerical study of the efficiency of the proposed method, in terms of accuracy, memory saving and CPU time reduction and the application is in particular consider for both acoustic and elastodynamics benchmark cases. The second part presents the application of the scheme to some soft scattering problems.

3.4.1 Example 1. Numerical study of the efficiency of the proposed method.

Let Ω be the unit disk centered at $(0, 0)$, so that $\Gamma = \{\mathbf{x} \in \mathbf{R}^2 \, : \, \mathbf{x} = (\cos\alpha, \sin\alpha)^\top, \ \alpha \in (-\pi, \pi]\}$. We consider the Problem (3.1) with the final time instant $T = 4\pi$.

Here, we aim at testing the accuracy and the efficiency of the approximations we obtain by using the energetic approach combined with the ACA technique. Since, to the best of our knowledge, for both the acoustic and the elastodynamic problems it is not possible to choose a Dirichlet datum $\mathbf{g}_{\mathcal{D}}(\mathbf{x}, t)$ such that an analytical expression of the exact solution of the problem is known, we construct the corresponding reference solution by solving the problem with the standard energetic BEM, by using M_e degrees of freedom for the space discretization and N_e sub-intervals for the time interval $[0, 4\pi]$. We refer to the reference solution as $\boldsymbol{\Phi}^*_{M_e,N_e}(\mathbf{x}, t)$ and to the corresponding reference displacement solution as $\mathbf{u}^*_{M_e,N_e}(\mathbf{x}, t)$, obtained replacing $\boldsymbol{\Phi}^*_{M_e,N_e}(\mathbf{x}, t)$ in the integral representation formula (3.2). Moreover, we denote by $\boldsymbol{\Phi}_{M,N}(\mathbf{x}, t)$ and $\mathbf{u}_{M,N}(\mathbf{x}, t)$ the approximate solution and the corresponding displacement obtained with the proposed ACA algorithm applied to compress the temporal blocks, choosing the space and time discretization parameters M and N, respectively.

To test the accuracy of our method, we introduce the absolute error

$$E^{\boldsymbol{\Phi}}_{M,N} := \max_{t\in(0,T]} \left\| \boldsymbol{\Phi}^*_{M_e,N_e}(\cdot,t) - \boldsymbol{\Phi}_{M,N}(\cdot,t) \right\|_{L^2(\Gamma)}, \tag{3.35}$$

associated to the approximate solution $\boldsymbol{\Phi}_{M,N}(\mathbf{x},t)$, the error made on the calculation of the external solution at a fixed point $\mathbf{x}_0 = (0,2)^\top$

$$E^{\mathbf{u}}_{M,N} := \max_{t\in(0,T]} \left| \mathbf{u}^*_{M_e,N_e}(\mathbf{x}_0,t) - \mathbf{u}_{M,N}(\mathbf{x}_0,t) \right|. \tag{3.36}$$

To test how the error decreases with respect to a doubling of the degrees of freedom, we compute the corresponding Estimated Order of Convergence (EOC), by means of the following standard formula:

$$\mathrm{EOC} := \log_2 \left| \frac{E^*_{M,N}}{E^*_{2M,2N}} \right| \qquad \text{with } * = \boldsymbol{\Phi}, \mathbf{u}. \tag{3.37}$$

Moreover, we focus our attention on the percentage of the memory saved, defined as

$$\mathrm{mem}(\%) := 100 \cdot \left(1 - \frac{1}{N} \sum_{l=0}^{N-1} \frac{k_l}{M} \right), \tag{3.38}$$

where k_l/M denotes the ratio between the size of the compressed block $\mathbb{E}^{(l)}$ and the size of its complete (not compressed) form.

Acoustics

For the acoustic problem, we consider the Dirichlet boundary datum

$$g_{\mathcal{D},1}(\mathbf{x},t) = t^4 e^{-2t} \cos\left(x_1^2 + 2x_2^2\right), \quad g_{\mathcal{D},2}(\mathbf{x},t) = 0.$$

We observe that, since the acoustic BIE (3.9) is decoupled, with this boundary datum the vertical density $\Phi_2(\mathbf{x},t)$ is identically null. In the sequel, we report the numerical results corresponding to the reference parameters $M_e = 4096$ and $N_e = 8192$. Although to the previous underlined limitations of the standard energetic BEM, this choice of M_e and N_e is possible, because the considered geometry of Γ allows us to take advantage of the Toeplitz structure of the blocks $\mathbb{E}^{(l)}$ in (3.15), for $l = 0, 1, \ldots, N_e - 1$. Therefore, in this test we need to construct and store only the first row of each block. In Figures 3.2 and 3.3, we show the behaviour of the horizontal components of $\boldsymbol{\Phi}^*_{M_e,N_e}(\mathbf{x},t)$ and $\mathbf{u}^*_{M_e,N_e}(\mathbf{x}_0;t)$, for two values of the speed of wave propagation, i.e. $c = 1$ and $c = 343$.

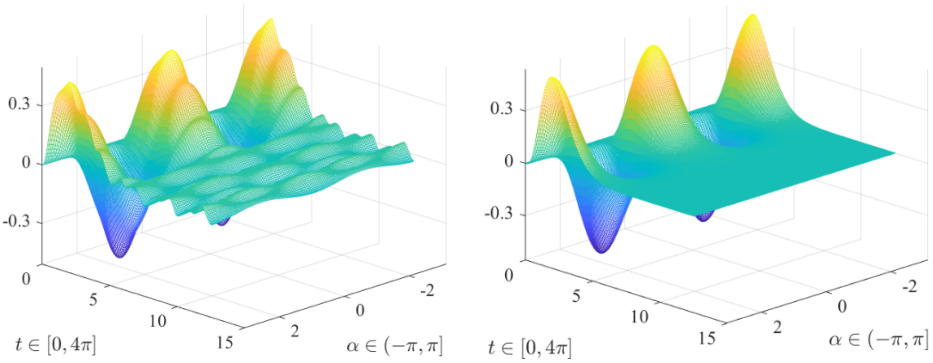

(a) (b)

Figure 3.2: Acoustic. Horizontal component of the reference density solution $\mathbf{\Phi}^*_{M_e,N_e}(\mathbf{x}, t)$ for $\mathbf{x} = (\cos\alpha, \sin\alpha)^\top$, with $\alpha \in (-\pi, \pi]$, and $t \in (0, 4\pi]$. Two values of the speed propagation are considered: $c = 1$ (a) and $c = 343$ (b).

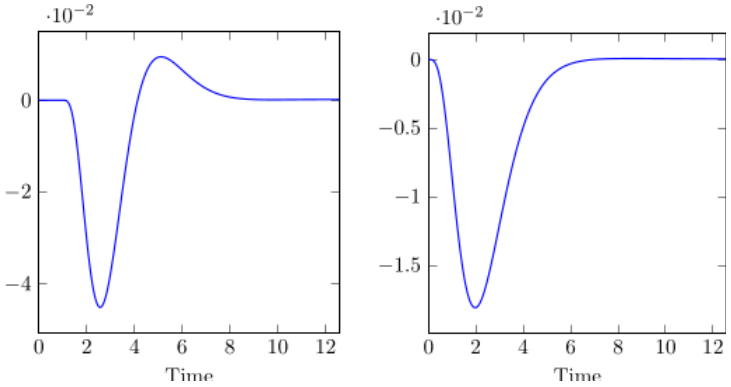

(a) (b)

Figure 3.3: Acoustics. Horizontal component of the reference displacement $\mathbf{u}^*_{M_e,N_e}((0,2)^\top, t)$ for $t \in (0, 4\pi]$. Two values of the speed propagation are considered: $c = 1$ (a) and $c = 343$ (b).

In Tables 3.2 and 3.3, we report the errors $E^{\mathbf{\Phi}}_{M,N}$ and $E^{\mathbf{u}}_{M,N}$, the corresponding EOCs and the percentages of memory saved, obtained by setting in (3.31) $\varepsilon_{\text{ACA}} = 1.0e-03$, $\varepsilon_{\text{ACA}} = 1.0e-04$ and $\varepsilon_{\text{ACA}} = 1.0e-05$ for the value of the speed of wave propagation $c = 1$, and $\varepsilon_{\text{ACA}} = 1.0e-04$, $\varepsilon_{\text{ACA}} = 1.0e-05$ and $\varepsilon_{\text{ACA}} = 1.0e-06$ when we consider $c = 343$.

We remark that we have obtained the same accuracy (at least up to the second significant digit) for all the considered choices of the threshold parameters, as well as for the standard (without ACA based compression) energetic BEM. This phenomenon is due to the fact that the highest value of the error is associated to the first time instants, whose corresponding blocks are stored in the standard (not compressed) format. On the other hand, as time passes, the blocks tends to become identically zero with decreasing rank and so their compression does not change the maximum error of the method, rather they are necessary for the stability of the global procedure.

As expected, since we use constant shape functions in space and in time, we observe a linear convergence rate for the approximate density $\mathbf{\Phi}_{M,N}$ and a quadratic convergence rate for the approximated potential $\mathbf{u}_{M,N}$.
In Tables 3.2 and 3.3, the high memory saving obtained with the proposed compression technique is visible, too. In particular, we underline that the memory saving improves when we increase the problem size. In particular, when we consider the speed of wave propagation $c = 343$ and for the values $M = 512$ and $N = 1024$, approximatively at most only 1.7% entries of the original matrices are needed for all the three considered parameters ε_{ACA}.

M	N	$E^{\mathbf{\Phi}}_{M,N}$	EOC	$E^{\mathbf{u}}_{M,N}$	EOC	mem $\varepsilon_{\text{ACA}} = 1.0e-03$	mem $\varepsilon_{\text{ACA}} = 1.0e-04$	mem $\varepsilon_{\text{ACA}} = 1.0e-05$
8	16	$2.67e-01$		$3.42e-02$		0.0%	0.0%	0.0%
			0.6		1.8			
16	32	$1.77e-01$		$9.87e-03$		12.5%	0.0%	0.0%
			1.0		1.9			
32	64	$8.47e-02$		$2.56e-03$		47.9%	39.0%	31.6%
			1.0		2.0			
64	128	$4.22e-02$		$6.28e-04$		66.1%	60.9%	57.6%
			1.0		1.7			
128	256	$2.03e-02$		$1.92e-04$		74.4%	72.1%	70.2%
			1.1		2.1			
256	512	$9.44e-03$		$4.41e-05$		78.4%	77.3%	76.4%
			1.2		2.0			
512	1024	$4.04e-03$		$1.09e-05$		80.3%	79.7%	79.4%

Table 3.2: Acoustics. Energetic BEM combined with the partially pivoted ACA. Absolute errors in L^2-norm of the boundary solution $\mathbf{\Phi}_{M,N}$ and absolute error of the external solution $\mathbf{u}_{M,N}$, with corresponding EOCs (speed of wave propagation $c = 1$).

M	N	$E^{\mathbf{\Phi}}_{M,N}$	EOC	$E^{\mathbf{u}}_{M,N}$	EOC	mem $\varepsilon_{\text{ACA}} = 1.0e-04$	mem $\varepsilon_{\text{ACA}} = 1.0e-05$	mem $\varepsilon_{\text{ACA}} = 1.0e-06$
8	16	$5.94e-01$		$8.54e-03$		37.5%	34.4%	25.0%
			0.7		0.4			
16	32	$3.54e-01$		$1.13e-02$		67.2%	65.6%	59.4%
			1.0		2.0			
32	64	$1.78e-01$		$2.83e-03$		84.6%	83.6%	83.6%
			1.0		2.0			
64	128	$8.95e-02$		$7.04e-04$		92.1%	91.5%	91.0%
			1.0		2.0			
128	256	$4.41e-02$		$1.78e-04$		96.0%	95.7%	95.0%
			1.0		2.0			
256	512	$2.13e-02$		$4.33e-05$		97.6%	97.5%	97.1%
			1.1		2.0			
512	1024	$9.93e-03$		$1.06e-05$		98.3%	98.2%	98.0%

Table 3.3: Acoustics. Energetic BEM combined with the partially pivoted ACA. Absolute errors in L^2-norm of the boundary solution $\mathbf{\Phi}_{M,N}$ and absolute error of the external solution $\mathbf{u}_{M,N}$, with corresponding EOCs (speed of wave propagation $c = 343$).

The reduction of the memory requirement for the energetic BEM gives rise to an acceler-

ation of the method even in terms of computation time, since with the ACA compression we do not have to compute all the elements of the temporal blocks. In the plots of Figure 3.4, we compare the CPU time needed by the standard energetic BEM and its ACA based acceleration for the computation of the M-by-M blocks $\mathbb{E}^{(l)}$ for $l = 0, ..., N$. The reported results are relative to the same discretization parameters M and N and thresholds considered in Tables 3.2 and 3.3. For both the speeds of wave propagation $c = 1$ (left plot) and $c = 343$ (right plot), we underline that the growth of the CPU time (measured in seconds) is optimal, i.e. $\mathcal{O}(NM)$.

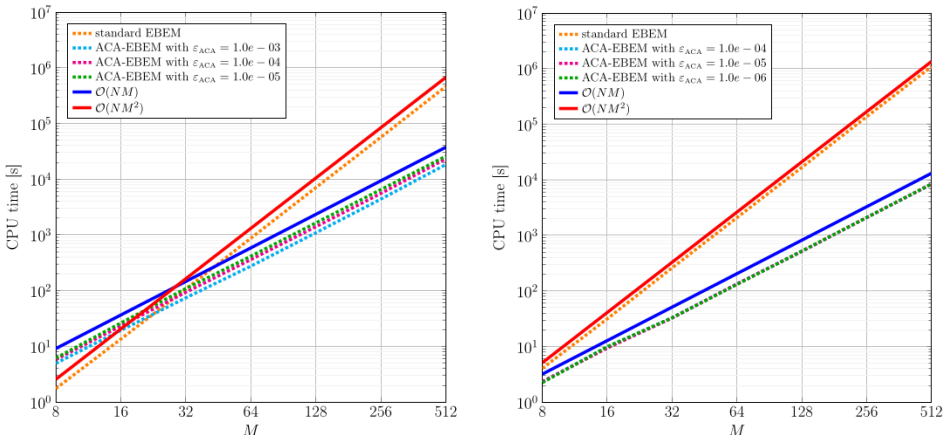

(a) (b)

Figure 3.4: Acoustics. CPU time required to assemble the BEM system by the standard energetic BEM and its ACA based acceleration with different values of ε_{ACA}, for the speeds of wave propagation $c = 1$ (a) and $c = 343$ (b).

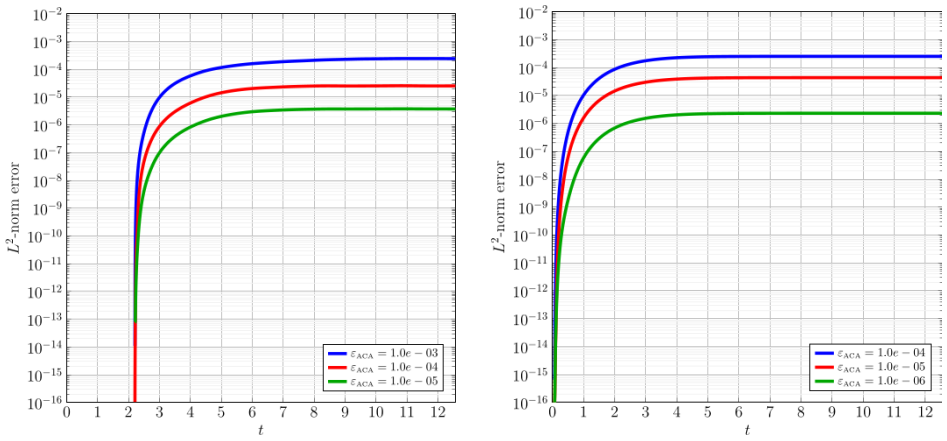

(a) (b)

Figure 3.5: Acoustics. Time history of the error in L^2 norm on the solution of the BEM system. In (a) the errors refers to the benchamarck problem with velocity $c = 1$, while in (b) the velocity considered is $c = 343$.

Finally, in the plots of Figure 3.5 we show the behaviour in time of the absolute error

$$E^{\mathbf{\Phi}}(t) := \left\| \mathbf{\Phi}^*_{M_e,N_e}(\cdot,t) - \mathbf{\Phi}_{M,N}(\cdot,t) \right\|_{L^2(\Gamma)} \qquad t \in [0,4\pi], \tag{3.39}$$

where the reference and the approximate solutions are obtained by choosing the same discretization parameters $M_e = M = 4096$ and $N_e = N = 8192$. In the left graph, the transient phase, where the blocks are stored in standard (not compressed) format, is cleary visible. For both the considered speeds of the wave propagation, we observe that, as time passes, the level of error introduced by the ACA can be controlled by the parameter ε_{ACA}, since the former is at most of the same order of magnitude of the latter.

Elastodynamics

Now, we consider an exterior Dirichlet elastic problem with the velocities $c_{\text{S}} = 1$ and $c_{\text{P}} = 2$ and the datum $\mathbf{g}_{\mathcal{D}}(\mathbf{x},t) = (g_{\mathcal{D},1}, g_{\mathcal{D},2})^\top(\mathbf{x},t)$, where

$$g_{\mathcal{D},1}(\mathbf{x},t) = t^4 e^{-2t} x_1 \quad \text{and} \quad g_{\mathcal{D},2}(\mathbf{x},t) = t^4 e^{-2t} x_2 \qquad \mathbf{x} \in \Gamma,\ t \in [0,4\pi].$$

Unfortunately the blocks of the energetic BEM in the elastodynamics case do not have the special Toeplitz structure thalt helped us, in the acoustic case, to construct a reference solution depending on an high level of mesh refinement in space and time. Therefore, to calculate a reference elastodynamics solution we have to compute and store all the entries of the BEM matrices, and due to that we are limited in the choice of the parameters $M_e = 512$ and $N_e = 2048$. In Figure 3.6, we plot the two components of the reference solution $\mathbf{\Phi}^*_{M_e,N_e}(\mathbf{x},t)$ on Γ, while in Figure 3.7 we show only the vertical component of the reconstructed field $\mathbf{u}^*_{M_e,N_e}(\mathbf{x}_0;t)$ at the point $\mathbf{x}_0 = (0,2)^\top$, because the horizontal ones is null.

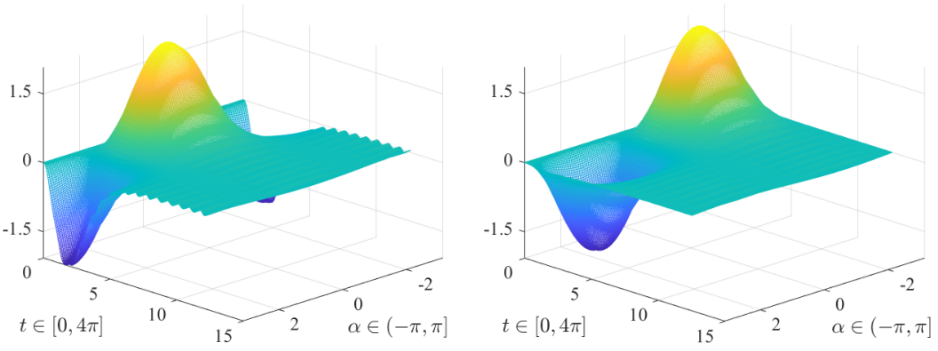

Figure 3.6: Elastodynamics. Horizontal (a) and vertical (b) components of the reference density solution $\mathbf{\Phi}^*_{M_e,N_e}(\mathbf{x},t)$ for $\mathbf{x} = (\cos\alpha, \sin\alpha)^\top$, with $\alpha \in (-\pi,\pi]$, and $t \in (0,4\pi]$. The two peculiar elastodynamics velocities are set to be $c_{\text{S}} = 1$ and $c_{\text{P}} = 2$.

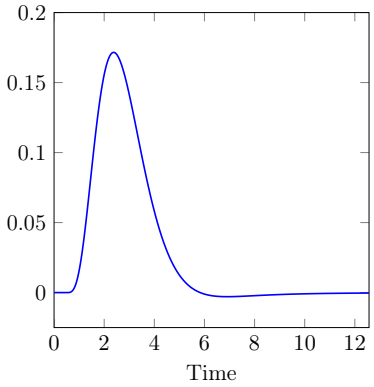

Figure 3.7: Elastodynamics. Time history of the vertical component of the reference potential solution $\mathbf{u}^*_{M_e,N_e}((0,2)^\top,t)$ for $t \in (0,4\pi]$ and for the two speeds of wave propagation $c_{\mathrm{S}} = 1$ and $c_{\mathrm{P}} = 2$.

In Table 3.4 we report the errors $E^{\boldsymbol{\Phi}}_{M,N}$ and $E^{\mathbf{u}}_{M,N}$, the corresponding estimated order of convergence (EOC) and the memory saving for three different values of the threshold parameter in (3.31), i.e. $\varepsilon_{\mathrm{ACA}} = 1.0e-03$, $\varepsilon_{\mathrm{ACA}} = 1.0e-04$ and $\varepsilon_{\mathrm{ACA}} = 1.0e-05$.

M	N	$E^{\boldsymbol{\Phi}}_{M,N}$	EOC	$E^{\mathbf{u}}_{M,N}$	EOC	mem $\varepsilon_{\mathrm{ACA}} = 1.0e-03$	mem $\varepsilon_{\mathrm{ACA}} = 1.0e-04$	mem $\varepsilon_{\mathrm{ACA}} = 1.0e-05$
8	32	$6.29e-01$		$1.81e-02$		0.0%	0.0%	0.0%
			1.0		1.9			
16	64	$3.11e-01$		$4.81e-03$		13.8%	0.0%	0.0%
			1.1		2.2			
32	128	$1.49e-01$		$1.07e-03$		48.4%	38.7%	30.5%
			1.2		1.9			
64	256	$6.44e-02$		$2.88e-04$		65.0%	60.2%	55.9%
			1.5		2.4			
128	512	$2.15e-02$		$5.35e-05$		73.2%	71.0%	68.3%

Table 3.4: Elastodynamics. Energetic BEM combined with the partially pivoted ACA. Absolute errors in L^2-norm of the boundary solution $\boldsymbol{\Phi}_{M,N}$ and absolute error of the external solution $\mathbf{u}_{M,N}$, with corresponding EOCs (speeds of wave propagation $c_{\mathrm{S}} = 1$ and $c_{\mathrm{P}} = 2$).

As in the acoustic case, the choice of the parameter $\varepsilon_{\mathrm{ACA}}$ does not influence the errors but only the memory saving. Furthermore, the EOCs reported in the above table confirm the first order convergence rate for the density function $\boldsymbol{\Phi}$ and the second order convergence rate for the solution $\mathbf{u}$. By comparing the results reported in Tables 3.2 and 3.4 we note the same level of accuracy and memory saving of the method for both the acoustic and the elastic models. As a consequence of the reduction of the memory requirement for the energetic BEM, we have an acceleration of the construction of the time blocks. In Figure 3.8 we show that the CPU time (measured in second) needed to assemble the energetic BEM system is proportional to NM, where the values of the discretization parameters are the same of the ones in Table 3.4.

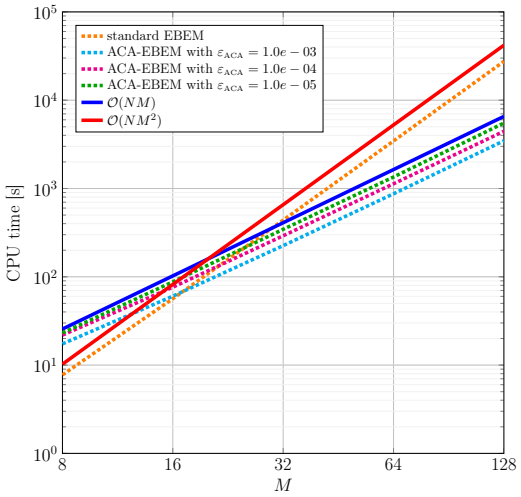

Figure 3.8: Elastodynamics. CPU time required to assemble the BEM system by the standard energetic BEM and its ACA based acceleration with different values of ε_{ACA}, for the speeds of wave propagation $c_{\text{S}} = 1$ and $c_{\text{P}} = 2$.

Finally, in Figure 3.9 we show the time history of the absolute L^2-error, calculated as in (3.39), between the approximate solution $\mathbf{\Phi}^*_{M_e,N_e}(\mathbf{x},t)$ obtained with the standard energetic BEM, and the approximate solution $\mathbf{\Phi}_{M,N}(\mathbf{x},t)$ obtained with the proposed ACA based acceleration, for the choice of the discretization parameters $M_e = M = 512$ and $N_e = N = 2048$. We have considered three different values of the threshold ε_{ACA} and, as in the acoustic case, the order of the error on the solution of the BEM system turns out to be controlled by the fixed parameter.

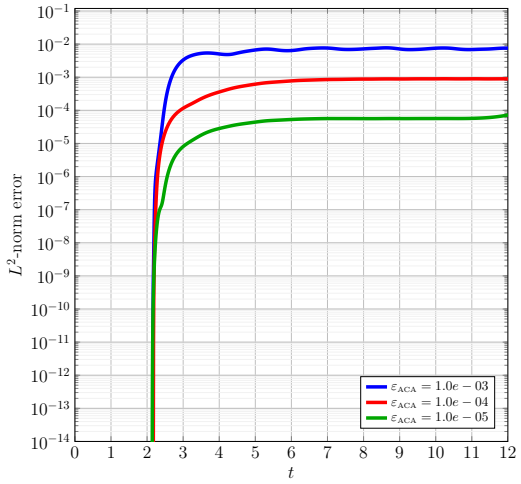

Figure 3.9: Elastodynamics. Time history of the error in L^2 norm on the solution of the BEM system.

3.4.2 Example 2. Application to scattering problems.

Let us consider, as example of application, the scattering of acoustic and elastic waves in homogeneous materials. The boundary we consider for these silmualtions is again the circumference of radius 1 centred in $(0,0)^\top$. The total wave field $\mathbf{u}^c$ is given by the sum of the incident wave $\mathbf{u}^{inc}$ and the scattered one $\mathbf{u}$, where the latter is the solution of problem (3.1) with the Dirichlet datum $\mathbf{g}_\mathcal{D}(\mathbf{x},t) = -\mathbf{u}^{inc}(\mathbf{x},t)$ on the boundary Γ.

Acoustics

In the acoustic case, the incident field is composed by four subsequent plane waves propagating from the right to the left:

$$\mathbf{u}^{inc}(\mathbf{x},t) = \left(\sum_{i=1}^{4} e^{-2(x_1-\xi_i+c(t+t_0))^2}, 0\right)^\top \qquad \text{with } t_0 = 0.13 \text{ and } \xi_i = 50, 55, 60, 65.$$

The four plane waves propagate with velocity $c = 343$, which is also the value of the peculiar velocity of the acoustic problem we want to solve. We solve the problem in the time interval $[0, 0.15]$ by means of the ACA based acceleration of the energetic BEM. For the space discretization we set the parameter $M = 128$, while the time interval of interest is subdivided into $N = 1049$ subintervals. In this numerical test the ACA threshold is $\varepsilon_{\text{ACA}} = 1.0e-04$ with a consequently memory saving of 87.3%.

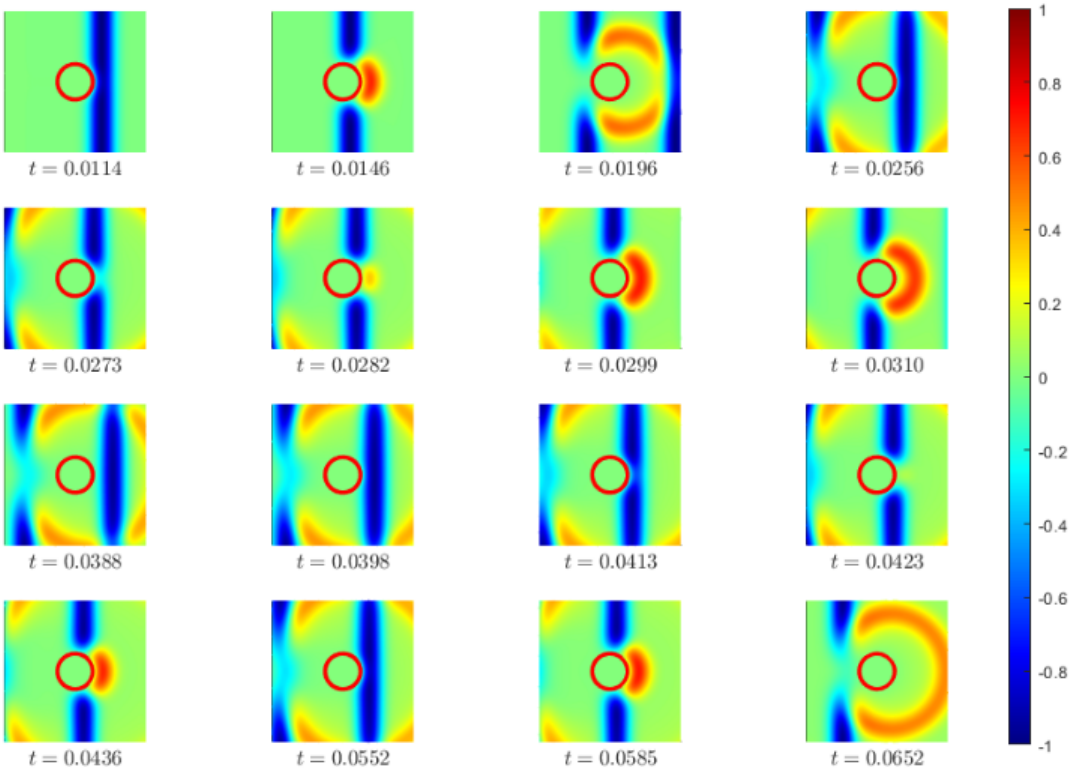

Figure 3.10: Acoustic scattering problem. Snapshots of the reconstructed horizontal component of the total field $\mathbf{u}^c$ around the obstacle at different time instants.

As observed previously, the boundary datum is purely horizontal, meaning that, for the acoustic case, the vertical components of the total wave field is trivial. Due to that, in Figure 3.10, we show the snapshots of the horizontal total field at different instants and in the points belonging to the square domain $[-4,4] \times [-4,4]$ and external also to the circumference.

Elastodynamics

We consider the total scatterer generated by the incident pressure plane wave

$$\mathbf{u}^{inc}(\mathbf{x},t) = \left(e^{-20(x_1-2+c_\mathrm{P}t-0.475)^2}, 0\right)^\top,$$

impinging on the obstacle from the right. Since in many elastic materials the Poisson's relation holds, i.e. $\lambda = \mu$, we assume $c_\mathrm{S} = 1$ and $c_\mathrm{P} = \sqrt{3}$. The spatial discretization parameter used to compute the approximate solution is $M = 128$ and we fix $N = 426$ equispaced time instants within the interval $[0, 12]$. The threshold parameter is $\varepsilon_{\mathrm{ACA}} = 1.0e{-}04$ that gives rise to a memory saving of 71.1%.
In Figures 3.11 and 3.12 we present several snapshots related to the horizontal and the vertical components of the total wave field, respectively, reconstructed in a square domain external to the obstacle for different time instants. As expected, the vertical component appears once the solution in horizontal direction, generated by the given Dirichlet datum, bumps against the obstacle and is reflected back.

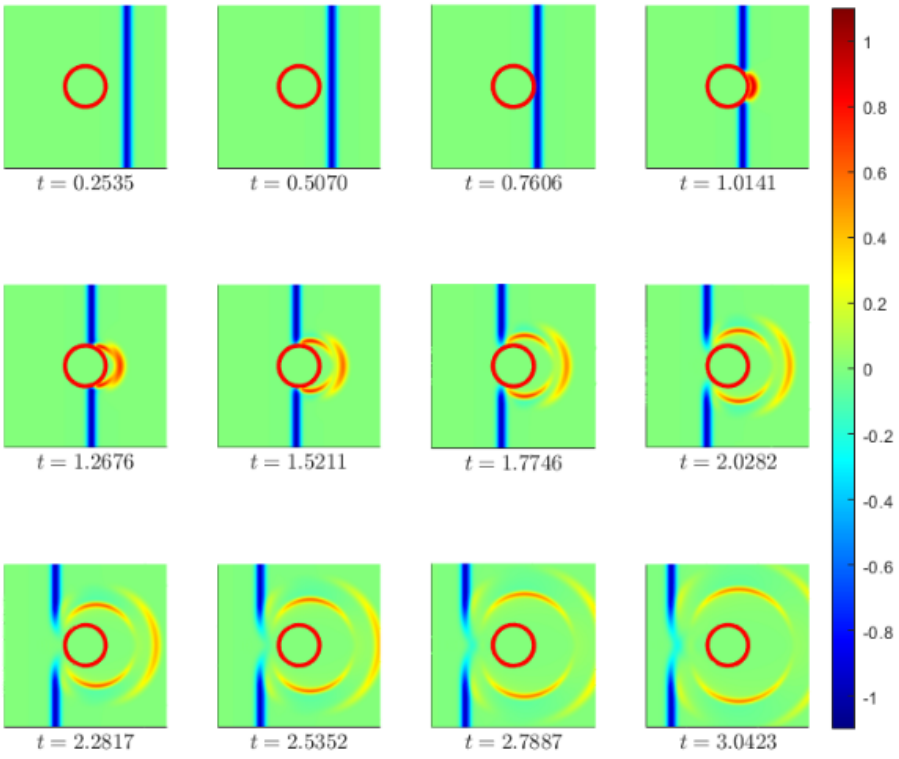

Figure 3.11: Elastodynamic scattering problem. Snapshots of the component in the horizontal direction of the reconstructed total field $\mathbf{u}^{\mathrm{c}}$ around the obstacle at different time instants.

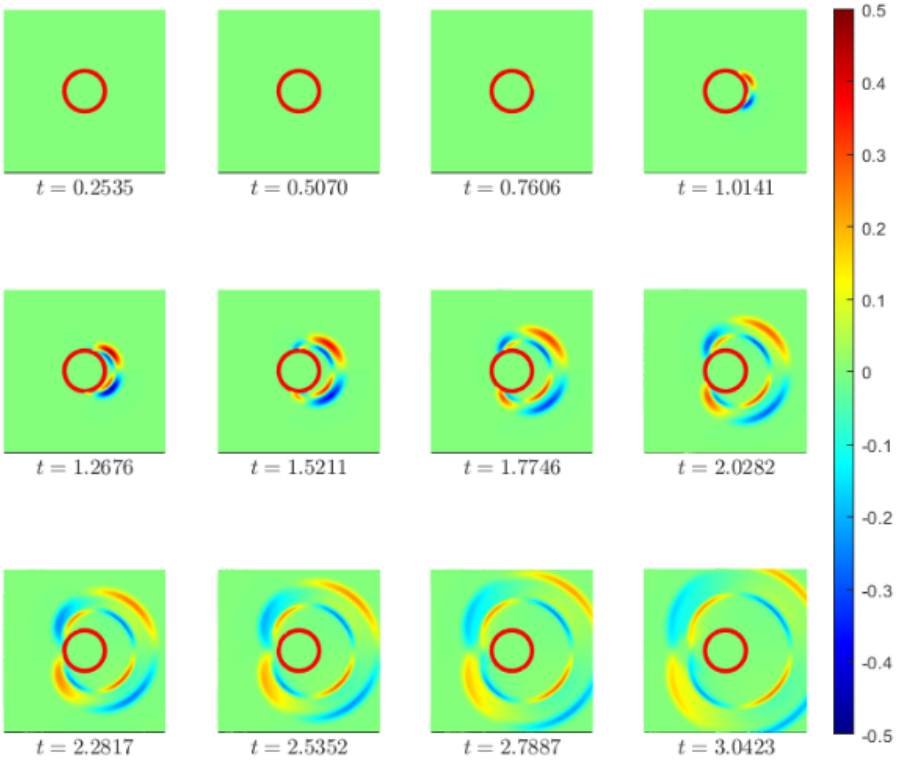

Figure 3.12: Elastodynamic scattering problem. Snapshots of the component in the vertical direction of the reconstructed total field $\mathbf{u}^c$ around the obstacle at different time instants.

Chapter 4

Quadrature strategies

The quadrature schemes adopted to compute, with high precision, the space integrals required to calculate the matrix entries defined in (1.78), (1.88) and (1.94) are the core of the entire chapter.
An explicit integration in the spatial variables, as done in time in Appendix A, is not adequate because of the dependence of the integrand on shape functions with generic polynomial degree. It is indeed necessary to employ quadrature formulas to perform as best as possible the spatial integration, and the choice of a correct numerical strategy is based on the peculiarity of the kernels ν_{ij}^V, ν_{ij}^D and ν_{ij}^K.
These are characterized by the discontinuous step functions $H[c_{\mathrm{P}}\Delta - r]$ and $H[c_{\mathrm{S}}\Delta - r]$, modeling the wave fronts propagating with the fundamental velocities c_{P} and c_{S}. It is worth to point out that the numerical approximation of the matrix entries by means of classical Gaussian integration formulas applied straightforward to the whole interval of integration could require a lot of quadrature nodes just to achieve the single precision accuracy. To overcome this drawback, in the following we propose an accurate study of suitable domain splittings that allows us to determine a priori the value of the step functions and to avoid their explicit expression in programming phase.
Moreover in the following, for what concerns the type of spatial singularities we can encounter in the computation of matrix entries, such as $\mathcal{O}(\log(r))$, $\mathcal{O}(1/r)$, $\mathcal{O}(1/r^2)$ and the mild singularities of the square roots $\sqrt{c_{\mathrm{S}}^2\Delta^2 - r^2}$ and $\sqrt{c_{\mathrm{P}}^2\Delta^2 - r^2}$, we will localize precisely the regions of the integration domain where they appear and we will propose ad hoc numerical techniques to treat them.

Remark. The dissertation in Section 4.1 is presented also in the Author's paper [6].

4.1 Mutual position of the integration segments and splitting of the integration domain

The space time-discretiziation described in Section 1.5 provides a decomposition of the obstacle Γ in a set of straight line segments $\mathcal{T} = \{e_1, \ldots, e_M\}$, so that the value of the matrix elements (1.78), (1.88) and (1.94) can be reduced to the sum of contributions

integrated over two generic segments $e_{\widetilde{m}}$ and e_m belonging to the spatial mesh $\mathcal{T}$:

$$\int_{e_{\widetilde{m}}} \int_{e_m} w_{\widetilde{m}}(\mathbf{x}) w_m(\boldsymbol{\xi}) B_{ij}(\mathbf{r}; \Delta) d\Gamma_{\boldsymbol{\xi}} d\Gamma_{\mathbf{x}} \tag{4.1}$$

where the function B_{ij} assumes the role of one of the peculiar kernels ν_{ij}^V, ν_{ij}^D or ν_{ij}^K, Δ is a positive time difference and $e_{\widetilde{m}}$, e_m belong to the supports of $w_{\widetilde{m}}$, w_m respectively. Upper apexes $\mathbf{p}$ and/or $\mathbf{u}$ are dropped out since the type of shape functions can be understood by the choice of the integral kernel B_{ij}. Moreover, with the notation $\mathbb{E}_B$, we will refer to the Toeplitz matrix corresponding to the integral kernel B_{ij}.
If we consider the following linear parametrization of the mesh segments

$$\mathbf{x} \in e_{\widetilde{m}} \leftrightarrows s \in [0, h_{\widetilde{m}}], \quad \boldsymbol{\xi} \in e_m \leftrightarrows z \in [0, h_m],$$

where $h_{\widetilde{m}}$ and h_m are the lengths of $e_{\widetilde{m}}$ and e_m respectively, the *contribution* (4.1) corresponds to the integral in the local variables s and z

$$\int_0^{h_{\widetilde{m}}} \int_0^{h_m} w_{\widetilde{\eta}}^{(d_{\widetilde{m}})}(s) w_{\eta}^{(d_m)}(z) B_{ij}(\mathbf{r}(s,z); \Delta) dz ds, \tag{4.2}$$

where $w_{\widetilde{\eta}}^{(d_{\widetilde{m}})}$ and $w_{\eta}^{(d_m)}$, with $\widetilde{\eta} = 1, ..., d_{\widetilde{m}}$ and $\eta = 1, ..., d_m$, denote the Lagrangian polynomials of degree $d_{\widetilde{m}}$ and d_m that determine the spatial basis functions $w_{\widetilde{m}}$ and w_m, respectively, over the mesh elements $e_{\widetilde{m}}$ and e_m. Also the degrees $d_{\widetilde{m}}$ and d_m are related to the type of integration kernel we consider in (4.2). The definitions of the vectorial components r_1 and r_2 and of the distance r between the field and the source point $\mathbf{x}$ and $\boldsymbol{\xi}$, introduced in (1.15), are closely related to the local geometry of the mesh elements and this leads to a different treatments of the domain subdivision schemes, based on the mutual position of the mesh elements $e_{\widetilde{m}}$ and e_m.

4.1.1 Coincident boundary elements

If $e_{\widetilde{m}} \equiv e_m$ the expression of r corresponds to the module $|s - z|$. The vectorial components r_1 and r_2 respectively read $(s-z)\cos\theta$ and $(s-z)\sin\theta$, where the angle θ represents the inclination of the e_m element in the reference system where Γ is defined, represented in Figure 4.1 with the two red dashed lines.
Setting

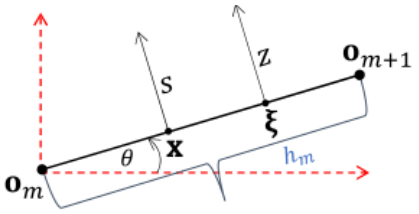

Figure 4.1: Parametrization of e_m.

$$E_{\mathsf{S}} = \left\{(s,z) \in \mathbf{R}^2 \ : \ 0 \leqslant r(s,z) \leqslant c_{\mathsf{S}}\Delta\right\}, \tag{4.3}$$

$$E_{\mathsf{S,P}} = \left\{(s,z) \in \mathbf{R}^2 \ : \ c_{\mathsf{S}}\Delta < r(s,z) \leqslant c_{\mathsf{P}}\Delta\right\}, \tag{4.4}$$

and identifying their intersections with the local square domain respectively with

$$\widehat{E}_{\mathsf{S}} := E_{\mathsf{S}} \cap [0, h_m]^2, \quad \widehat{E}_{\mathsf{S,P}} := E_{\mathsf{S,P}} \cap [0, h_m]^2,$$

the double integral (4.2) assumes the form

$$\begin{aligned}&\int_0^{h_m}\int_0^{h_m} w_{\widetilde{\eta}}^{(d_{\widetilde{m}})}(s)w_{\eta}^{(d_m)}(z)B_{ij}(\mathbf{r};\Delta)dzds\\ =&\int_{\widehat{E}_{\mathtt{S}}} w_{\widetilde{\eta}}^{(d_{\widetilde{m}})}(s)w_{\eta}^{(d_m)}(z)B_{ij}(\mathbf{r};\Delta)dzds+\int_{\widehat{E}_{\mathtt{S,P}}} w_{\widetilde{\eta}}^{(d_{\widetilde{m}})}(s)w_{\eta}^{(d_m)}(z)B_{ij}(\mathbf{r};\Delta)dzds\\ =:&\mathcal{I}_1+\mathcal{I}_2.\end{aligned}$$

The time difference Δ is related to the index l of the specific temporal block of $\mathbb{E}_B^{(l)}$ we intend to compute, meaning that its value increases as time evolves. In particular, if $c_{\mathtt{S}}\Delta \geqslant h_m$ then $\widehat{E}_{\mathtt{S}} = [0, h_m]^2$, as indicated in Figure 4.2 (d), and $\widehat{E}_{\mathtt{S,P}} = \emptyset$, so we do not need to split (4.2), because the argument of the Heaviside functions in B_{ij} (we remember that this can corresponds to one of the integral kernels defined in (1.79), (1.89) or (1.95)) is always positive.
Instead, for $c_{\mathtt{S}}\Delta < h_m$, the splitting is not trivial. In this case, we firstly focus on the integration domain of the addend $\mathcal{I}_1$: a point (s, z) belongs to $E_{\mathtt{S}}$ if and only if $s - c_{\mathtt{S}}\Delta < z < s + c_{\mathtt{S}}\Delta$. The two straight lines of equation $z = s \pm c_{\mathtt{S}}\Delta$ compose the boundary of $E_{\mathtt{S}}$ and determine the inner extremes of integration. Hence we can rewrite integral $\mathcal{I}_1$ as

$$\mathcal{I}_1 = \int_0^{h_m} w_{\widetilde{\eta}}^{(d_{\widetilde{m}})}(s)\int_{M_s}^{m_s} w_{\eta}^{(d_m)}(z)B_{ij}(\mathbf{r};\Delta)dzds,$$

where

$$M_s = \max\{0, s - c_{\mathtt{S}}\Delta\},\ m_s = \min\{h_m, s + c_{\mathtt{S}}\Delta\}.$$

Outer integration requires an additional subdivision since M_s and m_s have discontinuous derivatives respectively for $s = c_{\mathtt{S}}\Delta$ and $s = h_m - c_{\mathtt{S}}\Delta$, where $z = s \pm c_{\mathtt{S}}\Delta$ intersect the axes $z = 0$ and $z = h_m$. The position of the corner points can assume three different configurations, as shown in Figures 4.2 (a,b,c), and it can determine different types of subdivision of $\widehat{E}_{\mathtt{S}}$, telling us that integral $\mathcal{I}_1$ can be further rewritten as the sum of at most three contributions:

$$\begin{aligned}\mathcal{I}_1 =& \int_0^{a} w_{\widetilde{\eta}}^{(d_{\widetilde{m}})}(s)\int_0^{s+c_{\mathtt{S}}\Delta} w_{\eta}^{(d_m)}(z)B_{ij}(\mathbf{r};\Delta)dzds+\int_a^{b} w_{\widetilde{\eta}}^{(d_{\widetilde{m}})}(s)\int_{M_s}^{m_s} w_{\eta}^{(d_m)}(z)B_{ij}(\mathbf{r};\Delta)dzds\\ &+\int_b^{h_m} w_{\widetilde{\eta}}^{(d_{\widetilde{m}})}(s)\int_{s-c_{\mathtt{S}}\Delta}^{h_m} w_{\eta}^{(d_m)}(z)B_{ij}(\mathbf{r};\Delta)dzds,\end{aligned} \tag{4.5}$$

with $a = \min\{c_{\mathtt{S}}\Delta,\ h_m - c_{\mathtt{S}}\Delta\}$ and $b = \max\{c_{\mathtt{S}}\Delta,\ h_m - c_{\mathtt{S}}\Delta\}$. Trivially, the second term in (4.5) results null if $a = b$.
Let us now consider $\mathcal{I}_2$: a point (s, z) belongs to $E_{\mathtt{S,P}}$ if and only if $s - c_{\mathtt{P}}\Delta < z < s - c_{\mathtt{S}}\Delta$ or $s + c_{\mathtt{S}}\Delta < z < s + c_{\mathtt{P}}\Delta$, defining then two strips intersecting $[0, h_m]^2$. If $c_{\mathtt{P}}\Delta \geqslant h_m$ then the lines $z = s \pm c_{\mathtt{P}}\Delta$ lie outside the square (see Figure 4.3), so the unique splitting points on the s-axis are still $c_{\mathtt{S}}\Delta$ and $h_m - c_{\mathtt{S}}\Delta$ and we can therefore rewrite the double integral $\mathcal{I}_2$ as follows:

$$\mathcal{I}_2 = \int_0^{h_m - c_{\mathtt{S}}\Delta} w_{\widetilde{\eta}}^{(d_{\widetilde{m}})}(s)\int_{s+c_{\mathtt{S}}\Delta}^{h_m} w_{\eta}^{(d_m)}(z)B_{ij}(\mathbf{r};\Delta)dzds+\int_{c_{\mathtt{S}}\Delta}^{h_m} w_{\widetilde{\eta}}^{(d_{\widetilde{m}})}(s)\int_0^{s-c_{\mathtt{S}}\Delta} w_{\eta}^{(d_m)}(z)B_{ij}(\mathbf{r};\Delta)dzds.$$

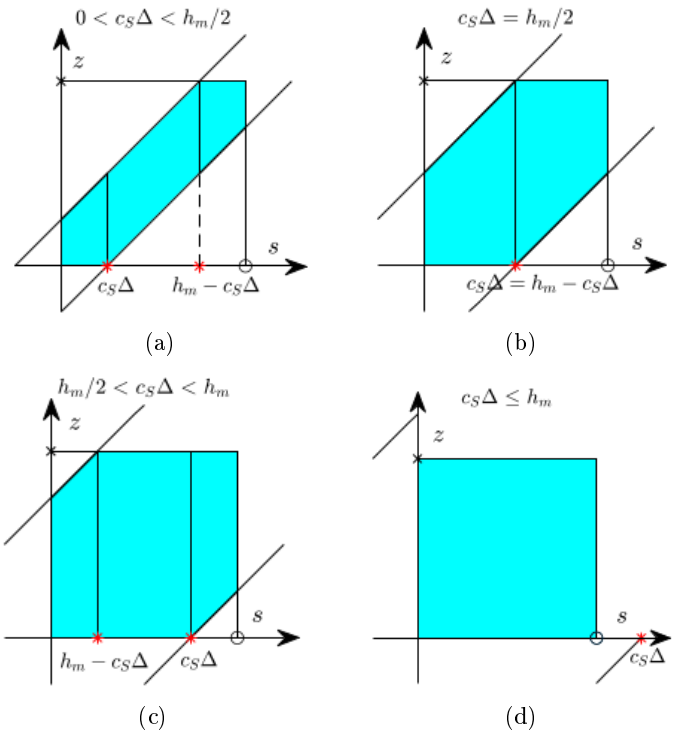

Figure 4.2: Shapes of domain $\widehat{E}_{\mathrm{S}}$ in relation to the position of the splitting points $s = c_{\mathrm{S}}\Delta$ and $s = h_m - c_{\mathrm{S}}\Delta$ on the s-axis. The symbols $\times$ and o indicate the points with local coordinates $(0, h_m)$ and $(h_m, 0)$, respectively.

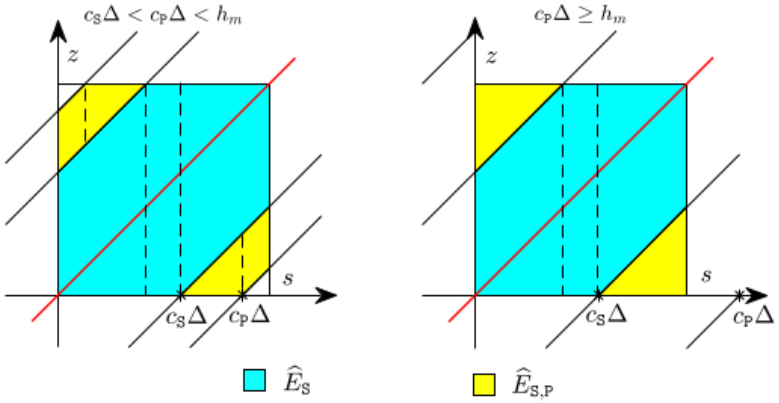

Figure 4.3: Example of two-dimensional integration domain (coincident elements) for two different values of $c_{\mathrm{P}}\Delta$: dashed lines inside the square $[0, h_m]^2$ represent the boundaries of the polygonal regions where we have to divide the domain. Black lines circumscribing $\widehat{E}_{\mathrm{S}}$ and $\widehat{E}_{\mathrm{S,P}}$ have equations $z = s \pm c_{\mathrm{S}}\Delta$ and $z = s \pm c_{\mathrm{P}}\Delta$ while the red line indicates the equation $z = s$, along which the kernel B_{ij} is singular.

If $0 < c_{\mathrm{P}}\Delta < h_m$ then the splitting points $c_{\mathrm{P}}\Delta$ and $h_m - c_{\mathrm{P}}\Delta$ are considered together with the previous ones, because they lie in the interval $[0, h_m]$. Hence, we can rewrite $\mathcal{I}_2$ as the

sum of four integrals

$$\mathcal{I}_2 = \int_0^{h_m - c_P\Delta} w_{\widetilde{\eta}}^{(d_{\widetilde{m}})}(s) \int_{s+c_S\Delta}^{s+c_P\Delta} w_{\eta}^{(d_m)}(z) B_{ij}(\mathbf{r};\Delta) dz ds + \int_{h_m - c_P\Delta}^{h_m - c_S\Delta} w_{\widetilde{\eta}}^{(d_{\widetilde{m}})}(s) \int_{s+c_S\Delta}^{h_m} w_{\eta}^{(d_m)}(z) B_{ij}(\mathbf{r};\Delta) dz ds$$
$$+ \int_{c_S\Delta}^{c_P\Delta} w_{\widetilde{\eta}}^{(d_{\widetilde{m}})}(s) \int_0^{s-c_S\Delta} w_{\eta}^{(d_m)}(z) B_{ij}(\mathbf{r};\Delta) dz ds + \int_{c_P\Delta}^{h_m} w_{\widetilde{\eta}}^{(d_{\widetilde{m}})}(s) \int_{s-c_P\Delta}^{s-c_S\Delta} w_{\eta}^{(d_m)}(z) B_{ij}(\mathbf{r};\Delta) dz ds.$$

If we keep focusing on Figure 4.3, we observe that the red line representing the axis $s = z$ lies totally inside the E_S domain, meaning that the singular behaviour of the kernel B_{ij} arises only in the integration domains typical of the splitting schemes of integral $\mathcal{I}_1$.
If the splitting scheme of (4.2) is not trivial ($c_S\Delta < h_m$ and, possibly, $c_P\Delta < h_m$) we have also to pay attention to the square root functions $\sqrt{c_S^2\Delta^2 - r^2}$ and $\sqrt{c_P^2\Delta^2 - r^2}$, which are characterized by mild singularities in the first derivative on the lines delimiting $E_{S,P}$ and E_S, respectively.

4.1.2 Consecutive boundary elements

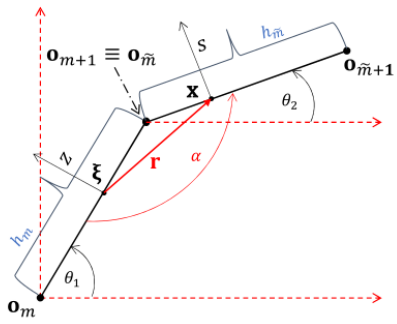

Figure 4.4: Parametrization of the two consecutive segments e_m and $e_{\widetilde{m}}$.

For this configuration we consider at first two elements e_m and $e_{\widetilde{m}}$ such that $\mathbf{o}_{m+1} \equiv \mathbf{o}_{\widetilde{m}}$. In addition we suppose that the convex angle α between them (see Figure 4.4) belongs to the interval $\left[\frac{\pi}{2}, \pi\right]$, hence analysis of aligned elements case is included. After the parametrization of the elements, the distance r in local coordinates $(s, z) \in [0, h_{\widetilde{m}}] \times [0, h_m]$ is given by

$$r = \sqrt{(h_m - z)^2 + s^2 - 2(h_m - z)s\cos\alpha}. \tag{4.6}$$

and the components of the vector $\mathbf{r} = \mathbf{x} - \boldsymbol{\xi}$ are

$$r_1 = (h_m - z)\tau_{11} + s\tau_{12}, \tag{4.7}$$
$$r_2 = (h_m - z)\tau_{21} + s\tau_{22}, \tag{4.8}$$

where $\tau_{1i} = \cos\theta_i$ and $\tau_{2i} = \sin\theta_i$ for $i = 1, 2$. We remark in addition that the angles θ_1 and θ_2 depend on the reference system as shown in Figure 4.4. Also for this configuration it is necessary to rewrite the double integral (4.2) as the sum of the two integrals $\mathcal{I}_1$ and $\mathcal{I}_2$ calculated over the intersection between the rectangle $[0, h_{\widetilde{m}}] \times [0, h_m]$ and the domains E_S and $E_{S,P}$, defined in (4.3)-(4.4). Also for consecutive elements we identify the mentioned intersections as

$$\widehat{E}_S := E_S \cap [0, h_{\widetilde{m}}] \times [0, h_m], \quad \widehat{E}_{S,P} := E_{S,P} \cap [0, h_{\widetilde{m}}] \times [0, h_m],$$

from which we deduce the first splitting of integral (4.2):

$$\int_0^{h_{\widetilde{m}}} \int_0^{h_m} w_{\widetilde{\eta}}^{(d_{\widetilde{m}})}(s) w_{\eta}^{(d_m)}(z) B_{ij}(\mathbf{r};\Delta) dz ds$$
$$= \int_{\widehat{E}_S} w_{\widetilde{\eta}}^{(d_{\widetilde{m}})}(s) w_{\eta}^{(d_m)}(z) B_{ij}(\mathbf{r};\Delta) dz ds + \int_{\widehat{E}_{S,P}} w_{\widetilde{\eta}}^{(d_{\widetilde{m}})}(s) w_{\eta}^{(d_m)}(z) B_{ij}(\mathbf{r};\Delta) dz ds$$
$$=: \mathcal{I}_1 + \mathcal{I}_2.$$

Let us consider $E_{\mathtt{S}}$. Due to the definition (4.6), for consecutive elements the boundary of this domain is characterized by the points satisfying the equation

$$(h_m - z)^2 + s^2 - 2(h_m - z)s\cos\alpha - c_{\mathtt{S}}^2\Delta^2 = 0. \tag{4.9}$$

If $\alpha \neq \pi$ the equation (4.9) describes an ellipse having center in the unique singular point $(0, h_m)$. Due to the range of α, the major semiaxis has direction $(1, 1)$. If $\alpha = \pi$, the elements result aligned and the elliptic region $E_{\mathtt{S}}$ becomes a domain bounded by two parallel lines, symmetric w.r.t. the line $z = h_m + s$. In any case, the $E_{\mathtt{S}}$ boundary can be seen as the union of the graphs of the functions:

$$z_{\mathtt{S}}^+(s) = h_m - s\cos\alpha + \sqrt{-s^2\sin^2\alpha + c_{\mathtt{S}}^2\Delta^2}, \quad z_{\mathtt{S}}^-(s) = h_m - s\cos\alpha - \sqrt{-s^2\sin^2\alpha + c_{\mathtt{S}}^2\Delta^2}, \tag{4.10}$$

with $s \in \left[-\frac{c_{\mathtt{S}}\Delta}{|\sin\alpha|}, \frac{c_{\mathtt{S}}\Delta}{|\sin\alpha|}\right]$. If $\alpha = \pi$ the s variable belongs to the whole $\mathbb{R}$ and the functions $z_{\mathtt{S}}^{\pm}(s)$ in (4.10) describe the superior and the inferior lines delimiting $E_{\mathtt{S}}$. In Figure 4.5 one can see a graphical representation of all the possible configurations for $E_{\mathtt{S}}$.

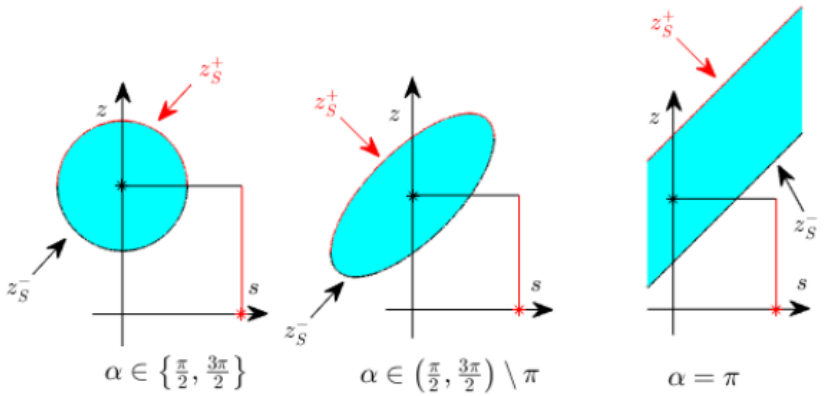

Figure 4.5: The domain $E_{\mathtt{S}}$, the rectangle $[0, h_{\widetilde{m}}] \times [0, h_m]$, the points $*= (h_{\widetilde{m}}, 0)$, $* = (0, h_m)$ and the functions $z_{\mathtt{S}}^{\pm}(s)$ for different values of α. We observe that, if $\alpha = \frac{\pi}{2}, \frac{2\pi}{3}$ then $E_{\mathtt{S}}$ is a circular region and if $\alpha = \pi$ then $E_{\mathtt{S}}$ is a strip.

To analyze the intersection $\widehat{E}_{\mathtt{S}}$ we also need to solve the equation (4.9) with respect to s, setting $z = 0, h_m$ in particular. Intersections with the axis $z = 0$ exist if and only if the discriminant $\mathcal{D}_{\mathtt{S}} = -h_m^2\sin^2\alpha + c_{\mathtt{S}}^2\Delta^2$ is non negative, and they correspond to the s-coordinates

$$s_{\mathtt{S}}^{(1)} = h_m\cos\alpha - \sqrt{\mathcal{D}_{\mathtt{S}}}, \quad s_{\mathtt{S}}^{(2)} = h_m\cos\alpha + \sqrt{\mathcal{D}_{\mathtt{S}}}.$$

The intersections with the axis $z = h_m$ always exist and have abscissas $s = \pm c_{\mathtt{S}}\Delta$. In case of not aligned elements, i.e. $\alpha \neq \pi$, we have $z_{\mathtt{S}}^+(s) = z_{\mathtt{S}}^-(s)$ at points

$$(s, z) = \left(\mp\frac{c_{\mathtt{S}}\Delta}{|\sin\alpha|}, h_m \pm c_{\mathtt{S}}\Delta\frac{\cos\alpha}{|\sin\alpha|}\right).$$

Now we consider the domain $E_{\mathtt{S},\mathtt{P}}$ defined in (4.4), which, due to its definition, contains the points of the elliptic annulus determined by the boundary of the ellipse (4.9) and the

closed curve

$$(h_m - z)^2 + s^2 - 2(h_m - z)s\cos\alpha - c_{\mathtt{P}}^2\Delta^2 = 0. \tag{4.11}$$

Equation (4.11) once again describes an ellipse with the same characteristics discovered for (4.9) and it can be defined as the union of the graphs of the functions

$$z_{\mathtt{P}}^+(s) = h_m - s\cos\alpha + \sqrt{-s^2\sin^2\alpha + c_{\mathtt{P}}^2\Delta^2}, \quad z_{\mathtt{P}}^-(s) = h_m - s\cos\alpha - \sqrt{-s^2\sin^2\alpha + c_{\mathtt{P}}^2\Delta^2},$$

with $s \in \left[-\frac{c_{\mathtt{P}}\Delta}{|\sin\alpha|}, \frac{c_{\mathtt{P}}\Delta}{|\sin\alpha|}\right]$. Then we can see the domain $E_{\mathtt{S},\mathtt{P}}$ as an elliptic annulus like in Figure 4.6(a) and in Figures 4.7-4.8. The intersections of the ellipse (4.11) with the axis $z = 0$ exist if and only if the discriminant $\mathcal{D}_{\mathtt{P}} = c_{\mathtt{P}}^2\Delta^2 - h_m^2\sin^2\alpha$ is non-negative with $s-$coordinates

$$s_{\mathtt{P}}^{(1)} = h_m\cos\alpha - \sqrt{\mathcal{D}_{\mathtt{P}}}, \quad s_{\mathtt{P}}^{(2)} = h_m\cos\alpha + \sqrt{\mathcal{D}_{\mathtt{P}}}.$$

For $\alpha = \pi$ the elliptic annulus $E_{\mathtt{S},\mathtt{P}}$ degenerates into the union of two strips, as shown in Figure 4.6(b).

Now we examine in depth all the possible regions into which we divide $\widehat{E}_{\mathtt{S}}$ and $\widehat{E}_{\mathtt{S},\mathtt{P}}$, remarking that the conformation of the ellipse that delimit $E_{\mathtt{S}}$ and $E_{\mathtt{S},\mathtt{P}}$ depends only on the half-length l_m (with which we determine the centre) and not on $l_{\widetilde{m}}$. In order to execute the splitting of the integration domain we also take into account that:

- the edges of the rectangle $[0, h_{\widetilde{m}}] \times [0, h_m]$ do not intersect the graphs of $z_{\mathtt{S}}^+$ and $z_{\mathtt{P}}^+$,
- if all the roots $s_{\mathtt{S}}^{(1,2)}$ and $s_{\mathtt{P}}^{(1,2)}$ exist, then it holds
$$s_{\mathtt{P}}^{(1)} < s_{\mathtt{S}}^{(1)} \leqslant s_{\mathtt{S}}^{(2)} < s_{\mathtt{P}}^{(2)},$$
- if the roots $s_{\mathtt{S}}^{(2)}$ and $s_{\mathtt{P}}^{(2)}$ exist, then
$$s_{\mathtt{P}}^{(2)} < c_{\mathtt{P}}\Delta,\ s_{\mathtt{S}}^{(2)} < c_{\mathtt{S}}\Delta$$
- for the considered values of α we have $s_{\mathtt{P}}^{(1)} < s_{\mathtt{S}}^{(1)} < 0$ (if these roots exist), i.e. they are not splitting points in the outer integration,
- for $\gamma = \mathtt{S}, \mathtt{P}$ we set the rule: if $\mathcal{D}_\gamma < 0$ then $s_\gamma^{(2)} = 0$.

In the following we identify with the symbol $(\cdot)^*$ the minimum between the argument of the round brackets and the length $h_{\widetilde{m}}$, to exclude in the outer integration the points that not do belong to the interval $[0, h_{\widetilde{m}}]$. The subdivision of the integration domain depends on the existence and on the position of the roots $s_\gamma^{(2)}$, $\gamma = \mathtt{S}, \mathtt{P}$, leading to the following kinds of splitting for the integral (4.2):

case 1: if $s_{\mathtt{P}}^{(2)} \leqslant 0$ ($s_{\mathtt{S}}^{(2)} \leqslant 0$ or $\mathcal{D}_{\mathtt{S}} < 0$) then

$$\mathcal{I}_1 = \int_{\widehat{E}_{\mathtt{S}}} w_{\widetilde{\eta}}^{(d_{\widetilde{m}})}(s) w_\eta^{(d_m)}(z) B_{ij}(\mathbf{r};\Delta)dzds = \int_0^{(c_{\mathtt{S}}\Delta)^*} w_{\widetilde{\eta}}^{(d_{\widetilde{m}})}(s) \int_{z_{\mathtt{S}}^-}^{h_m} w_\eta^{(d_m)}(z) B_{ij}(\mathbf{r};\Delta)dzds, \tag{4.12}$$

$$\begin{aligned}\mathcal{I}_2 &= \int_{\widehat{E}_{\mathtt{S},\mathtt{P}}} w_{\widetilde{\eta}}^{(d_{\widetilde{m}})}(s) w_\eta^{(d_m)}(z) B_{ij}(\mathbf{r};\Delta)dzds \\ &= \int_0^{(c_{\mathtt{S}}\Delta)^*} w_{\widetilde{\eta}}^{(d_{\widetilde{m}})}(s) \int_{z_{\mathtt{P}}^-}^{z_{\mathtt{S}}^-} w_\eta^{(d_m)}(z) B_{ij}(\mathbf{r};\Delta)dzds + \int_{(c_{\mathtt{S}}\Delta)^*}^{(c_{\mathtt{P}}\Delta)^*} w_{\widetilde{\eta}}^{(d_{\widetilde{m}})}(s) \int_{z_{\mathtt{P}}^-}^{h_m} w_\eta^{(d_m)}(z) B_{ij}(\mathbf{r};\Delta)dzds.\end{aligned}$$

For this kind of splitting points, the corresponding integration domains $\widehat{E}_{\mathtt{S}}$ and $\widehat{E}_{\mathtt{S},\mathtt{P}}$ are shown in Figure 4.6.

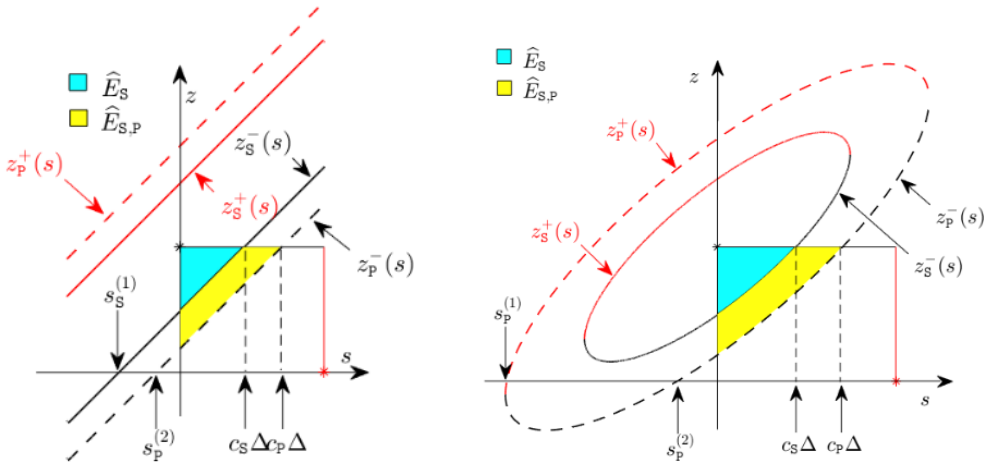

Figure 4.6: Shape of the domains $\widehat{E}_{\mathtt{S}}$ and $\widehat{E}_{\mathtt{S},\mathtt{P}}$ and related splitting points for $s_{\mathtt{P}}^{(2)} \leqslant 0$. In Figure (a) $\alpha \neq \pi$ while in Figure (b) $\alpha = \pi$ ($*= (h_{\widetilde{m}}, 0)$ and $* = (0, h_m)$).

The other two cases are obtained setting $a = \min\left\{s_{\mathtt{P}}^{(2)}, c_{\mathtt{S}}\Delta\right\}$ and $b = \max\left\{s_{\mathtt{P}}^{(2)}, c_{\mathtt{S}}\Delta\right\}$. Also in this case the symbol $(\cdot)^*$ means the minimum between the argument of the round brackets and the length $h_{\widetilde{m}}$, therefore:

case 2: if $s_{\mathtt{S}}^{(2)} \leqslant 0 < s_{\mathtt{P}}^{(2)}$ then

$$\mathcal{I}_1 = \int_{\widehat{E}_{\mathtt{S}}} w_{\widetilde{\eta}}^{(d_{\widetilde{m}})}(s) w_{\eta}^{(d_m)}(z) B_{ij}(\mathbf{r};\Delta)\,dz\,ds = \int_0^{(c_{\mathtt{S}}\Delta)^*} w_{\widetilde{\eta}}^{(d_{\widetilde{m}})}(s) \int_{z_{\mathtt{S}}^-}^{h_m} w_{\eta}^{(d_m)}(z) B_{ij}(\mathbf{r};\Delta)\,dz\,ds, \quad (4.13)$$

$$\begin{aligned}\mathcal{I}_2 &= \int_{\widehat{E}_{\mathtt{S},\mathtt{P}}} w_{\widetilde{\eta}}^{(d_{\widetilde{m}})}(s) w_{\eta}^{(d_m)}(z) B_{ij}(\mathbf{r};\Delta)\,dz\,ds \\ &= \int_0^{(a)^*} w_{\widetilde{\eta}}^{(d_{\widetilde{m}})}(s) \int_0^{z_{\mathtt{S}}^-} w_{\eta}^{(d_m)}(z) B_{ij}(\mathbf{r};\Delta)\,dz\,ds + \int_{(a)^*}^{(c_{\mathtt{S}}\Delta)^*} w_{\widetilde{\eta}}^{(d_{\widetilde{m}})}(s) \int_{z_{\mathtt{P}}^-}^{z_{\mathtt{S}}^-} w_{\eta}^{(d_m)}(z) B_{ij}(\mathbf{r};\Delta)\,dz\,ds \\ &+ \int_{(c_{\mathtt{S}}\Delta)^*}^{(b)^*} w_{\widetilde{\eta}}^{(d_{\widetilde{m}})}(s) \int_0^{h_m} w_{\eta}^{(d_m)}(z) B_{ij}(\mathbf{r};\Delta)\,dz\,ds + \int_{(b)^*}^{(c_{\mathtt{P}}\Delta)^*} w_{\widetilde{\eta}}^{(d_{\widetilde{m}})}(s) \int_{z_{\mathtt{P}}^-}^{h_m} w_{\eta}^{(d_m)}(z) B_{ij}(\mathbf{r};\Delta)\,dz\,ds.\end{aligned}$$

The integration domains generated by this position of the splitting points are shown in Figure 4.7: Figure 4.7(a) refers to the case $a = s_{\mathtt{P}}^{(2)}$, while Figure 4.7(b) refers to the case $a = c_{\mathtt{S}}\Delta$.

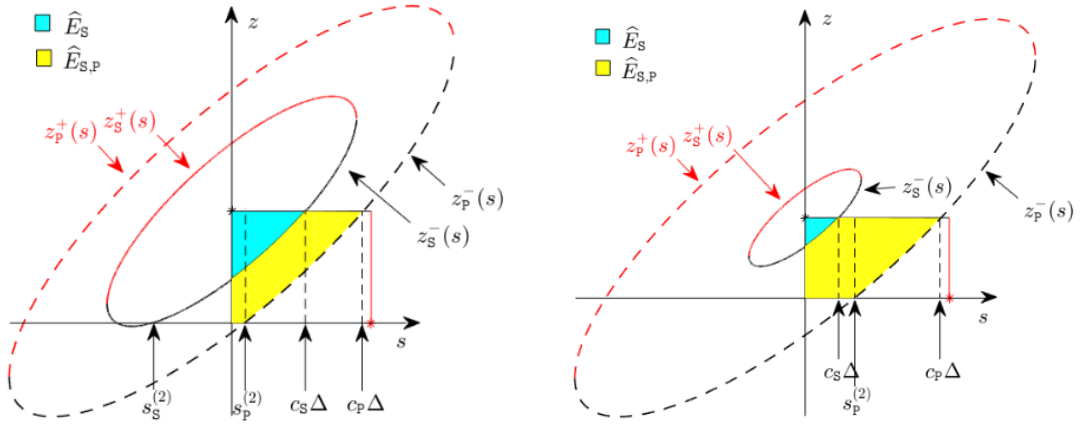

(a) (b)

Figure 4.7: Shape of the elliptic domains E_{S} and $E_{\mathrm{S,P}}$ and related splitting points for $s_{\mathrm{S}}^{(2)} \leqslant 0 < s_{\mathrm{P}}^{(2)}$ ($*= (h_{\widetilde{m}}, 0)$ and $* = (0, h_m)$).

case 3: if $s_{\mathrm{P}}^{(2)} > s_{\mathrm{S}}^{(2)} > 0$ then

$$\begin{aligned}\mathcal{I}_1 &= \int_{\widehat{E}_{\mathrm{S}}} w_{\widetilde{\eta}}^{(d_{\widetilde{m}})}(s) w_{\eta}^{(d_m)}(z) B_{ij}(\mathbf{r};\Delta)\,dz\,ds \\ &= \int_0^{\left(s_{\mathrm{S}}^{(2)}\right)^*} w_{\widetilde{\eta}}^{(d_{\widetilde{m}})}(s) \int_0^{h_m} w_{\eta}^{(d_m)}(z) B_{ij}(\mathbf{r};\Delta)\,dz\,ds + \int_{\left(s_{\mathrm{S}}^{(2)}\right)^*}^{(c_{\mathrm{S}}\Delta)^*} w_{\widetilde{\eta}}^{(d_{\widetilde{m}})}(s) \int_{z_{\mathrm{S}}^{-}}^{h_m} w_{\eta}^{(d_m)}(z) B_{ij}(\mathbf{r};\Delta)\,dz\,ds,\end{aligned} \tag{4.14}$$

$$\begin{aligned}\mathcal{I}_2 &= \int_{\widehat{E}_{\mathrm{S,P}}} w_{\widetilde{\eta}}^{(d_{\widetilde{m}})}(s) w_{\eta}^{(d_m)}(z) B_{ij}(\mathbf{r};\Delta)\,dz\,ds \\ &= \int_{\left(s_{\mathrm{S}}^{(2)}\right)^*}^{(a)^*} w_{\widetilde{\eta}}^{(d_{\widetilde{m}})}(s) \int_0^{z_{\mathrm{S}}^{-}} w_{\eta}^{(d_m)}(z) B_{ij}(\mathbf{r};\Delta)\,dz\,ds + \int_{(a)^*}^{(c_{\mathrm{S}}\Delta)^*} w_{\widetilde{\eta}}^{(d_{\widetilde{m}})}(s) \int_{z_{\mathrm{P}}^{-}}^{z_{\mathrm{S}}^{-}} w_{\eta}^{(d_m)}(z) B_{ij}(\mathbf{r};\Delta)\,dz\,ds \\ &+ \int_{(c_{\mathrm{S}}\Delta)^*}^{(b)^*} w_{\widetilde{\eta}}^{(d_{\widetilde{m}})}(s) \int_0^{h_m} w_{\eta}^{(d_m)}(z) B_{ij}(\mathbf{r};\Delta)\,dz\,ds + \int_{(b)^*}^{(c_{\mathrm{P}}\Delta)^*} w_{\widetilde{\eta}}^{(d_{\widetilde{m}})}(s) \int_{z_{\mathrm{P}}^{-}}^{h_m} w_{\eta}^{(d_m)}(z) B_{ij}(\mathbf{r};\Delta)\,dz\,ds.\end{aligned}$$

The last configuration of the splitting leads to the integration domains shown in Figure 4.8: Figure 4.8(a) refers to the case $a = s_{\mathrm{P}}^{(2)}$, while Figure 4.8(b) refers to the case $a = c_{\mathrm{S}}\Delta$. We remark that, for consecutive elements, there only exists one point returning a null value for the distance r, and it corresponds to the centre $(0, h_m)$ of the elliptic region E_{S}. This point is always contained in the domain of the first integral determined by the splitting of $\mathcal{I}_1$.

Lastly, we remember that this analysis concerns only the case $\mathbf{o}_{m+1} \equiv \mathbf{o}_{\widetilde{m}}$, but the $\mathbf{o}_{\widetilde{m}+1} \equiv \mathbf{o}_m$ configuration is comparable since $r = (h_{\widetilde{m}} - s)^2 + z^2 - 2(h_{\widetilde{m}} - s)z\cos(\alpha)$ and the study of the elliptic domains E_{S} and $E_{\mathrm{S,P}}$ is quite similar to what done previously. For the sake of simplicity we do not treat integrals depending on consecutive elements with angle $\alpha \in [0, \pi/2]$, but we observe that for this range local integration domains with similar elliptic boundaries are generated. Due to that the analysis of the domains splitting needs a procedure comparable to the one done before.

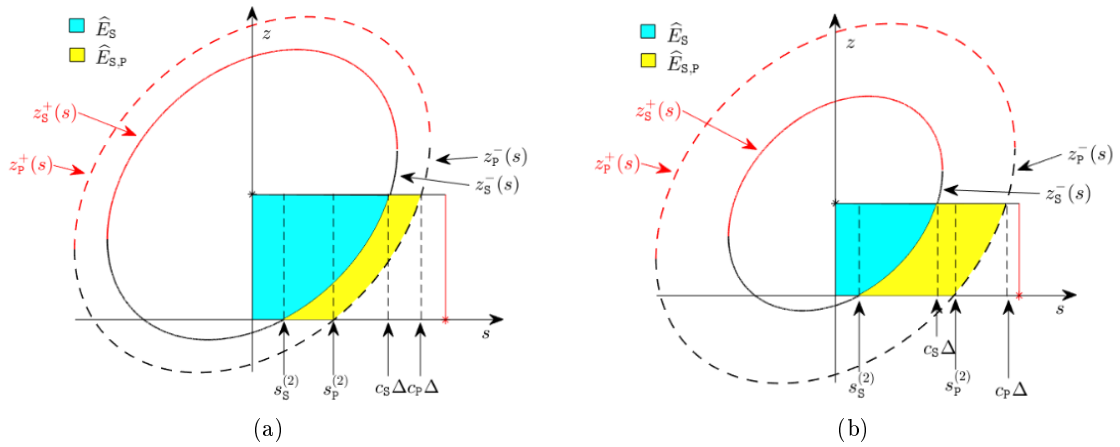

Figure 4.8: Shape of the elliptic domains E_{S} and $E_{\mathrm{S,P}}$ and related splitting points for $s_{\mathrm{P}}^{(2)} > s_{\mathrm{S}}^{(2)} > 0$ ($*= (h_{\widetilde{m}}, 0)$ and $* = (0, h_m)$).

4.1.3 Disjoint boundary elements

In the last configuration we consider two segments e_m and $e_{\widetilde{m}}$ such that $e_m \cap e_{\widetilde{m}} = \emptyset$, as shown in Figure 4.9. In this case the distance r can never vanish, which means that integral (4.2) can be approximated without taking care about the behaviour of the kernel when $r = 0$. However, the presence of Heaviside and square root functions in the kernel has to be carefully taken into account.
Let us firstly explicit the dependence of the two variables $\mathbf{x}, \boldsymbol{\xi}$ on the local coordinates s, z:

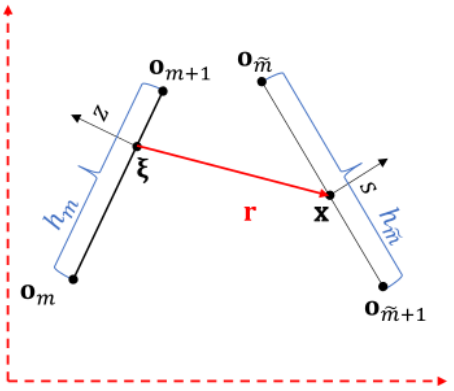

Figure 4.9: Parametrization of two disjoint segments e_m and $e_{\widetilde{m}}$.

$$\begin{aligned}\mathbf{x} &= (x_1, x_2)^\top \\ &= \left(o_{\widetilde{m},1} + \frac{s}{h_{\widetilde{m}}}(o_{\widetilde{m}+1,1} - o_{\widetilde{m},1}), o_{\widetilde{m},2} + \frac{s}{h_{\widetilde{m}}}(o_{\widetilde{m}+1,2} - o_{\widetilde{m},2})\right)^\top, \\ \boldsymbol{\xi} &= (\xi_1, \xi_2)^\top \\ &= \left(o_{m,1} + \frac{z}{h_m}(o_{m+1,1} - o_{m,1}), o_{m,2} + \frac{z}{h_m}(o_{m+1,2} - o_{m,2})\right)^\top.\end{aligned}$$

Consequently we can express $\mathbf{r}$ as

$$\mathbf{r} = \mathbf{x} - \boldsymbol{\xi} = (A + Bs - Cz, D + Es - Fz)^\top$$

with

$$A = o_{\widetilde{m},1} - o_{m,1},\ B = \frac{o_{\widetilde{m}+1,1} - o_{\widetilde{m},1}}{h_{\widetilde{m}}},\ C = \frac{o_{m+1,1} - o_{m,1}}{h_m},$$
$$D = o_{\widetilde{m},2} - o_{m,2},\ E = \frac{o_{\widetilde{m}+1,2} - o_{\widetilde{m},2}}{h_{\widetilde{m}}},\ F = \frac{o_{m+1,2} - o_{m,2}}{h_m}$$

and $r = \|\mathbf{r}\|_2 = \sqrt{(A+Bs-Cz)^2+(D+Es-Fz)^2}$. We remark that B, C, E and F correspond to the normalized components of the vectors $\overrightarrow{\mathbf{o}_m\mathbf{o}_{m+1}}$ and $\overrightarrow{\mathbf{o}_{\widetilde{m}}\mathbf{o}_{\widetilde{m}+1}}$ and thanks to that the equality $C^2+F^2 = B^2+E^2 = 1$ holds.
We exploit a particular expression of the kernel B_{ij}, in which the differences between the functions depending on the velocities $c_{\mathtt{S}}$ and $c_{\mathtt{P}}$ are highlighted:

$$B_{ij}(\mathbf{r};\Delta) = H[c_{\mathtt{S}}\Delta - r]B_{ij}^{(\mathtt{S})}(\mathbf{r};\Delta) + H[c_{\mathtt{P}}\Delta - r]B_{ij}^{(\mathtt{P})}(\mathbf{r};\Delta).$$

Due to the absence of any kind of singularity for kernel B_{ij}, when elements are disjoint the first split for integral (4.2) is

$$\begin{aligned}\int_0^{h_{\widetilde{m}}}\int_0^{h_m} w_{\widetilde{\eta}}^{(d_{\widetilde{m}})}(s)w_{\eta}^{(d_m)}(z)B_{ij}(\mathbf{r};\Delta)dzds = &\int_{\widehat{E}_{\mathtt{S}}} w_{\widetilde{\eta}}^{(d_{\widetilde{m}})}(s)w_{\eta}^{(d_m)}(z)B_{ij}^{(S)}(\mathbf{r};\Delta)dzds \\ &+ \int_{\widehat{E}_{\mathtt{P}}} w_{\widetilde{\eta}}^{(d_{\widetilde{m}})}(s)w_{\eta}^{(d_m)}(z)B_{ij}^{(P)}(\mathbf{r};\Delta)dzds\end{aligned}$$

where we have set the domains

$$E_\gamma = \left\{(s,z)\in\mathbf{R}^2 \,:\, r\in[0,c_\gamma\Delta]\right\}, \quad \gamma = \mathtt{S},\mathtt{P}$$

and

$$\widehat{E}_\gamma := E_\gamma \cap [0,h_{\widetilde{m}}]\times[0,h_m].$$

For each $\gamma = \mathtt{S},\mathtt{P}$, points belonging to E_γ satisfy the inequality: $(A+Bs-Cz)^2+(D+Es-Fz)^2 \leqslant c_\gamma^2\Delta^2$, while the boundary can be described by a second degree equation in the z variable

$$(C^2+F^2)z^2-2[(BC+EF)s+AC+DF]z+(A^2+D^2)+(B^2+E^2)s^2+2(AB+DE)s-c_\gamma^2\Delta^2 = 0.$$

The related discriminant, depending on the s variable, can be obtained after simple calculations:

$$\mathcal{D}_\gamma^{(1)} = 4[-(BF-EC)^2s^2+2(BF-EC)(CD-FA)s-(CD-FA)^2+(C^2+F^2)c_\gamma^2\Delta^2]. \tag{4.15}$$

If $\mathcal{D}_\gamma^{(1)}$ is positive, we define by $z_\gamma^+(s)$ and $z_\gamma^-(s)$ the two equations describing the boundary of E_γ. We remark that the value of the discriminant $\mathcal{D}_\gamma^{(1)}$ depends on the mutual position of the integration segments through the coefficients A, B, C, D, E and F. To study (4.15) as an equation in the s variable we need to know the values of the quantities

$$\frac{F}{C} = \frac{o_{m+1,2}-o_{m,2}}{o_{m+1,1}-o_{m,1}}, \quad \frac{E}{B} = \frac{o_{\widetilde{m}+1,2}-o_{\widetilde{m},2}}{o_{\widetilde{m}+1,1}-o_{\widetilde{m},1}}, \quad \frac{D}{A} = \frac{o_{\widetilde{m},2}-o_{m,2}}{o_{\widetilde{m},1}-o_{m,1}}$$

whose geometric meaning is explained in Figure 4.10. If e_m, $e_{\widetilde{m}}$ and the segment of end points $\mathbf{o}_m$ and $\mathbf{o}_{\widetilde{m}}$ are aligned, then the equalities $\frac{F}{C} = \frac{E}{B} = \frac{D}{A}$ hold (the case $\frac{F}{C} = \frac{E}{B} = \frac{D}{A} = \pm\infty$, arising if $C = B = A = 0$, is also considered); therefore we have $BF-EC = DC-FA = 0$ and the discriminant (4.15) is positive for all $s\in\mathbb{R}$, its value being $\mathcal{D}_\gamma^{(1)} = 4c_\gamma^2\Delta^2 \geqslant 0$. For this special alignment, E_γ boundary is composed by two straight lines having equations

$$z_\gamma^+(s) = (BC+FE)s+(AC+DF)+c_\gamma\Delta, \quad z_\gamma^-(s) = (BC+FE)s+(AC+DF)-c_\gamma\Delta$$

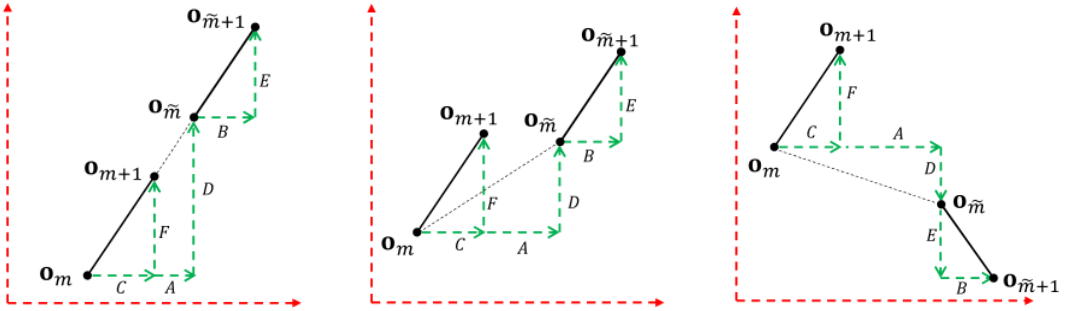

(a) aligned elements (b) parallel elements (c) generic configuration

Figure 4.10: Ratio F/C is the tangent value of the angle between e_m and the reference x_1-axis where the arc Γ is set, while ratios E/B and D/A respectively are the tangent values of the two angles formed by $e_{\widetilde{m}}$ and the segment of end points $\mathbf{o}_m$ and $\mathbf{o}_{\widetilde{m}}$ w.r.t to the reference x_1-axis.

and whose intersections with the axis $z = 0$ and $z = h_m$ always exist and have abscissas, respectively,

$$s_\gamma^{(1,2)} = -(AB + DE) \mp c_\gamma \Delta, \quad q_\gamma^{(1,2)} = -(AB + DE) + h_m(BC + EF) \mp c_\gamma \Delta.$$

If e_m and $e_{\widetilde{m}}$ are parallel but not aligned then $\frac{F}{C} = \frac{E}{B} \neq \frac{D}{A}$ and

$$BF - EC = 0,\ DC - FA \neq 0,\ BD - EA \neq 0.$$

The discriminant (4.15) has the value $\mathcal{D}_\gamma^{(1)} = 4[c_\gamma^2 \Delta^2 - (CD - FA)^2]$ and it is positive if and only if $c_\gamma^2 \Delta^2 - (CD - FA)^2 \geqslant 0$. In case it is positive E_γ is not empty and it is the strip delimited by the straight lines

$$z_\gamma^+(s) = (BC+FE)s+(AC+DF)+\frac{\sqrt{\mathcal{D}_\gamma^{(1)}}}{2}, \quad z_\gamma^-(s) = (BC+FE)s+(AC+DF)-\frac{\sqrt{\mathcal{D}_\gamma^{(1)}}}{2},$$

which intersect the axis $z = 0$ and $z = h_m$ respectively at points with abscissas

$$s_\gamma^{(1,2)} = -(AB + DE) \mp \sqrt{\mathcal{D}_\gamma^{(2)}}, \quad q_\gamma^{(1,2)} = -(AB + DE) + h_m(BC + EF) \mp \sqrt{\mathcal{D}_\gamma^{(2)}},$$

where $\mathcal{D}_\gamma^{(2)} = c_\gamma^2 \Delta^2 - (BD - EA)^2$. These intersections always exist since the relation $\mathcal{D}_\gamma^{(2)} \geqslant 0 \Leftrightarrow \mathcal{D}_\gamma^{(1)} \geqslant 0$ holds true.

The last case occurs when e_m and $e_{\widetilde{m}}$ are neither aligned nor parallel. In this configuration $\frac{F}{C} \neq \frac{E}{B}$, hence $BF - EC \neq 0$ and the discriminant $\mathcal{D}_\gamma^{(1)}$ defined in (4.15) preserves its dependence on s, becoming positive if only if s belongs to the interval $\left(p_\gamma^{(1)}, p_\gamma^{(2)}\right)$, with

$$p_\gamma^{(1)} = \min\left\{\frac{FA - CD \pm c_\gamma \Delta}{EC - BF}\right\}, \quad p_\gamma^{(2)} = \max\left\{\frac{FA - CD \pm c_\gamma \Delta}{EC - BF}\right\}.$$

For $\mathcal{D}_\gamma^{(1)} > 0$ the set E_γ is not empty and has an elliptic shape composed by the union of the curves

$$z_\gamma^+(s) = \frac{2[(BC+FE)s+(AC+DF)] + \sqrt{\mathcal{D}_\gamma^{(1)}}}{2},$$
$$z_\gamma^-(s) = \frac{2[(BC+FE)s+(AC+DF)] - \sqrt{\mathcal{D}_\gamma^{(1)}}}{2}$$

The intersections with the axis $z=0$ exist if and only if $\mathcal{D}_\gamma^{(2)} = c_\gamma^2\Delta^2 - (BD-EA)^2 \geqslant 0$ and the intersection points have abscissas

$$s_\gamma^{(1)} = -(AB+DE) - \sqrt{\mathcal{D}_\gamma^{(2)}}, \quad s_\gamma^{(2)} = -(AB+DE) + \sqrt{\mathcal{D}_\gamma^{(2)}}.$$

Instead the intersections with axis $z=h_m$ exist if an only if $\mathcal{D}_\gamma^{(3)} = 4[-(BD-EA)^2 - h_m^2(BF-EC)^2 + 2h_m(BD-EA)(BF-EC) + c_\gamma^2\Delta^2] \geqslant 0$ and the points at which the intersection occurs have abscissas

$$q_\gamma^{(1)} = \frac{2[-(AB+DE)+h_m(BC+EF)] - \sqrt{\mathcal{D}_\gamma^{(3)}}}{2},$$
$$q_\gamma^{(2)} = \frac{2[-(AB+DE)+h_m(BC+EF)] + \sqrt{\mathcal{D}_\gamma^{(3)}}}{2}.$$

Now we proceed with the computation of the integrals

$$\int_{\widehat{E}_\gamma} w_{\widetilde{\eta}}^{(d_{\widetilde{m}})}(s) w_\eta^{(d_m)}(z) B_{ij}^{(\gamma)}(\mathbf{r};\Delta)\,dz\,ds, \quad \gamma = \mathtt{S},\mathtt{P}, \tag{4.16}$$

whose sum returns the integral (4.2) when e_m and $e_{\widetilde{m}}$ are disjoint. To calculate (4.16) we need to define the outer integration splitting points generated by the intersection between the rectangle $[0,h_{\widetilde{m}}]\times[0,h_m]$ and E_γ, when the latter is not empty.

- For e_m and $e_{\widetilde{m}}$ aligned or parallel, each point $(s,z)\in E_\gamma$ has coordinate s without limitations in $\mathbb{R}$ because $\mathcal{D}_\gamma^{(1)}$ does not depend on this variable. In this case we set

$$p_\gamma^{(1)} = \min\left\{s_\gamma^{(1)}, s_\gamma^{(2)}, q_\gamma^{(1)}, q_\gamma^{(2)}\right\}, \quad p_\gamma^{(2)} = \max\left\{s_\gamma^{(1)}, s_\gamma^{(2)}, q_\gamma^{(1)}, q_\gamma^{(2)}\right\}$$

- Otherwise $p_\gamma^{(1)}$ and $p_\gamma^{(2)}$ are well defined but intersections of E_γ border with the axis $z=0$ or $z=h_m$ could not exist (it depends on the value of $\mathcal{D}_\gamma^{(2)}$ and $\mathcal{D}_\gamma^{(3)}$ as explained before). Hence we use the following notation to define these splitting points:

$$\mathcal{D}_\gamma^{(2)} > 0 \Rightarrow s_\gamma^{(1,2)} = -(AB+DE) \mp \sqrt{\mathcal{D}_\gamma^{(2)}}, \quad \mathcal{D}_\gamma^{(2)} \leqslant 0 \Rightarrow s_\gamma^{(1,2)} = p_\gamma^{(1,2)}$$
$$\mathcal{D}_\gamma^{(3)} > 0 \Rightarrow q_\gamma^{(1,2)} = \frac{2[-(AB+DE)+h_m(BC+EF)] \pm \sqrt{\mathcal{D}_\gamma^{(3)}}}{2}, \quad \mathcal{D}_\gamma^{(3)} \leqslant 0 \Rightarrow q_\gamma^{(1,2)} = p_\gamma^{(1,2)}.$$

With this convention, for each configuration we can define the set $\left\{k_\gamma^{(1)},...,k_\gamma^{(6)}\right\}$ made by the points $p_\gamma^{(1)}, p_\gamma^{(2)}, s_\gamma^{(1)}, s_\gamma^{(2)}, q_\gamma^{(1)}, q_\gamma^{(2)}$ sorted in ascending order. Afterwards we set $K_\gamma = \left\{\widehat{k}_\gamma^{(1)},...,\widehat{k}_\gamma^{(6)}\right\}$ where

$$\widehat{k}_\gamma^{(i)} = \begin{cases} k_\gamma^{(i)} & 0 < k_\gamma^{(i)} < h_{\widetilde{m}} \\ 0 & k_\gamma^{(i)} \leqslant 0 \\ h_{\widetilde{m}} & k_\gamma^{(i)} \geqslant h_{\widetilde{m}} \end{cases}, \quad i = 1,...,6.$$

This new set has the purpose to exclude the s-variable splitting points that are outside the outer integration interval $[0, h_{\widetilde{m}}]$. Consequently, we set the inner integration bounds as

$$m_\gamma(s) = \max\left\{z_\gamma^-(s), 0\right\}, \quad M_\gamma(s) = \min\left\{z_\gamma^+(s), h_m\right\},$$

and we observe that

$$\begin{aligned} m_\gamma|_{\left[\widehat{k}_\gamma^{(i)},\widehat{k}_\gamma^{(i+1)}\right]} &\equiv 0 \quad \text{or} \quad m_\gamma|_{\left[\widehat{k}_\gamma^{(i)},\widehat{k}_\gamma^{(i+1)}\right]} \equiv z_\gamma^-, \quad i = 1,...,5, \\ M_\gamma|_{\left[\widehat{k}_\gamma^{(i)},\widehat{k}_\gamma^{(i+1)}\right]} &\equiv h_m \quad \text{or} \quad M_\gamma|_{\left[\widehat{k}_\gamma^{(i)},\widehat{k}_\gamma^{(i+1)}\right]} \equiv z_\gamma^+, \quad i = 1,...,5, \end{aligned}$$

which means that, in the generic interval $\left[\widehat{k}_\gamma^{(i)}, \widehat{k}_\gamma^{(i+1)}\right]$ defined by two consecutive splitting points, the inner bounds have no change of behaviour. We also observe that the integral (4.16) is null if $M_\gamma < m_\gamma$ in one of the intervals defined by two consecutive outer splitting points. To catch this situation we define specific integrand function depending on the outer integration interval:

$$A_\gamma^{(l)}(s,z) = \begin{cases} w_{\widetilde{\eta}}^{(d_{\widetilde{m}})}(s) w_\eta^{(d_m)}(z) B_{ij}^{(\gamma)}(\mathbf{r};\Delta), & \text{if } M_\gamma(s) \geqslant m_\gamma(s),\ \forall s \in \left[\widehat{k}_\gamma^{(l)}, \widehat{k}_\gamma^{(l+1)}\right] \\ 0, & \text{if } M_\gamma(s) < m_\gamma(s),\ \forall s \in \left[\widehat{k}_\gamma^{(l)}, \widehat{k}_\gamma^{(l+1)}\right] \end{cases}.$$

At this stage we can write integral (4.16) as the sum of five contributions:

$$\int_{\widehat{E}_\gamma} w_{\widetilde{\eta}}^{(d_{\widetilde{m}})}(s) w_\eta^{(d_m)}(z) B_{ij}^{(\gamma)}(\mathbf{r};\Delta) dz ds = \sum_{l=1}^{5} \int_{\widehat{k}_\gamma^{(l)}}^{\widehat{k}_\gamma^{(l+1)}} \int_{m_\gamma(s)}^{M_\gamma(s)} A_\gamma^{(l)}(s,z) dz ds. \tag{4.17}$$

Each addend can be calculated by the Gauss-Legendre quadrature rule but the irregular behaviour of the spatial derivative of the square root $\sqrt{c_\gamma^2\Delta^2 - r^2}$ at the boundary of E_γ, where in fact $r = c_\gamma\Delta$, still remains. The quadrature strategy for this irregular integrand will be exposed in the next session.

4.2 Treatment of the kernels issues

In the following we describe the numerical quadrature formulas apt to integrate, with high precision, the different parts of the integration kernels ν_{ij}^V, ν_{ij}^D and ν_{ij}^K, possibly characterized by different types of singularities. The integration domains we refer in the

next section are in particular the regions in local variables determined by the splitting technique introduced in Section 4.1.
We remark that, whenever we cite in this section the *Gauss-Legendre quadrature formula*, we consider the following quadrature rule for function f at least belonging to $C^0([-1,1])$:

$$\int_{-1}^{1} f(z)dz = \sum_{k=0}^{n} \omega_{G,k} f(z_k) + R_{G,n}(f), \tag{4.18}$$

where the nodes in $\{z_k\}_{k=0,\dots,n}$ are the $n+1$ roots of the Legendre polynomial of degree $n+1$ and $\omega_{G,k}$ are the quadrature weights, whose definition can be found in [71]. It is well known that the Gauss-Legendre formula is of interpolatory kind, with degree of accuracy equal to $2n+1$, and that the following convergence theorem holds:

Theorem 4.2.1 (see [71]). *If we consider a function $f \in H^m([-1,1])$ with $m \geqslant 1$, then it holds that*

$$R_{G,n}(f) = \mathcal{O}\left(n^{-m}\right).$$

Lastly, we remark that the Gauss-Legendre formula (4.18) is applied in the following to integrals defined in generic intervals $[a,b]$, after performing a suitable change of variable.

4.2.1 Functions with irregular behaviour at the boundary

We focus here on the square roots functions $\sqrt{c_\gamma^2\Delta^2 - r^2}$, with $\gamma = \mathtt{S}, \mathtt{P}$, which appear in the expression of all the integral kernels ν_{ij}^V, ν_{ij}^D and ν_{ij}^K. We propose in what follows a common strategy to integrate them. Although this square roots are continuous in the domain defined by the step function $H[c_\gamma\Delta - r]$, their derivatives in r present an asymptote in $r = c_\gamma\Delta$; in fact

$$\frac{\partial}{\partial r}\sqrt{c_\gamma^2\Delta^2 - r^2} = -\frac{r}{\sqrt{c_\gamma^2\Delta^2 - r^2}}$$

and this causes a non accurate approximation by formula (4.18) if the extremes of integration correspond to the points, in local coordinates, for which $r(s,z) = c_\gamma\Delta$. Indeed it is known that the Gaussian quadrature looses efficiency in presence of points of the integrand function charachterized by a high gradient. This situations frequently occurs in the construction of the first temporal blocks of $\mathbb{E}_B$, characterized by a time step Δ sufficiently small to make some portions of the boundary of $E_{\mathtt{S}}$ and $E_{\mathtt{S},\mathtt{P}}$, defined in (4.3) and (4.4), part of the boundary of the integration domain of integral (4.2). To overcome this issue without increasing the number of quadrature nodes of the Gaussian formula (4.18), we combine the latter with the smoothing transformation $\Theta_{p,q}$:

$$\Theta_{p,q}(t) = \frac{(p+q-1)!}{(p-1)!(q-1)!}\int_0^t u^{p-1}(1-u)^{q-1}du, \quad t \in [0,1],\ p,q \geq 1. \tag{4.19}$$

This regularization procedure, discussed in the work by Monegato and Scuderi [63] and analised by the convergence point of view in [61], allows to suitably thicken the nodes towards the integration endpoints, according to the values of the positive parameters p and q as shown in figure 4.11. It is worth noting that for $p = q = 1$ the transformation

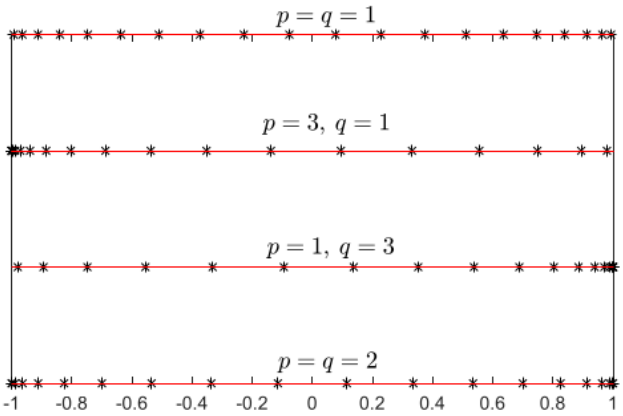

Figure 4.11: Application of the smoothing transformation $\Theta_{p,q}$ to the 20 nodes of the Gauss-Legendre formula for several values of p and q.

$\Theta_{p,q}$ corresponds to the identity.

To give an example on the use of this technique, let suppose to be in the case of coincident elements, whose splitting rules of the integration domain are reported in subsection 4.1.1. We consider the integral contribution

$$\int_a^b \int_{A(s)}^{B(s)} w_{\widetilde{\eta}}^{(d_{\widetilde{m}})}(s) w_{\eta}^{(d_m)}(z) f(s,z;\Delta) dz ds, \tag{4.20}$$

where $a = c_{\mathrm{S}}\Delta$, $b = h_m - c_{\mathrm{S}}\Delta$, $A(s) = s - c_{\mathrm{S}}\Delta$ and $B(s) = s + c_{\mathrm{S}}\Delta$, with in particular $c_{\mathrm{S}}\Delta < h_m - c_{\mathrm{S}}\Delta$. We take into account the integral kernel function $f(s,z;\Delta) = \log\left(c_{\mathrm{S}}\Delta + \sqrt{c_{\mathrm{S}}^2\Delta^2 - |s-z|^2}\right)$, which occurs in the definition of the single layer and the hypersingular kernels, respectively presented in (1.79) and in (1.89). The geometrical configuration of the integration domain is the same described in Figure 4.2(a); therefore, the integrand function is mildly singular in both the inner integration endpoints. We set $p = q > 1$ for the transformation $\Theta_{p,q}$ and we proceed with the following change of variable for the inner integration

$$z = g(\widetilde{z}) = [B(s) - A(s)]\Theta_{p,q}(\widetilde{z}) + A(s), \quad \widetilde{z} \in [0,1]$$

in order to write

$$\int_{A(s)}^{B(s)} w_{\eta}^{(d_m)}(z) f(s,z;\Delta) dz = \int_0^1 w_{\eta}^{(d_m)}\Big(h(\widetilde{z})\Big) f\Big(s, g(\widetilde{z}); \Delta\Big) g'(\widetilde{z}) d\widetilde{z}.$$

To apply the Gauss-Legendre quadrature we have to switch to a variable in $[-1,1]$, then if we set $\widetilde{z} = (z_G + 1)/2$ with $z_G \in [-1,1]$ we obtain

$$\int_0^1 w_{\eta}^{(d_m)}\Big(g(\widetilde{z})\Big) f\Big(s, g(\widetilde{z}); \Delta\Big) g'(\widetilde{z}) d\widetilde{z} = \frac{1}{2}\int_{-1}^1 F(z_G) dz_G \simeq \frac{1}{2}\sum_{k=0}^n \omega_{G,k} F(z_k)$$

with

$$F(z_G) = w_\eta^{(d_m)} \left(g\left(\frac{z_G+1}{2}\right)\right) f\left(s, g\left(\frac{z_G+1}{2}\right); \Delta\right) g'\left(\frac{z_G+1}{2}\right).$$

The approximation of the last form of the inner integral is obtained applying formula (4.18), z_k and $\omega_{G,k}$ being the nodes and the roots of the mentioned quadrature. The computation of integral (4.20) can completed applying the Gauss-Legendre formula again in the outer variable s.
This kind of procedure can be easily adapted to regularize the parts of all the integral kernels with mild boundary singularities and for all the typologies of shape of the integral domain, for instance it can be employed to integrate functions depending on $\sqrt{c_{\mathtt{P}}^2\Delta^2 - r^2}$ over domains with part of the boundary coincident with the contour of the set $E_{\mathtt{S},\mathtt{P}}$.

In order to test the efficacy of this formula we have performed several numerical tests: the following Tables show the numerical approximation of integral (4.20), calculated for different functions $f(s, z; \Delta)$ and considering coincident elements $e_m \equiv e_{\widetilde{m}}$ with angle of inclination $\theta = 0$. For all the tables the following data have been set: $m = \widetilde{m}$, $w_\eta^{(d_m)}(z) = w_{\widetilde{\eta}}^{(d_{\widetilde{m}})}(s)$ with degree $d_m = d_{\widetilde{m}} = 0$, $\Delta = 0.1$, $h_m = 0.2$, $c_{\mathtt{S}} = 0.4$, $c_{\mathtt{P}} = 0.7$. The values of the parameters $p = q = 1$ means that transformation (4.19) is reduced to the standard Gauss-Legendre rule and the symbol '–' indicates that the overall single precision accuracy is reached.

Table 4.1: Value of integral (4.20) with $f = h^V_{1,11}$ (defined in (1.83)): $a = c_{\mathtt{S}}\Delta$, $b = h_m - c_{\mathtt{S}}\Delta$, $A(s) = s - c_{\mathtt{S}}\Delta$, $B(s) = s + c_{\mathtt{S}}\Delta$. *Outer integration*: Gauss-Legendre formula; *Inner integration*: smoothing transformation $\Theta_{p,q}$ and Gauss-Legendre formula.

♯ outer and inner nodes	$p = 1$, $q = 1$	$p = 2$, $q = 2$	$p = 3$, $q = 3$
4	$-8.6902154 \cdot 10^{-02}$	$-8.6895507 \cdot 10^{-02}$	$-8.7032076 \cdot 10^{-02}$
8	$-8.6913640 \cdot 10^{-02}$	$-8.6914195 \cdot 10^{-02}$	$-8.6914193 \cdot 10^{-02}$
16	$-8.6914180 \cdot 10^{-02}$	$-8.6914201 \cdot 10^{-02}$	$-8.6914201 \cdot 10^{-02}$
32	$-8.6914200 \cdot 10^{-02}$	–	–

Table 4.2: Value of integral (4.20) with $f = h^V_{3,11}$ (defined in (1.86)): $a = 0$, $b = h_m - c_{\mathtt{P}}\Delta$, $A(s) = s + c_{\mathtt{S}}\Delta$, $B(s) = s + c_{\mathtt{P}}\Delta$. *Outer integration*: Gauss-Legendre formula; *Inner integration*: smoothing transformation $\Theta_{p,q}$ and Gauss-Legendre formula.

♯ outer and inner nodes	$p = 1$, $q = 1$	$p = 1$, $q = 2$	$p = 1$, $q = 3$
4	$-4.3977874 \cdot 10^{-03}$	$-4.4084188 \cdot 10^{-03}$	$-4.4244785 \cdot 10^{-03}$
8	$-4.4049310 \cdot 10^{-03}$	$-4.4061694 \cdot 10^{-03}$	$-4.4061753 \cdot 10^{-03}$
16	$-4.4060003 \cdot 10^{-03}$	$-4.4061693 \cdot 10^{-03}$	$-4.4061693 \cdot 10^{-03}$
32	$-4.4061472 \cdot 10^{-03}$	–	–

In Table 4.1 we show the results of the double integral once again in the subset of $\widehat{E}_{\mathtt{S}}$ with geometry of reference in Figure 4.2(a). The integral kernel depends on the square

root $\sqrt{c_{\mathtt{S}}^2\Delta^2 - r^2}$, that is non regular along the lines $z = s \pm c_{\mathtt{S}}\Delta$. Hence in the smoothing transformation for the inner integration it is necessary to increase both p and q. The single precision accuracy is achieved with 16 nodes and $p = q = 2$.
Table 4.2 shows the results of the double integral on a subset of $\widehat{E}_{\mathtt{S},\mathtt{P}}$ and with kernel depending on the square root $\sqrt{c_{\mathtt{P}}^2\Delta^2 - r^2}$, irregular along the line $z = s + c_{\mathtt{P}}\Delta$. Here the geometry of reference is on the left in Figure 4.3, left plot. Hence, using the same smoothing transformation in the inner integral, it is enough to increase only the parameter q. The single precision accuracy is achieved with 16 nodes and $q = 2$. Using $q = 3$ we obtain similar.

4.2.2 The functions $\mathcal{O}(\log(r))$

The logarithmic singularity is the main characteristic of the single layer integral kernel ν_{ij}^V but it is also a feature of the hypersingular kernel ν_{ij}^D. An accurate computation of integral of functions in a domain containing, in local coordinates, points in which the argument of the log vanishes, is an issue from the numerical point of view that we overcome employing a suitable quadrature rule that allows to absorb the singular function in the weights:

$$\int_{-1}^{1} \log\left(|z-y|\right) f(z)dz = \sum_{k=0}^{n} \omega_{\log,k}(y) f(z_k) + R_{\log,n}(f;y) \tag{4.21}$$

where, the set of nodes $\{z_k\}_{k=0}^n$ are, also in this case, the roots of the Legendre polynomial of degree $n+1$ and the weights $\omega_{\log,k}(y)$, for $k = 0, ..., n$, depending on $y \in (-1,1)$ and on the log kernel, can be computed by the recursive relation reported in [10]. The related theorem of convergence for formula (4.21) is the following:

Theorem 4.2.2 (see [11]). *Let be H_μ the space of Hölder continuous functions of order μ. If $f \in C^p([-1,1])$ with $p > 1$ and $f^{(p)} \in H_\mu([-1,1])$ for some $0 < \mu < 1$, then*

$$R_{\log,n}(f;y) = \mathcal{O}\left(n^{-p-\mu}\right)$$

Theorem 4.2.2 can be found in [11], with a generalized formulation for integral kernels of type $\log\left[(z-a(y))^2 + b(y)^2\right]$, with $b(y) \neq 0$, or defined as a rational function with factors of type $(z-a(y))$ and divisors of the type $(z-a(y))$ and $\left[(z-a(y))^2 + b(y)^2\right]$.

Formula (4.21) is of interpolatory kind, therefore consistent with our purposes since the integral kernels we considered are always multiplied by shape functions which are polynomials in local variables. As example of the use of (4.21) we consider again the case of coincident elements (see subsection 4.1.1) and we suppose to compute the following integral:

$$\int_a^b \int_{A(s)}^{B(s)} w_{\tilde{\eta}}^{(d_{\tilde{m}})}(s) w_{\eta}^{(d_m)}(z) C_{\log} \log\left(|s-z|\right) dzds, \tag{4.22}$$

a and b being two splitting points determined by the subdivision schemes for the set $\widehat{E}_{\mathtt{S}}$ in Figure 4.2, and $A(s)$ and $B(s)$ the related inner boundaries (each portion of the integration

domain contains the singular line $s = z$). The factor $C_{\log}$ is a non zero constant. For the inner integration we consider the change of variable

$$z = a_s z_G + b_s, \quad a_s = \frac{B(s) - A(s)}{2},\ b_s = \frac{B(s) + A(s)}{2},\ z_G \in [-1, 1]$$

and we write

$$\int_{A(s)}^{B(s)} w_\eta^{(d_m)}(z) \log\left(|s - z|\right) dz = a_s \int_{-1}^{1} w_\eta^{(d_m)}(a_s z_G + b_s) \log\left(|s - a_s z_G - b_s|\right) dz_G$$
$$= a_s \int_{-1}^{1} w_\eta^{(d_m)}(a_s z_G + b_s) \log\left(|a_s|\right) dz_G + a_s \int_{-1}^{1} w_\eta^{(d_m)}(a_s z_G + b_s) \log\left(\left|z_G - \frac{s - b_s}{a_s}\right|\right) dz_G. \tag{4.23}$$

The first addend of equality (4.23) can be calculated exactly, since the integrand function is reduced to a simple polynomial in the variable z_G, while the second addend can be performed analytically by formula (4.21), setting precisely $y = (s - b_s)/a_s$ and $n = d_m$. Going back to integral (4.22), for the outer integration in the s variable we can proceed applying the Gauss-Legendre formula (4.18), however the integrand function, could still present a mild singularity of kind $s\log(s)$ or $(h_m - s)\log(h_m - s)$, if the outer extremes of integration a and b correspond to 0 or to h_m, respectively. In this case, the combination of the gaussian formula with the smoothing transformation in (4.19), with an opportune setting of the smoothing parameters, can improve the precision of the outer integration.
We observe that formula (4.21), with suitable manipulations of the log argument, is useful also for integration on consecutive and aligned elements, for which the argument $r = h_m - z + s$ is linear in the local variable, if the integration domain contains the singular point with local coordinates $(s, z) = (0, h_m)$. The alternative formula for consecutive and not aligned elements, for which the distance r is quadratic in the local integration variables s and z, is furnished by the following interpolatory quadrature rule.

$$\int_{-1}^{1} \log\left((z - a_y)^2 + b_y^2\right) f(z) dz = \sum_{k=0}^{n} \overline{\omega}_{\log,k}(y) f(z_k) + \overline{R}_{\log,n}(f; y), \tag{4.24}$$

where the peculiar weights can be calculated by the recursive formula reported in [10]. For the related convergence result we refer again to paper [11].

Table 4.3: Value of integral (4.22): $a = 0$, $b = c_{\mathrm{S}}\Delta$, $A(s) = 0$, $B(s) = s + c_{\mathrm{S}}\Delta$ and $C_{\log} = -(c_{\mathrm{P}}^2 + c_{\mathrm{S}}^2)/(2c_{\mathrm{P}}^2 c_{\mathrm{S}}^2)$. *Outer integration*: smoothing transformation $\Theta_{p,q}$ and Gauss-Legendre formula; *Inner integration*: interpolatory formula for log kernel (4.21).

♯ outer nodes	$p = 1, q = 1$	$p = 2, q = 1$	$p = 3, q = 1$
4	$4.3635979 \cdot 10^{-02}$	$4.3631882 \cdot 10^{-02}$	$4.3631767 \cdot 10^{-02}$
8	$4.3631997 \cdot 10^{-02}$	$4.3631674 \cdot 10^{-02}$	$4.3631673 \cdot 10^{-02}$
16	$4.3631695 \cdot 10^{-02}$	$4.3631673 \cdot 10^{-02}$	–
32	$4.3631674 \cdot 10^{-02}$	–	–

Also for the calculation of the log singularity, we propose, in Table 4.3, the use of the

interpolatory formula (4.21) in case of integration on a particular subset of $\widehat{E}_{\mathtt{S}}$. The following discretization and elastic parameters have been considered: $d_m = d_{\widetilde{m}} = 0$, $\Delta = 0.1$, $h_m = 0.2$, $c_{\mathtt{S}} = 0.4$ and $c_{\mathtt{P}} = 0.7$. With the indicated value of $C_{\log}$, the integral kernel $C_{\log} \log(|s - z|)$ corresponds to the function $h^V_{2,11}$, reported in (1.84). The integration domain, to which the simulations refer, intersects the line $s = z$, where $\log(|s - z|)$ is weakly singular: due to that, inner integration has been performed with the interpolatory formula (4.21) (using only one node because we set $w_\eta^{(d_m)}(z)$ as the unique Lagrangian base with degree $d_m = 0$). Outer integrand function has a weak singularity of kind $s \log(s)$ at the lower boundary $s = 0$. This behaviour has been treated with the smoothing transformation $\Theta_{p,q}$ and the results are obtained by changing the parameter p. We remark that the single precision accuracy is reached for $p = 2$ and 16 quadrature nodes. For $p = 3$ there is a slight improvement in the results.

4.2.3 The functions $\mathcal{O}(1/r)$

Here we consider the singular behaviour which characterizes the double layer kernel defined in (1.95). As remarked at the beginning of the chapter, to evaluate the elements of the corresponding matrix $\mathbb{E}_K$, we need to calculate integrals of type (4.1), where the function B_{ij} corresponds to the double layer kernel ν^K_{ij}. For the splitting criteria exposed in Section 4.1 for integration on coincident and on consecutive elements e_m, $e_{\widetilde{m}}$, to compute integral (4.1) is necessary to distinguish, and integrate separately, the portion of integration domain containing the points in local coordinates giving possibly $r = 0$. This means that, taking into account the reduced form (1.96) of the double layer kernel for $0 \leqslant r \leqslant c_{\mathtt{S}}\Delta$, we need to calculate contributions of type:

$$\int_{e_{\widetilde{m}} \times e_m \cap \{0 \leqslant r \leqslant c_{\mathtt{S}}\Delta\}} w_{\widetilde{m}}(\mathbf{x}) w_m(\boldsymbol{\xi}) \frac{r_{,i} f(r;\Delta)}{r} d\Gamma_{\boldsymbol{\xi}} d\Gamma_{\mathbf{x}},\ i = 1, 2, \tag{4.25}$$

$$\int_{e_{\widetilde{m}} \times e_m \cap \{0 \leqslant r \leqslant c_{\mathtt{S}}\Delta\}} w_{\widetilde{m}}(\mathbf{x}) w_m(\boldsymbol{\xi}) \frac{r_{,i} r_{,j} r_{,k} f(r;\Delta)}{r} d\Gamma_{\boldsymbol{\xi}} d\Gamma_{\mathbf{x}}\ i, j, k = 1, 2, \tag{4.26}$$

where $f(r;\Delta)$ can correspond, without loss of generality, to the following functions

$$\sqrt{c_{\mathtt{S}}^2\Delta^2 - r^2},\ \sqrt{c_{\mathtt{P}}^2\Delta^2 - r^2},\ \frac{1}{c_{\mathtt{P}}\sqrt{c_{\mathtt{S}}^2\Delta^2 - r^2} + c_{\mathtt{S}}\sqrt{c_{\mathtt{P}}^2\Delta^2 - r^2}}, \tag{4.27}$$

and the factors $r_{,i}$ for $i = 1, 2$ are the normalized components of the vector $\mathbf{r} = \mathbf{x} - \boldsymbol{\xi}$, as indicated in the Appendix in formula (A.1). We observe that the elements of the double layer matrix, introduced in (1.94) for problems with mixed boundary conditions, are defined as double space integrals on $\Gamma_{\mathcal{N}}$ and $\Gamma_{\mathcal{D}}$, which compose a partition of the boundary with $\Gamma_{\mathcal{N}} \cap \Gamma_{\mathcal{D}} = \emptyset$. This means that, for this configuration, the unique case for which it is necessary to evaluate strongly singular integral elements happens when $e_{\widetilde{m}}$ and e_m are consecutive, since the mesh elements cannot belong to the same set of Γ partition. Nevertheless, here we expose also the case of integration on coincident element, namely $e_{\widetilde{m}} \equiv e_m$, because the discretized double layer operator K can be employed for BIEs of type $(\mathcal{D}_1)$, $(\mathcal{D}_2)$, $(\mathcal{N}_1)$ and $(\mathcal{N}_2)$, whose energetic weak formulations can be performed with a discretized double layer operator $\mathbb{E}_K$ whose elements are double space integrals defined

on the entire boundary Γ. This approach has been in particular employed to obtain the numerical results for Dirichlet problems in Subsection 1.6.1.

As previously discussed, the definitions in local variables of the distance r and the normalized components $r_{,i}$ are strictly connected to the local geometry determined by e_m and $e_{\widetilde{m}}$. Thus, if we consider the parametrization in local variables introduced in the subsections 4.1.1-4.1.2 (see Figures 4.1-4.4), we can observe that in case of coincident elements

$$\frac{r_{,i}}{r} = \frac{\sigma_i}{s-z}, \quad \frac{r_{,i}r_{,j}r_{,k}}{r} = \frac{\sigma_i\sigma_j\sigma_k}{s-z}, \quad \text{with } \sigma_1 = \cos(\theta),\ \sigma_2 = \sin(\theta), \tag{4.28}$$

where θ is the angle detected by the element e_m w.r.t. the horizontal cartesian axis. The situation is analogous for consecutive and aligned elements:

$$\frac{r_{,i}}{r} = \frac{\sigma_i}{s+h_m-z}, \quad \frac{r_{,i}r_{,j}r_{,k}}{r} = \frac{\sigma_i\sigma_j\sigma_k}{s+h_m-z}$$

while for consecutive and not aligned elements these peculiar ratios assume less trivial definitions:

$$\begin{aligned}\frac{r_{,i}}{r} &= \frac{k_1(h_m-z)+k_2 s}{s^2+(h_m-z)^2-2(h_m-z)s\cos(\alpha)},\\ \frac{r_{,i}r_{,j}r_{,k}}{r} &= \frac{\widetilde{k}_1(h_m-z)^3+\widetilde{k}_2(h_m-z)^2 s+\widetilde{k}_3(h_m-z)s^2+\widetilde{k}_4 s^3}{s^2+(h_m-z)^2-2(h_m-z)s\cos(\alpha)},\end{aligned}$$

where α is the angle between the elements e_m and $e_{\widetilde{m}}$. The coefficients in the formulas depend on the projections of the elements onto the cartesian axis; in fact, by exploring the definition of r_i and r_j in (4.7)-(4.8), we have

$$\begin{aligned}k_1 =&\tau_{i1}, \quad k_2 = \tau_{i2}, \quad \widetilde{k}_1 = \tau_{i1}\tau_{j1}\tau_{k1}, \quad \widetilde{k}_2 = \tau_{k1}(\tau_{i1}\tau_{j2}+\tau_{i2}\tau_{j1})+\tau_{i1}\tau_{j1}\tau_{k2},\\ \widetilde{k}_3 =&\tau_{k2}(\tau_{i1}\tau_{j2}+\tau_{i2}\tau_{j1})+\tau_{i2}\tau_{j2}\tau_{k1}, \quad \widetilde{k}_4 = \tau_{i2}\tau_{j2}\tau_{k2}.\end{aligned}$$

A discussion of the integration techniques for strongly singular integrals needs therefore to be based on the mutual position of the integration segments.

Coincident elements

In case of coincident elements we can treat in the same way the contributions (4.25) and (4.26), since both basically depend only on the factor $1/(s-z)$. Due to that, we consider the integral

$$\mathcal{I} = \int_a^b \int_{A(s)}^{B(s)} w_{\widetilde{\eta}}^{(d_{\widetilde{m}})}(s) w_{\eta}^{(d_m)}(z) \frac{f(r(s,z);\Delta)}{s-z} ds dz$$

with the outer extremes a, b forming a couple of splitting nodes typical of the domain subdivision schemes for coincident elements, as shown in Figure 4.2. As indicated in (4.2), the polynomials $w_{\widetilde{\eta}}^{(d_{\widetilde{m}})}$ and $w_{\eta}^{(d_m)}$ are, in local variables, the restriction of the shape functions $w_{\widetilde{m}}$ and w_m to the elements e_m and $e_{\widetilde{m}}$. The integration domain intersects the axis $s = z$, along which the integrand function is strongly singular. Therefore, we can

operate a Taylor expansion in the inner variable, centred in $z = s$, in order to rewrite $\mathcal{I}$ as the sum of the following integrals:

$$\mathcal{I} = \int_a^b w_{\widetilde{\eta}}^{(d_{\widetilde{m}})}(s) \int_{A(s)}^{B(s)} \frac{w_\eta^{(d_m)}(z) f(r(s,z);\Delta) - w_\eta^{(d_m)}(s) f(r(s,s);\Delta)}{s-z} ds dz$$
$$- \int_a^b w_{\widetilde{\eta}}^{(d_{\widetilde{m}})}(s) w_\eta^{(d_m)}(s) f(r(s,s);\Delta) \fint_{A(s)}^{B(s)} \frac{1}{z-s} dz ds = \mathcal{I}_1 + \mathcal{I}_2.$$

Integral $\mathcal{I}_1$ is no more singular, because the numerator of the integrand function is a $\mathcal{O}(s-z)$ for $z \to s$, and the inner integration can be performed by the use of the Gauss-Legendre formula (4.18), possibly combined with the smoothing transformation (4.19) if one or both of the inner extremes of integration coincides with one of the solutions in z of $|s-z| = c_{\mathrm{S}}\Delta$. For what concerns integral $\mathcal{I}_2$, it has to be defined in the Cauchy Principal Value sense, identified by the symbol $\fint$, in the inner variable z, and properly computed as follows:

$$\mathcal{I}_2 = - \int_a^b w_{\widetilde{\eta}}^{(d_{\widetilde{m}})}(s) w_\eta^{(d_m)}(s) f(r(s,z);\Delta) \fint_{A(s)}^{B(s)} \frac{1}{z-s} dz ds$$
$$= - \int_a^b w_{\widetilde{\eta}}^{(d_{\widetilde{m}})}(s) w_\eta^{(d_m)}(s) f(r(s,s);\Delta) \left[\log(B(s)-s) - \log(s-A(s))\right] ds.$$

The last integral now is characterized at most by a weak log singularity if $a = A(s) = 0$ or $b = B(s) = h_m$. In this case, to improve the numerical evaluation of $\mathcal{I}_2$, we can employ the transformation in (4.19) in order to thicken the outer quadrature nodes towards the extreme a, b or both.

Consecutive elements

The case of consecutive and aligned elements, that appears if the angle α between the elements is equal to π, results very similar to the previous one, since r is linear w.r.t. the local variable s and z. Computations become more complicate instead if $\alpha \neq \pi$ and this forces us to treat integrals (4.25) and (4.26) with slightly different approaches. Let us consider first the contribution (4.25): to evaluate it in case of consecutive generic segments we have to calculate contributions of type

$$\mathcal{I}_s = \int_0^b \int_{A(s)}^{h_m} w_{\widetilde{\eta}}^{(d_{\widetilde{m}})}(s) w_\eta^{(d_m)}(z) \frac{f(r(s,z);\Delta) s}{s^2 + (h_m - z)^2 - 2(h_m - z) s \cos(\alpha)} dz ds$$

and

$$\mathcal{I}_z = \int_0^b \int_{A(s)}^{h_m} w_{\widetilde{\eta}}^{(d_{\widetilde{m}})}(s) w_\eta^{(d_m)}(z) \frac{f(r(s,z);\Delta)(h_m - z)}{s^2 + (h_m - z)^2 - 2(h_m - z) s \cos(\alpha)} dz ds.$$

As stated in Subsection 4.1.2, the portion of local integration domain containing the singular point with coordinates $(s,z) = (0, h_m)$ is determined, in the integral, always by the inner upper extreme $z = h_m$ and the lower outer extreme $s = 0$. This is in particular visible in the first integrals of (4.12), (4.13) and (4.14), generated by the splitting schemes for consecutive elements. Thus we concentrate only on that kind of portion of

integral domain, and, as done previously, we proceed with a Taylor expansion of the factor $w_{\eta}^{(d_m)}(z)f(r(s,z);\Delta)$ at the denominator, centred in $z=h_m$ and calculated at $s=0$. The number of terms depends on the presence of the factor s or (h_m-z), in fact:

$$\begin{aligned}
\mathcal{I}_s = &\int_0^b w_{\widetilde{\eta}}^{(d_{\widetilde{m}})}(s)s \\
&\int_{A(s)}^{h_m} \frac{w_{\eta}^{(d_m)}(z)f(r(s,z);\Delta) - w_{\eta}^{(d_m)}(h_m)f(0;\Delta) - \frac{\partial}{\partial z}\left(w_{\eta}^{(d_m)}(z)f(r(s,z);\Delta)\right)_{|_{z=h_m,\ s=0}}(z-h_m)}{s^2+(h_m-z)^2-2(h_m-z)s\cos(\alpha)}dzds \\
&+\int_0^b w_{\widetilde{\eta}}^{(d_{\widetilde{m}})}(s)sw_{\eta}^{(d_m)}(h_m)f(0;\Delta)\int_{A(s)}^{h_m}\frac{1}{s^2+(h_m-z)^2-2(h_m-z)s\cos(\alpha)}dzds \\
&+\int_0^b w_{\widetilde{\eta}}^{(d_{\widetilde{m}})}(s)s\frac{\partial}{\partial z}\left(w_{\eta}^{(d_m)}(z)f(r(s,z);\Delta)\right)_{|_{z=h_m,\ s=0}}\int_{A(s)}^{h_m}\frac{(z-h_m)}{s^2+(h_m-z)^2-2(h_m-z)s\cos(\alpha)}dzds \\
&=\mathcal{I}_{s,1}+\mathcal{I}_{s,2}+\mathcal{I}_{s,3},
\end{aligned}$$

and

$$\begin{aligned}
\mathcal{I}_z = &\int_0^b w_{\widetilde{\eta}}^{(d_{\widetilde{m}})}(s)\int_{A(s)}^{h_m}\frac{(h_m-z)\left(w_{\eta}^{(d_m)}(z)f(r(s,z);\Delta)-w_{\eta}^{(d_m)}(h_m)f(0;\Delta)\right)}{s^2+(h_m-z)^2-2(h_m-z)s\cos(\alpha)}dzds \\
&+\int_0^b w_{\widetilde{\eta}}^{(d_{\widetilde{m}})}(s)w_{\eta}^{(d_m)}(h_m)f(0;\Delta)\int_{A(s)}^{h_m}\frac{h_m-z}{s^2+(h_m-z)^2-2(h_m-z)s\cos(\alpha)}dzds \\
&=\mathcal{I}_{z,1}+\mathcal{I}_{z,2}.
\end{aligned}$$

At this stage, in both integrals $\mathcal{I}_{s,1}$ and $\mathcal{I}_{z,1}$ the Taylor expansion has allowed to numerically avoid the singularity of the denominator $s^2+(h_m-z)^2-2(h_m-z)s\cos(\alpha)$ for $s=0$ and $z=h_m$. The additive integrals $\mathcal{I}_{s,2}$, $\mathcal{I}_{s,3}$ and $\mathcal{I}_{z,2}$ can be computed exactly in the inner integration variable, in fact

$$\int\frac{1}{s^2+(h_m-z)^2-2(h_m-z)s\cos(\alpha)}dz=-\frac{1}{\sin(\alpha)s}\arctan\left(\frac{h_m-z-\cos(\alpha)s}{\sin(\alpha)s}\right) \tag{4.29}$$

and

$$\begin{aligned}
&\int\frac{z-h_m}{s^2+(h_m-z)^2-2(h_m-z)s\cos(\alpha)}dz \\
=&\frac{1}{2}\log\left(s^2+(h_m-z)^2-2(h_m-z)s\cos(\alpha)\right)+\frac{\cos(\alpha)}{\sin(\alpha)}\arctan\left(\frac{h_m-z-\cos(\alpha)s}{\sin(\alpha)s}\right).
\end{aligned} \tag{4.30}$$

Exploiting then the last two integrals in the definition of $\mathcal{I}_{s,2}$, $\mathcal{I}_{s,3}$ and $\mathcal{I}_{z,2}$ we obtain

$$\begin{aligned}
\mathcal{I}_{s,2} = &\int_0^b \frac{w_{\widetilde{\eta}}^{(d_{\widetilde{m}})}(s)w_{\eta}^{(d_m)}(h_m)f(0;\Delta)}{\sin(\alpha)}w_{\widetilde{\eta}}^{(d_{\widetilde{m}})}(s)w_{\eta}^{(d_m)}(h_m)f(0;\Delta)\cdot \\
&\left[\arctan\left(\frac{h_m-A(s)-\cos(\alpha)s}{\sin(\alpha)s}\right)-\arctan\left(-\frac{\cos(\alpha)}{\sin(\alpha)}\right)\right]ds,
\end{aligned}$$

$$\mathcal{I}_{s,3} = \int_0^b w_{\widetilde{\eta}}^{(d_{\widetilde{m}})}(s) s \frac{\partial}{\partial z}\left(w_{\eta}^{(d_m)}(z) f(r(s,z);\Delta)\right)_{|_{z=h_m,\, s=0}} \cdot \left[\frac{1}{2}\log\left(\frac{s^2}{s^2+(h_m-A(s))^2-2(h_m-A(s))s\cos(\alpha)}\right) + \frac{\cos(\alpha)}{\sin(\alpha)}\left(\arctan\left(-\frac{\cos(\alpha)}{\sin(\alpha)}\right) - \arctan\left(\frac{h_m-A(s)-\cos(\alpha)s}{\sin(\alpha)s}\right)\right)\right] ds,$$

and

$$\mathcal{I}_{z,2} = \int_0^b w_{\widetilde{\eta}}^{(d_{\widetilde{m}})}(s) w_{\eta}^{(d_m)}(h_m) f(0;\Delta) \cdot \left[\frac{1}{2}\log\left(\frac{s^2}{s^2+(h_m-A(s))^2-2(h_m-A(s))s\cos(\alpha)}\right) + \frac{\cos(\alpha)}{\sin(\alpha)}\left(\arctan\left(-\frac{\cos(\alpha)}{\sin(\alpha)}\right) - \arctan\left(\frac{h_m-A(s)-\cos(\alpha)s}{\sin(\alpha)s}\right)\right)\right] ds.$$

Last computations reveal that the main characteristic of $\mathcal{I}_{s,2}$, $\mathcal{I}_{s,3}$ and $\mathcal{I}_{z,2}$ is a mild singularity in $s = 0$ that can be overcome approximating them again by the use of the transformation (4.19) combined with the Gaussian quadrature formula presented in (4.18). In the end, the correct procedure to approximate the integral contribution (4.26) follows exactly what has been done so far for the term (4.25): the integrand function needs to be expressed as the sum of addends depending respectively on the polynomials s^3, $s^2(h_m - z)$, $s(h_m - z)^2$ and $(h_m - z)^3$ and then, for each addend, we can apply a Taylor expansion of order depending on the degree of the factor $(h_m - z)$ at the numerator. The expansion gives rise to some additional integrals that can be computed exactly in the z variable and that at most present mild boundary singularities in the outer integration.

4.2.4 The functions $\mathcal{O}(1/r^2)$

Here we expose the numerical approach to approximate the integral depending on the hypersingular kernel ν_{ij}^K, having behaviour $\mathcal{O}(1/r^2)$ for $r \to 0$ (the mesh elements $e_{\widetilde{m}}$ and e_m are coincident or at most consecutive). Also in this case, we consider the reduced form of the kernel (1.90), defined for $0 \leqslant r \leqslant c_{\mathrm{S}}\Delta$. Evaluating the elements of the corresponding matrix $\mathbb{E}_D$ means that we have to deal with the following integral contributions:

$$\int_{e_{\widetilde{m}}\times e_m \cap \{r<c_{\mathrm{S}}\Delta\}} w_{\widetilde{m}}(\mathbf{x}) w_m(\boldsymbol{\xi}) \frac{f(r;\Delta)}{r^2} d\Gamma_{\boldsymbol{\xi}} d\Gamma_{\mathbf{x}},\ i = 1,2, \tag{4.31}$$

$$\int_{e_{\widetilde{m}}\times e_m \cap \{r<c_{\mathrm{S}}\Delta\}} w_{\widetilde{m}}(\mathbf{x}) w_m(\boldsymbol{\xi}) \frac{r_{,i} r_{,j} f(r;\Delta)}{r^2} d\Gamma_{\boldsymbol{\xi}} d\Gamma_{\mathbf{x}},\ i,j = 1,2, \tag{4.32}$$

$$\int_{e_{\widetilde{m}}\times e_m \cap \{r<c_{\mathrm{S}}\Delta\}} w_{\widetilde{m}}(\mathbf{x}) w_m(\boldsymbol{\xi}) \frac{r_{,i} r_{,j} r_{,k} r_{,l} f(r;\Delta)}{r^2} d\Gamma_{\boldsymbol{\xi}} d\Gamma_{\mathbf{x}},\ i,j,k,l = 1,2, \tag{4.33}$$

where $f(r;\Delta)$ corresponds to one of the functions introduced in (4.27). Also in this case it is useful to express the normalized component $r_{,i}$ making explicit the dependence on the local integration variable s and z. This, in case of coincident elements, allows us to write

the following ratios as

$$\frac{r_{,i}r_{,j}}{r^2} = \frac{\sigma_i\sigma_j}{(s-z)^2}, \quad \frac{r_{,i}r_{,j}r_{,k}r_{,l}}{r^2} = \frac{\sigma_i\sigma_j\sigma_k\sigma_l}{(s-z)^2},$$

where σ_i for $i = 1, 2$ are defined in (4.28). For consecutive and aligned elements it holds

$$\frac{r_{,i}r_{,j}}{r^2} = \frac{\sigma_i\sigma_j}{(s+h_m-z)^2}, \quad \frac{r_{,i}r_{,j}r_{,k}r_{,l}}{r^2} = \frac{\sigma_i\sigma_j\sigma_k\sigma_l}{(s+h_m-z)^2},$$

and, at last, for consecutive and not aligned elements, remembering the definition of the components r_i and r_j in (4.7)-(4.8), the ratios have the following expression:

$$\begin{aligned}
\frac{r_{,i}r_{,j}}{r^2} &= \frac{k_1(h_m-z)^2 + k_2(h_m-z)s + k_3s^2}{\left(s^2+(h_m-z)^2-2(h_m-z)s\cos(\alpha)\right)^2}, \\
\frac{r_{,i}r_{,j}r_{,k}r_{,l}}{r^2} &= \frac{\widetilde{k}_1(h_m-z)^4 + \widetilde{k}_2(h_m-z)^3s + \widetilde{k}_3(h_m-z)^2s^2 + \widetilde{k}_4(h_m-z)s^3 + \widetilde{k}_5s^4}{\left(s^2+(h_m-z)^2-2(h_m-z)s\cos(\alpha)\right)^3},
\end{aligned}$$

with

$$k_1 = \tau_{i1}\tau_{j1}, \quad k_2 = (\tau_{i1}\tau_{j2} + \tau_{i2}\tau_{j1}), \quad k_3 = \tau_{i2}\tau_{j2},$$

and

$$\begin{aligned}
\widetilde{k}_1 =& \tau_{i1}\tau_{j1}\tau_{k1}\tau_{l1}, \\
\widetilde{k}_2 =& \tau_{l1}(\tau_{k1}(\tau_{i1}\tau_{j2}+\tau_{i2}\tau_{j1}) + \tau_{i1}\tau_{j1}\tau_{k2}) + \tau_{i1}\tau_{j1}\tau_{k1}\tau_{l2}, \\
\widetilde{k}_3 =& \tau_{l2}(\tau_{k1}(\tau_{i1}\tau_{j2}+\tau_{i2}\tau_{j1}) + \tau_{i1}\tau_{j1}\tau_{k2}) + \tau_{l1}(\tau_{k2}(\tau_{i1}\tau_{j2}+\tau_{i2}\tau_{j1}) + \tau_{i2}\tau_{j2}\tau_{k1}), \\
\widetilde{k}_4 =& \tau_{l2}(\tau_{k2}(\tau_{i1}\tau_{j2}+\tau_{i2}\tau_{j1}) + \tau_{i2}\tau_{j2}\tau_{k1}) + \tau_{i2}\tau_{j2}\tau_{k2}\tau_{l1}, \\
\widetilde{k}_5 =& \tau_{i2}\tau_{j2}\tau_{k2}\tau_{l2}.
\end{aligned}$$

This again compels us to define different integration approaches to integrate the hypersingularity in (4.31), (4.32) and (4.33) based on the position of the mesh elements.

Coincident elements

This is the simplest geometrical configuration for the integration of mesh elements, for which all the integrals (4.31), (4.32) and (4.33) depend only on the factor $1/(s-z)^2$. Thanks to that, it is enough to furnish the procedure to compute numerically the integral

$$\mathcal{I} = \int_a^b \int_{A(s)}^{B(s)} w_{\widetilde{\eta}}^{(d_{\widetilde{m}})}(s) w_{\eta}^{(d_m)}(z) \frac{f(r(s,z);\Delta)}{(s-z)^2} ds dz.$$

A Taylor expansion in the inner variable, centred in $z = s$, still represents an effective strategy to manage the singular behaviour of the integrand function:

$$\begin{aligned}\mathcal{I} = &\int_a^b w_{\widetilde{\eta}}^{(d_{\widetilde{m}})}(s) \\ &\int_{A(s)}^{B(s)} \frac{w_\eta^{(d_m)}(z) f(r(s,z);\Delta) - w_\eta^{(d_m)}(s) f(r(s,s);\Delta) - \frac{\partial}{\partial z}\left(w_\eta^{(d_m)}(z) f(r(s,z);\Delta)\right)_{|z=s}(z-s)}{(s-z)^2} dz ds \\ &+ \int_a^b w_{\widetilde{\eta}}^{(d_{\widetilde{m}})}(s) w_\eta^{(d_m)}(s) f(r(s,s);\Delta) \int_{A(s)}^{B(s)} \frac{1}{(s-z)^2} dz ds \\ &- \int_a^b w_{\widetilde{\eta}}^{(d_{\widetilde{m}})}(s) \frac{\partial}{\partial z}\left(w_\eta^{(d_m)}(z) f(r(s,z);\Delta)\right)_{|z=s} \oint_{A(s)}^{B(s)} \frac{1}{(s-z)} dz ds \\ &= \mathcal{I}_1 + \mathcal{I}_2 + \mathcal{I}_3.\end{aligned}$$

The addend $\mathcal{I}_1$ can be treated again combining, for the appropriate configuration of the integration domain, the smoothing transformation (4.19) with the Gauss-Legendre formula. Instead, for what concerns $\mathcal{I}_2$ and $\mathcal{I}_3$, the inner integration can be performed analytically (the second one as a Cauchy Principal Value), leading to the results:

$$\mathcal{I}_2 = \oint_a^b w_{\widetilde{\eta}}^{(d_{\widetilde{m}})}(s) w_\eta^{(d_m)}(s) f(r(s,s);\Delta) \left[\frac{1}{s - B(s)} - \frac{1}{s - A(s)}\right] ds,$$

and

$$\mathcal{I}_3 = \int_a^b w_{\widetilde{\eta}}^{(d_{\widetilde{m}})}(s) \frac{\partial}{\partial z}\left(w_\eta^{(d_m)}(z) f(r(s,z);\Delta)\right)_{|z=s} \left[\log(B(s) - s) - \log(s - A(s))\right] ds,$$

Integral $\mathcal{I}_2$ could still save a hypersingular behaviour of kind $\mathcal{O}(1/s)$ if $a = A(s) = 0$ or of kind $\mathcal{O}(1/(h_m - s))$ if $b = B(s) = h_m$, meaning that, up to the value of the integration extremes, the outer integral requires to be calculated as Hadamard Finite Part integral, denoted by the symbol $\oint$ and indicated in the text with the acronym HFP. Numerically, we make use of the following interpolatory quadrature rule of Gauss-Radau type

$$\oint_0^1 \frac{f(s)}{s} ds = \omega_{\mathrm{GR},0} f(0) + \sum_{k=1}^{n} \omega_{\mathrm{GR},k} f(s_k) + R_{\mathrm{GR},n}(f) \tag{4.34}$$

where the nodes and the weights, defined in the following

$$s_k = \frac{1 + z_k}{2},\ \omega_{\mathrm{GR},k} = \frac{\lambda_k}{2 s_k},\ k = 1, ..., n, \quad \omega_{\mathrm{GR},0} = -\sum_{k=1}^{n} \omega_{\mathrm{GR},k},$$

depend on the set of the Legendre zeros $\{z_k\}$. We report here, for convenience of the reader, the convergence theorem related to quadrature formula (4.34)

Theorem 4.2.3. *(see [62]) If $f \in C^p([0,1])$ with $p > 1$ and $f^{(p)} \in H_\mu([0,1])$ for some $0 < \mu < 1$, with H_μ the space of Hölder continuous functions of order μ, then*

$$R_{\mathrm{GR},n}(f) = \mathcal{O}\left(n^{-p-\mu}\right)$$

The proof of Theorem 4.2.3 can be found in [62], together with more results about the properties of formula (4.34). In particular, the latter can be employed in the computation of $\mathcal{I}_2$ after the change of variable $s \in [a,b] \to \widetilde{s} \in [0,1]$.

Consecutive elements

The case of consecutive and aligned elements, namely $\alpha = \pi$, results very similar to the case of coincident ones, since r is linear in the local variables s, z. Thus, also here we discuss only the case of integration for not aligned elements, namely $\alpha \neq \pi$. Let us focus on the integral contributions (4.31) and (4.32) (the procedure to approximate (4.33) is analogous): to calculate these integrals we basically have to take into account the terms

$$\mathcal{I} = \int_0^b \int_{A(s)}^{h_m} w_{\widetilde{\eta}}^{(d_{\widetilde{m}})}(s) w_{\eta}^{(d_m)}(z) \frac{f(r(s,z);\Delta)}{s^2 + (h_m - z)^2 - 2(h_m - z)s\cos(\alpha)} dzds,$$

$$\mathcal{I}_{s^2} = \int_0^b \int_{A(s)}^{h_m} w_{\widetilde{\eta}}^{(d_{\widetilde{m}})}(s) w_{\eta}^{(d_m)}(z) \frac{f(r(s,z);\Delta)s^2}{\left(s^2 + (h_m - z)^2 - 2(h_m - z)s\cos(\alpha)\right)^2} dzds,$$

$$\mathcal{I}_{sz} = \int_0^b \int_{A(s)}^{h_m} w_{\widetilde{\eta}}^{(d_{\widetilde{m}})}(s) w_{\eta}^{(d_m)}(z) \frac{f(r(s,z);\Delta)(h_m - z)s}{\left(s^2 + (h_m - z)^2 - 2(h_m - z)s\cos(\alpha)\right)^2} dzds,$$

$$\mathcal{I}_{z^2} = \int_0^b \int_{A(s)}^{h_m} w_{\widetilde{\eta}}^{(d_{\widetilde{m}})}(s) w_{\eta}^{(d_m)}(z) \frac{f(r(s,z);\Delta)(h_m - z)^2}{\left(s^2 + (h_m - z)^2 - 2(h_m - z)s\cos(\alpha)\right)^2} dzds.$$

Computation of $\mathcal{I}$ is necessary to obtain integral (4.31), while $\mathcal{I}_{s^2}$, $\mathcal{I}_{sz}$ and $\mathcal{I}_{z^2}$ arise from making explicit the definition of the factor $r_{,i}r_{,j}/r^2$ in (4.32). Here again we calculate the integrals on the portion of the local domain containing the singular point $(s,z) = (0, h_m)$. To elaborate $\mathcal{I}$ we proceed as always with the Taylor expansion of the numerator of the integrand function:

$$\begin{aligned}
\mathcal{I} = & \int_0^b w_{\widetilde{\eta}}^{(d_{\widetilde{m}})}(s) \\
& \int_{A(s)}^{h_m} \frac{w_{\eta}^{(d_m)}(z) f(r(s,z);\Delta) - w_{\eta}^{(d_m)}(h_m) f(0;\Delta) - \frac{\partial}{\partial z}\left(w_{\eta}^{(d_m)}(z) f(r(s,z);\Delta)\right)_{|_{z=h_m,\, s=0}} (z - h_m)}{s^2 + (h_m - z)^2 - 2(h_m - z)s\cos(\alpha)} dzds \\
& + \int_0^b w_{\widetilde{\eta}}^{(d_{\widetilde{m}})}(s) w_{\eta}^{(d_m)}(h_m) f(0;\Delta) \int_{A(s)}^{h_m} \frac{1}{s^2 + (h_m - z)^2 - 2(h_m - z)s\cos(\alpha)} dzds \\
& + \int_0^b w_{\widetilde{\eta}}^{(d_{\widetilde{m}})}(s) \frac{\partial}{\partial z}\left(w_{\eta}^{(d_m)}(z) f(r(s,z);\Delta)\right)_{|_{z=h_m,\, s=0}} \int_{A(s)}^{h_m} \frac{(z - h_m)}{s^2 + (h_m - z)^2 - 2(h_m - z)s\cos(\alpha)} dzds \\
& = \mathcal{I}_1 + \mathcal{I}_2 + \mathcal{I}_3.
\end{aligned}$$

The inner integrals of $\mathcal{I}_2$ an $\mathcal{I}_3$ have been already analytically computed in (4.29) and (4.30), therefore we rewrite them as

$$\begin{aligned}
\mathcal{I}_2 = & \int_0^b \frac{w_{\widetilde{\eta}}^{(d_{\widetilde{m}})}(s) w_{\eta}^{(d_m)}(h_m) f(0;\Delta)}{\sin(\alpha)} w_{\widetilde{\eta}}^{(d_{\widetilde{m}})}(s) w_{\eta}^{(d_m)}(h_m) f(0;\Delta) \cdot \\
& \frac{1}{s}\left[\arctan\left(\frac{h_m - A(s) - \cos(\alpha)s}{\sin(\alpha)s}\right) - \arctan\left(-\frac{\cos(\alpha)}{\sin(\alpha)}\right)\right] ds,
\end{aligned}$$

$$\mathcal{I}_3 = \int_0^b w_{\widetilde{\eta}}^{(d_{\tilde{m}})}(s) \frac{\partial}{\partial z} \left(w_{\eta}^{(d_m)}(z) f(r(s,z);\Delta) \right)_{|_{z=h_m,\, s=0}} \cdot \left[\frac{1}{2} \log \left(\frac{s^2}{s^2 + (h_m - A(s))^2 - 2(h_m - A(s)) s \cos(\alpha)} \right) + \frac{\cos(\alpha)}{\sin(\alpha)} \left(\arctan\left(-\frac{\cos(\alpha)}{\sin(\alpha)} \right) - \arctan\left(\frac{h_m - A(s) - \cos(\alpha) s}{\sin(\alpha) s} \right) \right) \right] ds.$$

The only contribution that shows up a singularity for $s = 0$ is $\mathcal{I}_2$ because of the presence of the factor $1/s$. To treat this singular behaviour we employ, following a suitable change of the integration variable, the interpolatory formula for HFP integrals introduced in (4.34). Let us focus instead on the less trivial integrals $\mathcal{I}_{s^2}$. To overcome the hypersingularity we need to perform a Taylor expansion of the third order, leading to the following reformulation of the integral:

$$\begin{aligned}
\mathcal{I}_{s^2} =& \int_0^b w_{\widetilde{\eta}}^{(d_{\tilde{m}})}(s) s^2 \int_{A(s)}^{h_m} \frac{T(s,z;\Delta)}{\left(s^2 + (h_m - z)^2 - 2(h_m - z) s \cos(\alpha)\right)^2} dz ds \\
&+ \int_0^b w_{\widetilde{\eta}}^{(d_{\tilde{m}})}(s) s^2 T_1(\Delta) \int_{A(s)}^{h_m} \frac{1}{\left(s^2 + (h_m - z)^2 - 2(h_m - z) s \cos(\alpha)\right)^2} dz ds \\
&+ \int_0^b w_{\widetilde{\eta}}^{(d_{\tilde{m}})}(s) s^2 T_2(\Delta) \int_{A(s)}^{h_m} \frac{z - h_m}{\left(s^2 + (h_m - z)^2 - 2(h_m - z) s \cos(\alpha)\right)^2} dz ds \\
&+ \int_0^b w_{\widetilde{\eta}}^{(d_{\tilde{m}})}(s) s^2 T_3(\Delta) \int_{A(s)}^{h_m} \frac{(z - h_m)^2}{\left(s^2 + (h_m - z)^2 - 2(h_m - z) s \cos(\alpha)\right)^2} dz ds \\
&+ \int_0^b w_{\widetilde{\eta}}^{(d_{\tilde{m}})}(s) s^2 T_4(\Delta) \int_{A(s)}^{h_m} \frac{(z - h_m)^3}{\left(s^2 + (h_m - z)^2 - 2(h_m - z) s \cos(\alpha)\right)^2} dz ds \\
=& \mathcal{I}_{s^2,1} + \mathcal{I}_{s^2,2} + \mathcal{I}_{s^2,3} + \mathcal{I}_{s^2,4} + \mathcal{I}_{s^2,5}.
\end{aligned}$$

The numerator

$$\begin{aligned}
T(s,z;\Delta) =& w_{\eta}^{(d_m)}(z) f(r(s,z);\Delta) - w_{\eta}^{(d_m)}(h_m) f(0;\Delta) - \frac{\partial}{\partial z} \left(w_{\eta}^{(d_m)}(z) f(r(s,z);\Delta) \right)_{|_{z=h_m,\, s=0}} (z - h_m) \\
&- \frac{\partial^2}{\partial z^2} \left(w_{\eta}^{(d_m)}(z) f(r(s,z);\Delta) \right)_{|_{z=h_m,\, s=0}} (z - h_m)^2 - \frac{\partial^3}{\partial z^3} \left(w_{\eta}^{(d_m)}(z) f(r(s,z);\Delta) \right)_{|_{z=h_m,\, s=0}} (z - h_m)^3
\end{aligned}$$

contains the terms of the Taylor expansion of the factor $w_{\eta}^{(d_m)}(z) f(r(s,z);\Delta)$ and we observe again that the additional integrals $\mathcal{I}_{s^2,2}$, $\mathcal{I}_{s^2,3}$, $\mathcal{I}_{s^2,4}$ and $\mathcal{I}_{s^2,5}$ can be computed analytically in the

inner variable z, since in fact it holds

$$\begin{aligned}
&\int \frac{1}{\left(s^2+(h_m-z)^2-2(h_m-z)s\cos(\alpha)\right)^2}dz \\
=&-\frac{1}{2\sin(\alpha)^3 s^3}\arctan\left(\frac{h_m-z-\cos(\alpha)s}{\sin(\alpha)s}\right)-\frac{1}{2\sin(\alpha)^2 s^2}\frac{h_m-z-\cos(\alpha)s}{s^2+(h_m-z)^2-2(h_m-z)s\cos(\alpha)},
\end{aligned} \tag{4.35}$$

$$\begin{aligned}
&\int \frac{z-h_m}{\left(s^2+(h_m-z)^2-2(h_m-z)s\cos(\alpha)\right)^2}dz \\
=&\frac{\cos(\alpha)}{2\sin(\alpha)^3 s^2}\arctan\left(\frac{h_m-z-\cos(\alpha)s}{\sin(\alpha)s}\right)-\frac{1}{2\sin(\alpha)^2 s}\frac{-\cos(\alpha)(h_m-z)+s}{s^2+(h_m-z)^2-2(h_m-z)s\cos(\alpha)},
\end{aligned} \tag{4.36}$$

$$\begin{aligned}
&\int \frac{(z-h_m)^2}{\left(s^2+(h_m-z)^2-2(h_m-z)s\cos(\alpha)\right)^2}dz \\
=&-\frac{1}{2\sin(\alpha)^3 s}\arctan\left(\frac{h_m-z-\cos(\alpha)s}{\sin(\alpha)s}\right)-\frac{1}{2\sin(\alpha)^2}\frac{(\cos(\alpha)^2-\sin(\alpha)^2)(h_m-z)-\cos(\alpha)s}{s^2+(h_m-z)^2-2(h_m-z)s\cos(\alpha)},
\end{aligned} \tag{4.37}$$

$$\begin{aligned}
&\int \frac{(z-h_m)^3}{\left(s^2+(h_m-z)^2-2(h_m-z)s\cos(\alpha)\right)^2}dz \\
=&\frac{\cos(\alpha)(6-4\cos(\alpha)^2)}{4\sin(\alpha)^3}\arctan\left(\frac{h_m-z-\cos(\alpha)s}{\sin(\alpha)s}\right)+\frac{1}{2}\log\left(s^2+(h_m-z)^2-2(h_m-z)s\cos(\alpha)\right) \\
&+\frac{s}{2\sin(\alpha)^2}\frac{-\cos(\alpha)(3-4\cos(\alpha)^2)(h_m-z)+(1-2\cos(\alpha)^2)s}{s^2+(h_m-z)^2-2(h_m-z)s\cos(\alpha)}.
\end{aligned} \tag{4.38}$$

Substituting the explicit integration performed above in integrals $\mathcal{I}_{s^2,2}$, $\mathcal{I}_{s^2,3}$, $\mathcal{I}_{s^2,4}$ and $\mathcal{I}_{s^2,5}$, It turns out that only integral $\mathcal{I}_{s^2,2}$ still has a singularity of kind $\mathcal{O}(1/s)$, in fact

$$\begin{aligned}
\mathcal{I}_{s^2,2}=&\int_0^b w_{\widetilde{\eta}}^{(d_{\widetilde{m}})}(s)T_1(\Delta)\left\{-\frac{1}{2\sin(\alpha)^3 s}\arctan\left(-\frac{\cos(\alpha)}{\sin(\alpha)}\right)+\frac{1}{2\sin(\alpha)^2}\frac{\cos(\alpha)}{s}+\right. \\
&\left.+\frac{1}{2\sin(\alpha)^3 s}\arctan\left(\frac{h_m-A(s)-\cos(\alpha)s}{\sin(\alpha)s}\right)+\frac{1}{2\sin(\alpha)^2}\frac{h_m-A(s)-\cos(\alpha)s}{s^2+(h_m-A(s))^2-2(h_m-A(s))s\cos(\alpha)}\right\}ds.
\end{aligned}$$

Due to that, $\mathcal{I}_{s^2,2}$ can be computed by the HFP formula (4.34) and the other terms can be again treated with the Gauss-Legendre quadrature (4.18), possibly combined with the smoothing transformation (4.19) in case of mild boundary singularities.
We do not treat explicitly contributions $\mathcal{I}_{s,z}$ and $\mathcal{I}_{z^2}$: they just require respectively a Taylor expansion of the second and of the first order from which additionally contributions $\mathcal{I}_{s,z,2}$, $\mathcal{I}_{s,z,3}$, $\mathcal{I}_{s,z,4}$, $\mathcal{I}_{z^2,2}$ and $\mathcal{I}_{z^2,3}$ arise. These latter can be calculated exactly in the inner variable exploiting the integration already done in (4.35), (4.36), (4.37) and (4.38): integrals $\mathcal{I}_{s,z,2}$ and $\mathcal{I}_{z^2,2}$, both generated by the first term of the Taylor expansion, reveal to be affected by a $\mathcal{O}(1/s)$ singularity, that can be treated again with the HFP formula (4.34).

Appendix

In this section we present the time integration method to derive the kernels defined in (1.79), (1.95) and (1.89). We will frequently use the following notations for the calculation of the spatial derivatives of the Green's function. In particular the distance r is defined as

$$r := \|\mathbf{x} - \boldsymbol{\xi}\|_2 = \sqrt{(x_1 - \xi_1)^2 + (x_2 - \xi_2)^2} = \sqrt{r_1^2 + r_2^2}$$

and the normalized components of the vector $\mathbf{r} = \mathbf{x} - \boldsymbol{\xi}$ can be written as a partial derivative

$$r_{,i} := \frac{\partial r}{\partial x_i} = \frac{r_i}{r}. \tag{A.1}$$

Moreover we observe that the following properties hold:

$$\frac{\partial r_i}{\partial x_j} = \delta_{ij} = -(-\delta_{ij}) = -\frac{\partial r_i}{\partial \xi_j}, \tag{A.2}$$

$$r_{,ij} := \frac{\partial^2 r}{\partial x_i \partial x_j} = \frac{1}{r}(\delta_{ij} - r_{,i} r_{,j}), \tag{A.3}$$

$$r_{,1}^2 + r_{,2}^2 = 1, \tag{A.4}$$

$$\frac{\partial}{\partial x_i} f(r) = r_{,i} f'(r) \quad \Rightarrow \quad \frac{\partial}{\partial x_i}\left(\frac{1}{r^2}\right) = -\frac{2}{r^3} r_{,i}. \tag{A.5}$$

We consider the definition of the fundamental tensor components $G_{ij}^{\mathbf{uu}}$ reported in (1.15). After simple manipulations we can rewrite it as a sum of additional fundamental kernels:

$$\begin{aligned} G_{ij}^{\mathbf{uu}}(\mathbf{x}, \boldsymbol{\xi}; t, \tau) = \frac{1}{\varrho c_{\mathrm{P}}^2}\left[r_{,i} r_{,j} G_0^{\mathbf{uu}}(\mathbf{x}, \boldsymbol{\xi}; t, \tau; c_{\mathrm{P}}) + \left(2\frac{r_{,i} r_{,j}}{r^2} - \frac{\delta_{ij}}{r^2}\right) K_0^{\mathbf{uu}}(\mathbf{x}, \boldsymbol{\xi}; t, \tau; c_{\mathrm{P}})\right] \\ - \frac{1}{\varrho c_{\mathrm{S}}^2}\left[(r_{,i} r_{,j} - \delta_{ij})\, G_0^{\mathbf{uu}}(\mathbf{x}, \boldsymbol{\xi}; t, \tau; c_{\mathrm{S}}) + \left(2\frac{r_{,i} r_{,j}}{r^2} - \frac{\delta_{ij}}{r^2}\right) K_0^{\mathbf{uu}}(\mathbf{x}, \boldsymbol{\xi}; t, \tau; c_{\mathrm{S}})\right] \end{aligned} \tag{A.6}$$

where the first kernel

$$G_0^{\mathbf{uu}}(\mathbf{x}, \boldsymbol{\xi}; t, \tau; c) := \frac{c}{2\pi} \frac{H[c(t-\tau) - r]}{\sqrt{c^2(t-\tau)^2 - r^2}} \tag{A.7}$$

is the fundamental solution of the scalar wave diffusion problem and the auxiliary kernel $K_0^{\mathbf{uu}}$ is defined as follows

$$K_0^{\mathbf{uu}}(\mathbf{x}, \boldsymbol{\xi}; t, \tau; c) := \frac{c}{2\pi} H[c(t-\tau) - r] \sqrt{c^2(t-\tau)^2 - r^2}. \tag{A.8}$$

In the following we denote by the symbol $\Delta_{\tilde{n},n}$ the positive time difference $t_{\tilde{n}} - t_n$.

A.1 Computation of the single layer kernel ν_{ij}^V

The discrete weak formulation defined in (1.69) is characterized by the single layer operator V, depending directly on the fundamental solution $\mathbf{G^{uu}}$ as reported in formula (1.26). If we substitute in the bilinear form of (1.69) the related unknown approximation (1.73) and we consider as a test function $w_{\widetilde{m}}^{\mathbf{p}}(\mathbf{x})v_{\widetilde{n}}(t)$, we can derive the expression of the generic entry of the temporal block $\mathbb{E}_V^{(l)}$, which reads, for $l = n - \widetilde{n}$, as

$$\left(\mathbb{E}_{V,ij}^{(l)}\right)_{\widetilde{m},m} = \int_0^T \int_\Gamma \frac{\partial}{\partial t}\left(\int_0^t \int_\Gamma G_{ij}^{\mathbf{uu}}(\mathbf{x},\boldsymbol{\xi};t,\tau) w_m^{\mathbf{p}}(\boldsymbol{\xi}) v_n(\tau) d\tau d\Gamma_{\boldsymbol{\xi}}\right) w_{\widetilde{m}}^{\mathbf{p}}(\mathbf{x}) v_{\widetilde{n}}(t) dt d\Gamma_{\mathbf{x}},$$
$$i,j = 1,2, \;\; m,\widetilde{m} = 1,...,M_{\mathbf{p}}$$

Integration in space is totally independent of the time variable, thus, to perform the last integral, we have to compute the following contribute depending on t and τ. Trough an integration by parts we obtain the following equality, that holds since $v_{\widetilde{n}}(T) = 0$ for $\widetilde{n} = 0,...,N-2$:

$$\int_0^T \frac{\partial}{\partial t}\left(\int_0^t G_{ij}^{\mathbf{uu}}(\mathbf{x},\boldsymbol{\xi};t,\tau) v_n(\tau) d\tau\right) v_{\widetilde{n}}(t) dt = -\int_0^T \int_0^t G_{ij}^{\mathbf{uu}}(\mathbf{x},\boldsymbol{\xi};t,\tau) v_n(\tau) \frac{\partial}{\partial t}\left(v_{\widetilde{n}}(t)\right) d\tau dt;$$

the computations in case $\widetilde{n} = N-1$ can be performed in a similar way, leading to analogous results. Taking into account the definition of the piece-wise constant temporal basis functions in (1.71), we write

$$\begin{aligned}
&-\int_0^T \int_0^t G_{ij}^{\mathbf{uu}}(\mathbf{x},\boldsymbol{\xi};t,\tau) v_n(\tau) \frac{\partial}{\partial t}\left(v_{\widetilde{n}}(t)\right) d\tau dt \\
=&-\sum_{\xi,\varsigma=0}^{1} (-1)^{\xi+\varsigma} \int_0^T \int_0^t G_{ij}^{\mathbf{uu}}(\mathbf{x},\boldsymbol{\xi};t,\tau) H[\tau - t_{n+\varsigma}] \frac{\partial}{\partial t}\left(H[t - t_{\widetilde{n}+\xi}]\right) d\tau dt \\
=&-\sum_{\xi,\varsigma=0}^{1} (-1)^{\xi+\varsigma} \int_0^{t_{\widetilde{n}+\xi}} G_{ij}^{\mathbf{uu}}(\mathbf{x},\boldsymbol{\xi};t_{\widetilde{n}+\xi},\tau) H[\tau - t_{n+\varsigma}] d\tau,
\end{aligned}$$

since in the sense of distribution, the derivative of the Heaviside function $H[t]$ corresponds to the Dirac distribution $\delta(t)$. Therefore the final integral we have to calculate is the following:

$$\int_0^{t_{\widetilde{n}}} G_{ij}^{\mathbf{uu}}(\mathbf{x},\boldsymbol{\xi};t_{\widetilde{n}},\tau) H[\tau - t_n] d\tau. \tag{A.9}$$

Contribute (A.9) can be computed considering the integration of the auxiliary kernels (A.7) and (A.8), reported in the following computations:

$$\begin{aligned}
&\int_0^{t_{\widetilde{n}}} G_0^{\mathbf{uu}}(\mathbf{x},\boldsymbol{\xi};t_{\widetilde{n}},\tau;c) H[\tau - t_n] d\tau \\
=&\frac{c}{2\pi}\int_0^{t_{\widetilde{n}}} \frac{H[c(t_{\widetilde{n}} - \tau) - r]}{\sqrt{c^2(t_{\widetilde{n}} - \tau)^2 - r^2}} H[\tau - t_n] d\tau = \frac{c}{2\pi} H[c\Delta_{\widetilde{n},n} - r] \int_{t_n}^{t_{\widetilde{n}} - r/c} \frac{1}{\sqrt{c^2(t_{\widetilde{n}} - \tau)^2 - r^2}} d\tau \\
=&\frac{1}{2\pi} H[c\Delta_{\widetilde{n},n} - r] \int_r^{c\Delta_{\widetilde{n},n}} \frac{1}{\sqrt{z^2 - r^2}} dz = \frac{1}{2\pi} H[c\Delta_{\widetilde{n},n} - r] \left[\log\left(z + \sqrt{z^2 - r^2}\right)\right]_r^{c\Delta_{\widetilde{n},n}} \\
=&\frac{1}{2\pi} H[c\Delta_{\widetilde{n},n} - r] \left[\log\left(c\Delta_{\widetilde{n},n} + \sqrt{c^2\Delta_{\widetilde{n},n}^2 - r^2}\right) - \log(r)\right],
\end{aligned} \tag{A.10}$$

$$
\begin{aligned}
&\int_0^{t_{\widetilde{n}}} K_0^{\mathbf{uu}}(\mathbf{x},\boldsymbol{\xi};t_{\widetilde{n}},\tau;c)H[\tau-t_n]d\tau \\
=&\frac{c}{2\pi}\int_0^{t_{\widetilde{n}}} H[c(t_{\widetilde{n}}-\tau)-r]\sqrt{c^2(t_{\widetilde{n}}-\tau)^2-r^2}H[\tau-t_n]d\tau \\
=&\frac{c}{2\pi}H[c\Delta_{\widetilde{n},n}-r]\int_{t_n}^{t_{\widetilde{n}}-r/c}\sqrt{c^2(t_{\widetilde{n}}-\tau)^2-r^2}d\tau \\
=&\frac{1}{2\pi}H[c\Delta_{\widetilde{n},n}-r]\int_r^{c\Delta_{\widetilde{n},n}}\sqrt{z^2-r^2}dz \\
=&\frac{1}{4\pi}H[c\Delta_{\widetilde{n},n}-r]\left[z\sqrt{z^2-r^2}-r^2\log\left(z+\sqrt{z^2-r^2}\right)\right]_r^{c\Delta_{\widetilde{n},n}} \\
=&\frac{1}{4\pi}H[c\Delta_{\widetilde{n},n}-r]\left[c\Delta_{\widetilde{n},n}\sqrt{c^2\Delta_{\widetilde{n},n}^2-r^2}-r^2\log\left(c\Delta_{\widetilde{n},n}+\sqrt{c^2\Delta_{\widetilde{n},n}^2-r^2}\right)+r^2\log(r)\right]. \quad \text{(A.11)}
\end{aligned}
$$

Combining formula (A.9) with (A.10) and (A.11) we obtain the following equalities:

$$
\begin{aligned}
&\int_0^{t_{\widetilde{n}}} G_{ij}^{\mathbf{uu}}(\mathbf{x},\boldsymbol{\xi};t_{\widetilde{n}},\tau)H[\tau-t_n]d\tau \\
=&\frac{H[c_{\mathrm{P}}\Delta_{\widetilde{n},n}-r]}{\varrho c_{\mathrm{P}}^2}\left[r_{,i}r_{,j}\frac{1}{2\pi}\widehat{\varphi}_{\mathrm{P}}(r;\Delta_{\widetilde{n},n})+\left(2\frac{r_{,i}r_{,j}}{r^2}-\frac{\delta_{ij}}{r^2}\right)\frac{1}{4\pi}\left(c_{\mathrm{P}}\Delta_{\widetilde{n},n}\varphi_{\mathrm{P}}(r;\Delta_{\widetilde{n},n})-r^2\widehat{\varphi}_{\mathrm{P}}(r;\Delta_{\widetilde{n},n})\right)\right] \\
-&\frac{H[c_{\mathrm{S}}\Delta_{\widetilde{n},n}-r]}{\varrho c_{\mathrm{S}}^2}\left[(r_{,i}r_{,j}-\delta_{ij})\frac{1}{2\pi}\widehat{\varphi}_{\mathrm{S}}(r;\Delta_{\widetilde{n},n})+\left(2\frac{r_{,i}r_{,j}}{r^2}-\frac{\delta_{ij}}{r^2}\right)\frac{1}{4\pi}\left(c_{\mathrm{S}}\Delta_{\widetilde{n},n}\varphi_{\mathrm{S}}(r;\Delta_{\widetilde{n},n})-r^2\widehat{\varphi}_{\mathrm{S}}(r;\Delta_{\widetilde{n},n})\right)\right] \\
=&\frac{1}{2\pi\varrho}\left\{\left(\frac{r_ir_j}{r^4}-\frac{\delta_{ij}}{2r^2}\right)\left[\frac{H[c_{\mathrm{P}}\Delta_{\widetilde{n},n}-r]}{c_{\mathrm{P}}}\Delta_{\widetilde{n},n}\varphi_{\mathrm{P}}(r;\Delta_{\widetilde{n},n})-\frac{H[c_{\mathrm{S}}\Delta_{\widetilde{n},n}-r]}{c_{\mathrm{S}}}\Delta_{\widetilde{n},n}\varphi_{\mathrm{S}}(r;\Delta_{\widetilde{n},n})\right]\right. \\
&\left.+\frac{\delta_{ij}}{2}\left[\frac{H[c_{\mathrm{P}}\Delta_{\widetilde{n},n}-r]}{c_{\mathrm{P}}^2}\widehat{\varphi}_{\mathrm{P}}(r;\Delta_{\widetilde{n},n})+\frac{H[c_{\mathrm{S}}\Delta_{\widetilde{n},n}-r]}{c_{\mathrm{S}}^2}\widehat{\varphi}_{\mathrm{S}}(r;\Delta_{\widetilde{n},n})\right]\right\}
\end{aligned}
$$

where the functions φ_γ and $\widehat{\varphi}_\gamma$ are defined in (1.80) and (1.81). This leads to the definition of the matrix elements of the discretized single layer operator V as reported in (1.79).

A.2 Computation of the double layer kernel ν_{ij}^K

To derive the definition of the double layer kernel ν_{ij}^K, and consequently the definition of the entries of matrix $\mathbb{E}_K^{(l)}$ (1.94) we have to perform passages similar to those done for the single layer kernel. To be specific, the generic matrix entry of the block $\mathbb{E}_K^{(l)}$, for $l=\widetilde{n}-m$, reads as

$$
\left(\mathbb{E}_{K,ij}^{(l)}\right)_{\widetilde{m},m}=\int_0^T\int_{\Gamma_{\mathcal{D}}}\frac{\partial}{\partial t}\left(\int_0^t\int_{\Gamma_{\mathcal{N}}}G_{ij}^{\mathbf{up}}(\mathbf{x},\boldsymbol{\xi};t,\tau)w_m^{\mathbf{u}}(\boldsymbol{\xi})r_n(\tau)d\tau d\Gamma_{\boldsymbol{\xi}}\right)w_{\widetilde{m}}^{\mathbf{p}}(\mathbf{x})v_{\widetilde{n}}(t)dtd\Gamma_{\mathbf{x}},
$$
$$
i,j=1,2,\ \ m=1,...,M_{\mathbf{u}}\ \ \widetilde{m}=1,...,M_{\mathbf{p}}
$$

Also in this case, space integration is totally independent from the time variables, meaning that we can proceed, with an integration by parts, considering exclusively the temporal variables t and τ. If we take into account the definition of the fundamental traction $G_{ij}^{\mathbf{up}}$ in (1.22) and the expression of the piece-wise linear temporal basis in (1.72), to calculate the double layer matrix

element $\left(\mathbb{E}^{(l)}_{K,ij}\right)_{\widetilde{m},m}$ we need to analytically compute the following term:

$$\begin{aligned}
&\int_0^T \frac{\partial}{\partial t}\left(\int_0^t G^{\mathbf{up}}_{ij}(\mathbf{x},\boldsymbol{\xi};t,\tau)r_n(\tau)d\tau\right) v_{\widetilde{n}}(t)dt \\
&= -\int_0^T \int_0^t G^{\mathbf{up}}_{ij}(\mathbf{x},\boldsymbol{\xi};t,\tau)r_n(\tau)\frac{\partial}{\partial t}\left(v_{\widetilde{n}}(t)\right)d\tau dt \\
&= -\sum_{\xi,\varsigma=0}^{1}(-1)^{\xi+\varsigma}\int_0^{t_{\widetilde{n}+\xi}} C^{kl}_{jh}\frac{\partial G^{\mathbf{uu}}_{ki}}{\partial \xi_l}(\mathbf{x},\boldsymbol{\xi};t_{\widetilde{n}+\xi},\tau)n_h(\boldsymbol{\xi})H[\tau-t_{n+\varsigma}]\frac{\tau-t_{n+\varsigma}}{\Delta t}d\tau \\
&= \sum_{\xi,\varsigma=0}^{1}(-1)^{\xi+\varsigma}\int_0^{t_{\widetilde{n}+\xi}} C^{kl}_{jh}\frac{\partial G^{\mathbf{uu}}_{ki}}{\partial x_l}(\mathbf{x},\boldsymbol{\xi};t_{\widetilde{n}+\xi},\tau)n_h(\boldsymbol{\xi})H[\tau-t_{n+\varsigma}]\frac{\tau-t_{n+\varsigma}}{\Delta t}d\tau. \qquad \text{(A.12)}
\end{aligned}$$

Last equality in (A.12) holds because the fundamental solution $G^{\mathbf{uu}}$ depends on the spatial variables $\mathbf{x}$ and $\boldsymbol{\xi}$ trough the vector components r_1 and r_2, as stated in definition (A.6). Thank to that and remembering property (A.2), we can write

$$\frac{\partial G^{\mathbf{uu}}_{ki}}{\partial \xi_l} = \frac{\partial G^{\mathbf{uu}}_{ki}}{\partial r_q}\frac{\partial r_q}{\partial \xi_l} = -\frac{\partial G^{\mathbf{uu}}_{ki}}{\partial r_q}\frac{\partial r_q}{\partial x_l} = -\frac{\partial G^{\mathbf{uu}}_{ki}}{\partial x_l}, \qquad \text{(A.13)}$$

meaning in particular that we need to calculate exactly the contribute

$$\int_0^{t_{\widetilde{n}}} \frac{\partial G^{\mathbf{uu}}_{ki}}{\partial x_l}(\mathbf{x},\boldsymbol{\xi};t_{\widetilde{n}},\tau)H[\tau-t_n](\tau-t_n)d\tau. \qquad \text{(A.14)}$$

First of all we have to compute a generic partial derivative of the fundamental tensor. Thanks to formulas (A.1)-(A.5) we can write

$$\begin{aligned}
\frac{\partial G^{\mathbf{uu}}_{ki}}{\partial x_l}(\mathbf{x},\boldsymbol{\xi};t,\tau) =& \frac{1}{\varrho c_{\mathrm{P}}^2}\left[\left(r_{,kl}r_{,i}+r_{,k}r_{,il}\right)G^{\mathbf{uu}}_0(\mathbf{x},\boldsymbol{\xi};t,\tau;c_{\mathrm{P}}) + r_{,k}r_{,i}r_{,l}\frac{\partial G^{\mathbf{uu}}_0}{\partial r}(\mathbf{x},\boldsymbol{\xi};t,\tau;c_{\mathrm{P}})\right] \\
&+\frac{1}{\varrho c_{\mathrm{P}}^2}\left[\left(2\frac{r_{,kl}r_{,i}}{r^2}+2\frac{r_{,k}r_{,il}}{r^2}-4\frac{r_{,k}r_{,i}r_{,l}}{r^3}+2\delta_{ki}\frac{r_{,l}}{r^3}\right)K^{\mathbf{uu}}_0(\mathbf{x},\boldsymbol{\xi};t,\tau;c_{\mathrm{P}})\right. \\
&\qquad\left.+\left(2\frac{r_{,k}r_{,i}r_{,l}}{r^2}-\delta_{ki}\frac{r_{,l}}{r^2}\right)\frac{\partial K^{\mathbf{uu}}_0}{\partial r}(\mathbf{x},\boldsymbol{\xi};t,\tau;c_{\mathrm{P}})\right] \\
&-\frac{1}{\varrho c_{\mathrm{S}}^2}\left[\left(r_{,kl}r_{,i}+r_{,k}r_{,il}\right)G^{\mathbf{uu}}_0(\mathbf{x},\boldsymbol{\xi};t,\tau;c_{\mathrm{S}}) + \left(r_{,k}r_{,i}r_{,l}-\delta_{ki}r_{,l}\right)\frac{\partial G^{\mathbf{uu}}_0}{\partial r}(\mathbf{x},\boldsymbol{\xi};t,\tau;c_{\mathrm{S}})\right] \\
&-\frac{1}{\varrho c_{\mathrm{S}}^2}\left[\left(2\frac{r_{,kl}r_{,i}}{r^2}+2\frac{r_{,k}r_{,il}}{r^2}-4\frac{r_{,k}r_{,i}r_{,l}}{r^3}+2\delta_{ki}\frac{r_{,l}}{r^3}\right)K^{\mathbf{uu}}_0(\mathbf{x},\boldsymbol{\xi};t,\tau;c_{\mathrm{S}})\right. \\
&\qquad\left.+\left(2\frac{r_{,k}r_{,i}r_{,l}}{r^2}-\delta_{ki}\frac{r_{,l}}{r^2}\right)\frac{\partial K^{\mathbf{uu}}_0}{\partial r}(\mathbf{x},\boldsymbol{\xi};t,\tau;c_{\mathrm{S}})\right],
\end{aligned}$$

and thanks to relation (A.3) we get

$$\begin{aligned}
\frac{\partial G^{\mathbf{uu}}_{ki}}{\partial x_l}(\mathbf{x},\boldsymbol{\xi};t,\tau) =& \frac{1}{\varrho c_{\mathrm{P}}^2}\left[\frac{1}{r}A_{kli}G^{\mathbf{uu}}_0(\mathbf{x},\boldsymbol{\xi};t,\tau;c_{\mathrm{P}}) + B_{kli}\frac{\partial G^{\mathbf{uu}}_0}{\partial r}(\mathbf{x},\boldsymbol{\xi};t,\tau;c_{\mathrm{P}})\right] \\
&+\frac{1}{\varrho c_{\mathrm{P}}^2}\left[\frac{2}{r^3}C_{kli}K^{\mathbf{uu}}_0(\mathbf{x},\boldsymbol{\xi};t,\tau;c_{\mathrm{P}}) + \frac{1}{r^2}D_{kli}\frac{\partial K^{\mathbf{uu}}_0}{\partial r}(\mathbf{x},\boldsymbol{\xi};t,\tau;c_{\mathrm{P}})\right] \\
&-\frac{1}{\varrho c_{\mathrm{S}}^2}\left[\frac{1}{r}A_{kli}G^{\mathbf{uu}}_0(\mathbf{x},\boldsymbol{\xi};t,\tau;c_{\mathrm{S}}) + \widetilde{B}_{kli}\frac{\partial G^{\mathbf{uu}}_0}{\partial r}(\mathbf{x},\boldsymbol{\xi};t,\tau;c_{\mathrm{S}})\right] \\
&-\frac{1}{\varrho c_{\mathrm{S}}^2}\left[\frac{2}{r^3}C_{kli}K^{\mathbf{uu}}_0(\mathbf{x},\boldsymbol{\xi};t,\tau;c_{\mathrm{S}}) + \frac{1}{r^2}D_{kli}\frac{\partial K^{\mathbf{uu}}_0}{\partial r}(\mathbf{x},\boldsymbol{\xi};t,\tau;c_{\mathrm{S}})\right], \qquad \text{(A.15)}
\end{aligned}$$

where

$$\begin{aligned} A_{kli} =&\delta_{kl}r_{,i} + \delta_{il}r_{,k} - 2r_{,k}r_{,i}r_{,l}, \quad B_{kli} = r_{,k}r_{,i}r_{,l}, \quad \widetilde{B}_{kli} = r_{,k}r_{,i}r_{,l} - \delta_{ki}r_{,l} \\ C_{kli} =&\delta_{kl}r_{,i} + \delta_{il}r_{,k} + \delta_{ki}r_{,l} - 4r_{,k}r_{,i}r_{,l}, \quad D_{kli} = 2r_{,k}r_{,i}r_{,l} - \delta_{ki}r_{,l}. \end{aligned} \tag{A.16}$$

We proceed calculating the time integral of the auxiliary kernels $G_0^{\mathbf{uu}}$ and $K_0^{\mathbf{uu}}$. In the first case,

$$\begin{aligned} &\int_0^{t_{\tilde{n}}} G_0^{\mathbf{uu}}(\mathbf{x},\boldsymbol{\xi};t_{\tilde{n}},\tau;c)H[\tau-t_n](\tau-t_n)d\tau \\ =&\frac{1}{2\pi}\int_{t_n}^{t_{\tilde{n}}}(c\tau-ct_n)\frac{H[c(t_{\tilde{n}}-\tau)-r]}{\sqrt{c^2(t_{\tilde{n}}-\tau)^2-r^2}}d\tau = \frac{1}{2\pi}H[c\Delta_{\tilde{n},n}-r]\int_{t_n}^{t_{\tilde{n}}-\frac{r}{c}}\frac{c\tau-ct_n}{\sqrt{c^2(t_{\tilde{n}}-\tau)^2-r^2}}d\tau \\ =&\frac{1}{2\pi}H[c\Delta_{\tilde{n},n}-r]\int_{t_n}^{t_{\tilde{n}}-\frac{r}{c}}\frac{c\Delta_{\tilde{n},n}-c(t_{\tilde{n}}-\tau)}{\sqrt{c^2(t_{\tilde{n}}-\tau)^2-r^2}}d\tau = \frac{1}{2\pi c}H[c\Delta_{\tilde{n},n}-r]\int_r^{c\Delta_{\tilde{n},n}}\frac{c\Delta_{\tilde{n},n}-\xi}{\sqrt{\xi^2-r^2}}d\xi, \end{aligned}$$

and calculating the last integral in $d\xi$ leads us to the following result:

$$\begin{aligned} &\int_0^{t_{\tilde{n}}} G_0^{\mathbf{uu}}(\mathbf{x},\boldsymbol{\xi};t_{\tilde{n}},\tau;c)H[\tau-t_n](\tau-t_n)d\tau \\ =&\frac{1}{2\pi c}H[c\Delta_{\tilde{n},n}-r]\left[c\Delta_{\tilde{n},n}\log\left(\xi+\sqrt{\xi^2-r^2}\right)-\sqrt{\xi^2-r^2}\right]_r^{c\Delta_{\tilde{n},n}} \\ =&\frac{1}{2\pi c}H[c\Delta_{\tilde{n},n}-r]\left\{c\Delta_{\tilde{n},n}\left[\log\left(c\Delta_{\tilde{n},n}+\sqrt{c\Delta_{\tilde{n},n}^2-r^2}\right)-\log(r)\right]-\sqrt{c^2\Delta_{\tilde{n},n}^2-r^2}\right\}. \end{aligned} \tag{A.17}$$

We proceed similarly with the calculation of the integral depending on the auxiliary kernel $K_0^{\mathbf{uu}}$:

$$\begin{aligned} &\int_0^{t_{\tilde{n}}} K_0^{\mathbf{uu}}(\mathbf{x},\boldsymbol{\xi};t_{\tilde{n}},\tau;c)\chi_{\tilde{n}}^{\mathbf{u}}(\tau)d\tau \\ =&\frac{1}{2\pi}\int_{t_n}^{t_{\tilde{n}}}(c\tau-ct_n)H[c(t_{\tilde{n}}-\tau)-r]\sqrt{c^2(t_{\tilde{n}}-\tau)^2-r^2}d\tau \\ =&\frac{1}{2\pi}H[c\Delta_{\tilde{n},n}-r]\int_{t_n}^{t_{\tilde{n}}-\frac{r}{c}}(c\tau-ct_n)\sqrt{c^2(t_{\tilde{n}}-\tau)^2-r^2}d\tau \\ =&\frac{1}{2\pi}H[c\Delta_{\tilde{n},n}-r]\int_{t_n}^{t_{\tilde{n}}-\frac{r}{c}}[c\Delta_{\tilde{n},n}-(ct_{\tilde{n}}-c\tau)]\sqrt{c^2(t_{\tilde{n}}-\tau)^2-r^2}d\tau \\ =&\frac{1}{2\pi c}H[c\Delta_{\tilde{n},n}-r]\int_r^{c\Delta_{\tilde{n},n}}(c\Delta_{\tilde{n},n}-\xi)\sqrt{\xi^2-r^2}d\xi \\ =&\frac{1}{12\pi c}H[c\Delta_{\tilde{n},n}-r]\left[(2r^2+\xi(3c\Delta_{\tilde{n},n}-2\xi))\sqrt{\xi^2-r^2}-3r^2c\Delta_{\tilde{n},n}\log\left(\xi+\sqrt{\xi^2-r^2}\right)\right]_r^{c\Delta_{\tilde{n},n}} \\ =&\frac{1}{12\pi c}H[c\Delta_{\tilde{n},n}-r]\left\{(2r^2+c^2\Delta_{\tilde{n},n}^2)\sqrt{c^2\Delta_{\tilde{n},n}^2-r^2}-3r^2c\Delta_{\tilde{n},n}\left(\log\left(c\Delta_{\tilde{n},n}+\sqrt{c^2\Delta_{\tilde{n},n}^2-r^2}\right)-\log(r)\right)\right\}. \end{aligned} \tag{A.18}$$

Regarding the time integrals depending on the derivatives $\partial G_0^{\mathbf{uu}}/\partial r$ and $\partial K_0^{\mathbf{uu}}/\partial r$ we observe that, since the integration in (A.14) is totally independent from the space variable r, we can move the derivative operator outside the integral:

$$\begin{aligned} \int_0^{t_{\tilde{n}}}\frac{\partial}{\partial r}G_0^{\mathbf{uu}}(\mathbf{x},\boldsymbol{\xi};t_{\tilde{n}},\tau;c)(\tau-t_n)H[\tau-t_n]d\tau &= \frac{\partial}{\partial r}\left(\int_0^{t_{\tilde{n}}}G_0^{\mathbf{uu}}(\mathbf{x},\boldsymbol{\xi};t_{\tilde{n}},\tau;c)(\tau-t_n)H[\tau-t_n]d\tau\right), \\ \int_0^{t_{\tilde{n}}}\frac{\partial}{\partial r}K_0^{\mathbf{uu}}(\mathbf{x},\boldsymbol{\xi};t_{\tilde{n}},\tau;c)(\tau-t_n)H[\tau-t_n]d\tau &= \frac{\partial}{\partial r}\left(\int_0^{t_{\tilde{n}}}K_0^{\mathbf{uu}}(\mathbf{x},\boldsymbol{\xi};t_{\tilde{n}},\tau;c)(\tau-t_n)H[\tau-t_n]d\tau\right), \end{aligned}$$

meaning that we can quickly compute the integral contributes applying a derivative in the r variable to the results in (A.17) and (A.18). Here we stress the fact that the derivative applied to (A.17) and (A.18) may generate an addend with the factor $\delta\left(c\Delta_{\widetilde{n},n}-r\right)$. Anyway we do not consider this additive term since does not give any contribution in the double space integral that determines the elements in (1.94). Thus we can write

$$\int_0^{t_{\widetilde{n}}} \frac{\partial}{\partial r} G_0^{\mathbf{uu}}(\mathbf{x},\boldsymbol{\xi};t_{\widetilde{n}},\tau;c)(\tau-t_n)H[\tau-t_n]d\tau = -\frac{1}{2\pi c}H[c\Delta_{\widetilde{n},n}-r]\frac{\sqrt{c^2\Delta_{\widetilde{n},n}^2-r^2}}{r}, \tag{A.19}$$

$$\begin{aligned}&\int_0^{t_{\widetilde{n}}} \frac{\partial}{\partial r} K_0^{\mathbf{uu}}(\mathbf{x},\boldsymbol{\xi};t_{\widetilde{n}},\tau;c)(\tau-t_n)H[\tau-t_n]d\tau\\ =&\frac{1}{2\pi c}H[c\Delta_{\widetilde{n},n}-r]\left\{r\sqrt{c^2\Delta_{\widetilde{n},n}^2-r^2}-rc\Delta_{\widetilde{n},n}\left[\log\left(c\Delta_{\widetilde{n},n}+\sqrt{c^2\Delta_{\widetilde{n},n}^2-r^2}\right)-\log(r)\right]\right\}.\end{aligned} \tag{A.20}$$

The Hooke tensor in (A.12) acts directly on the coefficients $A_{kli}, B_{kli}, \widetilde{B}_{kli}, C_{kli}, D_{kli}$. Therefore we execute the following sums over the indexes k,l,i, getting to these equalities:

$$\begin{aligned}
C_{jh}^{kl}A_{kli}n_h(\boldsymbol{\xi}) &= (2\mu+\lambda)r_{,i}n_j(\boldsymbol{\xi})+\mu r_{,j}n_i(\boldsymbol{\xi})+\mu\delta_{ij}(r_{,h}n_h(\boldsymbol{\xi}))-4\mu r_{,i}r_{,j}(r_{,h}n_h(\boldsymbol{\xi})),\\
C_{jh}^{kl}B_{kli}n_h(\boldsymbol{\xi}) &= \lambda r_{,i}n_j(\boldsymbol{\xi})+2\mu r_{,i}r_{,j}(r_{,h}n_h(\boldsymbol{\xi})),\\
C_{jh}^{kl}\widetilde{B}_{kli}n_h(\boldsymbol{\xi}) &= -\mu r_{,j}n_i(\boldsymbol{\xi})-\mu\delta_{ij}(r_{,h}n_h(\boldsymbol{\xi}))+2\mu r_{,i}r_{,j}(r_{,h}n_h(\boldsymbol{\xi})),\\
C_{jh}^{kl}C_{kli}n_h(\boldsymbol{\xi}) &= 2\mu r_{,i}n_j(\boldsymbol{\xi})+2\mu r_{,j}n_i(\boldsymbol{\xi})+2\mu\delta_{ij}(r_{,h}n_h(\boldsymbol{\xi}))-8\mu r_{,i}r_{,j}(r_{,h}n_h(\boldsymbol{\xi})),\\
C_{jh}^{kl}D_{kli}n_h(\boldsymbol{\xi}) &= \lambda r_{,i}n_j(\boldsymbol{\xi})-\mu r_{,j}n_i(\boldsymbol{\xi})-\mu\delta_{ij}(r_{,h}n_h(\boldsymbol{\xi}))+4\mu r_{,i}r_{,j}(r_{,h}n_h(\boldsymbol{\xi})).
\end{aligned}$$

Therefore, combining the results (A.19),(A.20), (A.17) and (A.18), we observe that the last integral in formula (A.12) corresponds to

$$\begin{aligned}
&\int_0^{t_{\widetilde{n}+\xi}} C_{jh}^{kl}\frac{\partial G_{ki}^{\mathbf{uu}}}{\partial x_l}(\mathbf{x},\boldsymbol{\xi};t_{\widetilde{n}+\xi},\tau)n_h(\boldsymbol{\xi})H[\tau-t_{n+\varsigma}]\frac{\tau-t_{n+\varsigma}}{\Delta t}d\tau dt\\
=&\frac{H[c_{\mathrm{P}}\Delta_{\widetilde{n}+\xi,n+\varsigma}-r]}{2\pi\varrho\Delta t c_{\mathrm{P}}^3}\cdot\\
&\left\{\frac{1}{r}C_{jh}^{kl}A_{kli}n_h(\boldsymbol{\xi})\left[c_{\mathrm{P}}\Delta_{\widetilde{n}+\xi,n+\varsigma}\widehat{\varphi}_{\mathrm{P}}(r;\Delta_{\widetilde{n}+\xi,n+\varsigma})-\varphi_{\mathrm{P}}(r;\Delta_{\widetilde{n}+\xi,n+\varsigma})\right]-\frac{1}{r}C_{jh}^{kl}B_{kli}n_h(\boldsymbol{\xi})\varphi_{\mathrm{P}}(r;\Delta_{\widetilde{n}+\xi,n+\varsigma})\right.\\
&\quad+\frac{1}{3r^3}C_{jh}^{kl}C_{kli}n_h(\boldsymbol{\xi})\left[(2r^2+c_{\mathrm{P}}^2\Delta_{\widetilde{n}+\xi,n+\varsigma}^2)\varphi_{\mathrm{P}}(r;\Delta_{\widetilde{n}+\xi,n+\varsigma})-3r^2c_{\mathrm{P}}\Delta_{\widetilde{n}+\xi,n+\varsigma}\widehat{\varphi}_{\mathrm{P}}(r;\Delta_{\widetilde{n}+\xi,n+\varsigma})\right]\\
&\quad\left.+\frac{1}{r^2}C_{jh}^{kl}D_{kli}n_h(\boldsymbol{\xi})\left[r\varphi_{\mathrm{P}}(r;\Delta_{\widetilde{n}+\xi,n+\varsigma})-rc_{\mathrm{P}}\Delta_{\widetilde{n}+\xi,n+\varsigma}\widehat{\varphi}_{\mathrm{P}}(r;\Delta_{\widetilde{n}+\xi,n+\varsigma})\right]\right\}\\
&-\frac{H[c_{\mathrm{S}}\Delta_{\widetilde{n}+\xi,n+\varsigma}-r]}{2\pi\varrho\Delta t c_{\mathrm{S}}^3}\cdot\\
&\left\{\frac{1}{r}C_{jh}^{kl}A_{kli}n_h(\boldsymbol{\xi})\left[c_{\mathrm{S}}\Delta_{\widetilde{n}+\xi,n+\varsigma}\widehat{\varphi}_{\mathrm{S}}(r;\Delta_{\widetilde{n}+\xi,n+\varsigma})-\varphi_{\mathrm{S}}(r;\Delta_{\widetilde{n}+\xi,n+\varsigma})\right]-\frac{1}{r}C_{jh}^{kl}\widetilde{B}_{kli}n_h(\boldsymbol{\xi})\varphi_{\mathrm{S}}(r;\Delta_{\widetilde{n}+\xi,n+\varsigma})\right.\\
&\quad+\frac{1}{3r^3}C_{jh}^{kl}C_{kli}n_h(\boldsymbol{\xi})\left[(2r^2+c_{\mathrm{S}}^2\Delta_{\widetilde{n}+\xi,n+\varsigma}^2)\varphi_{\mathrm{S}}(r;\Delta_{\widetilde{n}+\xi,n+\varsigma})-3r^2c_{\mathrm{S}}\Delta_{\widetilde{n}+\xi,n+\varsigma}\widehat{\varphi}_{\mathrm{S}}(r;\Delta_{\widetilde{n}+\xi,n+\varsigma})\right]\\
&\quad\left.+\frac{1}{r^2}C_{jh}^{kl}D_{kli}n_h(\boldsymbol{\xi})\left[r\varphi_{\mathrm{S}}(r;\Delta_{\widetilde{n}+\xi,n+\varsigma})-rc_{\mathrm{S}}\Delta_{\widetilde{n}+\xi,n+\varsigma}\widehat{\varphi}_{\mathrm{S}}(r;\Delta_{\widetilde{n}+\xi,n+\varsigma})\right]\right\},
\end{aligned}$$

and with the explicit definition of the coefficients after the application of the Hooke tensor we obtain

$$\begin{aligned}
&\int_0^{t_{\widetilde{n}+\xi}} C_{jh}^{kl}\frac{\partial G_{ki}^{\mathbf{uu}}}{\partial x_l}(\mathbf{x},\boldsymbol{\xi};t_{\widetilde{n}+\xi},\tau)n_h(\boldsymbol{\xi})H[\tau-t_{n+\varsigma}]\frac{\tau-t_{n+\varsigma}}{\Delta t}d\tau dt\\
=&\frac{1}{\pi\varrho\Delta t}\left[H[c_{\mathrm{P}}\Delta_{\widetilde{n}+\xi,n+\varsigma}-r]\frac{\varphi_{\mathrm{P}}(r;\Delta_{\widetilde{n}+\xi,n+\varsigma})}{c_{\mathrm{P}}r}\left(\frac{K_{\mathrm{P}}^{ij}}{c_{\mathrm{P}}^2}+\frac{\Delta_{\widetilde{n}+\xi,n+\varsigma}^2\widetilde{K}_{\mathrm{P}}^{ij}}{r^2}\right)\right.\\
&\left.-H[c_{\mathrm{S}}\Delta_{\widetilde{n}+\xi,n+\varsigma}-r]\frac{\varphi_{\mathrm{S}}(r;\Delta_{\widetilde{n}+\xi,n+\varsigma})}{c_{\mathrm{S}}r}\left(\frac{K_{\mathrm{S}}^{ij}}{c_{\mathrm{S}}^2}+\frac{\Delta_{\widetilde{n}+\xi,n+\varsigma}^2\widetilde{K}_{\mathrm{S}}^{ij}}{r^2}\right)\right]
\end{aligned}$$

where coefficients K_{P}^{ij}, K_{S}^{ij} $\widetilde{K}_{\mathrm{P}}^{ij}$ and $\widetilde{K}_{\mathrm{S}}^{ij}$ are defined as follows:

$$\begin{aligned}
K_{\mathrm{P}}^{ij}=&\left(-\frac{1}{2}\lambda-\frac{1}{3}\mu\right)r_{,i}n_j(\boldsymbol{\xi})-\frac{1}{3}\mu r_{,j}n_i(\boldsymbol{\xi})-\frac{1}{3}\mu\delta_{ij}(r_{,h}n_h(\boldsymbol{\xi}))+\frac{1}{3}\mu r_{,i}r_{,j}(r_{,h}n_h(\boldsymbol{\xi})),\\
K_{\mathrm{S}}^{ij}=&-\frac{1}{3}\mu r_{,i}n_j(\boldsymbol{\xi})+\frac{1}{6}\mu r_{,j}n_i(\boldsymbol{\xi})+\frac{1}{6}\mu\delta_{ij}(r_{,h}n_h(\boldsymbol{\xi}))+\frac{1}{3}\mu r_{,i}r_{,j}(r_{,h}n_h(\boldsymbol{\xi})),\\
\widetilde{K}_{\mathrm{P}}^{ij}=&\widetilde{K}_{\mathrm{S}}^{ij}=\frac{1}{3}\mu r_{,i}n_j(\boldsymbol{\xi})+\frac{1}{3}\mu r_{,j}n_i(\boldsymbol{\xi})+\frac{1}{3}\mu\delta_{ij}(r_{,h}n_h(\boldsymbol{\xi}))-\frac{4}{3}\mu r_{,i}r_{,j}(r_{,h}n_h(\boldsymbol{\xi})).
\end{aligned}$$

This confirms the definition of the double layer kernels ν_{ij}^K reported in (1.95) and the definition of the related generic matrix element.

A.3 Computation of the hypersingular kernel ν_{ij}^D

To get the definition of the hypersingular kernel ν_{ij}^K, we have to study the elements of the generic temporal block $\mathbb{E}_D^{(l)}$, with $l=\widetilde{n}-n$. These can be derived substituting in the bilinear form (1.70) the discretized unknown (1.74) and the test function $w_{\widetilde{m}}^{\mathbf{u}}(\mathbf{x})r_{\widetilde{n}}(t)$, leading to the following expression of the entry

$$\left(\mathbb{E}_{D,ij}^{(l)}\right)_{\widetilde{m},m}=\int_0^T\int_\Gamma\left(\int_0^t\int_\Gamma G_{ij}^{\mathbf{pp}}(\mathbf{x},\boldsymbol{\xi};t,\tau)w_m^{\mathbf{u}}(\boldsymbol{\xi})r_n(\tau)d\tau d\Gamma_{\boldsymbol{\xi}}\right)\frac{\partial}{\partial t}\left(w_{\widetilde{m}}^{\mathbf{u}}(\mathbf{x})r_{\widetilde{n}}(t)\right)dtd\Gamma_{\mathbf{x}},$$
$$i,j=1,2,\ \ m,\widetilde{m}=1,...,M_{\mathbf{u}}.$$

From the definition of the hypersingular matrix elements we deduce that, to compute the kernel function ν_{ij}^D, as defined in (1.89), we need to perform the following double time integral, remembering the definition of the tensor function $G_{ij}^{\mathbf{pp}}$ in (1.34) and the equality (A.13)

$$\begin{aligned}
&\int_0^T\int_0^t G_{ij}^{\mathbf{pp}}(\mathbf{x},\boldsymbol{\xi};t,\tau)r_n(\tau)\frac{\partial}{\partial t}\left(r_{\widetilde{n}}(t)\right)d\tau dt\\
=&\sum_{\xi,\varsigma=0}^{1}(-1)^{\xi+\varsigma}\int_{t_{\widetilde{n}+\xi}}^T\int_0^t C_{ih}^{kl}C_{j\alpha}^{\beta\gamma}\frac{\partial^2 G_{k\beta}^{\mathbf{uu}}}{\partial x_l\partial\xi_\gamma}(\mathbf{x},\boldsymbol{\xi};t,\tau)\frac{\tau-t_{n+\varsigma}}{\Delta t^2}H[\tau-t_{n+\varsigma}]n_h(\mathbf{x})n_\alpha(\boldsymbol{\xi})d\tau dt\\
=&-\sum_{\xi,\varsigma=0}^{1}(-1)^{\xi+\varsigma}\int_{t_{\widetilde{n}+\xi}}^T\int_0^t C_{ih}^{kl}C_{j\alpha}^{\beta\gamma}\frac{\partial^2 G_{k\beta}^{\mathbf{uu}}}{\partial x_l\partial x_\gamma}(\mathbf{x},\boldsymbol{\xi};t,\tau)\frac{\tau-t_{n+\varsigma}}{\Delta t^2}H[\tau-t_{n+\varsigma}]n_h(\mathbf{x})n_\alpha(\boldsymbol{\xi})d\tau dt,
\end{aligned}\tag{A.21}$$

meaning that we are interested in computing exactly the contribute

$$\int_{t_{\widetilde{n}}}^T\int_0^t\frac{\partial^2 G_{k\beta}^{\mathbf{uu}}}{\partial x_l\partial x_\gamma}(\mathbf{x},\boldsymbol{\xi};t,\tau)(\tau-t_n)H[\tau-t_n]d\tau dt.\tag{A.22}$$

First of all, we need to compute a double spatial derivative of the fundamental function $G^{\mathbf{uu}}_{k\beta}$. To do that, we proceed with our computation on the basis of the results of formula (A.15):

$$
\begin{aligned}
&\frac{\partial^2 G^{\mathbf{uu}}_{k\beta}}{\partial x_l \partial x_\gamma}(\mathbf{x},\boldsymbol{\xi};t,\tau)\\
=&\frac{1}{\varrho c_{\mathrm{P}}^2}\left[\left(-\frac{r_{,l}}{r^2}A_{k\gamma\beta}+\frac{1}{r}\frac{\partial A_{k\gamma\beta}}{\partial x_l}\right)G_0^{\mathbf{uu}}(\mathbf{x},\boldsymbol{\xi};t,\tau;c_{\mathrm{P}})+\left(\frac{r_{,l}}{r}A_{k\gamma\beta}+\frac{\partial B_{k\gamma\beta}}{\partial x_l}\right)\frac{\partial G_0^{\mathbf{uu}}}{\partial r}(\mathbf{x},\boldsymbol{\xi};t,\tau;c_{\mathrm{P}})\right.\\
&+B_{k\gamma\beta}r_{,l}\frac{\partial^2 G_0^{\mathbf{uu}}}{\partial r^2}(\mathbf{x},\boldsymbol{\xi};t,\tau;c_{\mathrm{P}})+\left(-\frac{6r_{,l}}{r^4}C_{k\gamma\beta}+\frac{2}{r^3}\frac{\partial C_{k\gamma\beta}}{\partial x_l}\right)K_0^{\mathbf{uu}}(\mathbf{x},\boldsymbol{\xi};t,\tau;c_{\mathrm{P}})\\
&\left.+\left(\frac{2r_{,l}}{r^3}C_{k\gamma\beta}-\frac{2r_{,l}}{r^3}D_{k\gamma\beta}+\frac{1}{r^2}\frac{\partial D_{k\gamma\beta}}{\partial x_l}\right)\frac{\partial K_0^{\mathbf{uu}}}{\partial r}(\mathbf{x},\boldsymbol{\xi};t,\tau;c_{\mathrm{P}})+\frac{D_{k\gamma\beta}r_{,l}}{r^2}\frac{\partial^2 K_0^{\mathbf{uu}}}{\partial r^2}(\mathbf{x},\boldsymbol{\xi};t,\tau;c_{\mathrm{P}})\right]\\
&-\frac{1}{\varrho c_{\mathrm{S}}^2}\left[\left(-\frac{r_{,l}}{r^2}A_{k\gamma\beta}+\frac{1}{r}\frac{\partial A_{k\gamma\beta}}{\partial x_l}\right)G_0^{\mathbf{uu}}(\mathbf{x},\boldsymbol{\xi};t,\tau;c_{\mathrm{S}})+\left(\frac{r_{,l}}{r}A_{k\gamma\beta}+\frac{\partial B'_{k\gamma\beta}}{\partial x_l}\right)\frac{\partial G_0^{\mathbf{uu}}}{\partial r}(\mathbf{x},\boldsymbol{\xi};t,\tau;c_{\mathrm{S}})\right.\\
&+B'_{k\gamma\beta}r_{,l}\frac{\partial^2 G_0^{\mathbf{uu}}}{\partial r^2}(\mathbf{x},\boldsymbol{\xi};t,\tau;c_{\mathrm{S}})\left(-\frac{6r_{,l}}{r^4}C_{k\gamma\beta}+\frac{2}{r^3}\frac{\partial C_{k\gamma\beta}}{\partial x_l}\right)K_0^{\mathbf{uu}}(\mathbf{x},\boldsymbol{\xi};t,\tau;c_{\mathrm{S}})\\
&\left.+\left(\frac{2r_{,l}}{r^3}C_{k\gamma\beta}-\frac{2r_{,l}}{r^3}D_{k\gamma\beta}+\frac{1}{r^2}\frac{\partial D_{k\gamma\beta}}{\partial x_l}\right)\frac{\partial K_0^{\mathbf{uu}}}{\partial r}(\mathbf{x},\boldsymbol{\xi};t,\tau;c_{\mathrm{S}})+\frac{D_{k\gamma\beta}r_{,l}}{r^2}\frac{\partial^2 K_0^{\mathbf{uu}}}{\partial r^2}(\mathbf{x},\boldsymbol{\xi};t,\tau;c_{\mathrm{S}})\right]
\end{aligned}
\tag{A.23}
$$

where the coefficients $A_{k\gamma\beta}$, $B_{k\gamma\beta}$, $B'_{k\gamma\beta}$, $C_{k\gamma\beta}$ and $D_{k\gamma\beta}$ are the same defined in (A.16). Let us proceed with the computation of the integral contributes of the auxiliary kernels and their spatial derivative:

$$
\begin{aligned}
&\int_{\tilde{n}}^{T}\int_0^t G_0^{\mathbf{uu}}(\mathbf{x},\boldsymbol{\xi};t_{\tilde{n}},\tau;c)(\tau-t_n)H[\tau-t_n]d\tau dt\\
=&\frac{c}{2\pi}\int_{t_{\tilde{n}}}^{T}\int_0^t\frac{H[c(t-\tau)-r]}{\sqrt{c^2(t-\tau)^2-r^2}}(\tau-t_n)H[\tau-t_n]d\tau dt\\
=&\frac{1}{2\pi}\int_{t_{\tilde{n}}}^{T}H[t-t_n]\int_{t_n}^t\frac{H[c(t-\tau)-r]}{\sqrt{c^2(t-\tau)^2-r^2}}(c\tau-ct_n)d\tau dt\\
=&\frac{1}{2\pi}\int_{t_{\tilde{n}}}^{T}H[c(t-t_n)-r]\int_{t_n}^{t-\frac{r}{c}}\frac{c\tau-ct_n}{\sqrt{c^2(t-\tau)^2-r^2}}d\tau dt\\
=&\frac{1}{2\pi c}\int_{t_{\tilde{n}}}^{T}H[c(t-\tau)-r]\int_r^{c(t-t_n)}\frac{c(t-t_n)-\xi}{\sqrt{\xi^2-r^2}}d\xi dt\\
=&\frac{1}{2\pi c}\int_{t_{\tilde{n}}}^{T}H[c(t-t_n)-r]\left\{c(t-t_n)\log\left(c(t-t_n)+\sqrt{c^2(t-t_n)^2-r^2}\right)-c(t-t_n)\log(r)\right.\\
&\left.-\sqrt{c^2(t-t_n)^2-r^2}\right\}dt
\end{aligned}
$$

focusing on the last integral we observe that

$$
\int_{t_{\tilde{n}}}^{T}H[c(t-t_n)-r]\{\ldots\}\,dt=H[c(T-t_n)-r]\int_{t_n+\frac{r}{c}}^{T}\{\ldots\}\,dt-H[c\Delta_{\tilde{n},n}-r]\int_{t_n+\frac{r}{c}}^{t_{\tilde{n}}}\{\ldots\}\,dt. \tag{A.24}
$$

The first addend of the right-hand-side gives null contribution in the summation over ξ index in the integral (A.21), meaning that we can ignore this term and write

$$
\begin{aligned}
&\int_{t_{\tilde{n}}}^{T}\int_{0}^{t} G_0^{\mathbf{uu}}(\mathbf{x},\boldsymbol{\xi};t,\tau;c)(\tau-t_n)H[\tau-t_n]d\tau dt \\
=&-\frac{1}{2\pi c}H[c\Delta_{\tilde{n},n}-r]\int_{t_n+\frac{r}{c}}^{t_{\tilde{n}}}\Big\{c(t-t_n)\log\left(c(t-t_n)+\sqrt{c^2(t-t_n)^2-r^2}\right)-c(t-t_n)\log(r) \\
&-\sqrt{c^2(t-t_n)^2-r^2}\Big\}dt \\
=&-\frac{1}{2\pi c}H[c\Delta_{\tilde{n},n}-r]\left\{\frac{c(t-t_n)^2}{2}\log\left(c(t-t_n)+\sqrt{c^2(t-t_n)^2-r^2}\right)\right. \\
&-\frac{1}{4c}\left[c(t-t_n)\sqrt{c^2(t-t_n)^2-r^2}+r^2\log\left(c(t-t_n)+\sqrt{c^2(t-t_n)^2-r^2}\right)\right] \\
&\left.-\frac{c(t-t_n)^2}{2}\log(r)-\frac{1}{2c}\left[c(t-t_n)\sqrt{c^2(t-t_n)^2-r^2}-r^2\log\left(c(t-t_n)+\sqrt{c^2(t-t_n)^2-r^2}\right)\right]\right\}_{t_n+\frac{r}{c}}^{t_{\tilde{n}}} \\
=&-\frac{1}{2\pi c}H[c\Delta_{\tilde{n},n}-r]\left\{\left(\frac{c\Delta_{\tilde{n},n}^2}{2}+\frac{r^2}{4c}\right)\left[\log\left(c\Delta_{\tilde{n},n}+\sqrt{c^2\Delta_{\tilde{n},n}^2-r^2}\right)-\log(r)\right]-\frac{3}{4}\Delta_{\tilde{n},n}\sqrt{c^2\Delta_{\tilde{n},n}^2-r^2}\right\}
\end{aligned}
\tag{A.25}
$$

For what regards the auxiliary kernel $K_0^{\mathbf{uu}}$ we write

$$
\begin{aligned}
&\int_{t_{\tilde{n}}}^{T}\int_{0}^{t} K_0^{\mathbf{uu}}(\mathbf{x},\boldsymbol{\xi};t,\tau;c)(\tau-t_n)H[\tau-t_n]d\tau dt \\
=&\frac{c}{2\pi}\int_{t_{\tilde{n}}}^{T}\int_{0}^{t} H[c(t-\tau)-r]\sqrt{c^2(t-\tau)^2-r^2}(\tau-t_n)H[\tau-t_n]d\tau dt \\
=&\frac{1}{2\pi}\int_{t_{\tilde{n}}}^{T} H[t-t_n]\int_{t_n}^{t} H[c(t-\tau)-r]\sqrt{c^2(t-\tau)^2-r^2}(c\tau-ct_n)d\tau dt \\
=&\frac{1}{2\pi}\int_{t_{\tilde{n}}}^{T} H[c(t-t_n)-r]\int_{t_n}^{t-\frac{r}{c}}\sqrt{c^2(t-\tau)^2-r^2}(c\tau-ct_n)d\tau dt \\
=&\frac{1}{2\pi c}\int_{t_{\tilde{n}}}^{T} H[c(t-t_n)-r]\int_{r}^{c(t-t_n)}(c(t-t_n)-\xi)\sqrt{\xi^2-r^2}d\xi dt \\
=&\frac{1}{2\pi c}\int_{t_{\tilde{n}}}^{T}\frac{H[c(t-t_n)-r]}{6}\Big\{-3r^2c(t-t_n)\left[\log\left(c(t-t_n)+\sqrt{c^2(t-t_n)^2-r^2}\right)-\log(r)\right] \\
&\left(2r^2+c^2(t-t_n)^2\right)\sqrt{c^2(t-t_n)^2-r^2}\Big\}dt.
\end{aligned}
$$

With the same argument used in (A.24) we continue the computations as follows

$$
\begin{aligned}
&\int_{t_{\tilde{n}}}^{T}\int_{0}^{t} K_0^{\mathbf{uu}}(\mathbf{x},\boldsymbol{\xi};t,\tau;c)(\tau-t_n)H[\tau-t_n]d\tau dt\\
=&-\frac{1}{12\pi c}H[c\Delta_{\tilde{n},n}-r]\int_{t_n+\frac{r}{c}}^{t_{\tilde{n}}}\left\{-3r^2c(t-t_n)\left[\log\left(c(t-t_n)+\sqrt{c^2(t-t_n)^2-r^2}\right)-\log(r)\right]\right.\\
&\left.\left(2r^2+c^2(t-t_n)^2\right)\sqrt{c^2(t-t_n)^2-r^2}\right\}dt\\
=&-\frac{1}{12\pi c^2}H[c\Delta_{\tilde{n},n}-r]\left\{r^2\left(z\sqrt{z^2-r^2}-r^2\log\left(z+\sqrt{z^2-r^2}\right)\right)+\frac{\sqrt{z^2-r^2}}{4}\left(z^3-\frac{r^2z}{2}\right)\right.\\
&-\frac{r^4}{8}\log\left(z+\sqrt{z^2-r^2}\right)-3r^2\frac{z^2}{2}\left[\log\left(z+\sqrt{z^2-r^2}\right)-\log(r)\right]\\
&\left.+\frac{3r^2}{4}\left[z\sqrt{z^2-r^2}+r^2\log\left(z+\sqrt{z^2-r^2}\right)\right]\right\}_{r}^{c\Delta_{\tilde{n},n}}\\
=&\frac{1}{12\pi c}H[c\Delta_{\tilde{n},n}-r]\left\{\left(\frac{3}{8c}r^2+\frac{3c\Delta_{\tilde{n},n}^2}{2}\right)r^2\left[\log\left(c\Delta_{\tilde{n},n}+\sqrt{c^2\Delta_{\tilde{n},n}^2-r^2}\right)-\log(r)\right]\right.\\
&\left.-\left(\frac{13}{8}r^2+\frac{c^2\Delta_{\tilde{n},n}^2}{4}\right)\Delta_{\tilde{n},n}\sqrt{c^2\Delta_{\tilde{n},n}^2-r^2}\right\}.
\end{aligned}
\tag{A.26}
$$

As observed previously for the computations of the double layer kernel, we remark that the global integral (A.22) is independent from the space variables, meaning that the integral contributes depending on the derivatives $\partial G_0^{\mathbf{uu}}/\partial r$, $\partial^2 G_0^{\mathbf{uu}}/\partial r^2$, $\partial K_0^{\mathbf{uu}}/\partial r$ and $\partial^2 K_0^{\mathbf{uu}}/\partial r^2$ can be easily calculated applying a space derivatives to (A.25) and (A.26):

$$
\begin{aligned}
&\int_{t_{\tilde{n}}}^{T}\int_{0}^{t}\frac{\partial}{\partial r}G_0^{\mathbf{uu}}(\mathbf{x},\boldsymbol{\xi};t,\tau;c)(\tau-t_n)H[\tau-t_n]d\tau dt\\
=&\frac{\partial}{\partial r}\left(\int_{t_{\tilde{n}}}^{T}\int_{0}^{t}G_0^{\mathbf{uu}}(\mathbf{x},\boldsymbol{\xi};t,\tau;c)(\tau-t_n)H[\tau-t_n]d\tau dt\right),\\
&\int_{t_{\tilde{n}}}^{T}\int_{0}^{t}\frac{\partial}{\partial r}K_0^{\mathbf{uu}}(\mathbf{x},\boldsymbol{\xi};t,\tau;c)(\tau-t_n)H[\tau-t_n]d\tau dt\\
=&\frac{\partial}{\partial r}\left(\int_{t_{\tilde{n}}}^{T}\int_{0}^{t}K_0^{\mathbf{uu}}(\mathbf{x},\boldsymbol{\xi};t,\tau;c)(\tau-t_n)H[\tau-t_n]d\tau dt\right),
\end{aligned}
$$

and

$$
\begin{aligned}
&\int_{t_{\tilde{n}}}^{T}\int_{0}^{t}\frac{\partial^2}{\partial r^2}G_0^{\mathbf{uu}}(\mathbf{x},\boldsymbol{\xi};t,\tau;c)(\tau-t_n)H[\tau-t_n]d\tau dt\\
=&\frac{\partial}{\partial r}\left(\int_{t_{\tilde{n}}}^{T}\int_{0}^{t}\frac{\partial}{\partial r}G_0^{\mathbf{uu}}(\mathbf{x},\boldsymbol{\xi};t,\tau;c)(\tau-t_n)H[\tau-t_n]d\tau dt\right),\\
&\int_{t_{\tilde{n}}}^{T}\int_{0}^{t}\frac{\partial^2}{\partial r^2}K_0^{\mathbf{uu}}(\mathbf{x},\boldsymbol{\xi};t,\tau;c)(\tau-t_n)H[\tau-t_n]d\tau dt\\
=&\frac{\partial}{\partial r}\left(\int_{t_{\tilde{n}}}^{T}\int_{0}^{t}\frac{\partial}{\partial r}K_0^{\mathbf{uu}}(\mathbf{x},\boldsymbol{\xi};t,\tau;c)(\tau-t_n)H[\tau-t_n]d\tau dt\right).
\end{aligned}
$$

Therefore, exploiting the previous formulas we write:

$$\begin{aligned}
&\int_{t_{\tilde{n}}}^{T}\int_{0}^{t}\frac{\partial}{\partial r}G_0^{\mathbf{uu}}(\mathbf{x},\boldsymbol{\xi};t_{\tilde{n}},\tau;c)(\tau-t_n)H[\tau-t_n]d\tau dt\\
=&\frac{1}{2\pi c}H[c\Delta_{\tilde{n},n}-r]\left\{\frac{1}{2r}\Delta_{\tilde{n},n}\sqrt{c^2\Delta_{\tilde{n},n}^2-r^2}-\frac{r}{2c}\left[\log\left(c\Delta_{\tilde{n},n}+\sqrt{c^2\Delta_{\tilde{n},n}^2-r^2}\right)-\log(r)\right]\right\},
\end{aligned}\tag{A.27}$$

$$\begin{aligned}
&\int_{t_{\tilde{n}}}^{T}\int_{0}^{t}\frac{\partial^2}{\partial r^2}G_0^{\mathbf{uu}}(\mathbf{x},\boldsymbol{\xi};t_{\tilde{n}},\tau;c)(\tau-t_n)H[\tau-t_n]d\tau dt\\
=&\frac{1}{2\pi c}H[c\Delta_{\tilde{n},n}-r]\left\{-\frac{1}{2r^2}\Delta_{\tilde{n},n}\sqrt{c^2\Delta_{\tilde{n},n}^2-r^2}-\frac{1}{2c}\left[\log\left(c\Delta_{\tilde{n},n}+\sqrt{c^2\Delta_{\tilde{n},n}^2-r^2}\right)-\log(r)\right]\right\},
\end{aligned}\tag{A.28}$$

$$\begin{aligned}
&\int_{t_{\tilde{n}}}^{T}\int_{0}^{t}\frac{\partial}{\partial r}K_0^{\mathbf{uu}}(\mathbf{x},\boldsymbol{\xi};t_{\tilde{n}},\tau;c)(\tau-t_n)H[\tau-t_n]d\tau dt\\
=&-\frac{1}{2\pi c}H[c\Delta_{\tilde{n},n}-r]\left\{-\left(\frac{cr\Delta_{\tilde{n},n}^2}{2}+\frac{r^3}{4c}\right)\left[\log\left(c\Delta_{\tilde{n},n}+\sqrt{c^2\Delta_{\tilde{n},n}^2-r^2}\right)-\log(r)\right]\right.\\
&\left.+\frac{3r}{4}\Delta_{\tilde{n},n}\sqrt{c^2\Delta_{\tilde{n},n}^2-r^2}\right\},
\end{aligned}\tag{A.29}$$

$$\begin{aligned}
&\int_{t_{\tilde{n}}}^{T}\int_{0}^{t}\frac{\partial^2}{\partial r^2}K_0^{\mathbf{uu}}(\mathbf{x},\boldsymbol{\xi};t_{\tilde{n}},\tau;c)(\tau-t_n)H[\tau-t_n]d\tau dt\\
=&\frac{1}{2\pi c}H[c\Delta_{\tilde{n},n}-r]\left\{\left(\frac{c\Delta_{\tilde{n},n}^2}{2}+\frac{3r^2}{4c}\right)\left[\log\left(c\Delta_{\tilde{n},n}+\sqrt{c^2\Delta_{\tilde{n},n}^2-r^2}\right)-\log(r)\right]\right.\\
&\left.-\frac{5}{4}\Delta_{\tilde{n},n}\sqrt{c^2\Delta_{\tilde{n},n}^2-r^2}\right\}.
\end{aligned}\tag{A.30}$$

Taking into account the explicit expressions of the contributes (A.25), (A.26), (A.27), (A.28), (A.29) and (A.30) and the definition of the second derivative of the fundamental tensor in (A.23) we can rewrite the integral in (A.21) as

$$\begin{aligned}
&-\sum_{\xi,\varsigma=0}^{1}(-1)^{\xi+\varsigma}\int_{t_{\tilde{n}+\xi}}^{T}\int_{0}^{t}C_{ih}^{kl}C_{j\alpha}^{\beta\gamma}\frac{\partial^2 G_{k\beta}^{\mathbf{uu}}}{\partial x_l\partial x_\gamma}(\mathbf{x},\boldsymbol{\xi};t,\tau)\frac{\tau-t_{n+\varsigma}}{\Delta t^2}H[\tau-t_{n+\varsigma}]n_h(\mathbf{x})n_\alpha(\boldsymbol{\xi})d\tau dt\\
=&-\sum_{\xi,\varsigma=0}^{1}(-1)^{\xi+\varsigma}\left[\frac{1}{2\pi\varrho\Delta t^2}\left(\frac{f_{\mathtt{P}}\left(r;\Delta_{\tilde{n}+\xi,n+\varsigma}\right)}{c_{\mathtt{P}}^3}-\frac{f_{\mathtt{S}}\left(r;\Delta_{\tilde{n}+\xi,n+\varsigma}\right)}{c_{\mathtt{S}}^3}\right)\right]
\end{aligned}\tag{A.31}$$

where the expressions of the functions $f_{\mathtt{P}}(r;\Delta)$ and $f_{\mathtt{S}}(r;\Delta)$ are

$$
\begin{aligned}
&f_{\mathtt{P}}(r;\Delta) = H[c_{\mathtt{P}}\Delta - r] \\
&\left\{ C_{ih}^{kl} C_{j\alpha}^{\beta\gamma} \left(-\frac{r_{,l}}{r^2} A_{k\gamma\beta} + \frac{1}{r}\frac{\partial A_{k\gamma\beta}}{\partial x_l} \right) n_h(\mathbf{x}) n_\alpha(\boldsymbol{\xi}) \left[-\left(\frac{c_{\mathtt{P}}\Delta^2}{2} + \frac{r^2}{4c_{\mathtt{P}}} \right) \widehat{\varphi}_{\mathtt{P}}(r;\Delta) + \frac{3}{4}\Delta\varphi_{\mathtt{P}}(r;\Delta) \right] \right. \\
&+ C_{ih}^{kl} C_{j\alpha}^{\beta\gamma} \left(\frac{r_{,l}}{r} A_{k\gamma\beta} + \frac{\partial B_{k\gamma\beta}}{\partial x_l} \right) n_h(\mathbf{x}) n_\alpha(\boldsymbol{\xi}) \left[-\frac{r}{2c_{\mathtt{P}}} \widehat{\varphi}_{\mathtt{P}}(r;\Delta) + \frac{\Delta}{2r}\varphi_{\mathtt{P}}(r;\Delta) \right] \\
&- C_{ih}^{kl} C_{j\alpha}^{\beta\gamma} B_{k\gamma\beta} r_{,l} n_h(\mathbf{x}) n_\alpha(\boldsymbol{\xi}) \left[\frac{1}{2c_{\mathtt{P}}} \widehat{\varphi}_{\mathtt{P}}(r;\Delta) + \frac{\Delta}{2r^2}\varphi_{\mathtt{P}}(r;\Delta) \right] \\
&+ C_{ih}^{kl} C_{j\alpha}^{\beta\gamma} \left(-\frac{6r_{,l}}{r^4} C_{k\gamma\beta} + \frac{2}{r^3}\frac{\partial C_{k\gamma\beta}}{\partial x_l} \right) n_h(\mathbf{x}) n_\alpha(\boldsymbol{\xi}) \left[\frac{1}{6} \left(\frac{3r^4}{8c_{\mathtt{P}}} + \frac{3r^2 c_{\mathtt{P}}\Delta^2}{2} \right) \widehat{\varphi}_{\mathtt{P}}(r;\Delta) \right. \\
&\qquad \left. - \frac{1}{6} \left(\frac{13r^2}{8} + \frac{c_{\mathtt{P}}^2\Delta^2}{4} \right) \Delta\varphi_{\mathtt{P}}(r;\Delta) \right] \\
&+ C_{ih}^{kl} C_{j\alpha}^{\beta\gamma} \left(\frac{2r_{,l}}{r^3} C_{k\gamma\beta} - \frac{2r_{,l}}{r^3} D_{k\gamma\beta} + \frac{1}{r^2}\frac{\partial D_{k\gamma\beta}}{\partial x_l} \right) n_h(\mathbf{x}) n_\alpha(\boldsymbol{\xi}) \left[\left(\frac{r^3}{4c_{\mathtt{P}}} + \frac{r c_{\mathtt{P}}\Delta^2}{2} \right) \widehat{\varphi}_{\mathtt{P}}(r;\Delta) \right. \\
&\qquad \left. - \frac{3r}{4}\Delta\varphi_{\mathtt{P}}(r;\Delta) \right] \\
&\left. - C_{ih}^{kl} C_{j\alpha}^{\beta\gamma} \frac{D_{k\gamma\beta} r_{,l}}{r^2} n_h(\mathbf{x}) n_\alpha(\boldsymbol{\xi}) \left[-\left(\frac{3r^2}{4c_{\mathtt{P}}} + \frac{c_{\mathtt{P}}\Delta^2}{2} \right) \widehat{\varphi}_{\mathtt{P}}(r;\Delta) + \frac{5}{4}\Delta\varphi_{\mathtt{P}}(r;\Delta) \right] \right\},
\end{aligned}
$$

and

$$
\begin{aligned}
&f_{\mathtt{S}}(r;\Delta) = H[c_{\mathtt{S}}\Delta - r] \\
&\left\{ C_{ih}^{kl} C_{j\alpha}^{\beta\gamma} \left(-\frac{r_{,l}}{r^2} A_{k\gamma\beta} + \frac{1}{r}\frac{\partial A_{k\gamma\beta}}{\partial x_l} \right) n_h(\mathbf{x}) n_\alpha(\boldsymbol{\xi}) \left[-\left(\frac{c_{\mathtt{S}}\Delta^2}{2} + \frac{r^2}{4c_{\mathtt{S}}} \right) \widehat{\varphi}_{\mathtt{S}}(r;\Delta) + \frac{3}{4}\Delta\varphi_{\mathtt{S}}(r;\Delta) \right] \right. \\
&+ C_{ih}^{kl} C_{j\alpha}^{\beta\gamma} \left(\frac{r_{,l}}{r} A_{k\gamma\beta} + \frac{\partial B'_{k\gamma\beta}}{\partial x_l} \right) n_h(\mathbf{x}) n_\alpha(\boldsymbol{\xi}) \left[-\frac{r}{2c_{\mathtt{S}}} \widehat{\varphi}_{\mathtt{S}}(r;\Delta) + \frac{\Delta}{2r}\varphi_{\mathtt{S}}(r;\Delta) \right] \\
&- C_{ih}^{kl} C_{j\alpha}^{\beta\gamma} B'_{k\gamma\beta} r_{,l} n_h(\mathbf{x}) n_\alpha(\boldsymbol{\xi}) \left[\frac{1}{2c_{\mathtt{S}}} \widehat{\varphi}_{\mathtt{S}}(r;\Delta) + \frac{\Delta}{2r^2}\varphi_{\mathtt{S}}(r;\Delta) \right] \\
&+ C_{ih}^{kl} C_{j\alpha}^{\beta\gamma} \left(-\frac{6r_{,l}}{r^4} C_{k\gamma\beta} + \frac{2}{r^3}\frac{\partial C_{k\gamma\beta}}{\partial x_l} \right) n_h(\mathbf{x}) n_\alpha(\boldsymbol{\xi}) \left[\frac{1}{6} \left(\frac{3r^4}{8c_{\mathtt{S}}} + \frac{3r^2 c_{\mathtt{S}}\Delta^2}{2} \right) \widehat{\varphi}_{\mathtt{S}}(r;\Delta) \right. \\
&\qquad \left. - \frac{1}{6} \left(\frac{13r^2}{8} + \frac{c_{\mathtt{S}}^2\Delta^2}{4} \right) \Delta\varphi_{\mathtt{S}}(r;\Delta) \right] \\
&+ C_{ih}^{kl} C_{j\alpha}^{\beta\gamma} \left(\frac{2r_{,l}}{r^3} C_{k\gamma\beta} - \frac{2r_{,l}}{r^3} D_{k\gamma\beta} + \frac{1}{r^2}\frac{\partial D_{k\gamma\beta}}{\partial x_l} \right) n_h(\mathbf{x}) n_\alpha(\boldsymbol{\xi}) \left[\left(\frac{r^3}{4c_{\mathtt{S}}} + \frac{r c_{\mathtt{S}}\Delta^2}{2} \right) \widehat{\varphi}_{\mathtt{S}}(r;\Delta) \right. \\
&\qquad \left. - \frac{3r}{4}\Delta\varphi_{\mathtt{S}}(r;\Delta) \right] \\
&\left. - C_{ih}^{kl} C_{j\alpha}^{\beta\gamma} \frac{D_{k\gamma\beta} r_{,l}}{r^2} n_h(\mathbf{x}) n_\alpha(\boldsymbol{\xi}) \left[-\left(\frac{3r^2}{4c_{\mathtt{S}}} + \frac{c_{\mathtt{S}}\Delta^2}{2} \right) \widehat{\varphi}_{\mathtt{S}}(r;\Delta) + \frac{5}{4}\Delta\varphi_{\mathtt{S}}(r;\Delta) \right] \right\}.
\end{aligned}
$$

We calculate then the coefficients in $f_{\mathtt{P}}(r;\Delta)$ and $f_{\mathtt{S}}(r;\Delta)$ involving the derivatives of the terms defined in (A.16):

$$\begin{aligned}
&\frac{1}{r}\frac{\partial A_{k\gamma\beta}}{\partial x_l}-\frac{r_{,l}}{r^2}A_{k\gamma\beta}\\
&\quad=\frac{1}{r^2}\left(-2\delta_{k\gamma}r_{,\beta}r_{,l}-2\delta_{\beta\gamma}r_{,k}r_{,l}+8r_{,k}r_{,\beta}r_{,\gamma}r_{,l}+\delta_{k\gamma}\delta_{\beta l}+\delta_{\beta\gamma}\delta_{kl}-2\delta_{kl}r_{,\beta}r_{,\gamma}-2\delta_{\beta l}r_{,k}r_{,\gamma}\right.\\
&\qquad\left.-2\delta_{\gamma l}r_{,k}r_{,\beta}\right),\\
&\frac{r_{,l}}{r}A_{k\gamma\beta}+\frac{\partial B_{k\gamma\beta}}{\partial x_l}\\
&\quad=\frac{1}{r}\left(-5r_{,k}r_{,\beta}r_{,\gamma}r_{,l}+\delta_{k\gamma}r_{,\beta}r_{,l}+\delta_{\beta\gamma}r_{,k}r_{,l}+\delta_{kl}r_{,\beta}r_{,\gamma}+\delta_{\beta l}r_{,k}r_{,\gamma}+\delta_{\gamma l}r_{,k}r_{,\beta}\right),\\
&\frac{r_{,l}}{r}A_{k\gamma\beta}+\frac{\partial B'_{k\gamma\beta}}{\partial x_l}\\
&\quad=\frac{1}{r}\left(-5r_{,k}r_{,\beta}r_{,\gamma}r_{,l}+\delta_{k\gamma}r_{,\beta}r_{,l}+\delta_{\beta\gamma}r_{,k}r_{,l}+\delta_{kl}r_{,\beta}r_{,\gamma}+\delta_{\beta l}r_{,k}r_{,\gamma}+\delta_{\gamma l}r_{,k}r_{,\beta}+\delta_{k\beta}r_{,\gamma}r_{,l}\right.\\
&\qquad\left.-\delta_{k\beta}\delta_{\gamma l}\right),\\
&\frac{2}{r^3}\frac{\partial C_{k\gamma\beta}}{\partial x_l}-\frac{6r_{,l}}{r^4}C_{k\gamma\beta}\\
&\quad=\frac{1}{r^4}\left(48r_{,k}r_{,\beta}r_{,\gamma}r_{,l}-8\delta_{k\gamma}r_{,\beta}r_{,l}-8\delta_{\beta\gamma}r_{,k}r_{,l}-8\delta_{kl}r_{,\beta}r_{,\gamma}-8\delta_{\beta l}r_{,k}r_{,\gamma}-8\delta_{\gamma l}r_{,k}r_{,\beta}\right.\\
&\qquad\left.-8\delta_{k\beta}r_{,\gamma}r_{,l}+2\delta_{k\beta}\delta_{\gamma l}+2\delta_{\beta\gamma}\delta_{kl}+2\delta_{k\gamma}\delta_{\beta l}\right),\\
&\frac{2r_{,l}}{r^3}C_{k\gamma\beta}-\frac{2r_{,l}}{r^3}D_{k\gamma\beta}+\frac{1}{r^2}\frac{\partial D_{k\gamma\beta}}{\partial x_l}\\
&\quad=\frac{1}{r^3}\left(-18r_{,k}r_{,\beta}r_{,\gamma}r_{,l}+2\delta_{k\gamma}r_{,\beta}r_{,l}+2\delta_{\beta\gamma}r_{,k}r_{,l}+2\delta_{kl}r_{,\beta}r_{,\gamma}+2\delta_{\beta l}r_{,k}r_{,\gamma}+2\delta_{\gamma l}r_{,k}r_{,\beta}\right.\\
&\qquad\left.+5\delta_{k\beta}r_{,\gamma}r_{,l}-\delta_{k\beta}\delta_{\gamma l}\right),
\end{aligned}$$

and we proceed with the double application of the Hooke tensors, summing up over the indexes $h,k,l,\alpha,\beta,\gamma$:

$$\begin{aligned}
&C_{ih}^{kl}C_{j\alpha}^{\beta\gamma}r_{,k}r_{,\beta}r_{,\gamma}r_{,l}n_\alpha(\boldsymbol{\xi})n_h(\mathbf{x})=\lambda^2e+2\mu\lambda f+2\mu\lambda a+4\mu^2c,\\
&C_{ih}^{kl}C_{j\alpha}^{\beta\gamma}\delta_{k\gamma}r_{,\beta}r_{,l}n_\alpha(\boldsymbol{\xi})n_h(\mathbf{x})=\lambda^2e+2\mu\lambda f+2\mu\lambda a+\mu^2g+\mu^2d+\mu^2o+\mu^2b,\\
&C_{ih}^{kl}C_{j\alpha}^{\beta\gamma}\delta_{\beta\gamma}r_{,k}r_{,l}n_\alpha(\boldsymbol{\xi})n_h(\mathbf{x})=\lambda(2\lambda+2\mu)e+2\mu(2\lambda+2\mu)f,\\
&C_{ih}^{kl}C_{j\alpha}^{\beta\gamma}\delta_{kl}r_{,\beta}r_{,\gamma}n_\alpha(\boldsymbol{\xi})n_h(\mathbf{x})=\lambda(2\lambda+2\mu)e+2\mu(2\lambda+2\mu)a,\\
&C_{ih}^{kl}C_{j\alpha}^{\beta\gamma}\delta_{k\beta}\delta_{\gamma l}n_\alpha(\boldsymbol{\xi})n_h(\mathbf{x})=(2\lambda^2+4\mu\lambda)e+2\mu^2s+2\mu^2m,\\
&C_{ih}^{kl}C_{j\alpha}^{\beta\gamma}\delta_{\beta\gamma}\delta_{kl}n_\alpha(\boldsymbol{\xi})n_h(\mathbf{x})=(2\lambda+2\mu)^2e
\end{aligned}$$

where we have defined

$$\begin{aligned}
&a=r_{,j}n_i(\mathbf{x})(r_{,k}n_k(\boldsymbol{\xi})), && b=r_{,j}n_i(\boldsymbol{\xi})(r_{,k}n_k(\mathbf{x})), && c=r_{,j}r_{,i}(r_{,k}n_k(\boldsymbol{\xi}))(r_{,h}n_h(\mathbf{x})),\\
&d=r_{,j}r_{,i}(n_k(\boldsymbol{\xi})n_k(\mathbf{x})), && e=n_j(\boldsymbol{\xi})n_i(\mathbf{x}), && f=r_{,i}n_j(\boldsymbol{\xi})(r_{,k}n_k(\mathbf{x})),\\
&g=\delta_{ij}(r_{,k}n_k(\boldsymbol{\xi}))(r_{,h}n_h(\mathbf{x})), && o=r_{,i}n_j(\mathbf{x})(r_{,k}n_k(\boldsymbol{\xi})), && m=n_i(\boldsymbol{\xi})n_j(\mathbf{x}),\\
&s=\delta_{ij}(n_k(\boldsymbol{\xi})n_k(\mathbf{x})).
\end{aligned}\tag{A.32}$$

Moreover, taking into account the symmetry properties in (1.5), from the previous computations it is possible to derive the results of the double application of the Hooke tensor to the terms $\delta_{\beta l}r_{,k}r_{,\gamma}$, $\delta_{\gamma l}r_{,k}r_{,\beta}$, $\delta_{k\beta}r_{,\gamma}r_{,l}$ and $\delta_{k\gamma}\delta_{\beta l}$. Therefore, making explicit the coefficients of the functions

$f_{\mathtt{P}}(r;\Delta)$ and $f_{\mathtt{S}}(r;\Delta)$ and collecting all the contribute of the peculiar kernels $\varphi_\gamma(r;\Delta)$ and $\widehat{\varphi}_\gamma(r;\Delta)$ we obtain the definitive form of the integral contribute (A.21):

$$
\begin{aligned}
&-\sum_{\xi,\varsigma=0}^{1}(-1)^{\xi+\varsigma}\int_{t_{\widetilde{n}+\xi}}^{T}\int_{0}^{t}C_{ih}^{kl}C_{j\alpha}^{\beta\gamma}\frac{\partial^2 G_{k\beta}^{\mathbf{uu}}}{\partial x_l\partial x_\gamma}(\mathbf{x},\boldsymbol{\xi};t,\tau)\frac{\tau-t_{n+\varsigma}}{\Delta t^2}H[\tau-t_{n+\varsigma}]n_h(\mathbf{x})n_\alpha(\boldsymbol{\xi})d\tau dt\\
&=-\sum_{\xi,\varsigma=0}^{1}(-1)^{\xi+\varsigma}\\
&\quad\left\{\frac{H[c_{\mathtt{P}}\Delta_{\widetilde{n}+\xi,n+\varsigma}-r]}{2\pi\varrho\Delta t^2c_{\mathtt{P}}^3}\left[\left(D_{\varphi,c_{\mathtt{P}}}^{ij}\Delta_{\widetilde{n}+\xi,n+\varsigma}+D_{c_{\mathtt{P}}}^{ij}\frac{\Delta_{\widetilde{n}+\xi,n+\varsigma}^3c_{\mathtt{P}}^2}{r^2}\right)\frac{\varphi_{\mathtt{P}}(r,\Delta_{\widetilde{n}+\xi,n+\varsigma})}{r^2}\right.\right.\\
&\qquad\left.+\,D_{\widehat{\varphi},c_{\mathtt{P}}}^{ij}\frac{\widehat{\varphi}_{\mathtt{P}}(r,\Delta_{\widetilde{n}+\xi,n+\varsigma})}{c_{\mathtt{P}}}\right]\\
&\quad-\frac{H[c_{\mathtt{S}}\Delta_{\widetilde{n}+\xi,n+\varsigma}-r]}{2\pi\varrho\Delta t^2c_{\mathtt{S}}^3}\left[\left(D_{\varphi,c_{\mathtt{S}}}^{ij}\Delta_{\widetilde{n}+\xi,n+\varsigma}+D_{c_{\mathtt{S}}}^{ij}\frac{\Delta_{\widetilde{n}+\xi,n+\varsigma}^3c_{\mathtt{S}}^2}{r^2}\right)\frac{\varphi_{\mathtt{S}}(r,\Delta_{\widetilde{n}+\xi,n+\varsigma})}{r^2}\right.\\
&\qquad\left.\left.+\,D_{\widehat{\varphi},c_{\mathtt{S}}}^{ij}\frac{\widehat{\varphi}_{\mathtt{S}}(r,\Delta_{\widetilde{n}+\xi,n+\varsigma})}{c_{\mathtt{S}}}\right]\right\},
\end{aligned}
\tag{A.33}
$$

where the coefficients D_{ψ,c_γ}^{ij}, $\widetilde{D}_{\psi,c_\gamma}^{ij}$ and $D_{\varphi,c_\gamma}^{ij}$ are defined as follows:

$$
\begin{aligned}
D_{\varphi,c_{\mathtt{P}}}^{ij}=&-\frac{2\mu}{3}(3\lambda+2\mu)a-\frac{4}{3}\mu^2b+4\mu^2c-\frac{4}{3}\mu^2d+\frac{\mu}{6}(12\lambda+5\mu)e-\frac{2}{3}\mu(3\lambda+2\mu)f-\frac{4}{3}\mu^2g,\\
&-\frac{4}{3}\mu^2o+\frac{5}{6}\mu^2m+\frac{5}{6}\mu^2s,\\
D_{\varphi,c_{\mathtt{S}}}^{ij}=&-\frac{4}{3}\mu^2a-\frac{\mu^2}{3}b+4\mu^2c-\frac{\mu^2}{3}d+\frac{5}{6}\mu^2e-\frac{4}{3}\mu^2f-\frac{\mu^2}{3}g-\frac{\mu^2}{3}o-\frac{\mu^2}{6}m-\frac{\mu^2}{6}s,\\
D_{\widehat{\varphi},c_{\mathtt{P}}}^{ij}=&-\frac{2\lambda^2+4\lambda\mu+\mu^2}{2}e-\frac{\mu^2}{2}m-\frac{\mu^2}{2}s,\\
D_{\widehat{\varphi},c_{\mathtt{S}}}^{ij}=&-\frac{\mu^2}{2}e+\frac{\mu^2}{2}m+\frac{\mu^2}{2}s,\\
D_{c_{\mathtt{P}}}^{ij}=&D_{c_{\mathtt{S}}}^{ij}=\frac{4}{3}\mu^2a+\frac{4}{3}\mu^2b-8\mu^2c+\frac{4}{3}\mu^2d-\frac{\mu^2}{3}e+\frac{4}{3}\mu^2(f+g+o)-\frac{\mu^2}{3}(m+s),
\end{aligned}
$$

with a, b, c, d, e, f, g, o, m and s defined in (A.32).

Conclusions and future perspectives

Final considerations

In this thesis we have investigated and implemented the Energetic Boundary Element Method for the resolution of 2D elastic wave propagation problems, external to a bounded domain Ω or to an open obstacle Γ. In particular, we have considered a time domain approach, which is preferable to the frequency domain ones because allows to observe the phenomena as they evolve.
The application of energetic BEM has been investigated in depth by a theoretical point of view, exploring several integral representation formulas, fundamental for the implementation of the method itself, and demonstrating, following a Fouruier transform approach similar to the one used in [19], the existence of peculiar Sobolev spaces which guarantee the well posedness of energetic weak problems depending on the single layer integral elastodynamics operator V.
The link with the energy of the elastodynamics system is a fundamental tool that allows to overcome the instabilities typical of the implementation of classical BEMs, as stated in numerous works by Aimi and collaborators, where the energetic BEM has been implemented for the resolution of scalar waves propagation problems [9, 8, 12]. Based on the extensive numerical testing presented throughout the thesis, we can confirm that energetic BEM can be successfully applied in the elastodynamics context.

After an exact double integration in the time variables, reported for all the elastodynamic integral operators V, K, K^* and D in the Appendix of the thesis, the space-time discretization of the weak boundary integral problems we considered leads to the construction of peculiar linear systems with matrices $\mathbb{E}_V$, $\mathbb{E}_K$, $\mathbb{E}_{K^*}$ and $\mathbb{E}_D$ of Toeplitz structure. The related entries can be obtained by the computation, with suitable quadrature formulas, of double integrals defined on the elements of the mesh imposed on the boundary Γ. The efficacy of the method relies on the precise numerical computation of the peculiar integral elements, which presents irregularities determined by the Heaviside function of the fundamental elastodynamic tensor $\mathbf{G}^{uu}$ and space singularities of order $\log(r)$, $\mathcal{O}(1/r)$ and $\mathcal{O}(1/r^2)$, for r tending to zero, respectively for the elements of $\mathbb{E}_V$, $\mathbb{E}_K$, and $\mathbb{E}_D$. in Chapter 4, the detailed explanation of the quadrature strategies applied to overcome these issues has been fundamental for the correct execution of the several numerical simulations presented and discussed. The resolved 2D elastodynamic problems, characterized by Dirichlet or Neumnann datum at the boundary, confirm the stability of the energetic method for application on long-time experiments. Moreover, it has been possible to check the correctness of the results resolving benchmark problems whose solutions tend to static functions analytically calculated.

In Chapter 2 we have successfully caught the singularities that characterize the traction $\mathbf{p}$ and the unknown displacement $\mathbf{u}$ in a neighborhood of corner points of a polygonal domain Ω or near the extremes of an open obstacle Γ. The order of the singular behaviour can be determined, thanks to the singular expansions carried out for these functions, by the amplitude of the corner we are considering. We have also proved that this value, together with the parameters of the employed algebraically or geometrically graded meshes in space, influences the error committed in the ap-

proximation of the solution of the energetic weak problems we solved, both in case of Dirichlet and Neumann boundary constraints. The numerical results presented have confirmed what theoretically stated, and they moreover confirmed that the accuracy of the energetic method is not affected by the use of non-uniform spatial meshes.

In Chapter 3 we presented a simple and effective resolution of the problem of computation of the temporal blocks of the Toeplitz matrix arising from the discretization of the single layer integral operator V, which become fully populated as the time index goes on. These blocks can be represented with a low rank representation obtained by Adaptive Cross Approximation, a method that does not require a previous storage of the blocks we intend to compress. The feasibility of the proposed compression technique is theoretically proved for the single layer blocks of both acoustic and elastic wave propagation problems and numerous experiments have shown a remarkable saving in computational time and memory storage, without affecting the quality of the results carried out in combination with the energetic BEM.

In the end we recall that all the numerical experiments in this thesis have been executed by means of parallel FORTRAN® codes, used principally to assemble the first column of temporal blocks related to the discretized elastodynamics integral operators V, K, K^* and D.

Future perspectives

The points of the outgoing research related to this work are different and interesting. First of all it is possible to proceed with the investigation of elastodynamics problems with mixed boundary conditions. The scheme of the space time-discretization of a possible energetic weak formulation for this kind of boundary conditions is presented in Chapter 1 and can be applied for the resolution of realistic benchmark problems such us the study of the stress of a thin bar subjected to both traction from one or two opposite sides (for further benchmark examples see [53]).

It is possible moreover to combine energetic BEM with the Finite Element Method to study the propagation of elastic waves, in time-domain, trough sections of the media characterized by different elasticity parameters (a proposal of this approach for scalar waves propagation in 2D multidomains can be found in [4]). The coupling of techniques require an easy implementation of the interface conditions, allowing to take advantage of both methodologies, such as the implicit accomplishment of the radiation conditions at infinity for BEM and the fact that classical schemes like FEM helpful to treat possible nonlinear parts of the problems in bounded domains.

Physical situations that can be modelled by an elastodynamics problem with particular interfaces conditions are the *Contact Problems*, which find numerous applications in mechanics, from fracture dynamics and crash tests to rolling car tires (see [39] for application in the context of scalar wave propagation problems). The energetic Boundary Element Method applied to solve problems in this context is an easy to implement tool, since it basically requires, at the discrete level, the Toeplitz blocks $\mathbb{E}_V$, $\mathbb{E}_K$, $\mathbb{E}_{K^*}$ and $\mathbb{E}_D$, implemented in this thesis, in order to assemble the Poincarè-Steklov operator, which depends in its symmetric formulation on all the integral operators.

In the end, a 3D extension of the Energetic BEM for the resolution of elastodynamics problems is surely one of the main goals of the future research. This can be performed retracing some of the algorithmic details proposed in the thesis for the simpler case of the 2D propagation. However this extension is not trivial for two reasons: the increasing of the dimensional complexity and the fact that the 3D integral operators V, K, K^* and D generate discretized matrices characterized respectively by integral elements with singularities of different order ($\mathcal{O}(1/r)$, $\mathcal{O}(1/r^2)$ and $\mathcal{O}(1/r^3)$, for r tending to zero). These features required a different approach in the computation

of the matrix elements, especially for what regards the study of the splitting domains in relation to the two typical elastodynamics wave fronts propagation in the 3D space. The computational costs related to the construction of the discretized operators could represent moreover a challenge for the implementation of the 3D Energetic BEM, but a possible solution, at least for the single layer weak formulations, can be an adaptation of the compression technique reported in Chapter 3 of the thesis. With these expedients the resolution by Energetic BEM of more complex 3D problems becomes feasible and it leads to other possible scenarios, such as the implementation of the coupling BEM-FEM for the study of seismic waves propagation trough layers of medium with different physical characteristics, in order to treat more realistic geological problems.

Bibliography

[1] B. T. Aagaard, J. F. Hall & T. H. Heaton, *Characterization of near-source ground motions with earthquake simulations*, Earthquake Spectra **17.2** (2001): 177-207.

[2] A. Aimi, G. Buffoni & M. Groppi, *Decomposition of a planar vector field into irrotational and rotational components*, Applied Mathematics and Computation **244** (2014): 63-90.

[3] A. Aimi, L. Desiderio & G. Di Credico, *Partially pivoted ACA based acceleration of the Energetic BEM for time-domain acoustic and elastic waves exterior problems*, (2021, under review).

[4] A. Aimi, L. Desiderio, M. Diligenti, & C. Guardasoni, *A numerical study of energetic BEM-FEM applied to wave propagation in 2D multidomains*, Publications de l'Institut Mathematique **96.110** (2014): 5-22.

[5] A. Aimi, L. Desiderio, M. Diligenti & C. Guardasoni, *Application of Energetic BEM to 2D Elastodynamic Soft Scattering Problems*, Communications in Applied and Industrial Mathematics **10.1** (2019): 182–198.

[6] A. Aimi, G. Di Credico, M. Diligenti & C. Guardasoni, *Highly accurate quadrature schemes for singular integrals in energetic BEM applied to elastodynamics*, (2022, accepted).

[7] A. Aimi, G. Di Credico, H. Gimperlein & E.P. Stephan, *Higher-order time domain boundary elements for elastodynamics - graded meshes and hp-versions*, (2021, under review).

[8] A. Aimi, M. Diligenti & C. Guardasoni, *Numerical integration schemes for application of energetic Galerkin BEM to wave propagation problems*, Rivista Matematica della Università di Parma **2** (2010): 147-187.

[9] A. Aimi, M. Diligenti, C. Guardasoni, I. Mazzieri, & S. Panizzi, *An energy approach to space–time Galerkin BEM for wave propagation problems*, International journal for numerical methods in engineering **80.9** (2009): 1196-1240.

[10] A. Aimi, M. Diligenti & G. Monegato, *New numerical integration schemes for applications of Galerkin BEM to 2-D problems*, International Journal for Numerical Methods in Engineering **40.11** (1997): 1977-1999.

[11] A. Aimi, M. Diligenti & G. Monegato, *Numerical integration schemes for the BEM solution of hypersingular integral equations*, International journal for numerical methods in engineering **45.12** (1999): 1807-1830.

[12] A. Aimi, M. Diligenti & S. Panizzi, *Energetic Galerkin BEM for wave propagation Neumann exterior problems*, Computer Modeling in Engineering & Sciences **58.2** (2010): 185-219.

[13] B. Alpert, G. Beylkin, R. Coifman & V. Rokhlin, *Wavelet-like bases for the fast solution of second-kind integral equations*, SIAM journal on Scientific Computing **14.1** (1993): 159-184.

[14] L. Andersen, *Linear elastodynamic analysis*, (2006).

[15] T. Ha Duong, A. Bamberger & J. C. Nedelec, *Formulation variationnelle espace-temps pour le calcul par potentiel retardé de la diffraction d'une onde acoustique (I)*, Mathematical methods in the applied sciences **8.1** (1986): 405-435.

[16] T. Ha Duong, A. Bamberger & J. C. Nedelec, *Formulation variationnelle pour le calcul de la diffraction d'une onde acoustique par une surface rigide*, Mathematical methods in the applied sciences **8.1** (1986): 598-608.

[17] M. Bebendorf, *Approximation of boundary element matrices*, Numerische Mathematik **86.4** (2000): 565-589.

[18] M. Bebendorf & S. Rjasanow, *Adaptive low-rank approximation of collocation matrices*, Computing **70** (2003): 1-24.

[19] E. Becache & T. Ha Duong, *A space-time variational formulation for the boundary integral equation in a 2D elastic crack problem*, ESAIM: Mathematical Modelling and Numerical Analysis **28.2** (1994): 141-176.

[20] A. Ben-Menahem, *A concise history of mainstream seismology: Origins, legacy, and perspectives*, Bulletin of the Seismological Society of America **85.4** (1995): 1202-1225.

[21] S. Bertoluzza, S. Falletta & L. Scuderi, *Wavelets and convolution quadrature for the efficient solution of a 2D space-time BIE for the wave equation*, Applied Mathematics and Computation **366** (2020): 1-21.

[22] A. Bespalov & N. Heuer, *The pi-version of the Boundary Element Method for a three-dimensional crack problem*, The Journal of Integral Equations and Applications **17.3** (2005): 243-258.

[23] J. Bielak, J. Xu & O. Ghattas, *Earthquake ground motion and structural response in alluvial valleys*, Journal of Geotechnical and Geoenvironmental Engineering **125.5** (1999): 413-423.

[24] B. Birgisson, E Siebrits & A. P. Peirce, *Elastodynamic direct boundary element methods with enhanced numerical stability properties*, International journal for numerical methods in engineering **46.6** (1999): 871-888.

[25] A. Burel, S. Imperiale & P. Joly, *Solving the homogeneous isotropic linear elastodynamics equations using potentials and finite elements. the case of the rigid boundary condition*, Numerical Analysis and Applications **5.2** (2012): 136-143.

[26] S. Chaillat, L. Desiderio & P. Ciarlet, *Theory and implementation of H-matrix based iterative and direct solvers for Helmholtz and elastodynamic oscillatory kernels*, Journal of Computational physics **351** (2017): 165-186.

[27] T. A. Cruse & F. J. Rizzo, *A direct formulation and numerical solution of the general transient elastodynamic problem. I*, Journal of Mathematical Analysis and Applications **22.1** (1968): 244-259.

[28] L. Desiderio, & S. Falletta, *Efficient Solution of Two-Dimensional Wave Propagation Problems by CQ-Wavelet BEM: Algorithm and Applications*, SIAM Journal on Scientific Computing **42.4** (2020): B894-B920.

[29] G. Di Credico, A. Aimi & C. Guardasoni, *Energetic Galerkin Boundary Element Method for 2D Elastodynamics: integral operators with weak and strong singularities*, Boundary Elements and other Mesh Reduction Methods XLIV **131** (2021): 17-29.

[30] C. Erath, S. Ferraz-Leite, S. Funken & D. Praetorius, *Energy norm based a posteriori error estimation for boundary element methods in two dimensions*, Applied Numerical Mathematics **59** (2009): 2713–2734.

[31] A. C. Eringen & E. Suhubi, *Elastodynamics, Linear Theory, vol. 2*, (1975).

[32] S. Falletta, G. Monegato & L. Scuderi, *A space-time BIE method for wave equation problems: the (two-dimensional) Neumann case*, IMA Journal of Numerical Analysis **34.1** (2014): 390-434.

[33] S. Falletta, G. Monegato & L. Scuderi, *Two boundary integral equation methods for linear elastodynamics problems on unbounded domains*, Computers and Mathematics with Applications **78.12** (2019): 3841-3861.

[34] S. Falletta & S. A. Sauter, *The panel-clustering method for the wave equation in two spatial dimensions*, Journal of Computational Physics **305** (2016): 217-243.

[35] A. Frangi, *Elastodynamics by BEM: a new direct formulation*, International Journal for Numerical Methods in Engineering **45.6** (1999): 721-740.

[36] A. Frangi & G. Novati, *On the numerical stability of time-domain elastodynamic analyses by BEM*, Computer Methods in Applied Mechanics and Engineering **173.3-4** (1999): 403-417.

[37] N. Fusco, P. Marcellini & C. Sbordone, *Analisi matematica due*, Liguori, (1996).

[38] H. Gimperlein, F. Meyer, C. Özdemir, D. Stark & E. P. Stephan, *Boundary elements with mesh refinements for the wave equation*, Numerische Mathematik **139.4** (2018): 867-912.

[39] H. Gimperlein, F. Meyer, C. Özdemir & E. P. Stephan, *Time domain boundary elements for dynamic contact problems*, Computer Methods in Applied Mechanics and Engineering **333** (2018): 147-175.

[40] H. Gimperlein, Z. Nezhi & E. P. Stephan, *A priori error estimates for a time-dependent boundary element method for the acoustic wave equation in a half-space*, Mathematical Methods in the Applied Sciences **40** (2017): 448-462.

[41] H. Gimperlein, C. Özdemir, D. Stark & E. P. Stephan, *hp-version time domain boundary elements for the wave equation on quasi-uniform meshes*, Computer Methods in Applied Mechanics and Engineering **356** (2019): 145-174.

[42] H. Gimperlein, C. Özdemir, D. Stark & E. P. Stephan, *A residual a posteriori error estimate for the time–domain boundary element method*, Numerische Mathematik **146.2** (2020): 239-280.

[43] P. Grisvard, *Le probleme de Dirichlet pour les equations de Lamè*, C. R. Acad. Sci. Paris Ser. I Math. **304** (1987): 71-73.

[44] P. Grisvard, *Singularités en elasticité*, Archive for rational mechanics and analysis **107.2** (1989): 157-180.

[45] J. Gwinner & E. P. Stephan, *Advanced Boundary Element Methods - Treatment of Boundary Value, Transmission and Contact Problems*, Springer Series in Computational Mathematics, vol. 52, (2018).

[46] T. Ha-Duong, *On retarded potential boundary integral equations and their discretisation*, Topics in computational wave propagation Springer, Berlin, Heidelberg, (2003): 301-336.

[47] W. Hackbusch, *A sparse matrix arithmetic based on H-matrices. part i: Introduction to H-matrices*, Computing **62.2** (1999): 89-108.

[48] W. Hackbusch & Z. P. Nowak, *On the fast matrix multiplication in the boundary element method by panel clustering*, Numerische Mathematik **54.4** (1989): 463-491.

[49] T. JR Hughes & G. M. Hulbert, *Space-time finite element methods for elastodynamics: formulations and error estimates*, Computer methods in applied mechanics and engineering **66.3** (1988): 339-363.

[50] A. Y. Kokotov, P. Neittaämaki & B. A. Plamenevskiĭ, *The Neumann problem for the wave equation in a cone*, Journal of Mathematical Sciences **102.5** (2000): 4400-4428.

[51] A. Y. Kokotov & B. A. Plamenevskiĭ, *On the Cauchy– Dirichlet problem for a hyperbolic system in a wedge*, Algebra i Analiz **11.3** (1999): 140–195.

[52] A. Y. Kokotov & B. A. Plamenevskiĭ, *On the asymptotic behavior of solutions to the Neumann problem for hyperbolic systems in domains with conical points*, St. Petersburg Math. J. **16** (2005): 477-506.

[53] K. M. Liew & Y. Cheng, *Complex variable boundary element-free method for two-dimensional elastodynamic problems*, Computer Methods in Applied Mechanics and Engineering **198.49-52** (2009): 3925-3933.

[54] C. Lubich, *Convolution quadrature and discretized operational calculus. I*, Numerische Mathematik **52.2** (1988): 129-145.

[55] C. Lubich, *Convolution quadrature and discretized operational calculus. II*, Numerische Mathematik **52.4** (1988): 413-425.

[56] T. Mach, L. Reichel, M. Van Barel & R. Vandebril, *Adaptive cross approximation for ill-posed problems*, Journal of Computational and Applied Mathematics **303** (2016): 206-217.

[57] G. D. Manolis & D. E. Beskos, *Dynamic stress concentration studies by boundary integrals and Laplace transform*, International Journal for Numerical Methods in Engineering **17.4** (1981): 573-599.

[58] S. I. Matyukevich & B. A. Plamenevskiĭ, *Elastodynamics in domains with edges*, Algebra i Analiz **18** (2006): 158-233.

[59] M. Messner & M. Schanz, *An Accelerated symmetric time-domain boundary element formulation for elasticity*, Engineering Analysis with Boundary Elements **34.11** (2010): 944-955.

[60] G. Mikhailov, *L'Ottocento: matematica. Elasticità e idrodinamica*, su Treccani (2003), https://www.treccani.it/enciclopedia/l-ottocento-matematica-elasticita-e-idrodinamica_%28Storia-della-Scienza%29/

[61] G. Monegato, *Product integration for one-dimensional integral equations of Fredholm type*, Atti Sem. Mat. Fis. Univ. Modena **40.2** (1992): 653-666.

[62] G. Monegato, *The numerical integration of 2-D Cauchy principal value integral arising in boundary integral equation methods*, Mathematics of computation **62.206** (1994): 765-777.

[63] G. Monegato & L. Scuderi, *Numerical integration of functions with boundary singularities*, Journal of Computational and Applied Mathematics **112.1-2** (1999): 201-214.

[64] F. L. Müller & C. Schwab, *Finite Elements with mesh refinement for wave equations in polygons*, Journal of Computational and Applied Mathematics **283** (2015): 163-181.

[65] F. L. Müller & C. Schwab, *Finite elements with mesh refinement for elastic wave propagation in polygons*, Mathematical Methods in the Applied Sciences **39** (2016): 5027-5042.

[66] S. Nicaise, *About the Lamé system in a polygonal or a polyhedral domain and a coupled problem between the Lamé system and the plate equation. I: Regularity of the solutions*, Annali della Scuola Normale Superiore di Pisa-Classe di Scienze **19.3** (1992): 327-361.

[67] T. von Petersdorff, *Randwertprobleme der Elastizitätstheorie für Polyeder-Singularitäten und Approximation mit Randelementmethoden*, Ph.D. thesis, Technische Universität Darmstadt (1989).

[68] B. A. Plamenevskiĭ, *On the Dirichlet problem for the wave equation in a cylinder with edges*, Algebra i Analiz **10** (1998): 197-228.

[69] D. Pölz and M. Schanz, *Space-time discretized retarded potential boundary integral operators: Quadrature for collocation methods*, SIAM journal on scientific computing **41.6** (2019): A3860-A3886.

[70] F. V. Postell & E. P. Stephan, *On the h-, p-and hp versions of the boundary element method: numerical results*, Computer methods in applied mechanics and engineering **83.1** (1990): 69-89.

[71] A. Quarteroni, *Modellistica Numerica per Problemi Differenziali, 4th edition*, Springer Science & Business Media, (2009).

[72] M. Schanz & H. Antes, *A new visco-and elastodynamic time domain boundary element formulation*, Computational Mechanics **20.5** (1997): 452-459.

[73] M. Schanz & H. Antes, *Application of 'operational quadrature methods' in time domain boundary element methods*, Meccanica **32.3** (1997): 179-186.

[74] C. Schwab, *p- and hp- finite element methods: theory and applications in solid and fluid mechanics*, Oxford University Press, (1998).

[75] W. S. Slaughter, *The linearized theory of elasticity*, Springer Science & Business Media, (2012).

[76] T. Toshinawa & T. Ohmachi, *Love-wave propagation in a three-dimensional sedimentary basin*, Bulletin of the Seismological Society of America **82.4** (1992): 1661-1677.

[77] V. S. Vladimirov, *Equations of Mathematical Physics*, MIR, Moscow Russia, (1984).

[78] O. C. Zienkiewicz, R. L. Taylor & J. Z. Zhu, *The finite element method: its basis and fundamentals*, Elsevier, (2005).

Acknowledgements

Three years have passed and I still cannot believe that I am about to discuss my Ph.D. Thesis in Mathematics. This fills me with satisfaction and even more with gratitude to those who have made it possible to achieve this incredible milestone.

First of all, it is my pleasure to acknowledge my Tutor Prof. Alessandra Aimi and my Co-Tutor Prof. Chiara Guardasoni not only for the infinite support and trust they have placed in me as a young researcher, but also for guiding me on this incredible journey without ever leaving me alone and for transmitting me their passion and competence for this field of research.
The friendship that has been created over the years is something I will always be grateful for. I could not have been luckier in having them as mentors.
I would also like to thank Prof. Mauro Diligenti, who I first met at his Numerical Analysis course back when I was a bachelor's degree student. He followed me during part of my doctoral work and made me grow in this field thanks to his precious advice coming from his wisdom and his great experience.

Several of the results presented in this Thesis were obtained thanks to fruitful collaborations with other collegues. Among them, I would like to thank Prof. Heiko Gimperlein and Prof. Ernst Peter Stephan, with which, despite the current pandemic situation, we have been able to start an international collaboration whose outcomes had wide relevance in this Thesis and that I look forward to continuing.
I would also like to thank Dr. Luca Desiderio. I am grateful to him not only for the important scientific results achieved thanks to our collaboration, but also because I have found in him a loyal and sincere friend.

A dutiful acknowledgement goes to Prof. Silvia Falletta and Prof. Martin Schanz, that kindly accepted to review this Thesis and gave me valuable suggestions which allowed me to improve the drafting of this work.

A lifegoal like this is not only a matter of study and hard work. Without the constant help and support of some people who have been close to me I would not have had the resources to face the challenges of these years.

First of all, it is a joy to thank once again Maria and Franco, my beloved parents. What I am and what I have done in my life I owe to them, I could not have asked for parents more loving and present than them. I would also like to thank my older brothers, Fabio and Federico. They have supported me all these years and I have never felt alone in my life because of them.

A mention of honor must be done to Gloria, sister by choice and companion of adventures of a lifetime. The tenacity with which she struggles every day to make her dreams come true is a true inspiration. *For better or worse*, I know that I can always count on her. Thank you my friend!

Last, but not least at all, I must thank my boyfriend Andrea. There are so many things for what I am grateful to him, one hundred pages are not enough to list them all. He always believed in my potential, more than I ever did myself, and with him I know that I will never give up on the challenges that await us in the future. I am sure that for us the best is yet to come!